Computational Explorations of Enhanced Nonlinearities and Quantum Optical Effects in Photonic Nanostructures

Qun Ren

A dissertation submitted in partial fulfillment
of the requirements for the degree of
Doctor of Philosophy
of
University College London.

Electronic and Electrical Engineering
University College London

July 18, 2019

I, Qun Ren, confirm that the work presented in this thesis is my own. Where information has been derived from other sources, I confirm that this has been indicated in the work.

Abstract

In this thesis, we present a comprehensive theoretical analysis and computataional study of optical nonlinearities in the graphene-based and silicon-based metamaterials. The novel numerical methods and corresponding results described in this work give a significant impact on our understanding of surface plasmon resonance in artificial optical materials, which facilitates the design and fabrication of new photonic devices with enhanced nonlinear optical functionalities.

Two generic nonlinear metasurfaces are elaborated in this dissertation, namely, graphene-based metasurfaces and silicon-based metasurfaces. Employing a novel homogenization technique, the effective second-order susceptibility of graphene metasurfaces is calculated, which can be enhanced by more than two orders of magnitude as compared to the intrinsic value of graphene sheet. There is excellent agreement between the predictions of the homogenization method and those based on rigorous numerical solutions of Maxwell equations. Moreover, we also illustrate that the effective Raman susceptibilities of silicon-based metasurfaces can be enhanced by 3 to 4 orders of magnitude as compared to the intrinsic value of silicon. Even though the homogenization method for silicon-based metasurfaces is not as accurate as graphene-based, this result still gives a qualitative analysis on the effective Raman susceptibility of silicon-based metasurfaces.

Additionally, the optical nonlinearity is utilized to design a two-mode quantum waveguide made of coupled silicon photonic crystal nanocavities in the last part of the thesis. Finally, we also explore the implications of our work to the development of new active photonic nanodevices with new or improved functionalities.

Acknowledgements

First of all, I would like to sincere gratitude to my supervisor Prof. Nicolae C. Panoiu for his continuous and patient guidance of my PhD study. His immense knowledge, rich experience as well as his insightful directions helped and inspired me all the time of research and the writing of this thesis. He would always be the greatest benefactor in my professional career. I will always appreciate his guidance and support.

Besides my supervisor, I would also thank my second supervisor Prof. David Selviah who gave me inspiring conversations and advices throughout my time as a PhD student. All the minor corrections he spent time to check for me as well as various of questions he asked during the transfer viva indeed carried me to a good level of researching.

I would also like to show my deep gratitude to my colleagues in Prof. Nicolae C. Panoiu's group (Dr. Jian Wei You, Dr. Zhihao Lan, Dr. Wei. E. I. Sha, Dr. David Zsolt Manrique, Dr. Abiola Oladipo, Dr. Jie You, Dr. Daniel Timbrell, Victor Manuel Fernandez Laguna, Dr. Spyros Lavdas, Dr. Martin Weismann, Yu Pei Wang, Dr. Ivan Sekulic and Dr. Galbadrakh Dagvadorj) as well as the visiting scholars (Han Ying Deng and Cheng Yi Tian) for their help and friendship during my PhD years. In the past years, we together experienced the tough time of solving research difficulties and also had fun time when harvesting various achievements both on study and in life.

Last but not the least, I would like to thank my parents for respecting all of my personal choices in my life. Their warm encouragement and spiritual support mustered up all my courage to face any difficult challenges.

Impact Statement

This thesis mainly theoretically and computationally explores the enhanced optical nonlinearities of different metamaterials, and further studies the quantum dynamics of two-mode photonic nanostructures designed by utilizing optical nonlinearities. In general, our research work is of vital importance for the development and practical uses of nonlinear optics and quantum optics.

The nonlinear optics we studied provides varieties of practical uses such as multi-photon absorption for plasma-materials interaction, coherent light of different wavelengths, materials analysis and spectroscopy, communications and sensors, etc. In particular, the efficient generation of short-wavelength coherent light opens up a wide variety of infrared lasers. Additionally, lasers can make permanent changes in materials through nonlinear optical processes, such as ps and fs pulses which are used for laser machining. Another dominant advanced technology impacted by nonlinear optics is fiber optic telecommunications. Since the nonlinear optics was found to be the fundamental limit to the amount of data that can be transmitted on a single optical fiber, figuring out the threshold of corresponding nonlinear optical processes becomes important for developing the technology in telecommunications.

The theoretical method we used to analyze the enhanced optical nonlinearities of metamaterials is the homogenization method, which is based on field-averaging theory. Field averaging actually provides a useful means of characterizing the effective-medium parameters of an arbitrary metamaterial. It is particularly useful for complex structures in which the transmitted and reflected amplitudes are not easily interpreted by solving Maxwell equations. When the homogenization method is combined with dispersion curve calculations, it would provide a wealth of information distinct and complementary to that obtained by S-parameter analysis and retrieval.

Another research subject we were committed to is quantum dynamics, which is relevant for many burgeoning fields like quantum computing and quantum entanglement. Quantum dynamics is promising to revolutionize computer science and telecommunication. Although most of the investigations on quantum optics is still in theoretical research stage, there are now several laboratories beginning experimental investigations as well.

The quantum optics we researched is playing an important role in the development of todays new technology. For instance, the process of quantum entanglement is now studied with the aim of applying it to stronger cryptography, higher resolution microscopy and other applications. In addition to cryptography, computing and communication would soon rely on high-fidelity readouts of entangled photons that are detected by the most sensitive optical imagers including EMCCD, intensified CCD and sCMOS cameras.

The nonlinear optics and quantum optics we explored are rapidly growing fields of science as they have been generating huge interest in many new and exciting optical phenomena and a plethora of important emerging applications in active photonic nanodevices, integrated photonics, optoelectronics, etc. The pace at which research in photonic nanostructures has been expanding also predicts that many exciting new physics pertaining to the nonlinear optics and quantum optics are yet to be explored. These impending future developments will bring about more novel photonic nanodevices with new or improved functionalities.

List of Journal Publications

1. Qun Ren, Jian Wei You and Nicolae C. Panoiu, "Giant enhancement of the effective Raman susceptibility in metasurfaces made of silicon photonic crystal nanocavities," *Optics Express* **26**, 30383-30392 (2018).
2. Qun Ren, Jian Wei You and Nicolae C. Panoiu, "Enhancement of effective second-harmonic optical nonlinearities of graphene-based metasurfaces," *Phys. Rev. B* **99**, 205404 (2019).
3. Qun Ren, Jian Wei You and Nicolae C. Panoiu, "Comparison of homogenization approach on graphene and silicon-based metasurfaces," *J. Opt.* (under review)
4. Qun Ren, David Zs. Manrique and Nicolae C. Panoiu, "Light transport in two-mode Raman quantum waveguides made of coupled photonic crystal nanocavities," *Phys. Rev. A* (to be submitted)

List of Conference Publications

1. [invited] Qun Ren, Jian Wei You and Nicolae C. Panoiu, "Large enhancement of effective Raman susceptibility of a metasurface made of silicon photonic crystal cavities," *PIERS 2018, Toyama*, 1-4 Aug.
2. Qun Ren, Jian Wei You and Nicolae C. Panoiu, "Enhanced optical nonlinearity of metasurfaces made of patterned graphene nanoribbons," *Advanced Photonics 2018 Congress*, 2-5 July, ETH, Zurich, Switzerland.
3. Qun Ren, Jian Wei You and Nicolae C. Panoiu, "Enhancement of effective second- and third-order optical nonlinearities of graphene-based metasurfaces," *Photon 2018*, 3-6 September 2018, Aston University, Birmingham, UK.
4. Victor Manuel Fernandez Laguna, Qun Ren and Nicolae C. Panoiu, "Pulsed dynamics in a system of coupled silicon photonic crystal cavity-waveguide nanostructures," *SPIE Optics + Photonics 2019*, 11-15 August 2019, San Diego, California, United States.
5. Victor Manuel Fernandez Laguna, Qun Ren and Nicolae C. Panoiu, "Optical Pulse Dynamics in a Silicon Photonic Crystal Waveguide Coupled with a set of Photonic Crystal Optical Cavities," *International Workshop on Optical Wave and Waveguide Theory and Numerical Modelling*, Malaga, Spain, 10-11 May, 2019.
6. J. W. You, Qun Ren, and N. C. Panoiu, "Strongly Enhanced Second- and Third-harmonic Generation in Graphene Metasurfaces," *19th IEEE International Conference on Nanotechnology*, Parisian Macao, Macau, China, 22-26 July 2019.

List of notations and acronyms

1D, 2D, 3D	one-dimensional, two-dimensional, three-dimensional
AGNR	armchair graphene nanoribbons
BDT	benzodithiophene
CGNR	chiral graphene nanoribbons
DNG	double negative materials
ε_0	electric permittivity of vacuum (8.854 $\times 10^{12} F \cdot m^{1}$)
ε	electric permittivity
ε_r	relative electric permittivity
EM	electromagnetic
FF	fundamental frequency
FDTD	finite-difference time-domain method
GQD	graphene quantum dots
GNR	graphene nanoribbons
LHM	left-handed materials
λ	wavelength
NIM	negative-refractive index materials
NP	nanoparticles
ν_0	magnetic permeability of vacuum (1.257 $\times 10^{6} H \cdot m^{1}$)
ν	magnetic permeability
ν_r	relative magnetic permeability
PhC	photonic crystal
PCB	printed circuit boards
RHM	right-handed materials
SHG	second-harmonic generation
SRR	split-ring resonators
SPP	Surface plasmon polaritons
TPL	two-photon luminescence
ZGNR	zigzag graphene nanoribbons

Contents

List of Figures

Chapter 1

Introduction

Research in photonics, aiming at utilizing the distinct characteristics of light and light-matter interaction in different nanostructures, plays an essential role in the field of science and engineering nowadays. It covers the fields of nonlinear optics, classical optics, and quantum optics. Research on photonic devices and materials nowadays enables an exciting platform on which various photonic applications are increasingly achieved and employed. In addition, a wide range of photonic applications are emerging with the rapid advancement of photonics technology, like lasers, biological and chemical sensing, telecommunications, information processing and solar cells.

Photonic technology has gone through a long and rich history, which laid the foundation for current silicon photonics and further growth of photonics. In the early 1990s, the photonic crystals developed but they operate only in the "microwave" regime. Then 3D photonic crystals based on alignment and stacking emerged, which can control spontaneous emission as well as the interaction of light to the surfaces of materials [1]-[5]. Calculation and fabrication techniques developed for 3D photonic crystals also induced rapid progress in the field of photonics [8]-[9]. The next stage of photonics technology is manipulating and trapping photons by introducing a cavity within a 2D photonic crystal [11]-[10]. Afterwards, research on photonics focus on increasing and controlling the Q factor of photonic crystal nanocavity. Researchers found that by shifting the edge air holes of the nanocavity to make it larger, the Q factor can be increased by several orders of magnitude [12]. Subsequently, overcoming the limited understanding of light-matter interaction with photonic crystals, the quantum applications stepped into researchers' attention [16]-[20]. One of the developments in this research area is to combine the high-Q nanocavity with quantum dots to introduce a strong coupling. Another significant progress is applying coupled cavities to realize flexible architecture and on-demand dynamic control without cross talk.

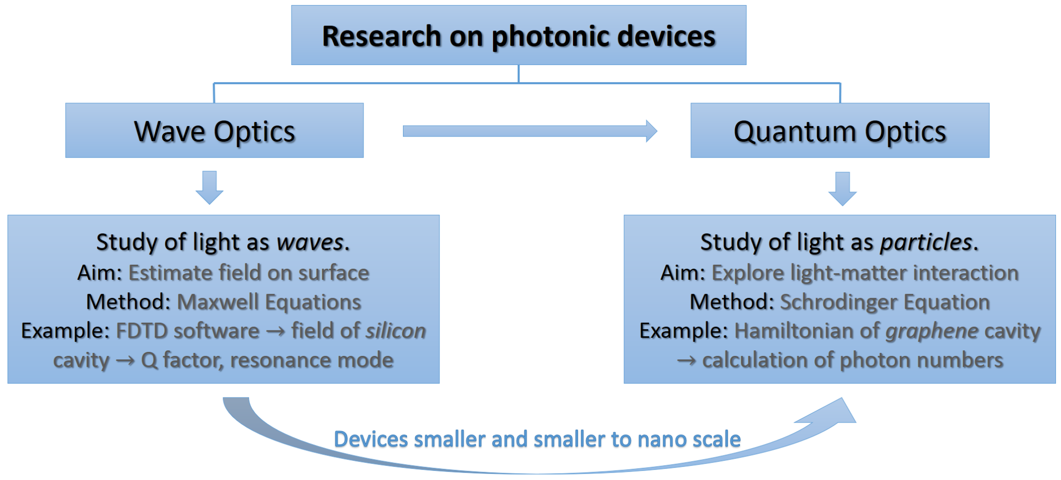

Figure 1.1: Profile of introduction.

The advancement of photonics ranges from wave optics to quantum optics, minimizing the photonic devices and quantizing the optical field. Although we have progressed significantly on fabrication and manipulation of photonic devices, there are still quite a few sub-domains to explore and perfect. For our project, these two parts of nanophotonics (wave optics and quantum optics) are included, which we will present the details in the later chapters. Here we just introduce the two branches.

Wave optics, principally founded on classical Maxwell equations, is the study of light as electromagnetic waves. Specifically, it realizes the light confinement within certain photonic nanostructures. Using certain software based on finite-difference time-domain (FDTD) method, research in wave optics aims mainly to estimate the electromagnetic field of specific material structure. In our case, we investigate a photonic crystal nanocavity waveguide made of silicon, where a high-index contrast lattice creates ”photonic bandgaps”, so as to forbid light propagation beyond the cavity defect. We also calculate the resonance modes and corresponding quality factors of our designed structure, which could characterize valuable properties of nanocavity. In many applications, high Q and small volume are highly desired for the high finesse required for laser and filters. From small-scale but high-quality nanocavities to ultra-compact waveguides, various issues of light confinement phenomena and near-field optics have already been included in several books [21]-[25]. However, soon after the classical photonic devices no longer meet the increasing demand of extremely tiny devices with excellent optical properties, the quantum devices emerge in quite a few areas in photonics technology.

Quantum optics, which deals with the light-matter interaction in phtonic nanostructures, is the study of light as particles known as photons [26]-[28]. Since the light as well as its energy and momentum are quantized, the classical Maxwell equations must be modified when used. On the contrary, theory of quantum mechanics come in handy now: light is described in terms of field operators for creation and annihilation of photons, i.e. in the language of quantum electrodynamics. Additionally, in quantum optics, atoms are now considered as quantum mechanical oscillators with a discrete energy spectrum, with the transitions between the energy eigenstates being driven by the absorption or emission of light according to Einstein's theory. There are many sub-domains within quantum optics for people to explore, like coincidence correlation, quantum communication, quantum entanglement and quantum information processing [29]-[34]. In any event, building the Hamiltonian of the specific system is the key step to obtaining the density matrix, which is the critical variable to calculate expected values for various quantities, such as the expected number of photons. One research topic in my thesis is just about simulating the photon number rate in time domain for coupled-cavity waveguides. The next section will describe the objectives of this thesis in more detail.

1.1 Main Objectives of the Thesis

In this thesis, two main objectives are to be achieved, and are related both to the classical optics as well as quantum optics.

The first objective, which is founded in the classical physics, is related to the investigation of the linear and nonlinear optical response of two generic metasurfaces (graphene-based metasurface and silicon photonic crystal metasurface) and their corresponding homogenized counterparts. The metasurface is a single layer of metamaterial, which is formed by arranging many tiny structural elements in a periodic manner and possesses significant optical properties that cannot be achieved naturally. In particular, using the homogenization method, the corresponding effective nonlinear susceptibilities (effective second-order susceptibility and effective Raman susceptibility) are calculated and compared with the intrinsic values of pristine materials. Our investigation revealed that the effective nonlinear susceptibilities of both the homogenized metasurfaces are enhanced by several orders of magnitude.

In the case of graphene-based metasurfaces, the graphene-nanoribbon, graphene-rectangle and graphene-cruciform constituents are considered, respectively. Several physical quantities characterizing the original and homogenized metasurfaces are compared, such as the optical absorption, transmittance and reflectance. Our analysis revealed that for graphene metasurfaces whose unit cell has characteristic size of a few hundreds of nanometers, there is an excellent agreement between the predictions of the homogenization method and the results obtained by rigorously solving the Maxwell equations (calculation without approximation), which is explained by the fact that the characteristic size of graphene resonators is much smaller than their resonance wavelength.

In so far as the silicon photonic crystal (PhC) metasurfaces consisting of a periodic distribution of specially engineered PhC cavities are concerned, the effective Raman susceptibility of the nonlinear metasurface, calculated using the same homogenization technique, is significantly larger than the intrinsic Raman susceptibility of silicon. In order to achieve this dramatic enhancement of the nonlinear optical response of the metasurface, the basic constituents of the silicon-based metasurface are the PhC cavities which possess two optical modes separated by the Raman frequency of silicon. One can achieve large optical field enhancement at both the pump and Stokes frequencies. This homogenization method is also valid even when the period of the metasurface is comparable or larger than the wavelength of the interacting beams.

The second objective based on quantum optics centers upon the photon propagation through a two-mode light-guiding waveguide consisting of coupled photonic nanocavities made of silicon. Since Hamiltonian is the crux of solving problems on quantum dynamics, we need to start with constructing the creation and annihilation operators which make up the system Hamiltonian. Here we should take the consideration of the potential energy for each particle as well as the interaction between the particles. After figuring out the system Hamiltonian, we could in turn readily obtain the density matrix, photon number, as well as transmission rates.

The optical nanocavities are designed to have high-quality-factor optical modes whose frequency separation is equal to the Raman frequency of silicon, so that the quantum waveguide can be used as a Raman amplifier. The novelty of this work is coupling any amount of nanocavities to realize the quantum manipulation of light in waveguides. This research work also provides a valuable reference for practical applications in quantum interconnects and quantum information processing, which aim at guiding light in nanostructures at a quantum level.

1.2 Outline

In Chapter 2, we give an overview of the basic concepts and principles for this thesis. The fundamentals of graphene are firstly illustrated in detail so as to pave the way for quantum computation of coupled graphene structures. Then we also introduce the primary theory of silicon photonics from the perspective of classical physics. The final part is about the quantum electrodynamics techniques, which shows how to establish the Hamiltonian as well as to derive the density matrix of the system.

In Chapter 3, we demonstrated that stimulated Raman amplification can be enhanced by more than four orders of magnitude in a silicon metasurface consisting of a periodic distribution of specially engineered PhC cavities in a silicon PhC slab waveguide. In particular, by designing the PhC cavities so that they possess two optical modes separated by the Raman frequency of silicon, one can achieve large optical field enhancement at both the pump and Stokes frequencies. As a consequence, the effective Raman susceptibility of the nonlinear metasurface, calculated using a novel homogenization technique, is significantly larger than the intrinsic Raman susceptibility of silicon. Implications to technological applications of our theoretical study are discussed, too.

In Chapter 4, we discussed about one- and two-dimensional graphene metasurfaces, which are homogenized both at the fundamental frequency (FF) and second-harmonic (SH) using a powerful homogenization technique. In both cases, there is excellent agreement between the predictions of the homogenization method and those based on rigorous numerical solutions of Maxwell equations. The homogenization technique is then employed to demonstrate that, owing to a double-resonant plasmon excitation mechanism that leads to strong, simultaneous field enhancement at the FF and SH, the effective second-order susceptibility of graphene metasurfaces can be enhanced by more than three orders of magnitude as compared to the intrinsic second-order susceptibility of a graphene sheet placed on the same substrate. In addition, we explore the implications of our results to the development of new active nanodevices that incorporate nanopatterned graphene structures.

In Chapter 5, we used a versatile homogenization approach to model the linear and nonlinear optical response of two metasurfaces: a plasmonic metasurface consisting of a square array of graphene cruciform patches and a dielectric metasurface consisting of a rectangular array of photonic crystal (PhC) cavities in a silicon PhC slab waveguide. The former metasurface is resonant at wavelengths that are much larger than the graphene elements of the metasurface, whereas the resonance wavelengths of the latter one are comparable to the size of its resonant components. By computing and comparing the effective permittivities and nonlinear susceptibilities of the two metasurfaces, we derive some general principles regarding the conditions under which homogenization methods of metallic and dielectric metasurfaces are valid. In particular, we show that in the case of the graphene metasurface the homogenization method describes very well both its linear and nonlinear optical properties, whereas in the case of the silicon PhC metasurface the homogenization method is less accurate because the size of silicon unit cell is comparable with the resonance wavelength.

In Chapter 6, we studied at the quantum level the optical properties of light propagation in a quantum waveguide consisting of coupled photonic nanocavities made of silicon. The optical nanocavities are designed to have high-quality-factor optical modes whose frequency separation equals the Raman frequency of silicon, so that two resonance modes (pump mode and Stokes mode) exist in each nanocavity. In order to describe the quantum transport of photons in this waveguide, we firstly construct a Hamiltonian that describes the photon number at the pump and Raman frequencies, and subsequently use the corresponding equations of motions to compute the photon dynamics with different physical quantities of the quantum system. Practical implications of our theoretical analysis are considered, too.

In Chapter 7, we presented a rigorous approach to derive the Hamiltonian of graphene nanostructures and the coupling between two graphene patterns with different spacings. This part is essentially grounded in the quantum physics principle and provides a foundation for our later research on functional graphene.

Chapter 8 is about theory of scattering and diffraction of electromagnetic waves for core-gap-shell nanoparticles and numerical simulations for modelling corresponding experimental results. In particular, we will first discuss the experimental results on scattering, near field intensity and two-photon luminescence (TPL) of core-gap-shell nanoparticles (NPs), and then we present theoretical and numerical methods that are commonly used to study electromagnetic wave scattering problems. In the end, we compare the computational results with the corresponding experimentally measured values.

The main conclusions of this thesis will be summarized in Chapter 9 and the contributions of this work to the fields of nonlinear optics and quantum optics will be highlighted. Future prospects for extending this work are also presented in this concluding chapter.

Bibliography

[1] S. Noda, K. Tomoda, N. Yamamoto, and A. Chutinan, "Full three-dimensional photonic bandgap crystals at near-infrared wavelengths," Science **289** 604-606 (2000).

[2] K. Ishizaki and S. Noda, "Manipulation of photons at the surface of three-dimensional photonic crystals," Nature **460** 367 (2009).

[3] S. Ogawa, M. Imada, S. Yoshimoto, M. Okano, and S. Noda, "Control of light emission by 3D photonic crystals," Science, **305** 227-229 (2004).

[4] S. Noda, M. Fujita, and T. Asano, "Spontaneous-emission control by photonic crystals and nanocavities," Nat. Photonics **1** 449 (2007).

[5] S. Takahashi, K. Suzuki, M. Okano, M. Imada, T. Nakamori, Y. Ota, and S. Noda, "Direct creation of three-dimensional photonic crystals by a top-down approach," Nat. Mater. **8** 721 (2009).

[6] S. Kawashima, K. Ishizaki, and S. Noda, "Light propagation in three-dimensional photonic crystals," Opt. Exp. **18** 386-392 (2010).

[7] S. Ogawa, K. Ishizaki, T. Furukawa, and S. Noda, "Spontaneous emission control by 17 layers of three-dimensional photonic crystals," Electron. Lett. **44** 377-378 (2008).

[8] D. C. Dobson, J. Gopalakrishnan, and J. E. Pasciak, "An efficient method for band structure calculations in 3D photonic crystals," J. Comput. Phys. **161** 668-679 (2000).

[9] T. Ding, K. Song, K. Clays, and C. H. Tung, “Fabrication of 3D photonic crystals of ellipsoids: convective selfassembly in magnetic field,” Adv. Mater. **21** 1936-1940 (2009).

[10] B. S. Song, S. Noda, T. Asano, and Y. Akahane, “Ultra-high-Q photonic double-heterostructure nanocavity,” Nat. Mater. **4** 207 (2005).

[11] S. Noda, A. Chutinan, and M. Imada, “Trapping and emission of photons by a single defect in a photonic bandgap structure,” Nature **407** 608 (2000).

[12] Y. Akahane, T. Asano, B. S. Song, and S. Noda, “High-Q photonic nanocavity in a two-dimensional photonic crystal,” Nature **425** 944 (2003).

[13] B. S. Song, S. Noda, T. Asano, and Y. Akahane, “Ultra-high-Q photonic double-heterostructure nanocavity,” Nature materials **4** 207 (2005).

[14] B. S. Song, S. Noda, and T. Asano, “Photonic devices based on in-plane hetero photonic crystals,” Science **300** 1537-1537 (2003).

[15] Y. Akahane, T. Asano, B. S. Song, and S. Noda, “Fine-tuned high-Q photonic-crystal nanocavity,” Opt. Express **13** 1202-1214 (2005).

[16] H. Benisty, J. M. Lourtioz, A. Chelnokov, S. Combrie, and X. Checoury, “Recent advances toward optical devices in semiconductor-based photonic crystals,” Proc. IEEE **94** 997-1023 (2006).

[17] S. Strauf, K. Hennessy, M. T. Rakher, Y. S. Choi, A. Badolato, L. C. Andreani, and D. Bouwmeester, “Self-tuned quantum dot gain in photonic crystal lasers,” Phys. Rev. Lett. **96** 127404 (2006).

[18] K. Hennessy, A. Badolato, M. Winger, D. Gerace, M. Atature, S. Gulde, and A. Imamoglu, “Quantum nature of a strongly coupled single quantum dotcavity system,” Nature **445** 896 (2007).

[19] M. Nomura, N. Kumagai, S. Iwamoto, Y. Ota, and Y. Arakawa, “Photonic crystal nanocavity laser with a single quantum dot gain,” Opt. Express **17** 15975-15982 (2009).

[20] D. Englund, A. Faraon, I. Fushman, N. Stoltz, P. Petroff, and J. Vuckovic, “Controlling cavity reflectivity with a single quantum dot,” Nature **450** 857 (2007).

[21] M. Born and E. Wolf. *Principles of Optics* (New York: MacMillan, 1964).

[22] A. Yariv and P. Yeh. *Optical Waves in Crystals* (New York: John Wiley and Sons, 1984).

[23] J. D. Joannopoulos, R. D. Meade and J. N. Winn. *Photonic Crystals: Molding the Flow of Light* (Princeton: University Press, 1995).

[24] L. Novotny and B. Hecht. *Principles of Nano-Optics* (Cambridge: Cambridge University Press, 2007).

[25] A. M. Zheltikov. *Optics of Microstructured Fibers* (Moscow: Nauka, 2004) - in Russian.

[26] Y. Yamamoto, F. Tassone and H. Cao. *Semiconductor Cavity Quantum Electrodynamics* (Berlin: Springer-Verlag, 2000).

[27] V. P. Bykov. *Radiation of Atoms in a Resonant Environment* (Singapore: World Scientific, 1993).

[28] D. S. Mogilevtsev and S. Ya. Kilin. *Quantum Optics Methods of Structured Reservoirs.* (Minsk: Belorusskaya Nauka, 2007) in Russian.

[29] L. M. Duan, M. D. Lukin, J. I. Cirac, and P. Zoller, “Long-distance quantum communication with atomic ensembles and linear optics,” Nature **414** 413 (2001).

[30] N. Gisin, and R. Thew, “Quantum communication,” Nat. Photonics **1** 165 (2007).

[31] N. D. Mermin, “Extreme quantum entanglement in a superposition of macroscopically distinct states,” Phys. Rev. Lett. **65** 1838 (1990).

[32] R. Horodecki, P. Horodecki, M. Horodecki, and K. Horodecki, “Quantum entanglement,” Rev. Mod. Phys. **81** 865 (2009).

[33] C. H. Bennett, and D. P. DiVincenzo, “Quantum information and computation,” Nature **404** 247 (2000).

[34] A. Imamog, D. D. Awschalom, G. Burkard, D. P. DiVincenzo, D. Loss, M. Sherwin, and A. Small, “Quantum information processing using quantum dot spins and cavity QED,” Phys. Rev. Lett. **83** 4204 (1999).

Chapter 2

Background

In this chapter, we present the background knowledge for the three branches of my research. The first part introduces the elementary information of graphene, such as the electronic structure, conductivity, absorption, as well as the Hamiltonian. In the second section, we present the theory of photonic crystals in detail. Starting from Maxwell equations in periodic structures, we show the basic properties of photonic crystals and how the band structures of 1D, 2D and 3D photonic crystals look like. The third part is about the concepts of quantum optics, which illustrate the quantum principle of radiation, light-matter interaction, as well as the quantum theory of damping. The specific explanations for each part are elucidated in the following sections.

2.1 Fundamentals of Graphene

In recent years there has been increasing research and development on a crystalline form of carbon called graphene, due to its remarkable characteristics. Graphene is a form of a 2D plane honeycomb crystal lattice and has excellent mechanical, electrical, optical and chemical properties, which might lead to flexible touch-screen displays, new composite materials, terahertz electronics, graphene sensors, graphene plasmonic devices and many other applications [4]-[6]. Until 2004, it was believed that a single monolayer of graphene could not be fabricated because it is unstable in free form, until it was isolated at Manchester University by Andre Geim and Konstantin Novoselov [7]. The excellent electronic properties of graphene are due to the fact that graphene is a 2D zero-gap (no bandgap between the conduction band and valence band) semiconductor with high electron mobility, which supports good charge flow. Pristine graphene is almost transparent with only 2.3 percent light absorption of incident visible light (380∼740nm), which can be changed by doping. Figure 2.1 shows the arrangement of carbon atoms in graphene.

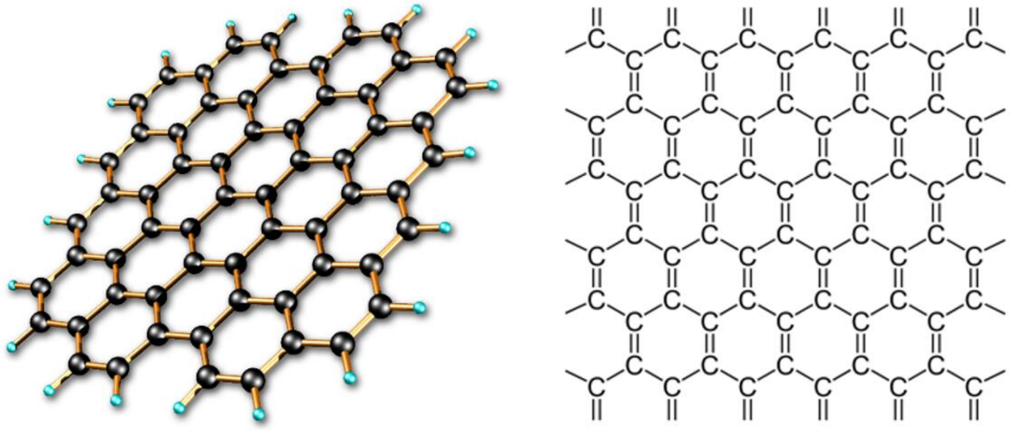

Figure 2.1: Arrangement of carbon atoms in graphene lattice.

Since its discovery in 2004, there has been an intense theoretical and experimental research on properties and potential applications of graphene, including light-emitting diodes, touch panels, and smart windows [9]-[10]. Being only one atom thick, it is the thinnest known material. Nevertheless, the largest size of graphene that could be produced until recently was only few square centimeters. However, it is already used as a means to increase mechanical and electrical properties of other materials, and the developments in this area have been remarkable [11]-[12].

2.1.1 Electronic Structure and Properties of Graphene

Graphene, a single atomic layer of graphite, is an allotrope of carbon that is made up of very tightly bonded carbon atoms organised into a hexagonal lattice. In this part, we discuss several properties of graphene, including electronic configuration, band structure as well as conductivity.

Electronic Configuration and Band Structure

Carbon is a group-four element with six electrons, two of which form a closed shell $1s^2$, and remaining four fill states $2s$ and $2p$, leading to a ground state configuration $2s^2 2p^2$. When a solid is formed, total energy decreases due to the overlapping of the electron wavefunctions and the forming of energy bands. In graphene lattice, only the two electrons in the $2p$ orbital are taking part in conduction, the other four are closely bound to the nucleus and practically cannot be excited to higher energy levels. The shape of the orbitals of the conducting electrons in each carbon atom ($2p_z$ orbital) is shown in Fig. 2.2 (a).

In the lattice, bands are formed out of the overlapping individual electrons wavefunctions resulting in the shape shown in Fig. 2.2 (b). The conduction and valence bands are touching at the K and K' symmetry points (conical points) at energy coinciding with Fermi level (in undoped material). The valence band is therefore completely filled, while the conduction band is empty, making graphene a gapless semiconductor. A formal similarity between ultrarelativistic particles (with energy much larger than the rest energy mc^2, such that one can consider the particles as massless) and electrons in graphene makes graphene a platform on which to study various quantum relativistic effects. The zero gap and high mobility of the electrons make the transfer of charge in graphene extremely fast (the relationship between the electrical conductivity σ and electron mobility μ_e: $\sigma = ne\mu_e$), which leads to its excellent conductive properties.

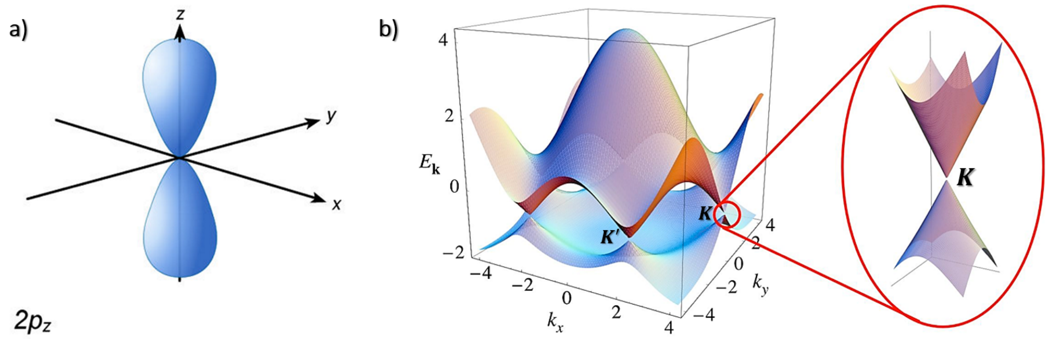

Figure 2.2: a) 3D plot of the wavefunction of 2pz orbital, b) Energy bands in graphene [8].

Conductivity in Graphene

As illustrated in the above discussion, one of the most useful properties of graphene is zero-overlap semimetal (with both holes and electrons as charge carriers) with extremely high electrical conductivity. Each carbon atoms has 6 electrons: 2 in the inner shell and 4 in the outer shell. The combination of one s-orbital with only two p-orbitals, namely orbital p_x and p_y, is the sp^2 hybridization, which forms the σ-bond. The additional p_z-orbital is perpendicular to the sp^2-hybrid orbitals. In other words, the 4 outer shell electrons in an individual carbon atom are available for chemical bonding, but for graphene, each atom is connected to 3 other carbon atoms on the two dimensional plane, leaving 1 electron freely available in the third dimension for electronic conduction (the sp^2-hybrid orbitals are not conducive to the conductivity of graphene).

Combined research over the last 50 years has proved that at the Dirac point in graphene, electrons and holes have zero effective mass (E-k relation is linear for low energies near the six corners of the two-dimensional hexagonal Brillouin zone of graphene, leading to zero effective mass for electrons and holes) [13]. This occurs because the energy-momentum relation (the spectrum for excitations) is linear for low energies near the 6 individual corners of the Brillouin zone. These electrons and holes are known as Dirac fermions, or Graphinos, and the 6 corners of the Brillouin zone are known as the Dirac points. Due to the zero density of states at the Dirac points, electronic conductivity is actually quite low. However, the Fermi level can be changed by doping (with electrons or holes) to create a material that is potentially better at conducting electricity than, for example, copper at room temperature.

Experiments have shown that the electronic mobility of graphene is very high, with previously reported results above $15\,000\,\mathrm{cm^2\,V^{-1}\,s^{-1}}$ and theoretically potential limits of $200\,000\,\mathrm{cm^2\,V^{-1}\,s^{-1}}$ (limited by the scattering of graphenes acoustic phonons) [14]. Graphene electrons act very much like photons in their mobility due to their lack of mass. These charge carriers are able to travel sub-micrometer distances without scattering, a phenomenon known as ballistic transport. However, the quality of the graphene and the substrate that is used will be the limiting factors. With silicon dioxide as the substrate, for example, mobility is potentially limited to $40\,000\,\mathrm{cm^2\,V^{-1}\,s^{-1}}$ [14].

Absorption in Graphene

Considering that graphene is only 1 atom thick, the ability to absorb 2.3 % of white light is also a unique and interesting property of graphene. This is due to its aforementioned electronic properties, namely, the electrons acting like massless charge carriers with very high mobility. A few years ago, it was proved that the amount of white light absorbed is based on the fine structure constant, rather than being dictated by material specifics [16]. Adding another layer of graphene increases the amount of white light absorbed by approximately the same value (2.3%). The opacity of graphene ($\pi\alpha \approx 2.3$ %) equates to a universal dynamic conductivity value of $G = \frac{e^2}{4\hbar}$ (2~3%) over the visible frequency range [17].

Various properties like conductivity or absorption can be modified by doping or patterning the graphene lattice. It was demonstrated that arrays of doped graphene nanodisks show 100% absorption when supported on a substrate under total internal reflection and also when lying in a dielectric layer coated metal [18]. Doped graphene, on the other hand, is predicted to have strong confinement and long-lived plasmons, which produce sharp IR resonances in nanodisks. This is an important discovery as light absorption plays an essential role in optical detectors and photovoltaics. The absorption cross-section of graphene might exceed the geometrical cross-section. Potentially this characteristic can be exploited to make very efficient and precise sensors.

2.1.2 Electronic States and Hamiltonian

In general, in quantum physics, the key step is to study the Hamiltonians of particular dynamic system. As illustrated in Fig. 2.3, there are in total four cases when it comes to the Hamiltonian description of graphene.

For non-relativistic quantum mechanics, the Hamiltonian reads

$$H = \frac{p^2}{2m_e} \tag{2.1}$$

with m_e denoting an effective mass and p the momentum, whilst the motion of charge carriers in condensed matter physics is described by the Schrodinger equation.

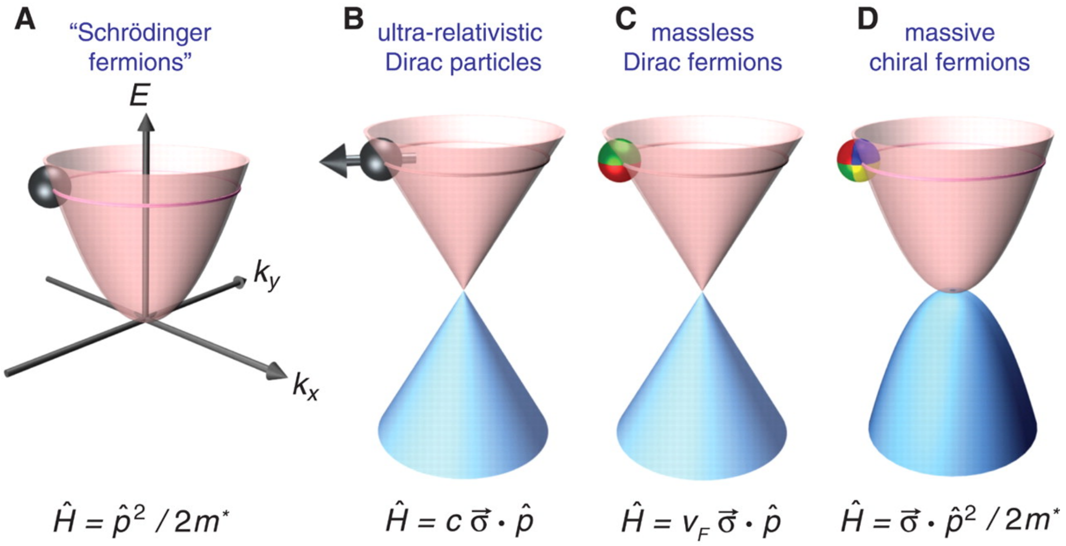

Figure 2.3: 4 profiles to describe graphene Hamiltonian: (a) Charge carriers in condensed matter physics are normally described by the Schrodinger equation. (b) Relativistic particles in the limit of zero rest mass follow the Dirac equation. (c) Charge carriers in graphene are called massless Dirac fermions and are described by a 2D analog of the Dirac equation. The pseudospin can be indicated by color (e.g., red and green). (d) Bilayer graphene provides us with yet another type of quasi-particles that have no analogies. The pseudospin changes its color index four times as it moves among four carbon sublattices [19].

For ultra-relativistic particles with zero rest mass, substituting the Dirac equation, the Hamiltonian becomes

$$H = c\overrightarrow{\sigma}\cdot\widehat{p} \tag{2.2}$$

with c denoting the speed of light, and the σ matrices are the standard 2×2 Pauli matrices, which are related to particle spins.

For charge carriers in monolayer graphene, which are categorized as massless fermions, the energy band is described by a 2 by 2 Hamiltonian matrix

$$\widehat{H} = v_F \begin{pmatrix} 0 & k_x - ik_y \\ k_x + ik_y & 0 \end{pmatrix} = v_F\overrightarrow{\sigma}\cdot\overrightarrow{p} \tag{2.3}$$

labelled by two indices denoting different sublattices, where the Fermi velocity $v_F \approx 1 \times 10^6$ m/s plays the role of the speed of light and a 2D pseudospin matrix $\overline{\sigma}$ describes two sublattices of the honeycomb lattice. The dynamics of the quasi-particles are determined by a 2D analogue Dirac equation, with Fermi velocity playing the role of speed of light and pseudo spin matrix describing sublattices.

Bilayer graphene provides a new type of quasi-particle known as massive chiral fermions, which has no analogies in existing quantum theory. The Hamiltonian of this system

$$H = \frac{\overrightarrow{\sigma} \cdot \widehat{p}^2}{2m} \tag{2.4}$$

combines both non-relativistic and relativistic features.

In summary, Fig. 2.3 provides a visual outline of how much our quantum playgrounds have expanded since the experimental discovery of graphene. The very different description of graphene crystal gives rise to a wide range of new physics phenomena to be further studied and understood.

2.1.3 Surface Plasmons

A plasmon is a quantum of plasma oscillation, a quasiparticle, similarly to a phonon being a quantum of mechanical vibration. Since they were first predicted in 1957 [24], subsequently it was proved that the usual reflection and transmission theory is not applicable to materials for which the surface electrodynamic polarization waves can propagate.

Surface plasmons (SPs) are oscillations of free electron density. Surface plasmons can be excited by photons and electrons. The theory behind plasmon origins is the following: when electrons move to screen an electric field, they tend to overshoot the mark. They are then pulled back towards the charge disturbance and overshoot again, setting up a weakly damped oscillation [25]. The SP resonance can be achieved when the frequency of light photons matches the natural frequency of surface electrons [26]. SPs in graphene are different to those in noble metals as they can be tuned by doping, are confined to smaller regions and do not show Ohmic losses [27]. The dispersion relation of a wave propagating on the surface can be expressed as

$$k = \frac{\omega}{c}\left(\frac{\varepsilon_1 \varepsilon_2}{\varepsilon_1 + \varepsilon_2}\right)^{\frac{1}{2}} = \frac{2\pi}{\lambda} \tag{2.5}$$

where k is the wavenumber, ε_1 and ε_2 are permittivities of the two media (metal and air), ω is the frequency and c the speed of light.

When photons hit the surface and couple with a SP, a surface plasmon polariton (SPP) is created. A SPP can propagate along the surface until it loses its energy. Graphene possesses intrinsic plasmons that are tunable, but a combination of graphene with noble-metal nanostructures promises a variety of exciting applications for conventional plasmons. Combining graphene with conventional plasmonics in metals could enhance optical properties of graphene, create graphene plasmonic photocells and other devices [15].

The schematic representation of an electron density wave propagating along a metal-dielectric interface is shown in Fig. 2.4. The charge density oscillations and associated electromagnetic fields are called surface plasmon-polariton waves. The exponential dependence of the electromagnetic field intensity on the distance away from the interface is colored by orange on the right. These waves can be excited very efficiently with light in the visible range of the electromagnetic spectrum.

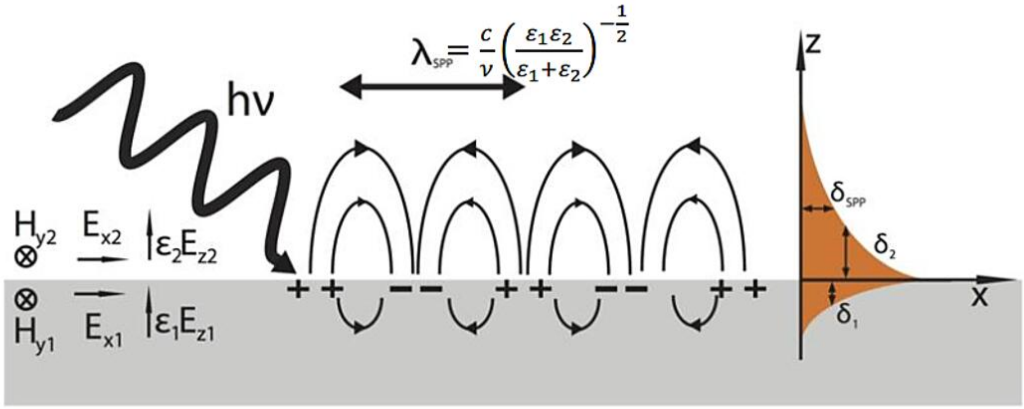

Figure 2.4: Sketch of a surface plasmon illustrating its propagation along the metal-dielectric boundary, the intensity of the evanescent fields in each layer, and showing the direction and variables names for fields involved. Equation in the figure is rearranged Eq. (2.5) [28].

Exciting Plasmons and Reducing Damping in Graphene

The advancement of nanophotonic devices demands the capability of confining light at scales much smaller than the wavelength of light. One, and perhaps the only, viable strategy for accomplishing this goal is to use surface plasmons and light at the interface between a conductor and a dielectric. Tight confinement can be attained at light frequencies close to the resonance frequency of the conductor because the plasmon wavelength is generally much smaller than the wavelength of light in air. A shorter wavelength implies a smaller diffraction limit in the plane of propagation, and thus rapid exponential decay (scaled by the plasmon wavelength) of the electromagnetic field away from the interface.

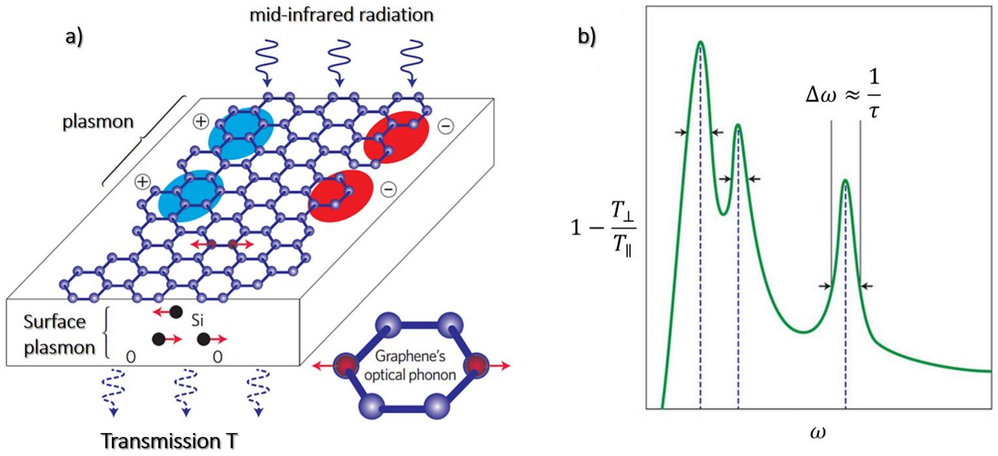

Figure 2.5: a) Illustration of plasmons, photon and experimental set-up. b) The characteristic response (excitation spectrum) used to measure the frequency and lifetime of plasmonic excitations. The peak correspond to coupled plasmon surface phonon modes, and their widths (damping rates) correspond to edge scattering and interaction with graphene's optical phonons [31].

The way to excite plasmons in graphene nanostructures was explored in recent years [29]. The experiment described in Ref. [29] is depicted in Fig. 2.5. Additionally, since there is a big obstacle of shorter propagation lengths (greater damping) of plasmonic excitations resulting from the strong interaction of light with the lossy conductor, these researchers also determined some of the damping pathways for mid-infrared plasmons. Graphene ribbons 50∼250 nm wide were placed on a dielectric substrate and then illuminated from above by mid-infrared radiation with wavelengths in the range of 4∼15 μm. The transmission of radiation through this system was measured, which provided information on the excitations in the system at a given frequency and wavenumber. The key result is the ability to disentangle various mechanisms that induce plasmon damping. The plasmon linewidth was found to increase greatly with decreasing ribbon width, indicating a dominant contribution from edge scattering effects. Furthermore, a substantial increase in the plasmon linewidth was observed at excitation energies higher than the energy of graphene's intrinsic optical phonons (a type of lattice vibration) at 1,580 cm^{-1} (0.2 eV, or a wavelength of $\sim$6 μm for photons in air); this indicates a damping channel through which a plasmon excites an optical phonon and an electron-hole pair.

The desirable strong subwavelength confinement of light is associated with the dilemma to excite plasmons experimentally. The plasmon wavelength can be much smaller than the wavelength of free-space photons. Therefore, these free-space photons have insufficient momentum to excite plasmons directly. To overcome this momentum mismatch, researchers use graphene sheets of finite width, called graphene ribbons. When the polarization of the incident radiation is perpendicular to the ribbons, the electric field induces oscillations of the charge across the ribbons, yielding a reduced transmission $T_{\perp}$. These charge oscillations are in fact plasmon oscillations whose wavelength is approximately half the nano-ribbon width (Fig. 2.5). The transmission $T_{\perp}$ decreases as the frequency of the incident wave approaches the plasmon frequency. Plasmons cannot be excited when the polarization of the incident wave is parallel to the nanoribbons because of a momentum mismatch, but the transmission $T_{||}$ serves as a reference point for obtaining the so-called extinction spectrum 1-$T_{\perp}/T_{||}$, which contains information on the excitations in this system. To obtain the plasmon dispersion relation, the researchers produced nanoribbons with widths down to 50 nm. Measurements of the extinction spectra in samples with different nanoribbon widths provide the plasmon dispersion $\omega_{pl}(q_{pl})$ and the lifetime (Fig. 2.5). Experiments with micrometre-sized ribbons have generated plasmons in graphene at terahertz frequencies. The plasmons supported by nanoribbons have infrared frequencies used in telecommunications, thus providing strong motivation for their study. However, the physics becomes more complex because graphene plasmons in the infrared region interact with optical phonons.

The dominant decay mechanism of plasmon losses is Landau damping (the damping of longitudinal space charge waves in plasma or a similar environment), in which a plasmon emits an electron-hole pair. This damping can be eliminated by using doping to increase the carrier concentration, as the Pauli principle then prohibits such transitions in a large region of the (q,ω) space. In contrast to bulk three-dimensional metallic structures, two-dimensional graphene can be doped by applying an electrostatic gate voltage. This leads to exciting and intriguing possibilities for potential applications as gating can be used to change dispersion or even turn plasmons on and off.

2.1.4 Edges, Nanoribbons and Quantum Dots

It is crucial to open a band gap in semimetallic graphene in order to realize certain potential applications of graphene in industry (so that graphene can behave as insulator for certain frequency). A number of approaches, such as dimensional confinement, structural engineering, chemical/physical modifications, introducing point or linear defects into graphene, electric-field engineering graphene with few layers, and interacting with external substrates, have proven to be able to open a band gap in graphene. However, most of these approaches lead to a reduction in the carrier mobility by several orders of magnitude. Cutting graphene into nanoribbons (GNRs) is one of the few approaches that are able to open a band gap and maintain graphene's high mobility.

Graphene Nanoribbons (GNRs), are strips of graphene with ultra-thin width ($<$ 50 nm), which were introduced as a theoretical model by Mitsutaka Fujita and coauthors to examine the edge and nanoscale size effect in graphene. Based on their edge configuration, GNRs can be classified into three types: armchair-GNR (AGNR); zigzag-GNR (ZGNR); and chiral-GNR (CGNR) edges; which are characterized as linear AC or ZZ sites with a periodicity of 0.426 nm, 0.246 nm and a combination of AC and ZZ sites, respectively (Fig. 2.6).

The electronic states of GNRs largely depend on the edge structure. Among the three types of GNRs, the ZGNR has distinct magnetic properties because of its spin polarization. ZGNR are semiconducting and present spin polarized edges. Their gap opens due to an unusual antiferromagnetic coupling between the magnetic moments at opposite edge carbon atoms, because then the nanostructures with zigzag edges are expected to host spin-polarized electronic edge states and can serve as key elements for graphene-based spintronics [30]. This gap size is inversely proportional to the ribbon width and its behavior can be traced back to the spatial distri-

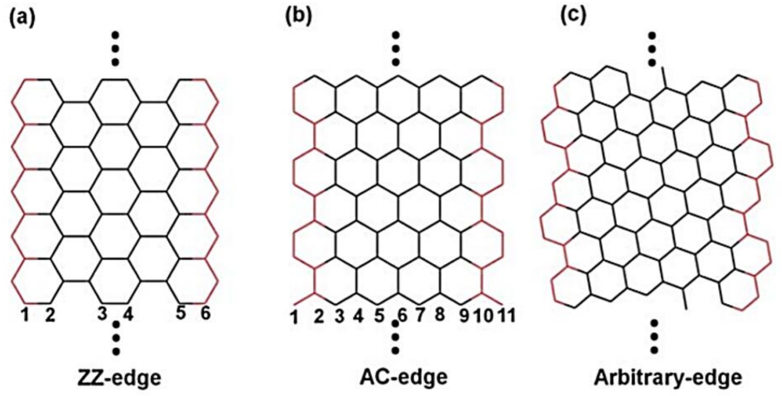

Figure 2.6: Various graphene nanoribbons (GNRs): (a) zigzag GNR (ZGNR); (b) armchair GNR (AGNR); and (c) chiral GNR (CGNR). The number 1, 2, 3,. in (a) and (b) indicate the zigzag and armchair chains of the GNRs and their width [32].

bution properties of edge-state wave functions, and the mostly local character of the exchange interaction that generates the spin polarization. Therefore, the quantum confinement, inter-edge superexchange, and intra-edge direct exchange interactions in zigzag GNR are important for its magnetism and band gap.

In addition to the above discussion, a bandgap can also be introduced by creating graphene quantum structures, such as graphene quantum dots (GQDs). When graphene is reduced to a size comparable to the exciton Bhor radius, quantum confinement effect will become observable, which controls the electron in behavior of graphene.

Graphene Quantum Dots (GQDs) are defined as single-layer to tens of layers of graphene of a size less than 30 nm. Due to its exceptional properties, such as low toxicity, stable photoluminescence, chemical stability and pronounced quantum confinement effect, GQDs are considered as a novel material for biological, optoelectronics, energy and environmental applications.

In contrast to graphene, most applications of GQDs have been focused on the photoluminescence (PL)-related fields since GQDs show a PL (GQDs possess a strong quantum confinment effect and emits PL from the excited state). In recent studies, additional excellent properties of GQDs such as high transparency and large surface area have been proposed for energy and display applications. Because of the large surface area, electrodes using GQDs are applied for capacitors and batteries, and the conductivity of GQDs is higher than that of graphene oxide (GO). In particular, their hole transporting ability is strong, therefore GQDs can be applied for hole transport layers. In addition, due to their nanometer size, GQDs easily disperse in various organic solvents to allow many organic reactions and solution processes. Therefore, with further modifications and with different synthesis conditions GQDs can be modified to show different PL colors, indicating changes in band gap. For commercially available products, the industrial-scale preparation of GQDs and simple device fabrication become important issues. For these purposes, the solution process with well-dispersed GQDs in various solvents is preferred.

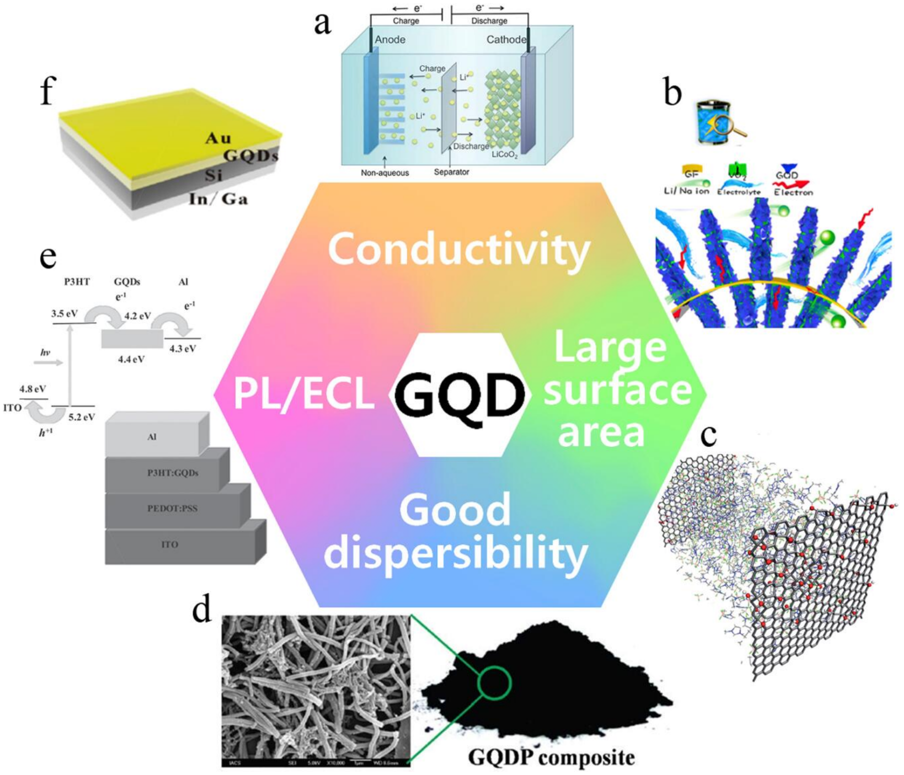

Figure 2.7: a) Illustration of general Li ion battery. b) Schematic illustration of the GVG electrode with bicontinuous electron and Li/Na ion transfer channels for Li/Na battery. c) Illustration of supercapacitor electrode. d) Solution processed GQDs with conducting polymer composite. e) Illustration of general mechanism of solar cell. f) Schematic illustration of Si/GQDs hetero junction solar cell [33].

The solution-process synthesis of GQDs uses a top-down method and energy-related applications such as capacitors, lithium ion batteries, and solar cells. Figure 2.7 illustrates the unique properties of GQDs with energy related applications.

2.2 Theory of Photonic Crystals

Photonic crystals (PhCs) are a class of optical media represented by natural or artificial structures with periodic modulation of the refractive index. Such optical media have some peculiar properties, which opens up new avenues for a number of applications to be implemented. This section comprises three parts. The first part presents the Maxwell equations for periodic structures, then the second part introduces the basic properties of 1D, 2D and 3D PhCs, whereas the properties of the band structures of three kinds of PhCs were discussed at the end of this section.

2.2.1 Maxwell Equations in Periodic Structures

Propagation of light in photonic crystals is described by Maxwell's equations:

$$\nabla \cdot \mathbf{D}(\mathbf{r},t) = \rho(\mathbf{r},t) \tag{2.6a}$$

$$\nabla \cdot \mathbf{B}(\mathbf{r},t) = 0 \tag{2.6b}$$

$$\nabla \times \mathbf{E}(\mathbf{r},t) = -\frac{\partial \mathbf{B}(\mathbf{r},t)}{\partial t} \tag{2.6c}$$

$$\nabla \times \mathbf{H}(\mathbf{r},t) = \mathbf{J}(\mathbf{r},t) + \frac{\partial \mathbf{D}(\mathbf{r},t)}{\partial t} \tag{2.6d}$$

where **E** and **H** are the electric and magnetic field, respectively, **D** is the electric displacement, **B** is the magnetic induction, and ρ and **J** are the charge and current densities, respectively. The real-valued electromagnetic (EM) field quantities depend on the location **r** and the time t. In the case of a homogeneous isotropic medium, Maxwell equations are complemented by a set of material constitutive relations, which relate the macroscopic fields $\mathbf{E}, \mathbf{H}, \mathbf{D}, \mathbf{B}$ to the electric polarization **P** and magnetization **M** inside the material:

$$\mathbf{D}(\mathbf{r},t) = \varepsilon_0 \mathbf{E}(\mathbf{r},t) + \mathbf{P}(\mathbf{r},t) \tag{2.7a}$$

$$\mathbf{H}(\mathbf{r},t) = \frac{1}{\mu_0} \mathbf{B}(\mathbf{r},t) - \mathbf{M}(\mathbf{r},t) \tag{2.7b}$$

where ε_0 is the electric permittivity and μ_0 the magnetic permeability of free space. The polarization **P** can also be related to both the bound charge and current density via:

$$\nabla \cdot \mathbf{P}(\mathbf{r},t) = -\rho(\mathbf{r},t) \tag{2.8a}$$

$$\mathbf{J}(\mathbf{r},t) = \frac{\partial \mathbf{P}(\mathbf{r},t)}{\partial t} \tag{2.8b}$$

The total charge and current density are constrained by the charge conservation, or continuity, equation:

$$\nabla \cdot \mathbf{J}(\mathbf{r},t) + \frac{\partial \rho(\mathbf{r},t)}{\partial t} = 0 \tag{2.9}$$

a relation that can be easily derived from Maxwell's equations above. Moreover, in linear and isotropic media, the electric field **E** and the magnetic field **H** can be related to the electric and magnetic inductions **D** and **B** by the constitutive relations:

$$\mathbf{D}(\mathbf{r},t) = \varepsilon_0 \varepsilon_r \mathbf{E}(\mathbf{r},t) \tag{2.10a}$$

$$\mathbf{B}(\mathbf{r},t) = \mu_0 \mu_r \mathbf{H}(\mathbf{r},t) \tag{2.10b}$$

where ε_r and μ_r are the relative permittivity and permeability of the medium, respectively. Eqs. (2.10a) and (2.10b), in conjunction with the material Eqs. (2.7a) and (2.7b), also show that the electric polarization and magnetization are proportional to the electric and magnetic field, respectively. This can be expressed by introducing the electric and magnetic susceptibilities χ_e and χ_m, respectively, namely $\mathbf{P} = \varepsilon_0 \chi_e \mathbf{E}$ and $\mathbf{M} = \mu_0 \chi_m \mathbf{H}$. From Eqs. (2.10a) and (2.10b), the relative permittivity and permeability can then be related to the susceptibilities by:

$$\varepsilon_r = 1 + \chi_e \tag{2.11a}$$

$$\mu_r = 1 + \chi_m \tag{2.11b}$$

It is worth noting here that a non-magnetic material, namely a medium in which $\mathbf{M} = 0$, is characterized by $\chi_m = 0$ and $\mu_r = 1$. In particular, most optical media are non-magnetic at optical frequencies.

One of the most important features of Maxwell's equations is that they allow for traveling wave solutions that carry energy. Consider for simplicity an infinite medium with no sources (i.e. $\rho = 0$ and $\mathbf{J} = 0$), which has a constant spatial distribution of the permittivity ε and permeability μ. Then, taking the curl of Eq. (2.6c) leads to:

$$\nabla \times \nabla \times \mathbf{E}(\mathbf{r},t) = -\mu \frac{\partial}{\partial t} \nabla \times \mathbf{H}(\mathbf{r},t) \tag{2.12}$$

which according to Eq. (2.6d) without sources can be written:

$$\nabla \times \nabla \times \mathbf{E}(\mathbf{r},t) = -\mu\varepsilon \frac{\partial^2 \mathbf{E}(\mathbf{r},t)}{\partial t^2} \tag{2.13}$$

Finally, using the vector relation $\nabla \times (\nabla \times \mathbf{E}) = \nabla(\nabla \cdot \mathbf{A}) - \nabla^2 \mathbf{A}$, where $\mathbf{A}$ is any vector function of $\mathbf{r}$, Eq. (2.13) can now be written:

$$\nabla^2 \mathbf{E}(\mathbf{r},t) - \mu\varepsilon \frac{\partial^2 \mathbf{E}(\mathbf{r},t)}{\partial t^2} = 0 \tag{2.14}$$

which is the electromagnetic wave equation for the electric field. Here, we have also made use of the fact that the divergence $\nabla \cdot \mathbf{D} = 0$ when no sources are present. For the magnetic field, the same line of reasoning can be followed, the result being that the dynamics of $\mathbf{B}$ can be described by Eq. (2.14), too.

One of the simplest solutions of Eq. (2.14) is the transverse plane wave. Assuming a harmonic spatial and temporal dependence of the fields, $\mathbf{E} \sim e^{i(\mathbf{k}\cdot\mathbf{r} - \omega t)}$, Eq. (2.14) can be rewritten as:

$$\nabla^2 \mathbf{E} - \mu\varepsilon\omega^2 \mathbf{E} = 0 \tag{2.15}$$

which is the Helmholtz equation. The wave vector $\mathbf{k}$ is related to the frequency ω and properties of the medium by $\mathbf{k}^2 = \mu\varepsilon\omega^2$, which implies a phase velocity of $v \equiv \omega/k = 1/\sqrt{\varepsilon\mu}$. The phase velocity can also be expressed in terms of the refractive index, n, and the speed of light in vacuum, c, as $v = c/n$, which leads to the expression for the refractive index, $n = \sqrt{\varepsilon_r \mu_r}$.

Bloch States

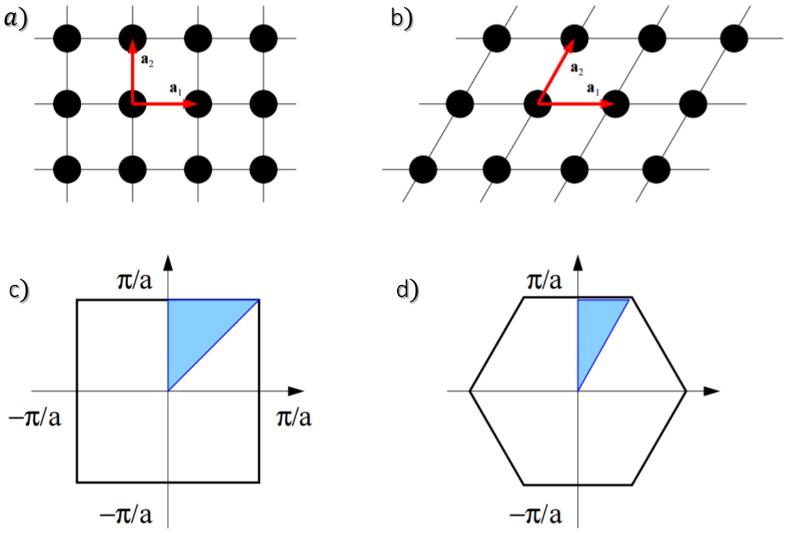

Figure 2.8: a) and b) Two dimensional crystal lattices and corresponding lattice vectors. c) and d) First Brillouin zones corresponding to the configurations of a) and b).

To transfer the Maxwell equations from general cases to the periodic media, we need to follow the Bloch theory to derive the Maxwell equations. As shown in Fig. 2.8 a) and b), the black regions denote the presence of a material with higher permittivity. And we can always associate their first irreducible Brillouin zone as the shaded regions in Fig. 2.8 c) and d), where $\mathbf{a}_1$ and $\mathbf{a}_2$ are the basic vectors of the primitive cell. The first Brillouin zone is a uniquely defined primitive cell in reciprocal space, and the reciprocal lattice represents the Fourier transform of another lattice.

In the periodic medium, we now know that the field can be written in Bloch states as:

$$\mathbf{H}_{\mathbf{k}}(\mathbf{r}) = e^{i\mathbf{k}\cdot\mathbf{r}}\mathbf{u}_{\mathbf{k}}(\mathbf{r}) \tag{2.16a}$$

$$\mathbf{u}_{k}(\mathbf{r}+\mathbf{R}) = \mathbf{u}_{\mathbf{k}}(\mathbf{r}) \tag{2.16b}$$

where $\mathbf{u}_{\mathbf{k}}(\mathbf{r})$ is a periodic function. We denote the Brillouin zone by K. Our

Maxwell equations above read

$$\nabla_k \times \varepsilon^{-1} \nabla_k \times \mathbf{u} = \omega^2 \mathbf{u} \in \Omega \tag{2.17a}$$

$$\nabla_k \times \mathbf{u} = 0 \in \Omega \tag{2.17b}$$

where Ω is the Bloch space (an important analytic function space for holomorphic functions defined on the open unit disc D).

2.2.2 Definition and Basic Properties of Photonic Crystals

Photonic crystals are periodic optical structures that affects the motion of photons in much the same way that ionic lattices affect electrons in solids. Depending on geometry of the structure, PhCs can be divided into three broad categories, namely one-dimensional (1D), two-dimensional (2D) and three-dimensional (3D) structures. Examples are shown in Fig. 2.9.

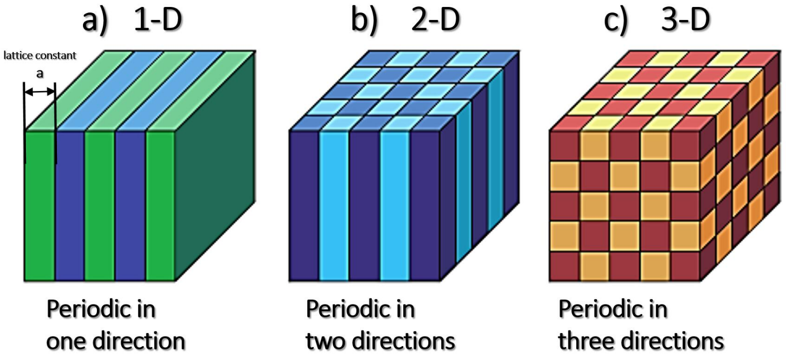

Figure 2.9: Schematic diagram of a) 1-D, b) 2-D, and c) 3-D photonic crystals.

One-dimensional PhCs in the form of periodic dielectric stacks have been used for a wide range of applications including high-efficiency mirrors, Fabry-Perot cavities, optical filters and distributed feedback lasers [1]-[3]. As illustrated in Fig.2.9 a), the simplest PhC is an alternating stack of two different dielectric materials. When light is incident on such a stack, each interface reflects some of the field. If the thickness of each layer has a specific value, the reflected fields can combine in phase, resulting in constructive interference and strong reflectance, also known as Bragg reflection. In contrast to two- and three-dimensional PhCs, 1D Bragg reflection occurs regardless of the index contrast, although a large number of periods is required to achieve a high reflectance if the contrast is small. Since the absorption in dielectric optical materials is very low, mirrors made from dielectric stacks are extremely efficient, and can be designed to reflect almost 100% of the incident light within a small range of frequencies. The main limitation of these dielectric mirrors is that they only operate for a limited range of angles close to normal incidence.

Two-dimensional PhCs typically consist of an array of dielectric cylinders in a homogeneous dielectric background material. If the refractive index contrast between the cylinders and the background is sufficiently large, 2D bandgaps can occur for propagation in the plane of periodicity perpendicular to the rods. Light at a frequency within the bandgap experiences Bragg reflection in all directions due to the periodic array of cylinders. As in semiconductor devices, much of the interest in photonic crystals actually arises not from the ability to create localised defect states within the bandgap by introducing a structural defect into an otherwise regular lattice. For example, the removal of a single cylinder from a 2D PhC creates a point-like defect or resonant cavity, and the removal of a line of cylinders can create a waveguide that supports propagating modes. Many potential applications (like Bragg mirrors, quantum cascade lasers and optical trapping) based on this concept have been proposed and demonstrated.

Three-dimensional PhCs has permittivity modulation along all three directions. Because of this, the number of possible PhC configurations is much larger than in case of 1D or 2D PhC. Also, 3D PhCs have proved to be the most challenging PhC structures to fabricate. For this reason, it was more than three years after the initial proposal for 3D band gap materials before a structure was calculated to exhibit a bandgap for all directions and all polarizations [52]. The design consisted of dielectric spheres positioned at the vertices of a diamond lattice. Since these early studies, a wide range of 3D PhC geometries exhibiting complete bandgaps have been demonstrated both in theory and experiment. Due to the challenges involved in fabricating high-quality structures with features on the scale of optical wavelengths, early photonic crystal experiments were performed at microwave and mid-infrared frequencies [49]. With the improvement of fabrication and materials processing methods, smaller structures have become feasible, and in 1999 the first 3D PhC with a bandgap at telecommunications frequencies was reported [50]. Since then, various lattice geometries have been reported for operation at similar frequencies [51].

2.2.3 Photonic Band Structures of 1D, 2D and 3D Photonic Crystals

A complete photonic band gap is a range of frequencies in which there are no propagation solutions of Maxwell equations, surrounded by propagating states above and below the gap. We will discuss the band structure of 1D, 2D and 3D photonic crystals in the following subsections.

1D PhCs

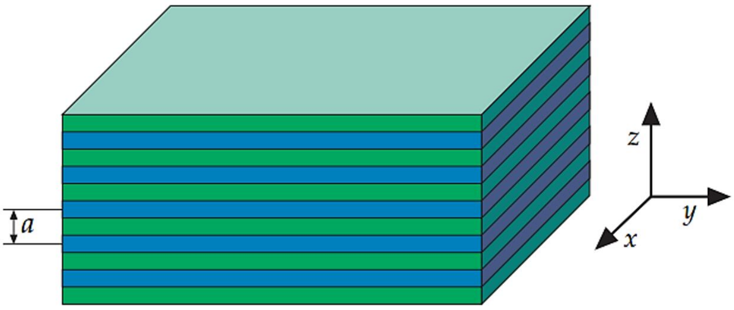

Figure 2.10: The multilayer film, one-dimensional photonic crystal. The dielectric function $\varepsilon(z)$ varies along z direction. Here we assume that each layer extends to infinity along the x and y directions.

The simplest possible photonic crystal, shown in Fig. 2.10, is made of alternating layers of material with different dielectric constants. For now, consider waves that propagate entirely in the z direction at normal incidence. We plot $\omega_n(k)$ for three different multilayer films as displayed in Fig. 2.11.

The first case (Fig. 2.11 (a)) is for a homogeneous dielectric medium. The TE/TM modes lie along the light line (light line is a useful tool to distinguish between guided and non-guided modes in the photonic structures), given by $\omega(k) = ck/\sqrt{\varepsilon}$. Since k repeats outside the Brillouin zone (the primitive cell in reciprocal space), the light line folds back into the zone when it reaches an edge, which can be regarded as a way of replacing $k+2\pi/a$ by k. The second case (Fig. 2.11 (b)), looks

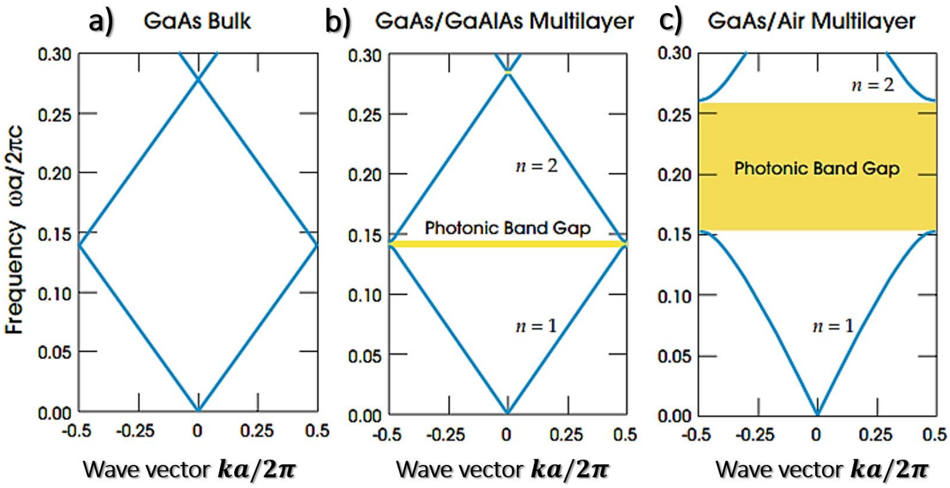

Figure 2.11: The band structures for three different multilayer films. The blue lines indicate the optical bands of the photonic structure. a) each layer has the dielectric constant $\varepsilon = 13$. b) layers alternate between ε of 13 and 12. c) layers alternate between ε of 13 and 1 [52].

like the homogeneous one with an essential difference: there is a gap in frequency between the upper and lower branches of the lines. There is no allowed mode in the crystal that has a frequency within the gap, regardless of k. We name this gap as *photonic band gap*. In the third case (Fig. 2.11 (c)), the band gap broadened because of the increased dielectric contrast.

2D PhCs

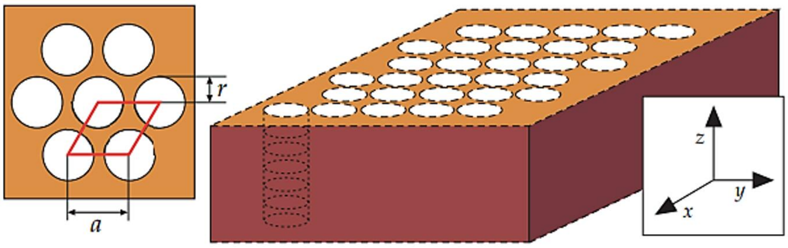

Figure 2.12: a two-dimensional photonic crystal of air colomns in a dielectric substrate (which we assume to extend infinity in the z direction. The left inset illustrates a view of the triangular lattice from above, with the unit cell framed in red, with the lattice constant of a.)

A 2-D PhC is periodic along two of its axes and homogeneous along the third axis. A typical such PhC consists of a triangular array of air columns drilled in a dielectric substrate ($\varepsilon = 13$). In this case, two-mode (TM and TE) band gaps appears. By arranging the dimensions of the lattice, we can make the band gaps to

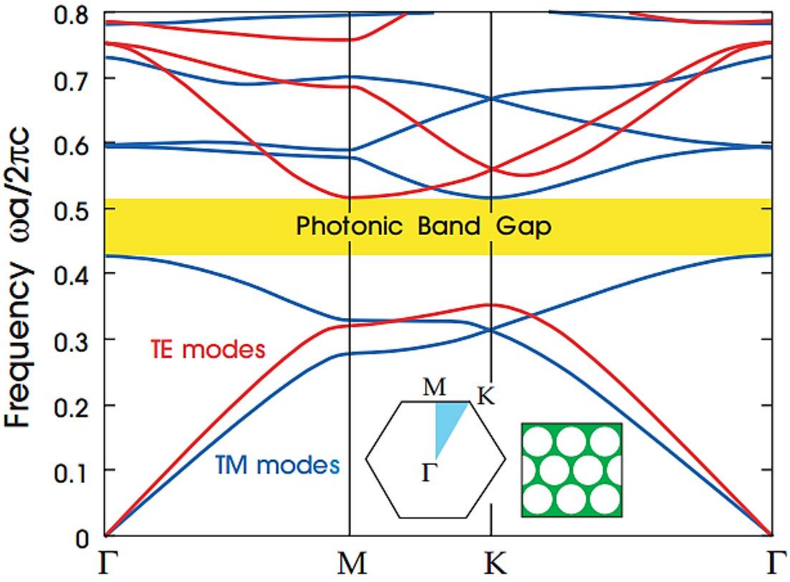

Figure 2.13: The band structures for modes of a triangular array of air columns in a dielectric substrate [52].

overlap, leading to a *complete band gap* for all polarizations. As shown in Fig. 2.13, the band structure has photonic band gaps for both the TE and TM polarizations. As a matter of fact, for the specific radius $r/a = 0.48$ and dielectric constant $\varepsilon = 13$, these gaps overlap, and we obtain an 18.6% complete photonic band gap.

Localization of light by point defects

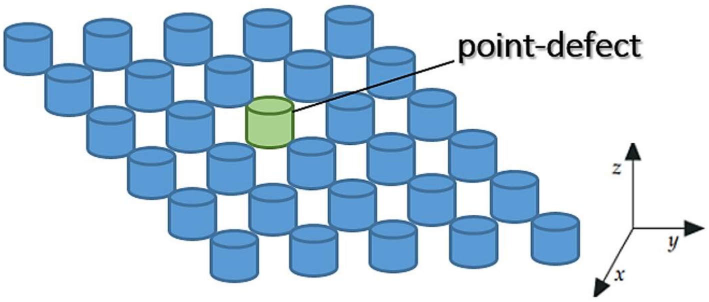

Figure 2.14: Schematic diagram of point defect in 2-D PhC.

Two-dimensional photonic crystals with band gaps were found for in-plane propagation . Within the band gap, no modes are allowed; the density of states (the number of possible modes per unit frequency) is zero. By perturbing a single lattice site, we can create a single localized mode or a set of closely space modes that have frequencies within the gap.

As depicted in Fig. 2.14, we can remove a single column from the crystal, or replace it with another material different from the original. Perturbing just one site breaks the translational symmetry of the lattice. Because the perturbation is localized to a particular point in plane, we refer to this perturbation as a *point defect*.

Removing one column may give rise to a peak into the crystal's density of states within the photonic band gap. If this defect cavity has an approximate size and refractive index to hold a mode in the band gap, then the light inside cannot escape, and we could attribute the mode to the defect. More details of defect mode within a PhC will be discussed later in Chapter 4.

3D PhCs

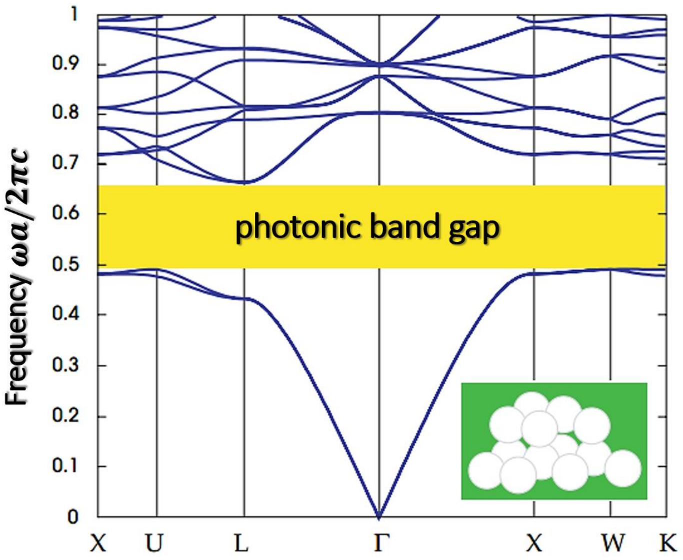

Figure 2.15: Band structure for the lowest bands of a diamond lattice of air spheres within a high dielectric ($\varepsilon = 13$) medium (inset). [52]

Similar to what we explained in the former section, a 3-D PhCs is a dielectric structure that is periodic along three different axes. They have different properties of band gaps and defect modes compared to 1-D and 2-D cases. Some examples of 3-D PhCs are a diamond lattice of air holes, a woodie stack of orthogonal dielectric columns and a stack of alternating 2-D crystals of rods and holes. Here we just focus on the first one: diamond lattice of air spheres.

The first structure with a complete 3-D photonic band gap by considering a diamond lattice of spheres was found by scientists in 1990 [53]. The band structure for a lattice of air spheres within a dielectric material is shown in Fig. 2.15. To maximize the size of the band gap, the sphere radius r is chosen to be 0.325 a, where a is the lattice constant of the cubic supercell. Most of this strucuture (81% by volume) is air. The diameter of the spheres exceeds the spacing between them, resulting in the air spheres superimposing. This eliminates the need for linking any ”bonds” between them.

2.3 Fundamentals of Stimulated Raman Scattering

Raman scattering is the inelastic scattering of a photon by molecules (atoms) which are excited to higher energy levels. It can be used in Raman spectroscopy to perform analysis on a given sample. When an sample is exposed to a monochromatic light in visible region, the sample absorbs light and the major portion of the light gets transmitted through the sample. However, a minute part of the light is scattered by the samples in all the directions. One can observe the scattering at right angle to the incident beam. The incident light has a particular frequency. If the scattered light has the frequency same as the incident light, then scattering is called as Rayleigh scattering. However, it has been discovered that about 1% of scattered light occurs at frequencies different from the incident frequency. This is called Raman scattering.

2.3.1 Stokes and Anti-Stokes Raman Scattering

The Raman scattering can be thought as a two photon process. As shown in Fig. 2.16, there are three different possibilities of light scattering: Rayleigh scattering, Stokes Raman scattering, anti-Stokes Raman scattering.

The electrons have different vibrational levels. When an incident monochromatic light interacts with an electron in the sample, the electron absorbs energy from the incident photon and rises to a virtual state of energy. The energy transferred is given by the formula $E = h\nu$, where ν is the frequency of incident light. The electron then falls back to an energy level by losing energy. Depending upon the final vibrational level of the electron, the Raman scattering leads to two possible outcomes. One is that the medium absorbs energy and the emitted photon

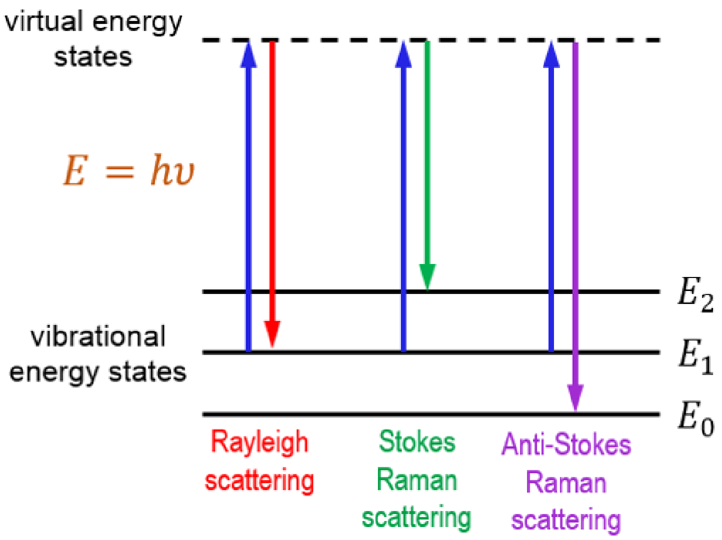

Figure 2.16: Schematic diagram of different possibilities of light scattering: Rayleigh scattering (the incident and scattered photon have the same energy), Stokes Raman scattering (the scattered photon has less energy than the incident photon) and anti-Stokes Raman scattering (scattered photon has more energy than the incident photon).

has a lower energy than the incident photon, which is labeled Stokes Raman scattering. Another outcome is that the material loses energy and the emitted photon has a higher energy than the absorbed photon, which is labeled anti-Stokes Raman scattering. Based on the final Raman spectrum we detected, the molecules of the sample can be identified.

The Raman transition from one state to another happens only if the molecule has anisotropic polarizability, namely the molecular polarizability of those states is different. Specifically, in atoms the polarizability is isotropic, then the atom acts like an antenna and re-radiates at the incident frequency – Rayleigh Scattering. In molecules the polarizability may be anisotropic, and depends in the rotational and vibrational coordinates. This circumstance can give rise to the Raman scattering.

2.3.2 Stimulated Raman Scattering and Raman Amplification

The Raman scattering first takes place spontaneously, which is called spontaneous Raman scattering. The stimulated Raman scattering takes place when injecting Stokes photons together with the original light. Stimulated Raman scattering is a nonlinear optical effect. It can be described using a third-order nonlinear susceptibility. The Raman nonlinear optical response of a medium can be determined by the nonlinear Raman polarization at the Stokes frequency:

$$\boldsymbol{P}_R(\omega_S;\boldsymbol{r}) = \frac{3}{2}\varepsilon_0 \boldsymbol{\chi}_R^{(3)}(\mathbf{r})\vdots \boldsymbol{E}(\omega_p;\mathbf{r})\boldsymbol{E}^*(\omega_p;\mathbf{r})\boldsymbol{E}(\omega_S;\mathbf{r}) \tag{2.18}$$

where $\boldsymbol{\chi}_R^{(3)}$ is the Raman susceptibility, $\boldsymbol{P}_R(\omega_S;\mathbf{r})$ is the Raman polarization at ω_S, and $\boldsymbol{E}(\omega_p;\mathbf{r})$ and $\boldsymbol{E}(\omega_S;\mathbf{r})$ are the optical fields at the pump and Stokes frequencies, respectively.

The Raman amplification is based on the stimulated Raman scattering phenomenon. When a stokes photon induces the inelastic scattering of a pump photon in the nonlinear medium, another stokes photon is produced, with the excess energy resonantly passed to the vibrational states of the medium. In this case, the total Raman scattering rate is increased beyond that of spontaneous Raman scattering, namely, pump photons are converted more rapidly into additional Stokes photons. This process allows all-optical amplification, which is exploited in Raman amplifiers and Raman lasers.

The Raman laser is a specific type of laser whose fundamental light amplification mechanism is the stimulated Raman scattering, while most conventional lasers (such as the ruby laser) rely on stimulated electronic transitions. The first Raman laser, which was realized in 1962, was intra-cavity-pumped inside a Q-switching ruby laser using nitrobenzene as the gain medium [54]. The biggest difference between Raman lasers and general lasers is that the Raman laser does not produce population inversion (more members in the excited state than in the lower energy state exist in a system). More recently, Raman lasing has been demonstrated by research group in UCLA utilizing the silicon photonics in 2004 [55]. In 2005, the second generation of silicon laser technology, continuous wave silicon laser, was demonstrated by Intel [56]. These developments received much attention because it was the first time that a laser was realized in silicon [57].

Another important application on the Raman effect is the Raman spectroscopy, which is used for substances analysis. The spectrum of the Raman scattered light depends on the constituents and state of the molecule, which can be used for material identification and analysis. The Raman spectroscopy can be used to analyze a wide range of materials, such as gases, liquids, and solids. Many highly complex materials such as biological organisms and human tissue can also be analyzed by Raman spectroscopy [58].

2.4 Fundamentals of Metamaterials

In the past years, there have been increasing interest in metamaterials. In this section, we explain what metamaterials are and describe the recent progress of metamaterials. We will also summarize the significant developemnts and future of metamaterials, including the optical transformation, effective medium theory for periodic structures, broadband and low-loss metamaterials, rapid design of metamaterials, and potential applications. The basics of computational electromagnetics on metamaterials are briefly discussed, too.

2.4.1 Introduction

Metamaterials, arranged in repeating patterns at scales that are smaller than the operating wavelengths, possess many useful functions due to both the structural architecture and the chemical composition. If the metamaterial is regarded as an effective medium (representative of the system with average optical properties), there is an additional requirement that the cell is smaller than or equal to the subwavelength. In this part, the metamaterials are required to have sub-wavelength for the unit cell so that they can be described using the effective medium theory [59].

Figure 2.17 shows two typical metamaterial structures in the microwave regime, in which Fig. 2.17(a) is a periodic structure that is equivalent to a homogeneous medium and Fig. 2.17(b) is a non-periodic structure that is equivalent to an inhomogeneous (gradient) medium. The microwave metamaterials are fabricated onto printed circuit boards (PCB) by making different metal architectures on PCB. The properties of such metamaterials are mainly due to the architecture, and also dependent on the PCB substrates. The dependence of metamaterial properties on the architecture provides great flexibility to control metamaterials. One can create new materials which are unavailable in nature but can be realized in practice us-

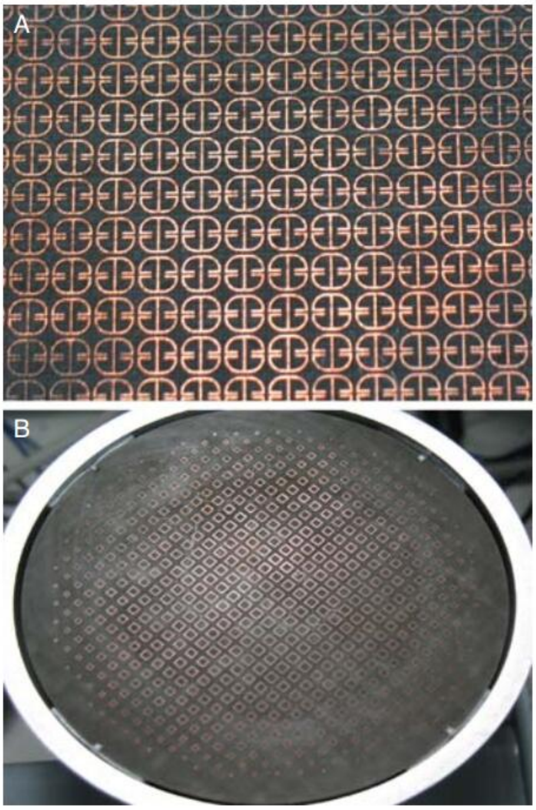

Figure 2.17: Two typical metamaterial structures within the microwave region. (a) A periodic structure, which is equivalent to a homogeneous medium (above). (b) A non-periodic structure, which is equivalent to an inhomogeneous (gradient) medium (below).

ing metamaterial structures. This is the biggest advantage of metamaterials. There are many important uses for metamaterials nowadays, for example, metamaterials enable ultra-fast data processing and could reduce the size of chips so that they would be tiny and speedy. Also, metamaterials have become the building blocks for a high-speed fiber-optic telecommunications network. Not only can they beam the internet to airplanes, metamaterials can make up the internet itself. Another important application is that the metamaterial technology could create better lenses in generalones that can do things existing lenses cannot.

Usually, the material properties are characterized by an electric permittivity (ε) and a magnetic permeability (μ). The relative permittivity and permeability of a material are defined as $\varepsilon_r = \varepsilon/\varepsilon_0$ and $\mu_r = \mu/\mu_0$ (ε_0 is the electric permittivity of air and μ_0 is the magnetic permeability of air, respectively), which define another important material parameter, the refractive index, as $n = \sqrt{\varepsilon_r \mu_r}$. In nature, most materials have the permeability μ_0 and permittivity larger than ε_0 (electric permittivity of air). The metamaterial opens a door to realize all possible material properties by designing different cellular architectures and using different substrate materials.

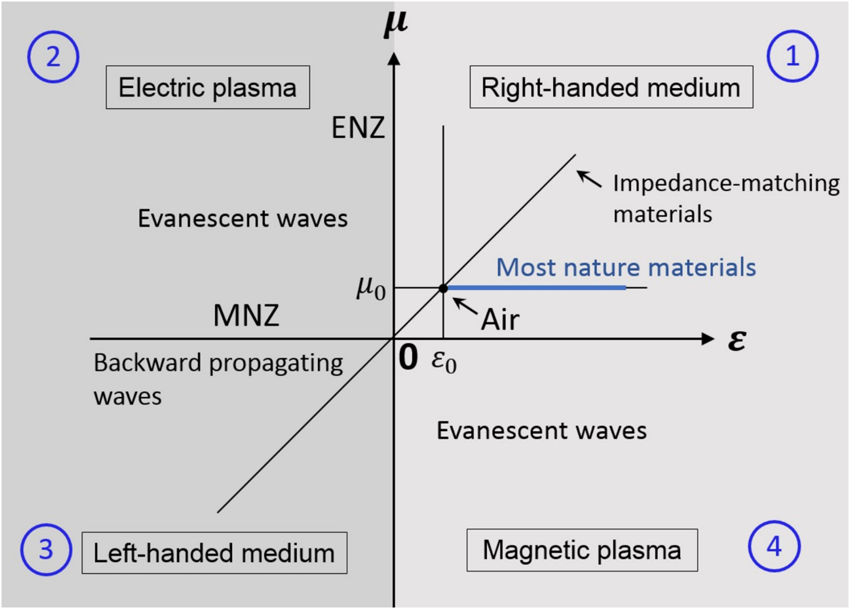

Figure 2.18: All possible properties of isotropic materials in the ε-μ domain.

Figure 2.18 illustrates all possible properties of isotropic and lossless materials in the ε-μ domain. In Fig. 2.18, the first quadrant ($\varepsilon > 0$ and $\mu > 0$) represents right-handed materials (RHM), which support the forward propagating waves. From the Maxwells equations, the electric field $\mathbf{E}$, the magnetic field $\mathbf{H}$, and the wave vector $\mathbf{k}$ form a right-handed system. The second quadrant ($\varepsilon < 0$ and $\mu > 0$) denotes electric plasma, which support evanescent waves. The third quadrant ($\varepsilon < 0$ and $\mu < 0$) is the left-handed materials (LHM), which supports the backward propagating waves. The fourth quadrant ($\varepsilon > 0$ and $\mu < 0$) represents magnetic plasma, which supports evanescent waves.

In Fig. 2.18, most natural materials only occur at certain discrete points on the line $\mu = \mu_0$ and $\varepsilon \geq \varepsilon_0$, and seldom natural electric plasma and magnetic plasma occur in very small parts in the second and fourth quadrants. Most of material properties have to be realized using metamaterials, even for right-handed materials.

Metamaterials have much broader scope than left-handed materials, as shown in Fig. 2.18. In the ε-μ domain, there are several special lines and points indicating special material properties. For example, the point $\mu = -\mu_0$ and $\varepsilon = -\varepsilon_0$ represents an anti-air in the left-handed materials region, which will produce perfect lens (an ideally corrected glass element that is free of aberration and focuses light onto a single point); the line $\mu = \varepsilon$ in both right-handed material and left-handed material regions represents impedance-matching materials, which have perfect impedance matching with air, resulting no reflections. Also, the vicinity of $\mu = 0$ is called μ-near zero (MNZ) material, and the vicinity of $\varepsilon = 0$ is called as ε-near zero (ENZ) material.

Actually, metamaterials have much more features beyond those shown in Fig. 2.18. Metamaterials can be designed as weakly and highly anisotropic, depending on different requirements. The flexibility to design various material properties together with the optical transformation makes it possible to control electromagnetic waves at will using metamaterials.

2.4.2 Negative Refractive Index Metamaterials

Negative-refractive index materials are extensively studied nowadays [61, 62, 63]. For backward wave propagation, an adequate choice of the sign of the refractive index $n(\omega)$ given by $n(\omega) = \pm\sqrt{\varepsilon(\omega)\mu(\omega)}$ is necessary. The determination of the sign in front of the square root is done thanks to causal properties which the solutions of wave propagation should respect the energy conservation principles. The choice of this sign allows to define, among other parameters, the direction of the outgoing wave with respect to an interface between a negative-refractive index material and a conventional material.

To demonstrate that for a material with $(\varepsilon(\omega) < 0, \mu(\omega) < 0)$, the sign of the refractive index should be negative, let us consider a current surface in $x = x_0$. The radiation of this surface current in the medium $(\varepsilon(\omega) < 0, \mu(\omega) < 0)$ is then studied as shown on figure 2.19. The wave equation in the medium can be written as following:

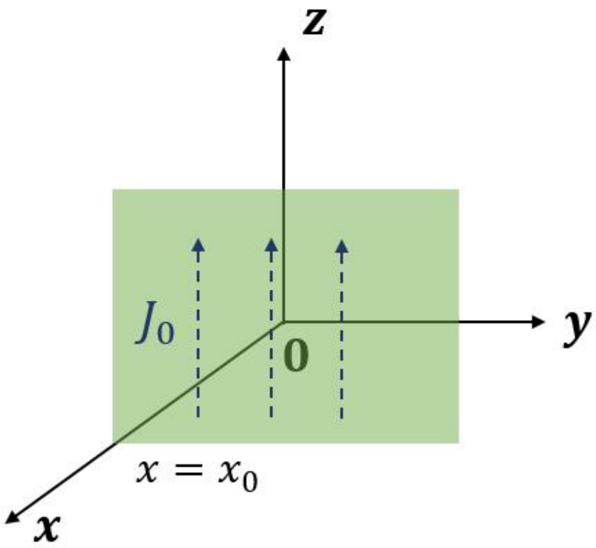

Figure 2.19: Surface current J_0 in $x = x_0$ radiating in the medium ($\varepsilon(\omega) < 0, \mu(\omega) < 0$). The current distribution is considered uniform and infinite in the YoZ plane.

$$\frac{\partial^2}{\partial x^2}E(x) + k^2 E(x) = -j\omega\mu J_0(z) \tag{2.19}$$

where $E(x)$ is the electric field component along $\mathbf{x}$, and $\mathbf{J}_0 = i_0\delta(x - x_0)\mathbf{z}$. The solution of this equation is given by:

$$E(x) = \alpha exp(jk|x - x_0|) \tag{2.20}$$

To determine α, let us first calculate:

$$\frac{\partial^2 E(x)}{\partial x^2} = -\alpha k^2 exp(jk|x - x_0|) + 2j\alpha k\delta(x - x_0) \tag{2.21}$$

substitute the expressions 2.21 and 2.20 in equation 2.19, α is then given by:

$$\alpha = -\frac{\mu\omega i_0}{2k_0 n} = -\frac{i_0\lambda_0}{2}\frac{\mu_r}{n} \tag{2.22}$$

and the wave equation becomes:

$$E(x) = -\frac{i_0\lambda_0}{2}\frac{\mu_r}{n} exp(jk|x - x_0|) \tag{2.23}$$

However, if the power P delivered by the current J_0 to the volume V is calculated, the following equation can be obtained:

$$P = -\frac{1}{2}\int_V \overrightarrow{E}\cdot\overrightarrow{J}_0^{*}dV = \frac{i_0^2\lambda_0}{2}\frac{\mu_r}{n} \tag{2.24}$$

This equation represents the work done by the source and it must be positive, which implies that $P > 0$. The ratio μ_r/n must also be positive. If μ_r is negative, then n must also be negative. An equivalent demonstration can be done for ε_r. For a propagative medium, the solution retained for the wave equation verifies backward wave propagation.

To determine the constraints with respect to the sign choice of the imaginary part of the refractive index, let us consider the electric field $\overrightarrow{E}(\overrightarrow{r},\omega)$ in a medium with $n = n' - jn''$ for a time dependence in $exp(j\omega t)$:

$$\overrightarrow{E}(\overrightarrow{r},t) = Re\left[|\overrightarrow{E}(\overrightarrow{r})|exp(-\overrightarrow{k}_0\cdot\overrightarrow{r}n'')exp[j(\omega t-\overrightarrow{k}_0\cdot\overrightarrow{r}n')]\overrightarrow{u}_E\right] \tag{2.25}$$

where $\overrightarrow{k}_0$ is the free space wave vector and $\overrightarrow{u}_E$ is the unit vector along the direction of the E-field vector $\overrightarrow{E}$. If a stable propagation is to be ensured, the magnitude of Re$[\overrightarrow{E}(\overrightarrow{r},t)]$ must decrease with time. This implies that the term $\overrightarrow{k}_0\cdot\overrightarrow{r}n''$ must be positive and:

$$n'' > 0 \tag{2.26}$$

Wave impedance Z is a physical interpretation based on the analogy between the impedance of a medium for wave propagation and the impedance of a transmission line in circuit.

The complex wave impedance of a medium is strongly related to the flux of energy of the wave propagating in the medium. This is why there are fundamental limitations to the values that Z can admit; one of the limitations is directly linked to the passivity of the medium. These limitations apply to both positive and negative refractive index medium.

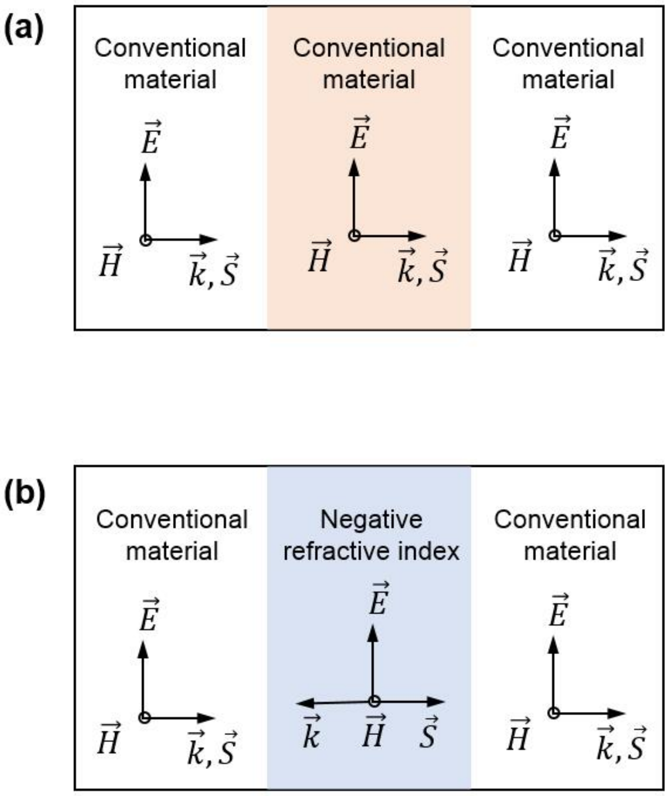

Figure 2.20: Direction of the field vectors (**E**,**H**,**k**) and the energy flux S for the interaction of a plane wave at the interface of (a) two conventional materials with positive refractive index, and (b) a conventional material and a negative refractive index material.

The passivity of absence of activity within a medium implies that a plane progressive electromagnetic wave, the mean energy flux must be directed inside the medium in which the wave propagates. The directions of the vectors $(\overrightarrow{E},\overrightarrow{H},\overrightarrow{k})$ and the energy flux $\overrightarrow{S}$ for a plane progressive wave at the interface between conventional material and negative-refractive index material is shown in Fig. 2.20.

The wave impedance is defined as the ratio of the electric field to the magnetic field component in the propagation plane. The real part is thus given by:

$$Re[Z(\omega)] = Re\left[\frac{\overline{E}(\omega)}{\overline{H}(\omega)}\right] = \cos(\varphi_H - \varphi_E) \tag{2.27}$$

where $\overline{E}(\omega) = |\overline{E}(\omega)|exp(-j\varphi_E)$ and $\overline{H}(\omega) = |\overline{H}(\omega)|exp(-j\varphi_H)$. Equation 2.27 is verified for both positive and negative refractive indices. The sign of Re$[Z(\omega)]$

depends only on the term $\cos(\varphi_H - \varphi_E)$.

The mean of Poynting's vector $\overrightarrow{S}_{av}$ is calculated:

$$\overrightarrow{S}_{av}(\overrightarrow{r},\omega) = \frac{1}{2} Re|\overrightarrow{E}(\overrightarrow{r},\omega) \times \overrightarrow{H}^*(\overrightarrow{r},\omega)| = \frac{1}{2}|\overrightarrow{E}(\overrightarrow{r},\omega)||\overrightarrow{H}(\overrightarrow{r},\omega)|\cos(\varphi_H - \varphi_E)\overrightarrow{u}_S \tag{2.28}$$

where $\overrightarrow{E}(\overrightarrow{r},\omega) = |\overrightarrow{E}(\overrightarrow{r},\omega)|exp(-j\varphi_E)$, $\overrightarrow{H}(\overrightarrow{r},\omega) = |\overrightarrow{H}(\overrightarrow{r},\omega)|exp(-j\varphi_H)$ and $\overrightarrow{u}_S$ is the unit vector of $\overrightarrow{S}_{av}(\overrightarrow{r})$.

Knowing that passivity of a medium implies that the energy flux must be directed inside the medium implies that $\overrightarrow{S}_{av}(\overrightarrow{r},\omega) > 0$. The term $\cos(\varphi_H - \varphi_E)$ is thus always positive for all medium irrespective of the sign of their refractive index. There is no particular sign restriction on the imaginary part of the wave impedance. The complex wave impedance provides information not only on wave propagation but it also allows physical understanding when there is no wave propagation in a medium as to which the field component is cancelled. This information is indeed interesting for the design of artificial magnetic medium. If the imaginary part of Z is negative, the medium can be said to be capacitive and there is no wave propagation because of H-field filtering. The response of the medium to an applied magnetic field is thus non-negligible and it can be considered as an artificial magnetic medium.

The concept of effective medium for the description of heterogeneous systems by a homogeneous one is very attractive in different fields of physics. Homogenization procedures allowing the definition of an effective macroscopic response from physical parameters characterizing the heterogeneous system are generally well developed mature techniques. In our case, from the microscopic parameters (geometrical and physical definitions) of the metamaterial, a macroscopic electromagnetic response can be obtained. If this macroscopic definition is performed in accordance with the electrodynamics of continuous media, they can afterwards be used in Maxwell equations to predict propagation phenomena and provide physical insight into the design of metamaterial-based microwave and optical devices.

In this part, the negative refractive index (NRI) metamaterials considered are assumed periodic and based on resonant inclusions such as the combination of split ring resonator and wire medium.

2.4.3 Nonlinear Optics with Metamaterials

A large portion of the experimental results on metamaterials reported thus far are focused on the linear response of metamaterials to external electromagnetic radiation. However, nonlinear optical effects in metamaterials have become an emerging field of study. A range of nonlinear phenomena in a variety of metamaterials, especially negative-index materials (NIMs), have been theoretically investigated to a considerable extent. The studied topics include general treatments for nonlinear wave propagation and nonlinear Schrodinger equations in negative-index materials, as well as specific nonlinear processes such as second-harmonic generation and parametric amplification.

The linear responses of metamaterials have substantially augmented the linear properties available from naturally-occurring materials. In the same way, the studies of nonlinear metamaterials have a significant impact on the entire field of nonlinear optics. Conventional studies of nonlinear optics are mainly focused on exploration of various high-order processes in different crystals. The capability to design custom nonlinear materials, which is possible in metamaterials, is bound to open entirely new outlooks for nonlinear light-matter interactions.

The optical properties of nonlinear metamaterials are sensitive to the strength of external fields. At microwave frequencies, such reconfigurable metamaterials can be achieved by introducing power-dependent lumped elements such as varactor diodes. Several microwave metamaterials based on the varactor devices have been experimentally reported, ranging from tunable split-ring resonators as notch filters to second-harmonic generation in transmission-line negative-index materials.

Nonlinear effects also provide hope for better, low-loss optical metamaterials. It has been suggested that the power absorption in negative-index materials can be efficiently compensated via different schemes, including optical parametric amplification and resonant four-wave mixing. In addition, nonlinear metamaterials may help in the development of a perfect lens that is more robust against material imperfections such as chromatic dispersion and power dissipation. With an appropriate quadratic nonlinear response, an image of the second-harmonic field with subwavelength resolution can be achieved even for a slab lens that is opaque at the fundamental frequency. The wave-mixing in second-order nonlinear negative-index materials can also be used for terahertz wave generation from optical signals. The efficiency of most nonlinear wave-mixing processes critically depends on the phase-matching of the participating waves.

2.5 Basic Concepts of Quantum Optics

In this section we presents the fundamental ideas of quantum optics, which comprises three parts. This first part is about the quantum mechanism of radiation. The electromagnetic field is expanded in the normal modes and then quantized. The second part deals with the Hamiltonian which describes the interaction of a radiation field and a single atom. In the third part, we describe the quantum theory of damping, which is due to the interaction between a system and reservoir.

2.5.1 Quantum Theory of Radiation

What is quantum theory of radiation? The distribution of energy in the spectrum of radiation emitted by a hot body should be explained by the quantum theory of radiation rather than the classical concepts of physics. Max Planck gave an explanation of his quantum theory of radiation. His theory says:

a) The radiant energy is always in the form of tiny bundles of light called quanta.

b) Each quantum has some definite energy E, which depends upon the frequency of radiation. $E = h\nu$ (E is the energy of each quantum, ν is the frequency of radiation, h is known as Planck's constant)

c) The energy emitted or absorbed by a body is always an entire multiple of a quantum.

First of all, we now think about the electric field dependence appropriate for a cavity resonator of length L (Fig. 2.21). We set the electric field to be linearly

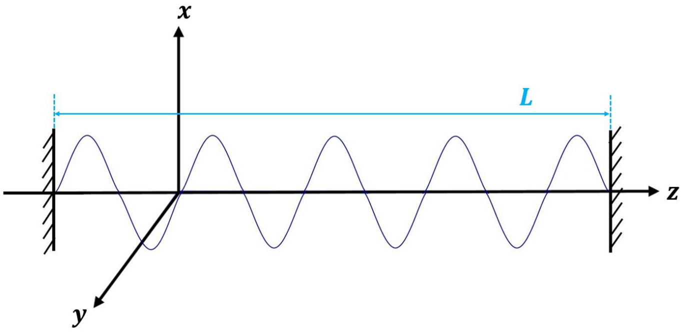

Figure 2.21: Electromagnetic field of frequency ν inside a cavity. The field is assumed to be transverse with the electric field polarized in the x direction.

polarized in the x direction and expand it in the normal modes of the cavity:

$$\mathbf{E}_x(z,t) = \sum_j A_j q_j \sin(k_j z) \tag{2.29}$$

where q_j is the normal mode amplitude with the dimension of a length $k_j = j\pi/L$, with $j = 1,2,3,...$, and

$$A_j = \left(\frac{2\nu_j^2 m_j}{V\varepsilon_0}\right)^{1/2} \tag{2.30}$$

with $\nu_j = j\pi c/L$ being the cavity eigenfrequency, $V = LA$ (A is the transverse area of the optical resonator) is the volume of the resonator and m_j is a constant with the dimension of mass. The constant m_j has been included only to set up the analogy between the dynamical problem of a single mode of electromagnetic field and that of the simple harmonic oscillator. The equivalent mechanical oscillator will have a mass m_j, and Cartesian coordinate q_j. The nonvanishing component of the magnetic field H_y in the cavity is obtained from Eq. (2.29):

$$\mathbf{H}_y = \sum_j A_j \left(\frac{q_j \varepsilon_0}{k_j}\right) \cos(k_j z) \tag{2.31}$$

The classical Hamiltonian for the field is

$$\mathscr{H} = \frac{1}{2}\int_V d\tau(\varepsilon_0 E_x^2 + \mu_0 H_y^2) \tag{2.32}$$

where the integration is over the volume of the cavity. Substituting from Eq. (2.29) and (2.31), the Hamiltonian can be rewritten as:

$$\mathscr{H} = \frac{1}{2}\sum_j (m_j \nu_j^2 q_j^2 + m_j q_j^2) \tag{2.33}$$

Equation (2.33) expresses the Hamiltonian of the radiation field can be viewed as a sum of independent oscillator energies. Each mode of the field thus corresponds to a mechanical harmonic oscillator.

The above dynamical problem can be quantized by identifying q_j and p_j as operators which follow the commutation relations:

$$[q_j, p_{j'}] = i\hbar\delta_{jj'} \tag{2.34a}$$

$$[q_j, q_{j'}] = [p_j, p_{j'}] = 0 \tag{2.34b}$$

It is convenient to employ a canonical transformation to operators a_j and $a_j^\dagger$:

$$a_j e^{-i\nu_j t} = \frac{1}{\sqrt{2m_j\hbar\nu_j}}(m_j\nu_j q_j + iq_j) \tag{2.35a}$$

$$a_j^\dagger e^{i\nu_j t} = \frac{1}{\sqrt{2m_j\hbar\nu_j}}(m_j\nu_j q_j - iq_j) \tag{2.35b}$$

In terms of a_j and $a_j^\dagger$, the Hamiltonian becomes

$$\mathscr{H} = \hbar\sum_j \nu_j \left(a_j^\dagger a_j + \frac{1}{2}\right) \tag{2.36}$$

The commutation relations between a_j and $a_j^\dagger$ can be derived from those between q_j and p_j:

$$[a_j, a_{j'}] = \delta_{jj'} \tag{2.37a}$$

$$[a_j, a_{j'}] = [a_j^\dagger, a_{j'}^\dagger] = 0 \tag{2.37b}$$

The operators a_j and $a_j^\dagger$ represent the annihilation and creation operators, respectively.

2.5.2 Atom-field Interaction

Instead of concerning the interaction of a classical field with matter, we now assume a quantized field, because in many instances a classical field fails to explain experimentally observed results, such as spontaneous emission in an atomic system. In this part, we thus discuss the interaction of the quantized radiation field with the two-level atomic system described by a Hamiltonian in the dipole and the rotating wave approximation.

The interaction of a radiation field $\mathbf{E}$ with a single electron atom can be described by the following Hamiltonian in the dipole approximation:

$$\mathscr{H} = \mathscr{H}_A + \mathscr{H}_F - e\mathbf{r} \cdot \mathbf{E} \tag{2.38}$$

Here $\mathscr{H}_A$ and $\mathscr{H}_F$ are the Hamiltonians of the atom and the radiation field, respectively, and $\mathbf{r}$ is the position operator of the electron. In the dipole approximation, the field is assumed to be uniform over the whole atom.

The Hamiltonian of the free field $\mathscr{H}_F$ is given in terms of the creation and annihilation operators by:

$$\mathscr{H}_F = \sum_k \hbar \nu_k \left(a_k^\dagger a_k + \frac{1}{2} \right) \tag{2.39}$$

We can describe $\mathscr{H}_A$ and $e\mathbf{r}$ on the basis of the atom transition operators:

$$\sigma_{ij} = |i\rangle\langle j| \tag{2.40}$$

$\{|i\rangle\}$ refers to a complete set of atomic energy eigenstates, i.e., $\sum_i |i\rangle\langle i| = 1$. Following the eigenvalue equation $\mathscr{H}_A|i\rangle = E_i|i\rangle$, $\mathscr{H}_A$ then becomes

$$\mathscr{H}_A = \sum_i E_i |i\rangle\langle i| = \sum_i E_i \sigma_{ii} \tag{2.41}$$

Also,

$$e\mathbf{r} = \sum_{i,j} e|i\rangle\langle i|\mathbf{r}|j\rangle\langle j| = \sum_{i,j} \wp_{ij}\sigma_{ij} \tag{2.42}$$

where $\wp_{ij} = e\langle i|\mathbf{r}|j\rangle$ is the electric-dipole transition matrix element. Due to the radiation field in terms of the plane waves ($\mathbf{E}(\mathbf{r},t) = \sum_k \hat{\varepsilon}_k \mathscr{E} a_k e^{-i\nu_k t + i\mathbf{kr}} + H.c.$), the electric field can be rewritten as

$$\mathbf{E} = \sum_k \hat{\varepsilon}_k \mathscr{E}_k (a_k + a_k^\dagger) \tag{2.43}$$

where $\mathscr{E}_k = (\hbar\nu_k/2\varepsilon_0 V)^{1/2}$.

It follows, on substituting for $\mathscr{H}_F$, $\mathscr{H}_A$, $e\mathbf{r}$, and $\mathbf{E}$, the Hamiltonian becomes

$$\mathscr{H} = \sum_k \hbar\nu_k a_k^\dagger a_k + \sum_i E_i \sigma_{ii} + \hbar \sum_{i,j} \sum_k g_k^{ij} \sigma_{ij} (a_k + a_k^\dagger) \tag{2.44}$$

where

$$g_k^{ij} = -\frac{\wp_{ij} \cdot \hat{\varepsilon}_k \mathscr{E}_k}{\hbar} \tag{2.45}$$

We now proceed to the case of a two-level atom. For $\wp_{ab} = \wp_{ba}$, we can know

$$g_k = g_k^{ab} = g_k^{ba} \tag{2.46}$$

The following form of the Hamiltonian is obtained

$$\mathscr{H} = \sum_k \hbar\nu_k a_k^\dagger a_k + (E_a\sigma_{aa} + E_b\sigma_{bb}) + \hbar \sum_k g_k (\sigma_{ab} + \sigma_{ba})(a_k + a_k^\dagger) \tag{2.47}$$

The second term in Eq. (2.47) can be written as

$$E_a\sigma_{aa} + E_b\sigma_{bb} = \frac{1}{2}\hbar\omega(\sigma_{aa} - \sigma_{bb}) + \frac{1}{2}(E_a + E_b) \tag{2.48}$$

where we use $(E_a - E_b) = \hbar\omega$ and $\sigma_{aa} + \sigma_{bb} = 1$. The constant energy term $(E_a + E_b)/2$ can be ignored. If we use the notation

$$\sigma_z = \sigma_{aa} - \sigma_{bb} = |a\rangle\langle a| - |b\rangle\langle b| \tag{2.49a}$$

$$\sigma_+ = \sigma_{ab} = |a\rangle\langle b| \tag{2.49b}$$

$$\sigma_- = \sigma_{ba} = |b\rangle\langle a|(a_j^\dagger a_{j'}^\dagger - a_{j'}^\dagger a_j^\dagger) = 0 \tag{2.49c}$$

Then the Hamiltonian takes the form

$$\mathscr{H} = \sum_k \hbar \nu_k a_k^\dagger a_k + \frac{1}{2}\hbar\omega\sigma_z + \hbar\sum_k g_k(\sigma_+ + \sigma_-)(a_k + a_k^\dagger) \tag{2.50}$$

In the matrix notation, σ_-, σ_+, and σ_z are given by

$$\sigma_- = \begin{pmatrix} 0 & 0 \\ 1 & 0 \end{pmatrix}, \qquad \sigma_+ = \begin{pmatrix} 0 & 1 \\ 0 & 0 \end{pmatrix}, \qquad \sigma_z = \begin{pmatrix} 1 & 0 \\ 0 & -1 \end{pmatrix} \tag{2.51}$$

The σ_- operator takes an atom in the upper state into the lower state whereas σ_+ takes an atom in the lower state into the upper state.

The interaction energy in Eq. (2.50) consists of four terms. The term $a_k^\dagger\sigma_-$ describes the process in which the atom is taken from the upper state into the lower state and a photon of mode **k** is created. The term $a_k\sigma_+$ describes the opposite process. The energy is conserved in both the processes. The term $a_k\sigma_-$ describes the process in which the atom makes a transition from the upper to the lower level and a photon is annihilated, leading to the loss of $2\hbar\omega$ in energy. Likewise, $a_k^\dagger\sigma_+$ contributes to the gain of $2\hbar\omega$ in energy. According to the rotating-wave approximation, the final simplified Hamiltonian is

$$\mathscr{H} = \sum_k \hbar \nu_k a_k^\dagger a_k + \frac{1}{2}\hbar\omega\sigma_z + \hbar\sum_k g_k(\sigma_+ a_k + a_k^\dagger\sigma_-) \tag{2.52}$$

This form of the Hamiltonian describing the inter action of a single two-level atom with a multi-mode field is the origin of many calculations in the area of quantum optics.

2.5.3 Quantum Theory of Damping - Density Operator and Wave Function Approach

In many physical systems pertaining to quantum optics, damping plays an important role, for instance, the decay of an atom in an excited state to a lower state as well as the decay of the radiation field inside a cavity with partially transparent mirrors. In short, damping of a system is described by its interaction with a reservoir with a large number of degrees of freedom.

Here, we first present a *theory of damping* based on the *density operator* where the reservoir variables are excluded by applying the reduced density operator for the system in the Schrodinger (interaction) picture.

Reservoir Theory

We now think about a system denoted by S interacting with a reservoir denoted by R. The combined density operator is denoted by ρ_{SR}. The reduced quantum state operator for the system ρ_S is obtained by taking a trace over the reservoir coordinates,

$$\rho_S = Tr_R(\rho_{SR}) \tag{2.53}$$

Assuming the system-reservoir interaction energy is given by $\gamma(t)$, the equation of motion for ρ_{SR} then becomes

$$i\hbar\dot{\rho}_{SR} = [\gamma(t), \rho_{SR}(t)] \tag{2.54}$$

Integrating this equation,

$$\rho_{SR}(t) = \rho_{SR}(t_i) - \frac{i}{\hbar}\int_{t_i}^{t}[\gamma(t', \rho_{SR}(t'))]dt' \tag{2.55}$$

Here t_i is the initial time when the interaction begins. Substituting $\rho_{SR}(t)$ back into Eq. (2.54), the equation of motion can be written as

$$\dot{\rho}_{SR} = \frac{i}{\hbar}[\gamma(t), \rho_{SR}(t_i)] - \frac{1}{\hbar^2}\int_{t^i}^{t}[\gamma(t), [\gamma(t'), \rho_{SR}(t')]]dt' \tag{2.56}$$

If the interaction energy $\gamma(t)$ is zero, the system and reservoir are independent and the density operator ρ_{SR} would factor as a direct product $\rho_{SR}(t) = \rho_S(t) \otimes \rho_R(t_i)$ where we assume the reservoir at equilibrium. Since γ is small, we look for a solution of Eq. (2.56) of the following form:

$$\rho_{SR}(t) = \rho_S(t) \otimes \rho_R(t_i) + \rho_c(t) \tag{2.57}$$

where $\rho_c(t)$ is of higher order in γ. To obey Eq. (2.53), we require

$$Tr_R[\rho_c(t)] = 0 \tag{2.58}$$

Substituting for $\rho_{SR}(t)$ from Eq. (2.57) into Eq. (2.56), and remaining terms up to order γ^2, we now have

$$\dot{\rho}_S = -\frac{i}{\hbar} Tr_R[\gamma(t), \rho_S(t_i) \otimes \rho_R(t_i)] - \frac{1}{\hbar^2} Tr_R \int_{t_i}^{t} [\gamma(t), [\gamma(t'), \rho_s(t') \otimes \rho_R(t_i)]] dt' \tag{2.59}$$

The reduced density operator $\rho_S(t)$, which defines the statistical properties of the system, depends upon its past history from $t = t_i$ to t'. Since damping destroys memory of the past, there is an assumption that the *Markovian* process occurs and the system density matrix $\rho_S(t')$ can be replaced by $\rho_S(t)$. The above Eq. (2.59) now can be cast in the following form

$$\dot{\rho}_S = -\frac{i}{\hbar} Tr_R[\gamma(t), \rho_S(t_i) \otimes \rho_R(t_i)] - \frac{1}{\hbar^2} Tr_R \int_{t_i}^{t} [\gamma(t), [\gamma(t'), \rho_s(t) \otimes \rho_R(t_i)]] dt' \tag{2.60}$$

This is a valid equation for a system determined by ρ_S interacting with a reservoir described by ρ_R.

Atomic Decay

We first consider the radiative decay of a two-level atom damped by a reservoir of harmonic oscillators described by annihilation (and creation) operators b_k (and $b_k^\dagger$ respectively) and the density distributed frequencies $\nu_k = ck$. In the interaction picture and the rotating-wave approximation, the Hamiltonian is

$$\gamma(t) = \hbar \sum_k g_k \left[b_k^\dagger \sigma_- e^{-i(\omega - \nu_k)t} + \sigma_+ b_k e^{i(\omega - \nu_k)t} \right] \tag{2.61}$$

where $\sigma_- = |b\rangle\langle a|$ and $\sigma_+ = |a\rangle\langle b|$ based on the excited ($|a\rangle$) and ground ($|b\rangle$)states. Inserting the interaction Hamiltonian γ Eq. (2.61) in the equation of motion Eq.

(2.59), we get

$$\begin{aligned}\dot{\rho}_{atom} &= -i\sum_k g_k\langle b_k\rangle[\sigma_-,\rho_{atom}(t_i)]e^{-i(\omega-\nu_k)t}\\ &-\int_{t_i}^{t}dt'\sum_{k,k'}g_kg_{k'}\{[\sigma_-\sigma_-\rho_{atom}(t')-2\sigma_-\rho_{atom}(t')\sigma_-+\rho_{atom}(t'\sigma_-\sigma_-)]\\ &\times e^{-i(\omega-\nu_k)t-i(\omega-\nu_{k'})t'}\langle b_k^\dagger b_{k'}^\dagger\rangle+[\sigma_-\sigma_+\rho_{atom}(t')-\sigma_+\rho_{atom}(t')\sigma_-]\\ &\times e^{-i(\omega-\nu_k)t-i(\omega-\nu_{k'})t'}\langle b_k^\dagger b_{k'}\rangle+[\sigma_+\sigma_-\rho_{atom}(t')-\sigma_-\rho_{atom}(t')\sigma_+]\\ &\times e^{-i(\omega-\nu_k)t-i(\omega-\nu_{k'})t'}\langle b_k b_{k'}^\dagger\rangle\}+H.c.\end{aligned} \tag{2.62}$$

where the expectation values refer to the initial state of the reservoir.

For instance, we suppose that the reservoir variables are spread in the uncorrelated thermal equilibrium mixture of states. The reservoir reduced density operator is the multi-mode extension of the thermal operator, expressed as

$$\rho_R=\prod_k\left[1-\exp\left(-\frac{\hbar\nu_k}{k_BT}\right)\right]exp\left(-\frac{\hbar\nu_k b_k^\dagger b_k}{k_BT}\right) \tag{2.63}$$

where k_B is the Boltzmann constant and T is the temperature. The thermal average boson number

$$\overline{n}_k=\frac{1}{exp\left(\frac{\hbar\nu_k}{k_BT}-1\right)} \tag{2.64}$$

It can easily be shown that

$$\langle b_k\rangle=\langle b_k^\dagger\rangle=0 \tag{2.65a}$$

$$\langle b_k^\dagger b_{k'}\rangle=\overline{n_k}\delta_{kk'} \tag{2.65b}$$

$$\langle b_k b_{k'}^\dagger\rangle=(\overline{n_k}+1)\delta_{kk'} \tag{2.65c}$$

$$\langle b_k b_{k'}\rangle=\langle b_k^\dagger b_{k'}^\dagger\rangle=0 \tag{2.65d}$$

Inserting the above four equations into Eq. (2.66), we obtain

$$\dot{\rho}_{atom} = -\int_{t_i}^{t} dt' \sum_k g_k^2 \{[\sigma_- \sigma_+ \rho_{atom}(t') - \sigma_+ \rho_{atom}(t') \sigma_-] \bar{n}_k e^{-i(\omega-\nu_k)(t-t')} + [\sigma_+ \sigma_- \rho_{atom}(t') - \sigma_- \rho_{atom}(t') \sigma_+](\bar{n}_{th}+1) e^{-i(\omega-\nu_k)(t-t'}\} + H.c. \quad (2.66)$$

With regard to the decay of a mode of electromagnetic field of frequency ν inside a cavity, we now use an interaction Hamiltonian of the following form:

$$\gamma = \hbar \sum_k g_k \left[b_k^\dagger a e^{-i(\nu-\nu_k)t} + a^\dagger b_k e^{i(\nu-\nu_k)t} \right] \quad (2.67)$$

where a (and $a^\dagger$) are the annihilation (and creation) operators of the mode of interest, the operators b and $b^\dagger$ indicate modes of the reservoir which damp the field.

Since the field equation of motion for reduced density operator parallels the one for atomic system, by replacing σ_- and σ_+ by the field operators a and $a^\dagger$, respectively, in Eq. , we can easily obtain the result as follows:

$$\dot{\rho} = -\frac{\mathscr{E}}{2} \bar{n}_{th} (a a^\dagger \rho - 2 a^\dagger \rho a + \rho a a^\dagger) - \frac{\mathscr{E}}{2} (\bar{n}_{th}+1)(a^\dagger a \rho - 2 a \rho a^\dagger + \rho a^\dagger a) \quad (2.68)$$

where the modes b_k are initially in the thermal equilibrium mixture of states, and $\mathscr{E}$ is the decay constant and $\bar{n}_{th} = \bar{n}_{k_0}$ is the mean number of quanta (at frequency ν) in the thermal reservoir. Here ρ refers to the reduced density operator for the field. Particularly, when the temperature equals to zero ($\bar{n}_{th} = 0$),

$$\dot{\rho} = -\frac{\mathscr{E}}{2} (a^\dagger a \rho - 2 a \rho a^\dagger + \rho a^\dagger a) \quad (2.69)$$

In this section, we first demonstrate the quantum theory of radiation, which describes the field with quantum theory rather than the classical concepts of physics. Then the Hamiltonian of atom-field interaction was demonstrated. Lastly the quantum theory of damping based on density operator and wave function approach, which is important for quantum computation in the open system. All the concepts in this section will be used in chapter 6.

Bibliography

[1] J. Villatoro, V. Finazzi, G. Coviello, and V. Pruneri, "Photonic-crystal-fiber-enabled micro-FabryPerot interferometer," Opt. Lett. **34** 2441-2443 (2009).

[2] M. Qiu, M. Mulot, M. Swillo, S. Anand, B. Jaskorzynska, A. Karlsson, and A. Forchel, "Photonic crystal optical filter based on contra-directional waveguide coupling," Appl. Phys. Lett. **83** 5121-5123 (2003).

[3] I. Vurgaftman, and J. R. Meyer, "Photonic-crystal distributed-feedback lasers," Appl. Phys. Lett. **78** 1475-1477 (2001).

[4] L. Vicarelli, M. S. Vitiello, D. Coquillat, A. Lombardo, A. C. Ferrari, W. Knap, and A. Tredicucci, "Graphene field-effect transistors as room-temperature terahertz detectors," Nat. Mater. **11** 865 (2012).

[5] G. S. Kulkarni, K. Reddy, Z. Zhong, and X. Fan, "Graphene nanoelectronic heterodyne sensor for rapid and sensitive vapour detection," Nat. Commun. **5** 4376 (2014).

[6] H. Yan, X. Li, B. Chandra, G. Tulevski, Y. Wu, M. Freitag, and F. Xia, "Tunable infrared plasmonic devices using graphene/insulator stacks," Nat. Nanotechnol. **7** 330 (2012).

[7] A. K. Geim and K. S. Novoselov, "The rise of graphene," Nat. Mater. **6** 183191 (2007).

[8] A. C. Neto, F. Guinea, N. M. Peres, K. S. Novoselov, and A. K. Geim, "The electronic properties of graphene," Rev. Mod. Phys. **81** 109 (2009).

[9] J. Phiri, P. Gane, and T. C. Maloney, “General overview of graphene: Production, properties and application in polymer composites,” Mater. Sci. Eng., B **215** 9-28 (2017).

[10] X. Cao, Z. Yin, and H. Zhang, “Three-dimensional graphene materials: preparation, structures and application in supercapacitors,” Energy Environ. Sci. **7** 1850-1865 (2014).

[11] M. J. Allen, V. C. Tung, and R. B. Kaner, “Honeycomb carbon: a review of graphene,” Chem. Rev. **110** 132-145 (2009).

[12] H. Chen, M. B. Muller, K. J. Gilmore, G. G. Wallace, and D. Li, “Mechanically strong, electrically conductive, and biocompatible graphene paper,” Adv. Mater. **20** 3557-3561 (2008).

[13] Y. Kopelevich, and P. Esquinazi, “Graphene physics in graphite,” Adv. Mater. **19** 4559-4563 (2007).

[14] D. S. L. Abergel, V. Apalkov, J. Berashevich, K. Ziegler, and T. Chakraborty, “Properties of graphene: a theoretical perspective,” Adv. Phys. **59** 261-482 (2010).

[15] T. J. Echtermeyer, L. Britnell, P. K. Jasnos, A. Lombardo, R. V. Gorbachev, A. N. Grigorenko, and K. S. Novoselov, “Strong plasmonic enhancement of photovoltage in graphene,” Nat. Commun. **2** 458 (2011).

[16] F. DSouza, and K. M. Kadish, *Handbook of carbon nano materials* World Scientific (2012).

[17] T. Low, and P. Avouris, “Graphene plasmonics for terahertz to mid-infrared applications,” ACS Nano **8** 1086-1101 (2014).

[18] S. Thongrattanasiri, F. H. Koppens, and F. J. G. De Abajo, “Complete optical absorption in periodically patterned graphene,” Phys. Rev. Lett. **108** 047401 (2012).

[19] A. K. Geim, “Graphene: status and prospects,” Science **324** 1530-1534 (2009).

[20] N. Stander, B. Huard, and D. Goldhaber-Gordon, “Evidence for Klein tunneling in graphene p n junctions,” Phys. Rev. Lett. **102** 026807 (2009).

[21] R. R. Nair, P. Blake, A. N. Grigorenko, K. S. Novoselov, T. J. Booth, T. Stauber, and A. K. Geim, “Fine structure constant defines visual transparency of graphene,” Science **320** 1308-1308 (2008).

[22] N. Levy, S. A. Burke, K. L. Meaker, M. Panlasigui, A. Zettl, F. Guinea, and M. F. Crommie, “Strain-induced pseudomagnetic fields greater than 300 tesla in graphene nanobubbles,” Science **329** 544-547 (2010).

[23] R. R. Nair, W. Ren, R. Jalil, I. Riaz, V. G. Kravets, L. Britnell, and M. I. Katsnelson, “Fluorographene: a twodimensional counterpart of Teflon,” Small **6** 2877-2884 (2010).

[24] A. R. Melnyk and M. J. Harrison, “Theory of optical excitation of plasmons in metals,” Phys. Rev. B **2** 835 (1970).

[25] A. N. Grigorenko, M. Polini, and K. S. Novoselov, “Graphene plasmonics,” Nat. Photonics **6** 749 (2012).

[26] S. Zeng, K. T. Yong, I. Roy, X. Q. Dinh, X. Yu, and F. Luan, “A review on functionalized gold nanoparticles for biosensing applications,” Plasmonics **6** 491 (2011).

[27] M. G. Cottam and D. R. Tilley, *Introduction to surface and superlattice excitations.* CRC Press (2004).

[28] Wikipedia, *https://en.wikipedia.org/wiki/Surface-plasmon*

[29] H. Buljan, M. Jablan, and M. Soljacic, “Graphene plasmonics: Damping of plasmons in graphene,” Nat. Photonics **7** 346 (2013).

[30] W. Han, R. K. Kawakami, M. Gmitra, and J. Fabian, “Graphene spintronics,” Nat. Nanotechnol. **9** 794807 (2014).

[31] H. Yan, T. Low, W. Zhu, Y. Wu, M. Freitag, X. Li, and F. Xia, "Damping pathways of mid-infrared plasmons in graphene nanostructures," Nat. Photonics **7** 394 (2013).

[32] Z. Liu, K. Suenaga, P. J. Harris, and S. Iijima, "Open and closed edges of graphene layers," Phys. Rev. Lett. **102** 015501 (2009).

[33] S. Bak, D. Kim, and H. Lee, "Graphene quantum dots and their possible energy applications: A review," Curr. Appl Phys. **16** 1192-1201 (2016).

[34] X. Yang and C. W. Wong, "Stimulated Raman amplification and lasing in silicon photonic band gap nanocavities," Sens. Actuators, A **133** 278-282 (2007).

[35] Y. Akahane, T. Asano, H. Takano, B. S. Song, Y. Takana, and S. Noda, "Two-dimensional photonic-crystal-slab channel-drop filter with flat-top response," Opt. Express **13** 2512-2530 (2005).

[36] H. G. Park, S. H.Kim, S. H. Kwon, Y. G. Ju, J. K. Yang, J. H. Baek, and Y. H. Lee, "Electrically driven single-cell photonic crystal laser," Science **305** 1444-1447 (2004).

[37] T. Yoshie, A. Scherer, J. Hendrickson, G. Khitrova, H. M. Gibbs, G. Rupper, and D. G. Deppe, "Vacuum Rabi splitting with a single quantum dot in a photonic crystal nanocavity," Nature **432** 200 (2004).

[38] M. Notomi, A. Shinya, S. Mitsugi, G. Kira, E. Kuramochi, and T. Tanabe, "Optical bistable switching action of Si high-Q photonic-crystal nanocavities," Opt. Express **13** 2678-2687 (2005).

[39] R. Claps, D. Dimitropoulos, Y. Han, and B. Jalali, "Observation of Raman emission in silicon waveguides," Opt. Express **10** 1305-1313 (2002).

[40] R. L. Espinola, J. I. Dadap, R. M. Osgood, S. J. McNab, and Y. A. Vlasov, "Raman amplification in ultrasmall silicon-on-insulator wire waveguides," Opt. Express **12** 3713-3718 (2004).

[41] Q. Xu, V. R. Almeida, and M. Lipson, "Time-resolved study of Raman gain in highly confined silicon-on-insulator waveguides," Opt. Express **12** 4437-4442 (2004).

[42] T. K. Liang and H. K. Tsang, "Efficient Raman amplification in silicon-oninsulator waveguides," Appl. Phys. Lett. **85** 33433345 (2004).

[43] A. Liu, H. Rong, M. Paniccia, O. Cohen, and D. Hak, "Net optical gain in a low loss silicon-on-insulator waveguide by stimulated Raman scattering," Opt. Express **12** 4261-4268 (2004).

[44] H. K. Tsang, C. S. Wong, T. K. Liang, I. E. Day, S. W. Roberts, A. Harpin, and M. Asghari, "Optical dispersion, two-photon absorption and self-phase modulation in silicon waveguides," Appl. Phys. Lett. **80** 416-418 (2002).

[45] BandSOLVE, FullWave. *URL: http://www.rsoftdesign. com.*

[46] Ramachandran, Prabhu, and Gael Varoquaux. "Mayavi: 3D visualization of scientific data." Computing in Science and Engineering 13.2 (2011): 40-51.

[47] Oskooi, Ardavan F., et al. "MEEP: A flexible free-software package for electromagnetic simulations by the FDTD method." Computer Physics Communications **181** 687-702 (2010).

[48] Studio, Microwave. "CST-Computer Simulation Technology." Bad Nuheimer Str 19 (2008): 64289.

[49] B. Temelkuran, and E. Ozbay, "Experimental demonstration of photonic crystal based waveguides," Appl. Phys. Lett. **74** 486-488 (1999).

[50] J. G. Fleming and S. Y. Lin, "Three-dimensional photonic crystal with a stop band from 1.35 to 1.95 um," Opt. Lett. **24** 4951 (1999).

[51] X. Zheng, M. Taverne, Y. L. Ho, and J. Rarity, "Cavity Design in Woodpile Based 3D Photonic Crystals," Appl. Sci. **8** 1087 (2018).

[52] J. D. Joannopoulos, et al. *Photonic crystals: molding the flow of light.* Princeton university press, 2011.

[53] K. M. Ho, C. T. Chan, and C. M. Soukoulis, "Existence of a photonic gap in periodic dielectric structures," Phys. Rev. Lett. **65** 3152 (1990).

[54] G. Eckhardt, R. W. Hellwarth, F. J. McClung, S. E. Schwarz, D. Weiner, and E. J. Woodbury, "Stimulated Raman scattering from organic liquids," Phys. Rev. Lett. **9** 455 (1962).

[55] O. Boyraz, and B. Jalali, "Demonstration of a silicon Raman laser," Opt. Express **12** 5269-5273 (2004).

[56] H. Rong, R. Jones, A. Liu, O. Cohen, D. Hak, A. Fang, and M. Paniccia, "A continuous-wave Raman silicon laser," Nature **433** 725 (2005).

[57] B. Jalali, "Making silicon lase," Sci. Am. **296** 58-65 (2007).

[58] D. A. Long, *Raman spectroscopy*, New York, 1-12 (1977).

[59] X. Zhang, and Y. Wu, "Effective medium theory for anisotropic metamaterials," Sci. Rep. **5** 7892 (2015).

[60] J. Zhou, L. Zhang, G. Tuttle, T. Koschny, and C. M. Soukoulis, "Negative index materials using simple short wire pairs," Phys. Rev. B **73** 041101 (2006).

[61] D. R. Smith, J. B. Pendry, and M. C. Wiltshire, "Metamaterials and negative refractive index," Science **305** 788-792 (2004).

[62] S. A. Ramakrishna, "Physics of negative refractive index materials," Reports on progress in physics **68** 449 (2005).

[63] C. M. Soukoulis, S. Linden, and M. Wegener, "Negative refractive index at optical wavelengths," Science **315** 47-49 (2007).

[64] S. Lan, L. Kang, D. T. Schoen, S. P. Rodrigues, Y. Cui, M. L. Brongersma, and W. Cai, "Backward phase-matching for nonlinear optical generation in negative-index materials," Nat. Mater. **14** 807 (2015).

Chapter 3

Giant enhancement of the effective Raman susceptibility in metasurfaces made of silicon photonic crystal nanocavities

3.1 Introduction

Metasurfaces, which are artificial optical thin films structured at subwavelength scale, have become widely used tools to engineer in unique ways light-matter interaction at the nanoscale [1, 2, 3, 4, 5]. These developments have been primarily facilitated by recent advancements in nanofabrication techniques, and have made possible to achieve planar structures that resonantly interact with light at specific frequencies. Compared to three-dimensional (3D) metamaterials, two-dimensional (2D) metasurfaces allow the manipulation of light using more compact devices [6] and exhibit lower optical power loss [7]. In addition, key nonlinear optical functionalities (including high-harmonics generation and frequency mixing) can be more easily implemented using metasurfaces [8, 9, 10, 11], since usually one does not have to be concerned with satisfying phase-matching conditions. These and other unique optical properties of metasurfaces have been opening up new avenues to pursue promising applications in areas such as quantum information processing

[12, 13] and photonic integrated circuits [14, 15].

There are two main approaches towards nonlinear metasurfaces, namely metasurfaces based on metallic (plasmonic) [8, 10, 16, 29, 18] and dielectric [4, 19, 20, 21] materials. Plasmonic metasurfaces can generate strong optical near-field enhancement, a key feature for nonlinear optics applications. This comes, however, at the price of relatively large optical losses, which reduces their conversion efficiency. Dielectric metasurfaces, on the other hand, are characterized by small optical losses but their limitations stem from the fact that the enhancement of the optical near-field is smaller than that achieved with plasmonic metasurfaces. In order to overcome this shortcoming of all-dielectric metasurfaces, one could engineer their primary building blocks so that they possess resonant optical modes with high quality- (Q) factor. These specially engineered modes are different in nature from Mie resonances of dielectric particles [22, 23], which are characterized by relatively small Q-factor. Due to the large set of parameters that can be tuned to optimize their Q-factor, photonic crystal (PhC) cavities represent an excellent choice for designing optical resonators with high Q-factor, although other solutions, such as whispering-gallery modes of resonators made of silica or other dielectric materials, are possible, too.

In order to illustrate this idea, in this chapter we demonstrate that the effective Raman susceptibility of a metasurface consisting of a periodic array of PhC cavities in a silicon PhC slab waveguide can be enhanced by more than 4 orders of magnitude, as compared to the intrinsic Raman susceptibility of silicon. This is achieved by designing a silicon PhC cavity that possesses two high-Q optical modes separated spectrally by the Raman frequency of silicon, $\Omega/2\pi = 15.6\,\mathrm{THz}$ [52]. The effective Raman susceptibility of the metasurface is calculated using a new homogenization procedure based on the effective-medium theory, an approach that is valid beyond the subwavelength unit cell regime. Importantly, this procedure can be applied to other multi-wavelength nonlinear optical interactions, such as four-wave mixing, optical parametric amplification, and second-harmonic generation, simply by designing PhC cavities that possess optical modes at the required frequencies.

The chapter is organized as follows. In the next section we present the geometrical configuration and optical properties of the nonlinear metasurface. Then, in Sec. 3.3 we introduce the homogenization method used to calculate the effective Raman susceptibility of the metasurface, whereas in Sec. 3.4 we present and discuss the main results. Finally, in Sec. 3.5 the main conclusions are summarizad.

3.2 Geometrical configuration and properties of the nonlinear metasurface

The nonlinear photonic metasurface and the homogenization procedure used to compute the corresponding effective Raman susceptibility are schematically illustrated in Fig. 3.1. It comprises of a rectangular array of PhC cavities in a PhC slab waveguide made of silicon ($n_{Si} = 3.4$). This structure can be fabricated with current technology readily. The slab waveguide consists of a 2D hexagonal lattice of air holes in a silicon slab, with lattice constant, a, hole radius, $r = 0.29a$, and slab thickness, $t = 0.6a$. The bandgap with these optical parameters is around the telecommunication wavelength. Moreover, in this study we use $L5$ PhC cavities, namely they are formed by filling in 5 consecutive holes located on a line oriented along the ΓK symmetry axis of the lattice. The center-to-center distance between adjacent PhC cavities along the longitudinal (x) and transverse (y) directions is $d_l = 17a$ and $d_t = 6\sqrt{3}a$, respectively. In order to increase the Q-factor of the optical modes of the cavity the end holes are shifted by $s_l = 0.15a$ [25].

The photonic band structure of the PhC slab waveguide and the frequencies of the cavity modes were computed using RSoft's BandSOLVE [26] and are presented in Fig. 3.2, whereas the Q-factors of the cavity modes were determined using MEEP [27], a freely available software that implements the finite-difference time-domain algorithm. Thus, the PhC cavity possesses two optical modes with normalized frequencies (measured in units of $2\pi c/a$) of $\bar{\omega}_p = 0.2778$ and $\bar{\omega}_S = 0.2605$ and Q-factors of $Q_p = 1804$ and $Q_S = 1.12 \times 10^5$. These cavity modes lie in the transverse-magnetic band-gap of the PhC slab waveguide, as per Fig. 3.2(b), the field profiles of the two optical modes being shown in this figure, too. Moreover, if the lattice constant is $a = 333\,\mathrm{nm}$, the frequencies of the two cavity modes are $\omega_p = 1572.5\,\mathrm{THz}$ and $\omega_S = 1474.6\,\mathrm{THz}$, that is they are separated by the Raman frequency of silicon, $\omega_p - \omega_S = \Omega = 2\pi \times 15.6\,\mathrm{THz}$. Under these circumstances, the PhC cavity can be viewed as a “meta-molecule” possessing strong Raman response, as schematically illustrated in Fig. 3.2(a).

Consider now that such PhC cavities are arranged in a rectangular 2D array, such that one creates a nonlinear metasurface that can potentially generate strongly enhanced stimulated Raman scattering as compared to that of intrinsic silicon. This is so because the existence of the two cavity modes ensures an effective optical coupling between the incident optical wave and the cavity mode at the pump frequency and provides an efficient mechanism for the Raman signal to be radiated in the continuum *via* the excitation of the cavity mode at the Stokes frequency. We have computed the effective Raman susceptibility of such a nonlinear optical metasurface using a newly developed homogenization technique, which we present in the next section.

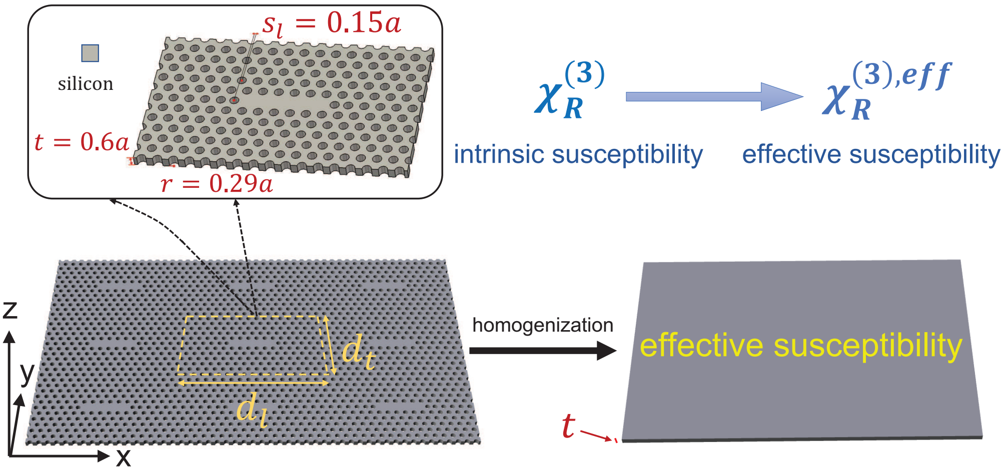

Figure 3.1: Schematic of a silicon nonlinear metasurface for enhancement of stimulated Raman scattering. The metasurface consists of a rectangular array of PhC cavities in a hexagonal PhC slab waveguide made of silicon. Also illustrated is the homogenization procedure used to compute the corresponding effective Raman susceptibility, $\boldsymbol{\chi}_R^{(3),\mathrm{eff}}$, of a homogeneous slab with the same thickness, t, from the intrinsic Raman susceptibility of silicon, $\boldsymbol{\chi}_R^{(3)}$.

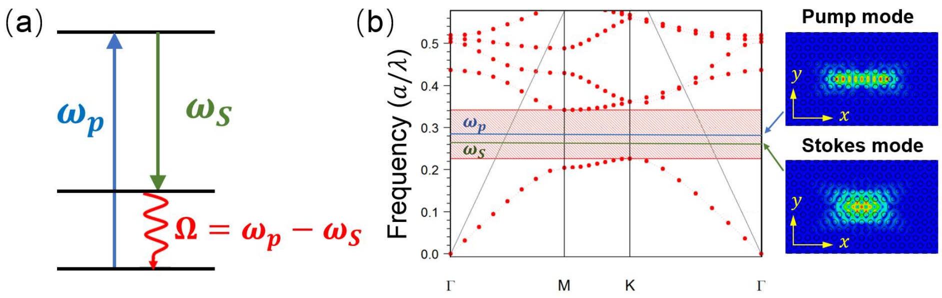

Figure 3.2: (a) Schematic diagram of stimulated Raman scattering: a pump photon with frequency ω_p interacts with a Raman-active optical medium and generates a Stokes photon with frequency ω_S and a phonon with frequency $\Omega = \omega_p - \omega_S$. (b) Transverse-magnetic band structure of the photonic crystal and the two cavity modes. The field profile of the cavity modes are shown in the right panels.

3.3 Homogenization approach for calculation of the effective Raman susceptibility

The most common approach to homogenize a metasurface is based on the effective-medium theory [28, 29, 30, 31]. Generally speaking, this approach amounts to averaging the electromagnetic field over the unit cells of the metasurface. Through the homogenization procedure, the photonic system is reduced to a slab of homogeneous optical medium characterized by effective electric permittivity and magnetic permeability [32, 33, 34]. On the other hand, in the nonlinear case, the nonlinear effective susceptibilities are calculated from a spatial overlap integral among fields excited in the structure by probing waves at pump and higher-harmonics, weighted by the local nonlinear susceptibility tensor and averaged over the volume of the unit cell [35, 36, 37, 38].

Before describing our homogenization method, we would like to point out that whereas the linear effective optical constants, such as the electric permittivity and magnetic permeability, can be calculated in an unambiguous way, in the case of the effective nonlinear susceptibilities the large number of nonvanishing components of these tensor quantities could lead to certain ambiguity in how they are defined and calculated. To be more specific, in most cases homogenization methods for nonlinear metasurfaces rely on the condition that the averaged nonlinear polarization of the metasurface is equal to the nonlinear polarization in the nonlinear homogenized slab of material. As mentioned, this approach results in ambiguities in the determination of the effective nonlinear susceptibility because three relations that ensure that the two nonlinear polarizations are identical must be used to determine a much larger number of components of the nonlinear susceptibility tensor. The key novel aspect of our homogenization approach is that the calculated effective nonlinear susceptibility is unique. This is achieved by imposing the condition that the averaged nonlinear polarization of the metasurface and the nonlinear polarization in the homogenized slab are *term-wise identical* (term by term identical) when expressed in terms of the components of the nonlinear susceptibilities and the electric field components.

The Raman nonlinear optical response of the metasurface is determined by the nonlinear Raman polarization at the Stokes frequency, ω_S [39]:

$$\mathbf{P}_R(\omega_S;\mathbf{r}) = \frac{3}{2}\varepsilon_0 \boldsymbol{\chi}_R^{(3)}(\mathbf{r}) \vdots \mathbf{E}(\omega_p;\mathbf{r})\mathbf{E}^*(\omega_p;\mathbf{r})\mathbf{E}(\omega_S;\mathbf{r}), \tag{3.1}$$

where $\boldsymbol{\chi}_R^{(3)}(\mathbf{r})$ is the Raman susceptibility, $\mathbf{P}_R(\omega_S;\mathbf{r})$ is the Raman polarization at ω_S, and $\mathbf{E}(\omega_p;\mathbf{r})$ and $\mathbf{E}(\omega_S;\mathbf{r})$ are the optical fields at the pump and Stokes frequencies, respectively. These fields correspond to plane-wave excitation at the two frequencies, such that standard experimental conditions are replicated. In order to avoid unnecessary complications, we assume that the cavities are distributed in a 2D rectangular array, with the symmetry axes of the array coinciding both with the x- and y-coordinates and with the principal axes of silicon. Then, the nonzero components of $\boldsymbol{\chi}_R^{(3)}$ are $\chi_{R,ijij}^{(3)} = \chi_{R,jiji}^{(3)} = \chi_{R,jiij}^{(3)} = \chi_{R,ijji}^{(3)}$, with $i,j = x,y,z$ and $i \neq j$, the value at resonance of the only independent component being $\chi_{R,1212}^{(3)} = -i11.2 \times 10^{-18}\,\mathrm{m}^2\,\mathrm{V}^{-2}$ [40].

The position-dependent Raman polarization defined by Eq. (3.1) can be used to calculate the spatially averaged effective Raman polarization:

$$\mathbf{P}_{R,\mathrm{eff}}(\omega_S) = \frac{1}{V}\int_V \mathbf{P}_R(\omega_S;\mathbf{r})d\mathbf{r}, \tag{3.2}$$

where the volume integration is taken over the unit cell of the metasurface. On the other hand, if one replaces the metasurface with a homogenized slab of nonlinear optical medium with the same thickness as that of the PhC slab, the corresponding effective Raman polarization can be written in terms of an effective Raman susceptibility, $\boldsymbol{\chi}_R^{(3),\text{eff}}$, as:

$$\bar{\mathbf{P}}_{R,\text{eff}}(\omega_S) = \frac{3}{2}\varepsilon_0 \boldsymbol{\chi}_R^{(3),\text{eff}} \vdots \bar{\mathbf{E}}_{\text{eff}}(\omega_p)\bar{\mathbf{E}}^*_{\text{eff}}(\omega_p)\bar{\mathbf{E}}_{\text{eff}}(\omega_S). \tag{3.3}$$

In this equation and in what follows, the bar symbol indicates that the field corresponds to the homogenized medium. Moreover, we stress that in Eq. (3.3) the fields $\bar{\mathbf{E}}_{\text{eff}}(\omega_p)$ and $\bar{\mathbf{E}}_{\text{eff}}(\omega_S)$ are the effective optical fields at the pump and Stokes frequencies, respectively, generated by an input field that is equal to the field that excites the metasurface. They are given by:

$$\bar{\mathbf{E}}_{\text{eff}}(\omega_\alpha) = \frac{1}{V}\int_V \bar{\mathbf{E}}(\omega_\alpha;\mathbf{r})d\mathbf{r}, \tag{3.4}$$

where $\alpha = p, S$.

The nonlinear optical response of the metasurface and homogenized slab are identical if the effective Raman polarizations described by Eqs. (3.2) and (3.3) are equal, which leads to three equations (one for each component). Note, however, that in the general case the effective Raman susceptibility tensor, $\boldsymbol{\chi}_R^{(3),\text{eff}}$, has 81 independent components, so that the corresponding system of equations is overdetermined. In order to circumvent this issue, we impose the condition that the r.h.s. of Eqs. (3.2) and (3.3) are *term-wise identical*. Using this constraint, it can be seen that the components of the effective Raman susceptibility tensor are determined by the following relations:

$$\chi_{R,ijkl}^{(3),\text{eff}} = \frac{\frac{1}{V}\int_V \chi_{R,ijkl}^{(3)}(\mathbf{r})E_j(\omega_p;\mathbf{r})E_k^*(\omega_p;\mathbf{r})E_l(\omega_S;\mathbf{r})d\mathbf{r}}{\bar{E}_{j,\text{eff}}(\omega_p)\bar{E}^*_{k,\text{eff}}(\omega_p)\bar{E}_{l,\text{eff}}(\omega_S)}. \tag{3.5}$$

Note that the components of $\boldsymbol{\chi}_R^{(3),\text{eff}}$ and $\boldsymbol{\chi}_R^{(3)}$ cancel for the same set of indices i, j, k, and l.

The remaining physical quantities needed to calculate the effective Raman susceptibility given in Eq. (3.5) are the effective fields in the homogenized slab. They can be calculated analytically (see the Appendix), but before this one needs to determine the effective electric permittivity of the slab. This can be calculated by imposing the condition that the spatially averaged electric displacement in the metasurface, $D_i(\omega_\alpha) = (1/V)\sum_j \int_V \varepsilon_{ij}(\mathbf{r})E_j(\omega_\alpha;\mathbf{r})d\mathbf{r}$, where $\varepsilon_{ij}(\mathbf{r}) = \varepsilon_0 n_{Si}^2 \delta_{ij}$ and $\varepsilon_{ij}(\mathbf{r}) = \varepsilon_0 \delta_{ij}$ for $\mathbf{r}$ in the silicon and air regions, respectively, with δ_{ij} being the Kronecker delta, is equal to the effective electric displacement in the homogenized slab, $\bar{D}_i(\omega_\alpha) = (1/V)\sum_j \bar{\varepsilon}_{ij}^{\text{eff}}(\omega_\alpha)\int_V E_j(\omega_\alpha;\mathbf{r})d\mathbf{r}$. If the two electric displacement fields are equal on a term by term basis, the effective permittivity is given by:

$$\bar{\varepsilon}_{ij}^{\text{eff}}(\omega_\alpha) = \frac{\displaystyle\int_V \varepsilon_{ij}(\mathbf{r})E_j(\omega_\alpha;\mathbf{r})d\mathbf{r}}{\displaystyle\int_V E_j(\omega_\alpha;\mathbf{r})d\mathbf{r}}. \tag{3.6}$$

This equation implies that the effective electric permittivity of the homogenized slab is described by a diagonal matrix, but the diagonal elements are not necessarily the same.

Finally, the effective permittivity in Eq. (3.6) is used to determine analytically the effective electric field in the homogenized slab. The details of these calculations are provided in the Appendix, so that here we only give the final result:

$$\bar{E}_{i,\text{eff}} = \frac{i(1+\rho_i)}{k_i t}\left(1 - \frac{1-\sigma_i + 2\sigma_i e^{ik_i t}}{e^{-ik_i t} + \sigma_i e^{ik_i t}}\right)E_{i,0}. \tag{3.7}$$

Here, $E_{i,0}$, $i = x,y$, is the amplitude of the incident field and

$$\sigma_i = \frac{Z_0 - Z_i}{Z_0 + Z_i}, \qquad \rho_i = \frac{\left(Z_i^2 - Z_0^2\right)\tan(k_i t)}{2iZ_i Z_0 + \left(Z_i^2 + Z_0^2\right)\tan(k_i t)}, \tag{3.8}$$

where $Z_0 = \sqrt{\mu_0/\varepsilon_0}$ is the vacuum impedance, $Z_i = \sqrt{\mu_0/\bar{\varepsilon}_{ii}^{\text{eff}}}$, and $k_i(\omega_\alpha) = \omega_\alpha\sqrt{\mu_0\bar{\varepsilon}_{ii}^{\text{eff}}}$.

Before we move on to illustrate how this homogenization method can be applied to our metasurface, we stress that although the method can be successfully used to describe metasufaces with period comparable or larger than the wavelength of the interacting beams, the resulting effective permittivity and effective nonlinear Raman susceptibility would depend on the polarization of the interacting beams and the angle of incidence. Thus, it is known that when the wavelength is comparable to the characteristic length of a photonic structure, *e.g.* the lattice constant of a PhC, physical quantities related to the spatial average of the microscopic electromagnetic field depend not only on the frequency but also on the wave vector, $\mathbf{k}$. This means that, for example, the dispersion relation of the electric permittivity has a more complex form, $\varepsilon = \varepsilon(\omega, \mathbf{k})$. This is valid for the nonlinear optical response of photonic structures, too, so that the nonlinear susceptibilities depend on the direction of propagation and polarization of the interacting fields. This is expected because when the wavelength is comparable to the characteristic length of a photonic structure the local fields, which determine the nonlinear polarization of the medium, depend on the direction of propagation and polarization of the incident fields.

3.4 Results and discussion

We have applied the homogenization procedure described in the preceding section to our nonlinear metasurface. The first step in our analysis was to compute the field distribution at the pump and signal frequencies of the corresponding cavity modes under plane-wave excitation conditions. The calculations were performed using the frequency-domain finite element method implemented in CST Studio, a commercially available software [41]. Thus, we first determined the spectral response of the metasurface and then, using a normally incident plane-wave excitation source polarized at $\pi/4$ with respect to the x-axis and with excitation frequency equal to the pump and Stokes frequencies we determined the field profiles at the corresponding resonance frequencies. The spectral response of the metasurface has been determined in the frequency domain ranging from 200 THz to 300 THz, that is a spectral domain that contains the two resonances of interest, by determining the frequency dependence of the electric field at an arbitrary point in the metasurface. Despite the fact that the spectrum varies with the position of the point in the metasurface where the electric field is probed, the location of the resonances does not depend on this choice.

We present in Fig. 3.3 the spectrum calculated using this approach, as well as the profiles of the field amplitude corresponding to the two cavity modes located at the pump and Stokes frequencies. These are the same modes shown in the inset of Fig. 3.2(b) and, as mentioned, were calculated using BandSOLVE. It can be seen that the spectral separation between the two resonances is equal to the Raman frequency, $\Delta\nu = \nu_R = 15.6\,\mathrm{THz}$, a result that validates our design approach.

Due to the symmetry properties of the metasurface and the orientation of the cavity array with respect to the principal axes of silicon, the only non-zero component of the effective Raman susceptibility is $\chi^{(3),\mathrm{eff}}_{R,1212}$. Therefore, in order to compute it, one only needs to calculate the effective permittivity components $\bar{\varepsilon}^{\mathrm{eff}}_{ij}$, $i,j = x,y$. Note that the effective permittivity must be calculated both at the pump and Stokes frequencies. The effective permittivity is determined using Eq. (3.6), the results being $\bar{\varepsilon}_{xx}(\omega_s) = 8.777 + 0.367\mathrm{i}$, $\bar{\varepsilon}_{yy}(\omega_s) = 9.034 - 0.003\mathrm{i}$, $\bar{\varepsilon}_{xx}(\omega_p) = 9.000 + 0.044\mathrm{i}$, $\bar{\varepsilon}_{yy}(\omega_p) = 8.921 + 0.049\mathrm{i}$, and $\bar{\varepsilon}_{xy}(\omega_s) = \bar{\varepsilon}_{yx}(\omega_s) = \bar{\varepsilon}_{xy}(\omega_p) = \bar{\varepsilon}_{yx}(\omega_p) = 0$. As expected, the effective permittivity is a complex, diagonal matrix, and the diagonal

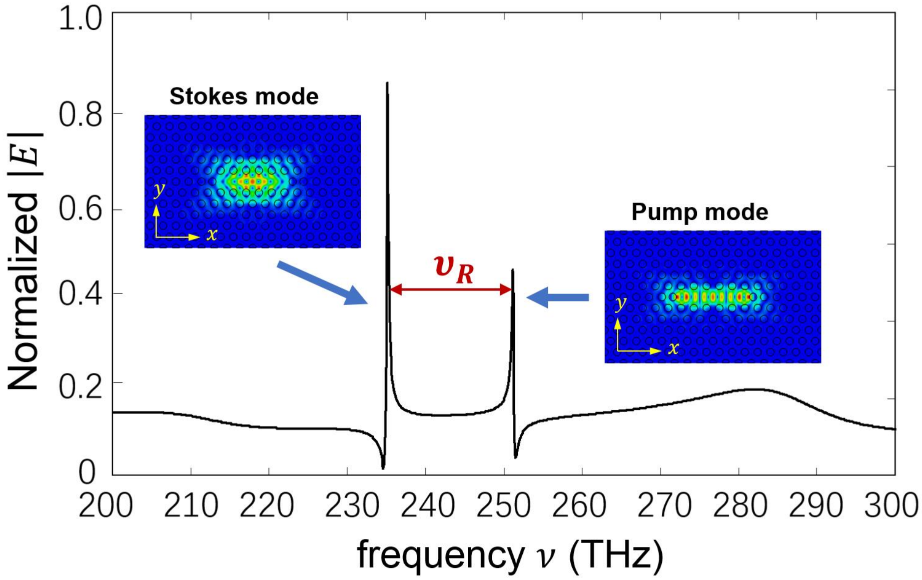

Figure 3.3: Spectrum of the optical response of the metasurface.

elements are not identical.

The last step of the homogenization procedure is to use Eq. (5.20) to calculate the effective Raman susceptibility of the metasurface, $\chi_{R,1212}^{(3),\text{eff}}$. For the nonlinear metasurface made of *L*5 PhC cavities described in Fig. 3.1 our calculations show that $\chi_{R,1212}^{(3),\text{eff}} = -i18.8 \times 10^{-14}\,\text{m}^2\,\text{V}^{-2}$, that is the effective Raman susceptibility is enhanced by $\eta = |\chi_{R,1212}^{(3),\text{eff}}/\chi_{R,1212}^{(3)}| = 1.67 \times 10^4$ as compared to that of silicon. Interestingly enough, similar values of the enhancement of the Raman interaction in silicon photonic structures have been observed in the case of silicon PhC waveguides operated in the slow-light regime [42].

In order to understand the dependence of the effective Raman susceptibility on the size of the unit cell of the metasurface, we varied the number of holes, N, located along the x-direction between the end of the cavity and the boundary of the unit cell. As illustrated in Fig. 3.4, in which we plot this dependence, the effective Raman susceptibility of the nonlinear metasurface decreases when N increases and remains practically unchanged for $N \geq 4.5$. The maximum enhancement is $\eta = 4.22 \times 10^4$, that is an additional increase by a factor of about 3. This dependence is readily explained by the fact that as N decreases there are more cavities per unit area and consequently the nonlinear optical response of the metasurface increases. It should be noted, however, that as the cavities are more closely packed together the mutual optical coupling can lead to a frequency shift of the resonance frequencies of the modes and thus to a decrease of the efficiency of the Raman interaction. This can be avoided by simply designing the cavity such that the frequency difference between the modes differs from the Raman frequency by exactly the frequency shift induced by the optical coupling between the cavities.

3.5 Conclusions

In conclusion, by designing a nonlinear optical metasurface made of a two-dimensional periodic array of silicon photonic crystal cavities, we have demonstrated that the effective nonlinear Raman susceptibility of the metasurface can be enhanced by more than 4 orders of magnitude as compared to that of silicon. In

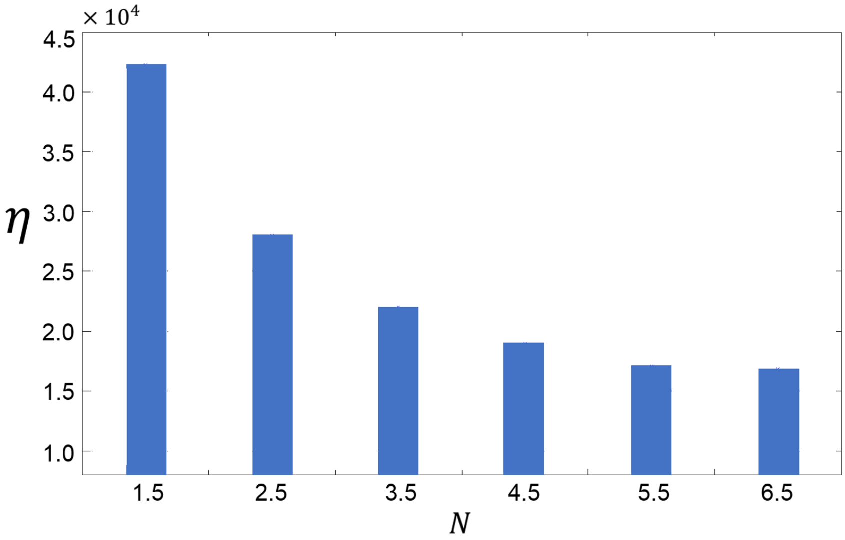

Figure 3.4: The enhancement of the effective Raman susceptibility of the nonlinear metasurface relative to the intrinsic Raman susceptibility of silicon vs. the number of holes located along the x-direction between the end of the nanocavity and the boundary of the unit cell.

order to achieve this dramatic enhancement of the nonlinear optical response of the metasurface, the photonic crystal cavities are designed so as to possess two optical cavity modes spectrally separated by the Raman frequency of silicon. Importantly, the linear and nonlinear optical response of the metasurface have been quantified using a new homogenization method, which is valid even when the period of the metasurface is comparable or larger than the wavelength of the interacting beams. The ideas presented in this chapter have wide applicability, as they can be easily extended to other nonlinear optical interactions of practical interest, including second- and third-harmonic generation, four-wave mixing, and sum- and difference-frequency generation.

Appendix: Average electric field in a homogeneous slab of material

In this Appendix we present a derivation for the averaged electric field in a slab of homogeneous material. The corresponding electromagnetic structure and field configuration are presented in Fig. 3.5. Thus, we assume that a homogeneous slab, *Medium 2*, with permittivity ε_2 is sandwiched in-between two media, *Medium 1* and *Medium 3*, which have permittivities ε_1 and ε_3, respectively. For simplicity, we assume that all media have the same permeability, $\mu_1 = \mu_2 = \mu_3 = \mu_0$. Moreover, incident on the slab is a plane wave propagating along the z-axis, with the electric and magnetic fields written as $\mathbf{E}_{1i}(z) = \hat{\mathbf{i}}E_{1i}e^{ik_1z}$ and $\mathbf{H}_{1i}(z) = \hat{\mathbf{j}}(E_{1i}/Z_1)e^{ik_1z}$, respectively, where $Z_1 = \sqrt{\mu_0/\varepsilon_1}$ and $k_1 = \omega\sqrt{\mu_0\varepsilon_1}$. Note that in this derivation we assume that ε_2 is diagonal but the diagonal elements are not necessarily equal. Under these circumstances, the fields in the three regions can be written as:

Medium 1:

$$\mathbf{E}_1(z) = \mathbf{E}_{1i}(z) + \mathbf{E}_{1r}(z) = \hat{\mathbf{i}}\left(E_{1i}e^{ik_1z} + E_{1r}e^{-ik_1z}\right), \tag{3.9}$$

$$\mathbf{H}_1(z) = \mathbf{H}_{1i}(z) + \mathbf{H}_{1r}(z) = \hat{\mathbf{j}}\frac{1}{Z_1}\left(E_{1i}e^{ik_1z} - E_{1r}e^{-ik_1z}\right). \tag{3.10}$$

Medium 2:

$$\mathbf{E}_2(z) = \mathbf{E}_{2+}(z) + \mathbf{E}_{2-}(z) = \hat{\mathbf{i}}\left(E_{2+}e^{ik_2(z-t)} + E_{2-}e^{-ik_2(z-t)}\right), \tag{3.11}$$

$$\mathbf{H}_2(z) = \mathbf{H}_{1+}(z) + \mathbf{H}_{1-}(z) = \hat{\mathbf{j}}\frac{1}{Z_2}\left(E_{2+}e^{ik_2(z-t)} - E_{2-}e^{-ik_2(z-t)}\right). \tag{3.12}$$

Medium 3:

$$\mathbf{E}_3(z) = \mathbf{E}_{3t}(z) = \hat{\mathbf{i}}E_{3t}e^{ik_3z}, \tag{3.13}$$

$$\mathbf{H}_3(z) = \mathbf{H}_{3t}(z) = \hat{\mathbf{j}}\frac{E_{3t}}{Z_3}e^{ik_3z}. \tag{3.14}$$

To simplify the notations, let us introduce the reflection coefficients at $z = 0$, $\Gamma(0) = E_{1r}/E_{1i}$, and at $z = t$, $\Gamma(t) = E_{2-}/E_{2+}$. Then, the fields in *Medium 1* and

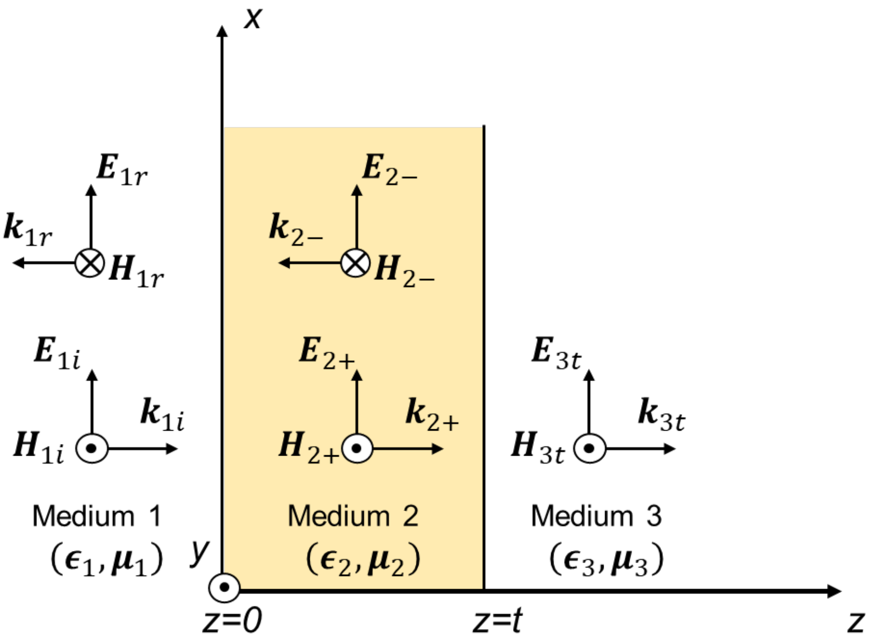

Figure 3.5: Wave configuration corresponding to a homogeneous slab (*Medium 2*) with thickness, t, sandwiched in-between two media (*Medium 1* and *Medium 3*).

Medium 2 can be expressed as:

$$\mathbf{E}_1(z) = \hat{\mathbf{i}} E_{1i} \left(e^{ik_1 z} + \Gamma(0) e^{-ik_1 z} \right), \tag{3.15}$$

$$\mathbf{H}_1(z) = \hat{\mathbf{j}} \frac{E_{1i}}{Z_1} \left(e^{ik_1 z} - \Gamma(0) e^{-ik_1 z} \right), \tag{3.16}$$

$$\mathbf{E}_2(z) = \hat{\mathbf{i}} E_{2+} \left(e^{ik_2(z-t)} + \Gamma(t) e^{-ik_2(z-t)} \right), \tag{3.17}$$

$$\mathbf{H}_2(z) = \hat{\mathbf{j}} \frac{E_{2+}}{Z_2} \left(e^{ik_2(z-t)} - \Gamma(t) e^{-ik_2(z-t)} \right). \tag{3.18}$$

The continuity of the tangent components of the fields at $z = 0$ and $z = t$ requires that:

$$\Gamma(0) = \frac{Z_2(Z_3 - Z_1) - i(Z_2^2 - Z_1 Z_3)\tan(k_2 t)}{Z_2(Z_3 + Z_1) - i(Z_2^2 + Z_1 Z_3)\tan(k_2 t)}; \quad \Gamma(t) = \frac{Z_3 - Z_2}{Z_3 + Z_2}. \tag{3.19}$$

In addition, using Eqs. (3.9)–(3.12) and the continuity of the electric field at $z = 0$, one can find the amplitude of the electric field in *Medium 2*

$$E_{2+} = \frac{1+\Gamma(0)}{e^{-ik_2t} + \Gamma(t)e^{ik_2t}} E_{1i}, \tag{3.20}$$

and subsequently the z-dependent electric field in *Medium 2*

$$\mathbf{E}_2(z) = \hat{\mathbf{i}} \frac{1+\Gamma(0)}{e^{-ik_2t} + \Gamma(t)e^{ik_2t}} \left[e^{ik_2(z-t)} + \Gamma(t)e^{-ik_2(z-t)} \right] E_0, \tag{3.21}$$

where we redefined $E_0 = E_{1i}$.

Finally, the effective electric field in *Medium 2* is defined as:

$$\bar{\mathbf{E}}_{2,\text{eff}} = \frac{1}{t} \int_0^t \mathbf{E}_2(z) dz. \tag{3.22}$$

Inserting Eq. (3.21) in the equation above and performing the integral one obtains Eq. (3.7) with the notations given in Eq. (3.8).

Bibliography

[1] N. Yu, P. Genevet, M. A. Kats, F. Aieta, J. P. Tetienne, F. Capasso, and Z. Gaburro, “Light propagation with phase discontinuities: generalized laws of reflection and refraction,” Science **334**(6054), 333–337 (2011).

[2] A. V. Kildishev, A. Boltasseva, and V. M. Shalaev, “Planar photonics with metasurfaces,” Science **339**(6125), 1232009 (2013).

[3] M. I. Shalaev, J. Sun, A. Tsukernik, A. Pandey, K. Nikolskiy, and N. M. Litchinitser, “High-efficiency all-dielectric metasurfaces for ultracompact beam manipulation in transmission mode,” Nano Lett. **15**(9), 6261–6266 (2015).

[4] S. Jahani and Z. Jacob, “All-dielectric metamaterials,” Nat. Nanotech. **11**(1), 23–36 (2016).

[5] Q. Wang, E. T. Rogers, B. Gholipour, C. M. Wang, G. Yuan, J. Teng, and N. I. Zheludev, “Optically reconfigurable metasurfaces and photonic devices based on phase change materials,” Nat. Photonics **10**(1), 60–65 (2016).

[6] Y. Yao, R. Shankar, M. A. Kats, Y. Song, J. Kong, M. Loncar, and F. Capasso, “Electrically tunable metasurface perfect absorbers for ultrathin mid-infrared optical modulators,” Nano Lett. **14**(11), 6526-6532 (2014).

[7] A. Zhan, S. Colburn, R. Trivedi, T. K. Fryett, C. M. Dodson, and A. Majumdar, “Low-contrast dielectric metasurface optics,” ACS Photonics **3**(2), 209-214 (2016).

[8] J. Lee, M. Tymchenko, C. Argyropoulos, P.-Y. Chen, F. Lu, F. Demmerle, G. Boehm, M.-C. Amann, A. Alu, and M. A. Belkin, "Giant nonlinear response from plasmonic metasurfaces coupled to intersubband transitions," Nature **511**(7507), 65-69 (2014).

[9] E. Almeida, G Shalem, and Y. Prior, "Subwavelength nonlinear phase control and anomalous phase matching in plasmonic metasurfaces," Nat. Commun. **7**, 10367 (2016).

[10] G. Li, S. Zhang, and T. Zentgraf T "Nonlinear photonic metasurfaces," Nat. Rev. Mater. **2**, 17010 (2017)

[11] A. Krasnok, M. Tymchenko, and A. Alu "Nonlinear metasurfaces: A paradigm shift in nonlinear optics," Mater. Today **21**(1), 8–21 (2018).

[12] X. Yin, Z. Ye, J. Rho, Y. Wang, and X. Zhang, "Photonic spin Hall effect at metasurfaces," Science **339**(6126), 1405–1407 (2013).

[13] G. Li, M. Kang, S. Chen, S. Zhang, E. Y. B. Pun, K. W. Cheah, and J. Li, "Spin-enabled plasmonic metasurfaces for manipulating orbital angular momentum of light," Nano Lett. **13**(9), 4148–4151 (2013).

[14] H. Wakatsuchi, S. Kim, J. J. Rushton, and D. F. Sievenpiper, "Circuit-based nonlinear metasurface absorbers for high power surface currents," Appl. Phys. Lett. **102**(21), 214103 (2013).

[15] S. V. Makarov, I. S. Sinev, V. A. Milichko, F. E. Komissarenko, D. A. Zuev, E. V. Ushakova, I. S. Mukhin, Y. F. Yu, A. I. Kuznetsov, P. A. Belov, I. V. Iorsh, A. N. Poddubny, A. K. Samusev, and Yu. S. Kivshar, "Nanoscale Generation of White Light for Ultrabroadband Nanospectroscopy," Nano Lett. **18**(1), 535–539 (2018).

[16] M. W. Klein, C. Enkrich, M. Wegener, and S. Linden, "Second-Harmonic Generation from Magnetic Metamaterials," Science **313**(5786), 502–504 (2006).

[17] W. Fan, S. Zhang, N. C. Panoiu, A. Abdenour, S. Krishna, R. M. Osgood, K. J. Malloy, and S. R. J. Brueck, “Second Harmonic Generation from a Nanopatterned Isotropic Nonlinear Material,“ Nano Lett. **6**, 1027 (2006).

[18] S. Chen, F. Zeuner, M. Weismann, B. Reineke, G. Li, V. K. Valev, K. W. Cheah, N. C. Panoiu, T. Zentgraf, and S. Zhang, “Giant Nonlinear Optical Activity of Achiral Origin in Planar Metasurfaces with Quadratic and Cubic Nonlinearities,” Adv. Mater. **28**, 2992 (2016).

[19] S. Liu, G. A. Keeler, J. L. Reno, M. B. Sinclair, and I. Brener, “III-V Semiconductor Nanoresonators-A New Strategy for Passive, Active, and Nonlinear All-Dielectric Metamaterials,” Adv. Opt. Mater. **10**(4), 1457–1462 (2016).

[20] S. Kruk, R. Camacho-Morales, L. Xu, M. Rahmani, D. A. Smirnova, L. Wang, H. H. Tan, C. Jagadish, D. N. Neshev, and Y. S. Kivshar, “Nonlinear Optical Magnetism Revealed by Second-Harmonic Generation in Nanoantennas,” Nano Lett. **17**, 3914–3918 (2017).

[21] D. Timbrell, J. W. You, Y. S. Kivshar, and N. C. Panoiu, “A comparative analysis of surface and bulk contributions to second-harmonic generation in centrosymmetric nanoparticles,” Sci. Rep. **8**, 3586 (2018).

[22] G. Mie, “Beiträge zur Optik trüber Medien, speziell kolloidaler Metallösungen,” *Ann. Phys. (Leipzig)* **25**, 377 (1908).

[23] A. I. Kuznetsov, A. E. Miroshnichenko, M. L. Brongersma, Y. S. Kivshar, and B. Lukyanchuk, “Optically resonant dielectric nanostructures,” Science **354**, aag2472 (2016).

[24] P. A. Temple and C. E. Hathaway, “Multiphonon Raman spectrum of silicon,” Phys. Rev. B **7**(8), 3685 (1973).

[25] X. Yang and C. W. Wong, “Design of photonic band gap nanocavities for stimulated Raman amplification and lasing in monolithic silicon,” Opt. Express **13**(12), 4723-4730 (2005).

[26] BandSOLVE$^{\text{TM}}$, https://www.synopsys.com.

[27] A. F. Oskooi, D. Roundy, M. Ibanescu, P. Bermel, J. D. Joannopoulos, and S. G. Johnson“MEEP: A flexible free-software package for electromagnetic simulations by the FDTD method,” Comput. Phys. Commun. **181**, 687–702 (2010).

[28] X. C. Zeng, D. J. Bergman, P. M. Hui, and D. Stroud, “Effective-medium theory for weakly nonlinear composites,” Phys. Rev. B **38**(15), 10970–10973 (1988).

[29] D. R. Smith, D. C. Vier, T. Koschny, and C. M. Soukoulis, “Electromagnetic parameter retrieval from inhomogeneous metamaterials,” Phys. Rev. E **71**(3), 036617 (2005).

[30] D. R. Smith and J. B. Pendry, “Homogenization of metamaterials by field averaging” J. Opt. Soc. Am. B **23**(3), 391–403 (2006).

[31] A. J. Hoffman, L. Alekseyev, S. S. Howard, K. J. Franz, D. Wasserman, V. A. Podolskiy, and C. Gmachl, “Negative refraction in semiconductor metamaterials,” Nat. Mater. **6**(12), 946–950 (2007).

[32] D. R. Smith, S. Schultz, P. Markos, and C. M. Soukoulis, “Determination of effective permittivity and permeability of metamaterials from reflection and transmission coefficients,” Phys. Rev. B **65**, 195104 (2002).

[33] C. G. Parazzoli, R. B. Greegor, K. Li, B. E. C. Koltenbah, and M. Tanielian, “Experimental verification and simulation of negative index of refraction using Snell’s law,” Phys. Rev. Lett. **90**(10), 107401 (2003).

[34] D. R. Smith, W. J. Padilla, D. C. Vier, S. C. Nemat-Nasser, and S. Schultz, “Composite medium with simultaneously negative permeability and permittivity,” Phys. Rev. Lett. **84**(18), 4184–4187 (2000).

[35] S. Roke, M. Bonn, and A. V. Petukhov, “Nonlinear optical scattering: The concept of effective susceptibility,” Phys. Rev. B **70**(11), 115106 (2004).

[36] A. G. F. de Beer and S. Roke, “Nonlinear Mie theory for second-harmonic and sum-frequency scattering,” Phys. Rev. B **79**, 155420 (2009).

[37] J. Butet and O. J. F. Martin, “Evaluation of the nonlinear response of plasmonic metasurfaces: Miller’s rule, nonlinear effective susceptibility method, and full-wave computation,” J. Opt. Soc. Am. B **33**(2), A8–A15 (2016).

[38] M. A. Gorlach, T. A. Voytova, M. Lapine, Y. S. Kivshar, and P. A. Belov, “Nonlocal homogenization for nonlinear metamaterials,” Phys. Rev. B **93**, 165125 (2016).

[39] R. W. Boyd, *Nonlinear Optics* (Academic, 2008).

[40] B. Jalali, R. Claps, D. Dimitropoulos, and V. Raghunathan, “Light Generation, Amplification, and Wavelength Conversion via Stimulated Raman Scattering in Silicon Microstructures,” in L. Pavesi and D. J. Lockwood (Eds.): *Silicon Photonics*, Top. Appl. Phys. **94**, 199 (Springer-Verlag Berlin Heidelberg 2004).

[41] CST Studio, https://www.cst.com.

[42] J. F. McMillan, X. Yang, N. C. Panoiu, R. M. Osgood, and C. W. Wong, “Enhanced stimulated Raman scattering in slow-light photonic crystal waveguides,” Opt. Lett. **31**(9), 1235–1237 (2006).

Chapter 4

Large enhancement of the effective second-order nonlinearity in graphene metasurfaces

4.1 Introduction

Metamaterials, which consist of artificial elements (so-called metaatoms or metamolecules) usually arranged in a periodic pattern, have been playing an increasingly important role in applications in which they emulate physical properties that otherwise cannot be achieved with naturally occurring materials. The broad available choice of particular geometries and material parameters of the constituents of metamaterials facilitates their use for the implementation of key functionalities, including, *inter alia*, phase engineering [1-3], light focusing [4-6], and local field enhancement [7-10]. These functionalities are beginning to impact a series of research fields by finding applications to bio-sensing [11-14], development of efficient absorbers [15-17], electromagnetic cloaking [18,19], and imaging beyond sub-diffraction limits [20-23]. Among these physical properties of metamaterials, local field enhancement is particularly relevant to nonlinear optics, as in this case the optical response of a metamaterial-based device depends nonlinearly on the externally applied optical field and thus can be widely tuned.

In many applications, the two-dimensional (2D) counterpart of metamaterials, the so-called metasurfaces, can provide the required functionality, especially in the case of devices with planar configuration. In addition, metasurfaces have the advantage of requiring much less laborious fabrication processes. Moreover, in many applications pertaining to nonlinear optics, especially those related to surface science and sensing, achieving the phase-matching of the interacting waves is not a prerequisite condition, and therefore the constraints imposed on metasurfaces in order to attain optimal energy conversion in nonlinear processes can be greatly relaxed [24-28].

Broadly speaking, there are two classes of optical metasurfaces: plasmonic metasurfaces based on metallic particles [29,30] and dielectric metasurfaces [31,32] relying on Mie resonances of dielectric particles. In the case of plasmonic metasurfaces, the local field can be dramatically enhanced at plasmon-resonance frequencies [33-36]; however, this effect is usually accompanied by a relatively large optical loss [37]. On the other hand, dielectric metasurfaces are characterized by much smaller optical losses but usually provide reduced optical field enhancement.

A promising alternative to plasmonic and all-dielectric metasurfaces is provided by graphene metasurfaces, as the (plasmon) resonance frequency of graphene nanostructures lies in the terahertz domain, namely where optical losses of graphene are relatively small. Equally important, the plasmonic nature of these resonances ensures that strong field enhancement can be achieved in graphene metasurfaces, too. In addition, the corresponding resonance wavelength is much larger than the size of graphene resonators, which means that a large number of such resonators can be packed inside a domain with size comparable to that of the operating wavelength. Consequently, the optical response of graphene metasurfaces can be highly isotropic, when the geometry of graphene unit cell is symmetric. In fact, patterned graphene has already been employed in the design of terahertz devices, such as perfect absorbers, filters, and tunable reflectors [38-43]. In this context, a particularly appealing physical property of graphene is the tunability of its dielectric constant, a unique functionality that is highly relevant to the design of active photonic devices.

In this chapter, we propose a powerful and versatile homogenization approach for graphene metasurfaces, and subsequently use it to demonstrate that the effective second-order susceptibility of such metasurfaces can be dramatically increased due to the field-enhancement effect at plasmon resonances. The novelty of the homogenization method used in this study consists in its ability to describe not only metasurfaces containing linear and isotropic materials, like the standard field-average methods, but also those made of anisotropic and nonlinear optical media. In addition, we find that when a so-called double-resonance phenomenon occurs in a graphene metasurface [44], the second-harmonic generation (SHG) can be further enhanced, leading to an overall increase in SHG of more than three orders of magnitude as compared to the SHG of a graphene sheet placed on the same substrate.

The chapter is organized as follows: In the next section, the configurations of the graphene metasurfaces investigated in this work as well as their material parameters are described. In Section 4.3, an improved homogenization approach for retrieving the effective linear and nonlinear properties of graphene metasurfaces is presented. Then, using this homogenization method, the geometrical parameters of the graphene metasurfaces are optimized so as to achieve plasmon resonances at both the fundamental frequency (FF) and second-harmonic (SH). In Section 4.4, the linear and nonlinear optical spectra of the graphene metasurfaces are calculated and a comparison of the effective second-order susceptibility of graphene metasurfaces with the second-order susceptibility of a graphene sheet placed on the same substrate is provided. Finally, the main conclusions are outlined in Section 4.5.

4.2 Physical configuration and material parameters of graphene metasurfaces

In this section, we present the configuration of the one-dimensional (1D) and 2D graphene metasurfaces studied in this work and describe the properties of the linear and nonlinear optical constants of graphene. Thus, the two generic nonlinear graphene-based metasurfaces, a 1D periodic metasurface consisting of a periodic arrangement of graphene ribbons and a 2D metasurface consisting of a rectangular array of graphene rectangular patches, are schematically illustrated in Figs. 4.1(a) and 4.1(b), respectively. The period of the 1D metasurface is $P_x = 100\,\mathrm{nm}$ and the width of the nanoribbons is w, whereas in the case of the 2D metasurface the periods along the x- and y-axis are $P_x = P_y = 100\,\mathrm{nm}$ and the length of the graphene patches along the y-axis is fixed at $w_y = 30\,\mathrm{nm}$. The width of the graphene nanoribbons and the length of the graphene patches along the x-axis, w_x, are free parameters that will be optimized so as to achieve a double-resonance effect. In both cases the graphene nanostructures are placed onto a silica substrate with $n_{\mathrm{SiO}_2} = 1.4$ and are illuminated by a normally incident, x-polarized plane wave with field amplitude $E_0 = 1\,\mathrm{V\,m^{-1}}$ (wave intensity $I_0 = 4.43 \times 10^{12}\,\mathrm{W\,m^{-2}}$). This choice of the wave polarization ensures that graphene plasmons exist in both metasurfaces.

Due to its metallic characteristics in the terahertz and infrared spectral regions, graphene supports surface-plasmon polaritons (SPPs), which are collective oscillations of free electrons. In the case of finite-size graphene nanostructures, the resonance frequency of SPPs is geometry dependent. Therefore, by properly choosing the size and shape of these graphene nanostructures, one can achieve a double-resonant phenomenon, namely SPPs exist both at the FF and SH. When this occurs, the optical near-fields at the FF and SH are strongly enhanced, which leads to a marked increase in the intensity of the SHG. Under these circumstances, one expects that the graphene metasurface can be viewed as a homogeneous sheet of nonlinear material with strongly enhanced effective second-order susceptibility.

Before we analyze in more detail the linear and nonlinear optical properties of the two graphene metasurfaces, we briefly summarize the optical properties of the main optical constants of graphene. Since graphene is a 2D semimetal, a surface optical conductivity, σ_s, is generally used to describe its main linear physical properties at optical frequencies. (The term optical conductivity means the conductivity arising from the optical excitation instead of applied electrical field.) Based on Kubo's formula derived within the random-phase approximation [46], σ_s can be expressed as the sum of the intra-band (σ_{intra}) and inter-band (σ_{inter}) contributions, $\sigma_s = \sigma_{\mathrm{intra}} + \sigma_{\mathrm{inter}}$. The intra-band part is given by:

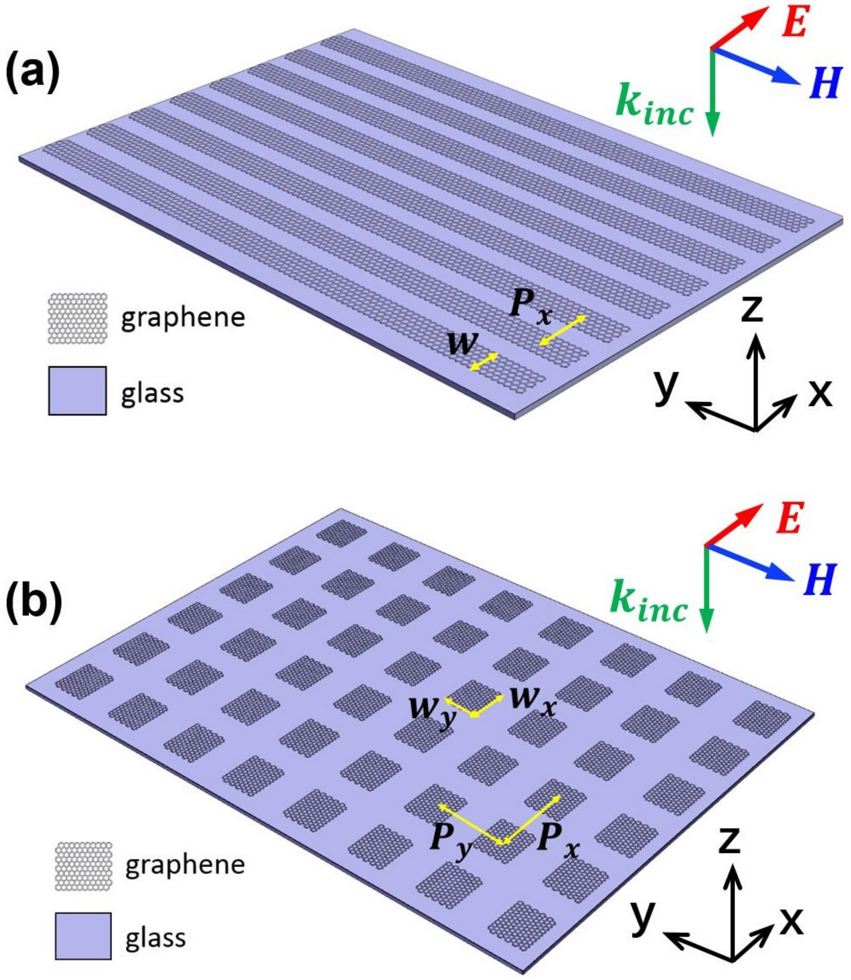

Figure 4.1: (a) Schematics of a 1D graphene metasurface, with the period P_x and width of graphene ribbons, w. (b) Schematics of a 2D graphene metasurface, with periods P_x and P_y, and side-length of the graphene patches of w_x and w_y. The two graphene metasurfaces are illuminated by an x-polarized plane wave normally incident onto the metasurfaces.

$$\sigma_{\text{intra}} = \frac{e^2 k_B T \tau}{\pi \hbar^2 (1 - i\pi\tau)} \left[\frac{\mu_c}{k_B T} + 2\ln(e^{-\frac{\mu_c}{k_B T}} + 1) \right], \tag{4.1}$$

where μ_c is the chemical potential, τ is the relaxation time, T is the temperature, e is the electron charge, k_B is the Boltzmann constant, and $\hbar$ is the reduced Planck's constant. Throughout our analysis, we use $\mu_c = 0.6\,\text{eV}$, $\tau = 0.25\,\text{ps}$, and $T = 300\,\text{K}$. Moreover, if $\mu_c \gg k_B T$, which usually holds at room temperature, the inter-band

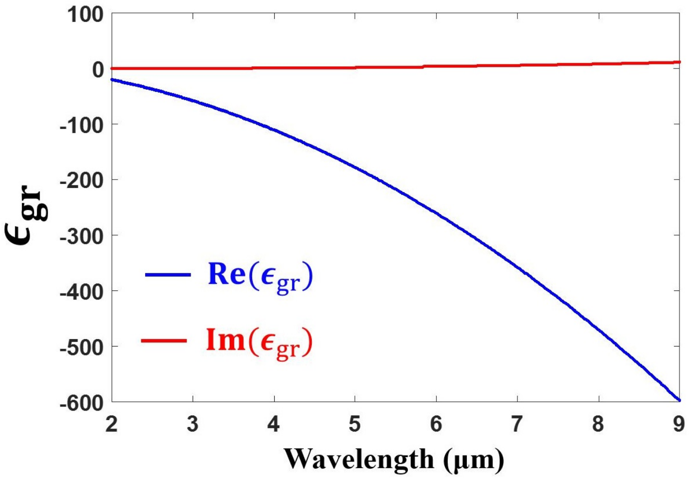

Figure 4.2: Relative electric permittivity of a graphene sheet with $h_{\text{eff}} = 0.3\,\text{nm}$.

part can be approximated as:

$$\sigma_{\text{inter}} = \frac{ie^2}{4\pi\hbar} \ln\left[\frac{2|\mu_c| - (\omega + i\tau^{-1})\hbar}{2|\mu_c| + (\omega + i\tau^{-1})\hbar}\right]. \tag{4.2}$$

If we assume that the effective thickness of graphene is h_{eff}, the relative electric permittivity can be calculated from the conductivity through the relation:

$$\varepsilon_{\text{gr}}(\omega) = 1 + \frac{i\sigma_s}{\varepsilon_0 \omega h_{\text{eff}}}. \tag{4.3}$$

The relative electric permittivity of graphene is depicted in Fig. 4.2 (the ε_{gr} in the above equation indicates the ε_{gr} in this figure), where $h_{\text{eff}} = 0.3\,\text{nm}$ has been used.

Similar to the case of three-dimensional (3D) bulk optical media, the nonlinear optical properties of 2D materials are generally determined by the symmetry properties of their atomic lattice and are quantified by (bulk) nonlinear susceptibility tensors, $\boldsymbol{\chi}^{(n)}(\Omega;\omega)$, where ω and Ω are the frequencies at the FF and higher-harmonic, respectively, and n is the order of the nonlinear optical process, or, equivalently, by surface nonlinear optical conductivities, $\boldsymbol{\sigma}_s^{(n)}(\Omega;\omega)$. These two physical quantities are related *via* the following relation:

$$\boldsymbol{\chi}^{(n)}(\Omega;\omega) = \frac{i}{\varepsilon_0 \Omega h_{\text{eff}}} \boldsymbol{\sigma}_s^{(n)}(\Omega;\omega). \tag{4.4}$$

Free-standing graphene is a centrosymmetric material and therefore second-order nonlinear optical processes and, in particular, SHG, are forbidden. If a graphene sheet, however, is placed onto a homogeneous substrate the inversion symmetry is broken and (dipole) SHG is allowed. In particular, such an optical configuration is characterized by a surface second-order nonlinear optical conductivity tensor, $\boldsymbol{\sigma}_s^{(2)}(\Omega;\omega)$, where $\Omega = 2\omega$. Symmetry considerations based on the fact that graphene belongs to the $\mathscr{D}_{6\mathrm{h}}$ symmetry group lead to the conclusion that this tensor has three independent nonzero components, $\sigma^{(2)}_{s,\perp\perp\perp}$, $\sigma^{(2)}_{s,\|\|\perp} = \sigma^{(2)}_{s,\|\perp\|}$, and $\sigma^{(2)}_{s,\perp\|\|}$, where the symbols $\perp$ and $\|$ refer to the directions perpendicular onto and parallel to the plane of graphene, respectively. The values of these parameters used in this paper are $\sigma^{(2)}_{s,\perp\perp\perp} = -9.71i\times 10^{-16}\,\mathrm{A\,m\,V^{-2}}$, $\sigma^{(2)}_{s,\|\|\perp} = \sigma^{(2)}_{s,\|\perp\|} = -2.56i\times 10^{-16}\,\mathrm{A\,m\,V^{-2}}$, and $\sigma^{(2)}_{s,\perp\|\|} = -2.09i\times 10^{-16}\,\mathrm{A\,m\,V^{-2}}$, [45,46] and correspond to graphene placed on a silica substrate. Note that similar to the case of surface nonlinear second-order susceptibility of nobel metals, the dominant component of the surface nonlinear second-order conductivity (susceptibility) is the $\sigma^{(2)}_{s,\perp\perp\perp}$ ($\chi^{(2)}_{s,\perp\perp\perp}$) component.

4.3 Theory of linear and nonlinear homogenization

In this section, we describe a theoretical method we recently introduced [47] for the homogenization of the linear and nonlinear optical response of graphene metasurfaces. In particular, we present an approach for extracting the effective linear and nonlinear optical coefficients of a homogenized layer of material, which in the far-field has the same linear and nonlinear optical response as that of the graphene metasurface. To be more specific, we use this method to compute the effective electric permittivity of the two generic graphene metasurfaces, as well as the effective surface second-order susceptibility of graphene metasurfaces, when they are optimized to achieve maximum nonlinearity enhancement. Note that although the homogenized metasurfaces can be characterized by effective surface quantities, such as linear and nonlinear surface conductivities [48,49], in this work we consider that the homogenized metasurfaces have a finite thickness, h_{eff}, and thus are described by bulk effective permittivities and nonlinear susceptibilities.

In order to develop a general homogenization method, we extend the traditional field-averaged method to include nonlinear optical effects and anisotropic 2D materials. Thus, the constitutive relation of a linear anisotropic material is expressed

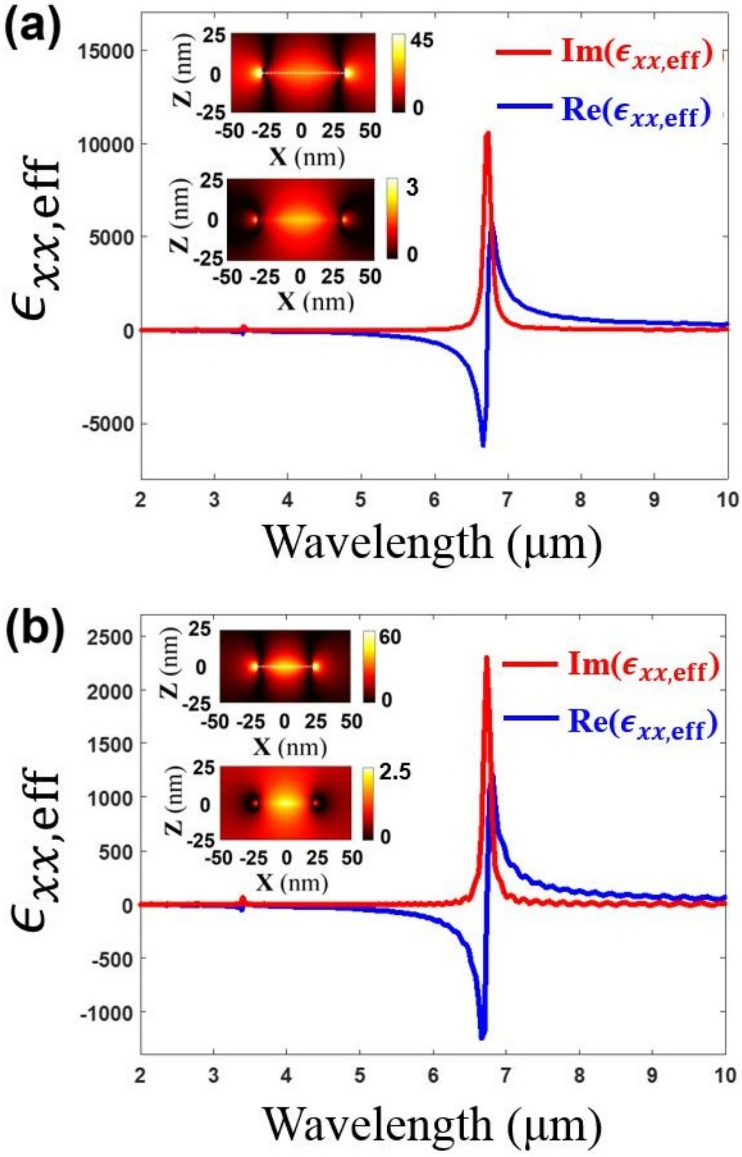

Figure 4.3: (a) Effective relative permittivity of homogenized graphene-nanoribbon metasurface with $w = 57.5\,\mathrm{nm}$. In insets, the spatial profile of $|E_x|$, calculated at the resonance wavelength $\lambda = 6.74\,\mu\mathrm{m}$ (top panel) and at $\lambda = 4\,\mu\mathrm{m}$ (bottom panel). (b) The same as in (a), but calculated for the 2D graphene metasurface with $w_x = 42.5\,\mathrm{nm}$. The resonance wavelength for the 2D graphene metasurface is $\lambda = 6.93\,\mu\mathrm{m}$

as:

$$D_i = \sum_j \varepsilon_{ij} E_j, \tag{4.5}$$

where **D** and **E** are the electric displacement and electric field, respectively, and the subscripts $i, j = x, y, z$. Then, we introduce the averaged fields, defined as:

$$\overline{\mathbf{D}}_{\text{eff}}(\omega) = \frac{1}{V} \int_V \mathbf{D}(\mathbf{r}, \omega) d\mathbf{r}, \tag{4.6a}$$

$$\overline{\mathbf{E}}_{\text{eff}}(\omega) = \frac{1}{V} \int_V \mathbf{E}(\mathbf{r}, \omega) d\mathbf{r}, \tag{4.6b}$$

where V is the volume of the unit cell of the (1D or 2D) metasurface. More specifically, the integration domains for the 1D and 2D metasurfaces are $V = [0, P_x] \times [0, h_{\text{eff}}]$ and $V = [0, P_x] \times [0, P_y] \times [0, h_{\text{eff}}]$, respectively. Using Eqs. (4.5) and (4.6), the effective electric permittivity tensor of the metasurface, defined by the constitutive relation $\overline{D}_{i,\text{eff}} = \sum_j \overline{\varepsilon}_{ij,\text{eff}} \overline{E}_{j,\text{eff}}$, can be written as:

$$\overline{\boldsymbol{\varepsilon}}_{ij,\text{eff}}(\omega) = \frac{\int_V \mathbf{D}_i(\mathbf{r}, \omega) d\mathbf{r}}{\int_V \mathbf{E}_j(\mathbf{r}, \omega) d\mathbf{r}} = \frac{\int_V \varepsilon(\mathbf{r}) \mathbf{E}_i(\mathbf{r}, \omega) d\mathbf{r}}{\int_V \mathbf{E}_j(\mathbf{r}, \omega) d\mathbf{r}}, \tag{4.7}$$

where $\varepsilon(\mathbf{r}) = \varepsilon_0$ if **r** is in air and $\varepsilon(\mathbf{r}) = \varepsilon_{\text{gr}}$ if **r** is in graphene. The formula above has been derived for metasurfaces made of isotropic optical materials, but it can be easily extended to anisotropic ones.

In order to assess the validity of our homogenization method, we have calculated the effective permittivity given by Eq. (4.7) and then compared the optical response of the homogenized metasurfaces, *i.e.*, the absorption, A, transmittance, T, and reflectance, R, with that of the two graphene metasurfaces. The optical near-fields needed to calculate $\overline{\boldsymbol{\varepsilon}}_{ij,\text{eff}}(\omega)$, as well as the absorption, transmittance, and reflectance of the two graphene metasurfaces, were computed using an in-house developed code [50,51].

The effective permittivities of the homogenized metasurfaces, $\varepsilon_{xx,\text{eff}}(\omega)$, retrieved using the algorithm just described, are presented in Fig. 4.3. The 1D and 2D metasurfaces considered here were optimized for maximum nonlinear response us-

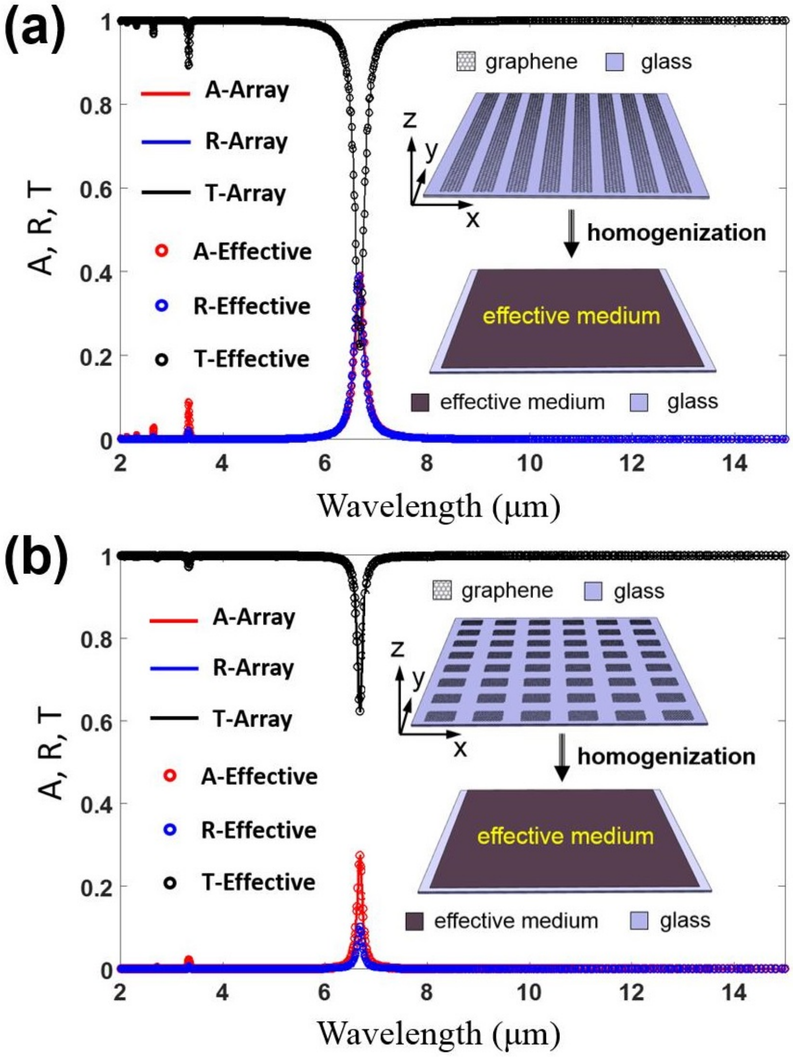

Figure 4.4: Linear response comparison of absorption, A, reflectance, R, and transmittance, T, calculated for the two graphene metasurfaces whose effective permittivities are presented in Fig. 4.3 (depicted with solid curves) and A, R, and T corresponding to their homogenized counterparts (depicted with dotted curves).

ing an approach that will be described in the next section, the corresponding values of the geometrical parameters being $w = 57.5\,\mathrm{nm}$ and $w_x = 42.5\,\mathrm{nm}$, respectively. In contrast to the intrinsic permittivity of a homogeneous graphene sheet shown in Fig. 4.2, the effective permittivities of the homogenized metasurfaces exhibit an evident Lorentzian resonant response around a wavelength of about 6.8 µm, which is reminiscent of the linear optical response of an optical medium containing Lorentz-type resonators (An applied electric field interact with the charge of the electron, causing stretching or compression of the spring-like force, which would set the electron into oscillating motion).

The field profiles presented in the insets of Figs. 4.3(a) and 4.3(b) suggest that at resonance the optical near-field is strongly enhanced, which is one of the main physical properties of SPPs (The SPPs are excited by the incident plane wave). Moreover, Fig. 4.3 shows that in addition to this main resonance, few other higher-order resonances exist at smaller wavelengths. These higher-order resonances correspond to the excitation of higher-order plasmon modes in the graphene nanoribbons or graphene patches. Interestingly, although graphene has metallic characteristics in the frequency range considered in our calculations, near the resonance $\mathfrak{Re}(\overline{\boldsymbol{\varepsilon}}_{xx,\mathrm{eff}}) > 0$, which means that the homogenized metasurfaces behave as a dielectric around this frequency.

The main aim of a homogenization theory is to reduce a patterned metasurface to a homogeneous sheet characterized by certain effective optical constants. A reliable way to assess the validity of this procedure is to compare the optical response of the homogenized metasurface and the original one, as quantified by physical quantities such as absorption, reflectance, and transmittance. We performed this analysis for the two graphene metasurfaces whose effective permittivities are presented in Fig. 4.3, the corresponding results being summarized in Fig. 4.4. This comparison clearly demonstrates that the linear response of the homogenized sheets perfectly agrees with that of the original graphene metasurfaces, thus proving the accuracy of the proposed linear homogenization approach (computing with the simulation results from CST studio). This is explained by the fact that the wavelengths considered in our computations, including those at which the graphene metasurfaces are strongly resonant, are much larger than the characteristic size of the graphene constituents of the metasurfaces, so that the two optical structures are operated deep in the metasurface regime.

We now extend the homogenization method to the nonlinear regime, and use SHG as an illustrative nonlinear optical process. Thus, this nonlinear optical interaction is determined by the following nonlinear polarization:

$$\mathbf{P}(\Omega;\mathbf{r}) = \varepsilon_0 \boldsymbol{\chi}^{(2)}(\Omega;\mathbf{r}) : \mathbf{E}(\omega;\mathbf{r})\mathbf{E}(\omega;\mathbf{r}), \tag{4.8}$$

where $\Omega = 2\omega$ and $\boldsymbol{\chi}^{(2)}(\Omega;\mathbf{r}) = \boldsymbol{\chi}^{(2)}_{\text{gr}}(\Omega)$ if $\mathbf{r}$ is in graphene and $\boldsymbol{\chi}^{(2)}(\Omega;\mathbf{r}) = 0$ if $\mathbf{r}$ is in air. Based on Eq. (4.8), the components of the SH polarization can be evaluated as:

$$P_i = \varepsilon_0 \sum_{jk} \chi^{(2)}_{ijk} E_j E_k \equiv \sum_{jk} q_{ijk}, \tag{4.9}$$

where we have introduced the auxiliary quantities, $q_{ijk} = \varepsilon_0 \chi^{(2)}_{ijk} E_j E_k$. The averaged value of these auxiliary quantities are:

$$\overline{q}_{ijk}(\Omega) = \frac{1}{V}\int \chi^{(2)}_{ijk}(\Omega;\mathbf{r}) E_j(\omega;\mathbf{r}) E_k(\omega;\mathbf{r}) d\mathbf{r}. \tag{4.10}$$

Similarly to Eq. (4.8), the nonlinear SH polarization in the homogenized metasurfaces can be written as:

$$\overline{\mathbf{P}}_{\text{eff}}(\Omega) = \varepsilon_0 \boldsymbol{\chi}^{(2)}_{\text{eff}}(\Omega) : \overline{\mathbf{E}}_{\text{eff}}(\omega)\overline{\mathbf{E}}_{\text{eff}}(\omega), \tag{4.11}$$

where $\boldsymbol{\chi}^{(2)}_{\text{eff}}(\Omega)$ is the effective second-order susceptibility of the homogenized metasurface.

The homogenized metasurface and the original one will have the same nonlinear optical response in the far-field if the averaged nonlinear polarization in Eq. (4.8) is *termwise equal* to the effective nonlinear polarization described by Eq. (4.11). Using this condition, the effective second-order susceptibility of the homogenized metasurface can be evaluated as:

$$\boldsymbol{\chi}^{(2)}_{\text{eff},ijk}(\Omega) = \frac{\overline{q}_{ijk}(\Omega)}{\overline{E}_{\text{eff},j}(\omega)\overline{E}_{\text{eff},k}(\omega)}. \tag{4.12}$$

4.4 Results and Discussion

In this section, we describe our approach to optimize the nonlinear optical response of graphene metasurfaces and quantify the nonlinearity enhancement of the optimized metasurfaces. In particular, we calculate the effective second-order susceptibility of the graphene metasurfaces and compare it to the second-order susceptibility of a graphene sheet placed onto the same silica substrate.

4.4.1 Linear optical response of 1D and 2D graphene metasurfaces

One effective approach to achieve a significant enhancement of the SHG in graphene metasurfaces is to engineer their geometrical parameters so as plasmons

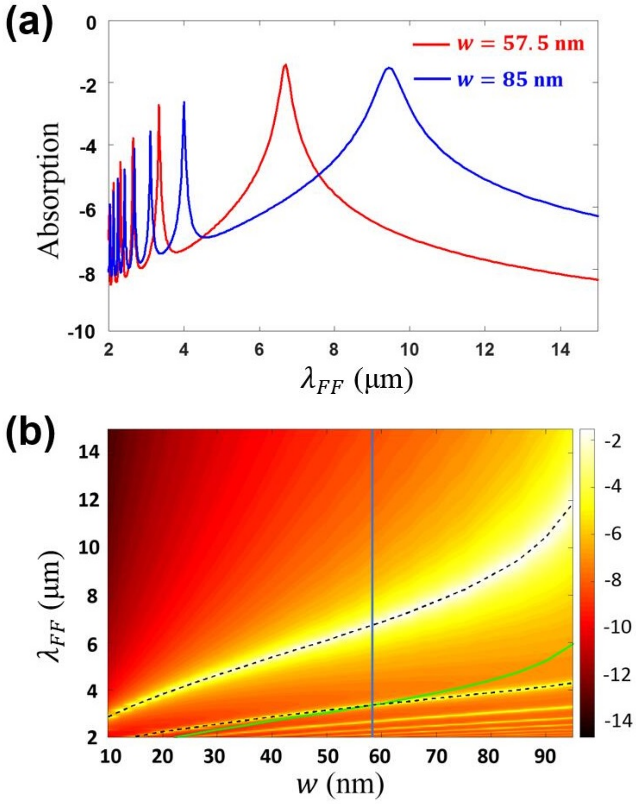

Figure 4.5: (a) Absorption spectra of the 1D graphene metasurface presented in Fig. 4.1(a), calculated for the optimum width, $w = 57.5\,\text{nm}$, for which a double-resonance phenomenon occurs, and for $w = 85\,\text{nm}$. (b) Dispersion map of absorption. Dashed curves indicate the plasmon bands, whereas the green curve indicates the half-wavelength of the fundamental plasmon band. The vertical line indicates that there is a double-resonance effect for $w = 57.5\,\text{nm}$.

exist at both the FF and SH. Under these conditions, the incoming light would in-couple effectively into the metasurface, as plasmons exist at the FF, which would lead to a strong enhancement of the optical near-field at the FF, and, as per Eq. (4.8), of the nonlinear polarization. Moreover, if plasmons exist at the SH, too, the nonlinear sources will radiate efficiently into the continuum, the graphene metasurface behaving in these conditions as an efficient nanoantenna.

One particularly useful tool for optimizing the linear and nonlinear optical response of graphene metasurfaces is the dispersion map of the absorption, namely the dependence of the optical absorption spectra on a certain parameter, such as the width of a graphene nanoribbon. Because the optical absorption increases when plasmons are excited in the structure, the absorption dispersion map provides valu-

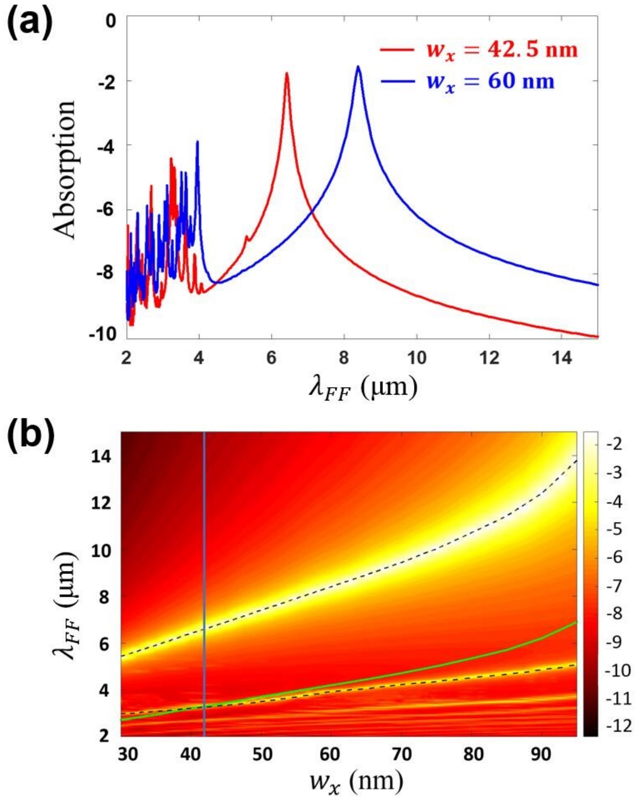

Figure 4.6: (a) Absorption spectra of the 2D graphene metasurface presented in Fig. 4.1(b), calculated for the optimum side-length, $w_x = 42.5\,\text{nm}$, for which a double-resonance phenomenon occurs, and for $w_x = 60\,\text{nm}$. (b) Dispersion map of absorption. Dashed curves indicate the plasmon bands, whereas the green curve indicates the half-wavelength of the fundamental plasmon band. The vertical line shows that there is a double-resonance effect for $w_x = 42.5\,\text{nm}$.

able information about the frequency dispersion of the plasmon modes. The corresponding absorption spectra have been calculated using a computational method [50,51] that rigorously incorporates both the frequency dispersion and nonlinearity of graphene.

We begin our analysis with the 1D graphene metasurface presented in Fig. 4.1(a). Thus, we show in Fig. 4.5(a) the linear absorption spectra determined for the optimum width of the graphene nanoribbons, $w = 57.5\,\mathrm{nm}$ (we will explain letter how this value was determined) and for some other arbitrary value, $w = 85\,\mathrm{nm}$. Moreover, the dispersion map of the optical absorption corresponding to this metasurface is plotted in Fig. 4.5(b). It can be seen in Fig. 4.5(a) that the absorption spectra present a series of plasmon resonances, whose amplitude decreases as the resonance wavelength decreases. These resonances appear in the absorption map as a series of geometry-dependent plasmon bands, indicated with dashed curves, with the resonance wavelength increasing with the increase of the width of the nanoribbons. Importantly, Fig. 4.5(b) suggests that for $w = 57.5\,\mathrm{nm}$ the nanoribbons support a (fundamental) plasmon at the FF and a second-order plasmon at the SH, namely the metasurface possesses a double-resonance feature.

Similar conclusions can be drawn in the case of the 2D graphene metasurface. Thus, similarly to the data summarized in Fig. 4.5, we present in Figs. 4.6(a) and

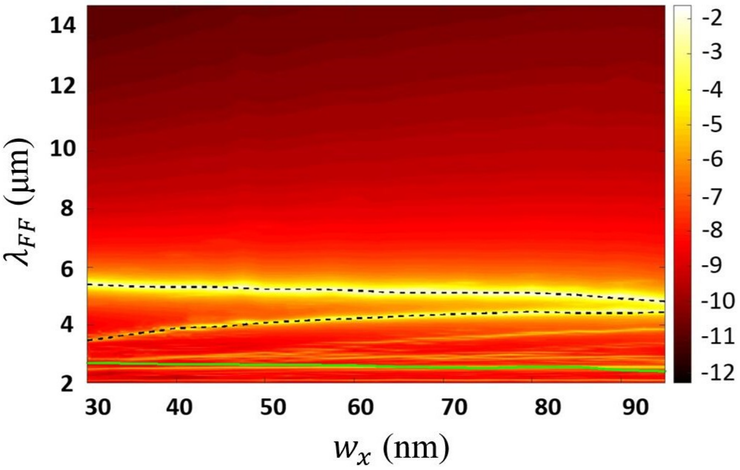

Figure 4.7: The same as in Fig. 4.6(b) but determined for an y-polarized incident plane wave.

4.6(b) two linear absorption spectra determined for the optimum side-length of the graphene patches, $w_x = 42.5\,\text{nm}$, and for an arbitrary value, $w_x = 60\,\text{nm}$, as well as the corresponding dispersion map of the optical absorption, respectively. It can be seen that in the 2D case, too, the resonance wavelength of the plasmon bands increases with w_x and that the double-resonance phenomenon also occurs in 2D graphene metasurfaces. To be more specific, if $w_x = 42.5\,\text{nm}$ plasmon resonances exit at both the FF of $\lambda_{\text{FF}} = 6.93\,\mu\text{m}$, which is a fundamental plasmon, and at the SH of $\lambda_{\text{SH}} = \lambda_{\text{FF}}/2 = 3.47\,\mu\text{m}$. Note that, as illustrated in Fig. 4.1(b), the 2D graphene metasurface is normally illuminated by an x-polarized plane wave.

The 2D graphene metasurface is anisotropic and therefor the optical absorption spectra depend on the polarization of the incident light. This idea is validated by the dispersion map of the optical absorption shown in Fig. 4.7, which has been determined for a normally incident, y-polarized incident plane wave. Thus, for this wave polarization the wavelength of fundamental-plasmon band increases with w_x, whereas the wavelength of the higher-order plasmon bands decrease with w_x.

It can also be seen that when w_x varies, the plasmon bands are more dispersive for x-polarized incident waves as compared to those in the case of y-polarized waves. This finding is explained by the fact that the wavelength of the plasmon resonance is primarily determined by the size of the patch along the direction of the electric field. More importantly, however, the results in Fig. 4.7 suggest that the double-resonance effect does not occur for y-polarized incident plane waves. In our analysis, we have only considered x- and y-polarized incident plane waves, chiefly because the conclusions for other polarizations can be derived from the results corresponding to the linear superposition of these two primary polarizations.

4.4.2 Nonlinear optical response of 1D and 2D graphene metasurfaces

We now turn our attention to SHG in 1D and 2D graphene metasurfaces and investigate the influence of plasmon excitation at the FF and SH on the nonlinear optical response of the two graphene metasurfaces. To this end, we used a generalized-source

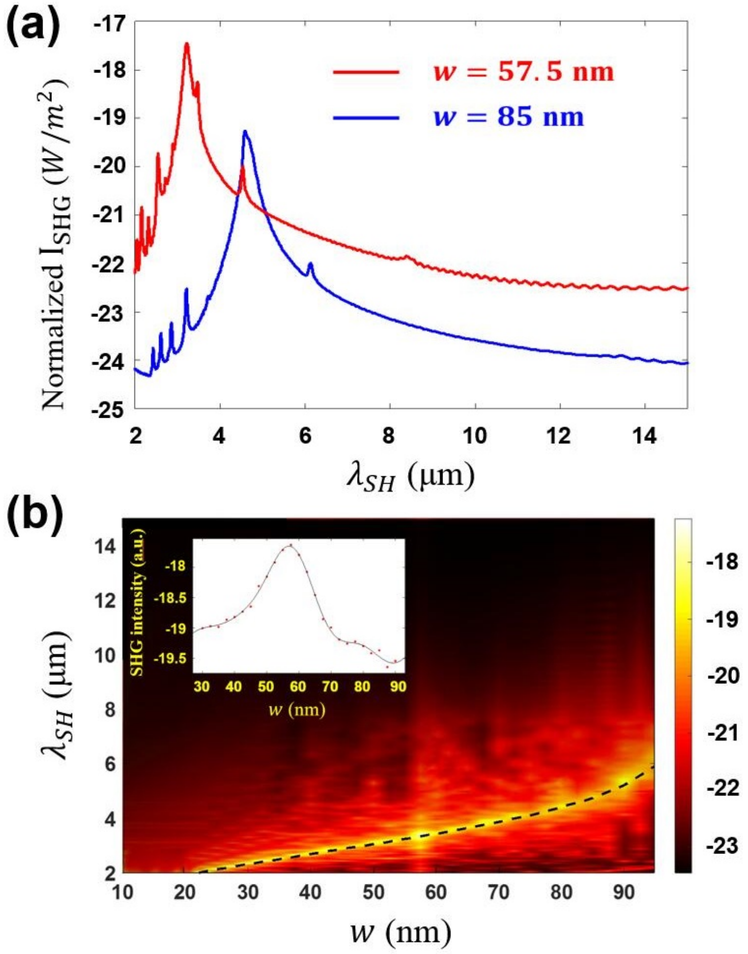

Figure 4.8: (a) Normalized SHG intensity spectra, I_{SHG}, of the 1D graphene metasurface presented in Fig. 4.1(a), calculated for the optimum width, $w = 57.5\,\mathrm{nm}$, and for $w = 85\,\mathrm{nm}$. (b) Dispersion map of I_{SHG}. The dashed curve indicates the fundamental-plasmon band. The inset shows the dependence of I_{SHG} *vs.* w, determined for the case when the wavelengths of the FF and fundamental plasmon are the same.

FDTD numerical method [51], to rigorously compute the SHG in the graphene metasurfaces. Since we want to compare the SHG intensity corresponding to different values of the width of the nanoribbons and rectangular patches, we normalize the SHG intensity to the area of the graphene structure contained in a unit cell (note that the periods P_x and P_y are not changed, so that the area of the unit cells do not vary). More specifically, the normalized SHG intensity spectra, I_{SHG}, were calculated as follows: in the 1D case we computed the SHG power per unit length and then divided the result by the corresponding area of the graphene nanoribbon. In the 2D case, we computed the SHG power coresponding to the unit cell with area

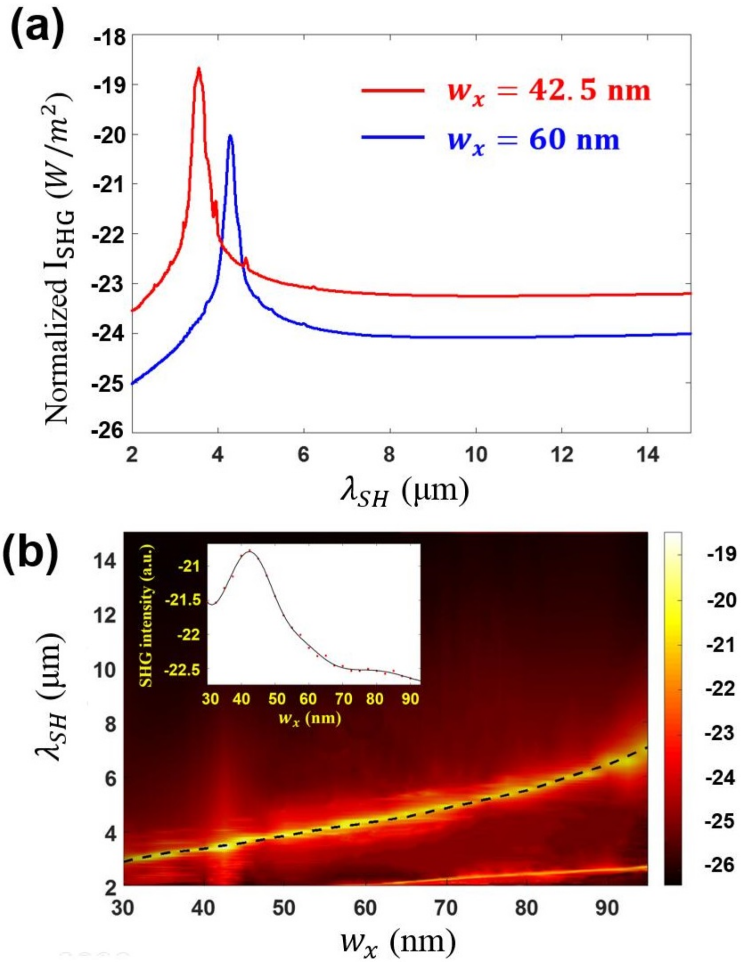

Figure 4.9: (a) Normalized SHG intensity spectra, I_{SHG}, of the 2D graphene metasurface presented in Fig. 4.1(b), calculated for the optimum side-length, $w_x = 42.5\,\text{nm}$ and for $w_x = 60\,\text{nm}$. (b) Dispersion map of I_{SHG}. Dashed curve indicates the fundamental-plasmon band. The inset shows the variation of I_{SHG} with w_x, computed for the case when the wavelengths of the FF and fundamental plasmon are the same.

$P_x \times P_y$ and divided the result to the area of the graphene patch, $w_x \times w_y$. Note that the normalized SHG intensity represents the sum of the SHG signals emitted in the transmission and reflection directions.

The results of these calculations are presented in Fig. 4.8 and Fig. 4.9 and correspond to the 1D and 2D metasurfaces, respectively. As Eq. (4.8) shows, the nonlinear polarization is proportional to the square of the optical near-field at the FF and therefore the SHG intensity is proportional to the FF field amplitude to the fourth. As a result, the resonance peaks of normalized SHG intensity spectra and the plasmon bands of the corresponding dispersion maps of the normalized SHG intensity should be observed at exactly the half-wavelength of the resonance peaks of linear optical absorption spectra and the corresponding plasmon bands of the dispersion maps of the linear optical absorption. This prediction is fully validated by a comparison between the results presented in Fig. 4.5 and Fig. 4.8 on the one hand, results that correspond to the 1D graphene metasurface, and, on the other hand, the results plotted in Fig. 4.6 and Fig. 4.9, which correspond to the 2D graphene metasurface.

Importantly, the insets in Fig. 4.8(b) and Fig. 4.9(b) demonstrate the SHG enhancement due to the double-resonance mechanism. Indeed, it can be inferred from these plots that for the 1D graphene metasurface maximum SHG intensity is achieved for a width of the graphene nanoribbons of $w = 57.5\,\mathrm{nm}$, whereas in the case of the 2D graphene metasurface the optimum value of the side-length of the graphene patch that leads to maximum SHG intensity is $w_x = 42.5\,\mathrm{nm}$. This clearly proves that in addition to plasmon-enhanced SHG, the double-resonance mechanism can be employed to achieve further significant enhancement of the nonlinear optical response of graphene metasurfaces.

4.4.3 Enhancement of the effective second-harmonic susceptibility of 1D and 2D graphene metasurfaces

A suitable physical quantity that measures the enhancement of the nonlinear optical response of a nonlinear optical system is the nonlinear susceptibility. Therefore, we have used the homogenization method described in Sec. 4.3 to calculate the effective second-order susceptibility of the two graphene metasurfaces. In particular, we retrieved the three independent components of this nonlinear susceptibility, $\chi^{(2)}_{\mathrm{eff},zzz}$, $\chi^{(2)}_{\mathrm{eff},xxz}$, and $\chi^{(2)}_{\mathrm{eff},zxx}$. The results of these calculations are summarized in Fig. 4.10 and Fig. 4.11, and correspond to the 1D and 2D metasurfaces, respectively. The Fresnel coefficient has been taken into account by the numerical method in our research work.

One important conclusion that can be inferred from the data presented in these figures is that, similar to the case of the effective permittivity of the homogenized graphene metasurfaces, all components of the effective second-order susceptibilities show a resonant behavior around the plasmon resonance wavelength (fundamental and higher-order wavelength), which means that the enhancement of the nonlinearity of the graphene metasurfaces can be traced to the excitation of graphene SPPs. The maximum enhancement occurs when the fundamental plasmon is excited. Moreover, the spectra of these components of the second-order susceptibil-

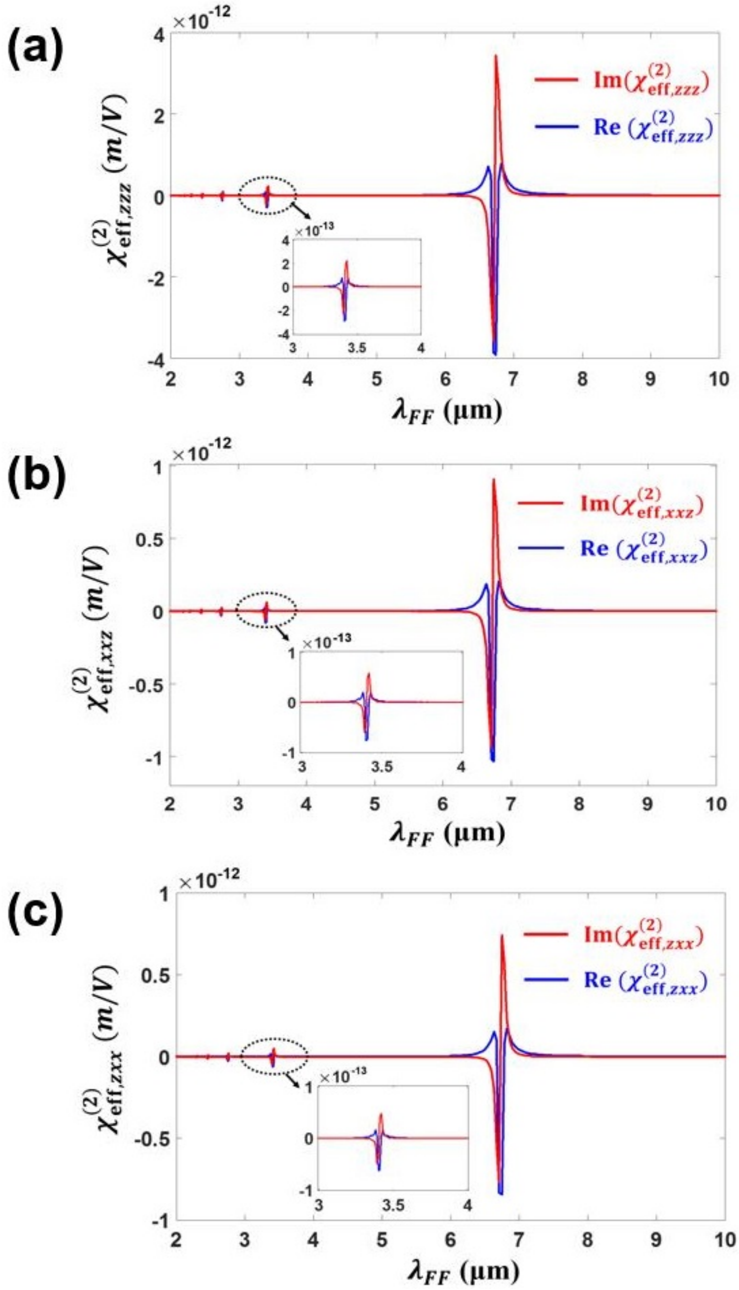

Figure 4.10: Wavelength dependence of the three independent components of the effective second-order susceptibility, $\boldsymbol{\chi}^{(2)}_{\mathrm{eff}}$, of the 1D graphene metasurface.

ities are similar to those of a nonlinear optical medium containing resonators of Lorentzian nature, which suggests that the graphene nanostructures that constitute the building blocks of the two metasurfaces can be viewed as metaatoms responsible for the effective nonlinear optical response of these optical nanostructures. Since

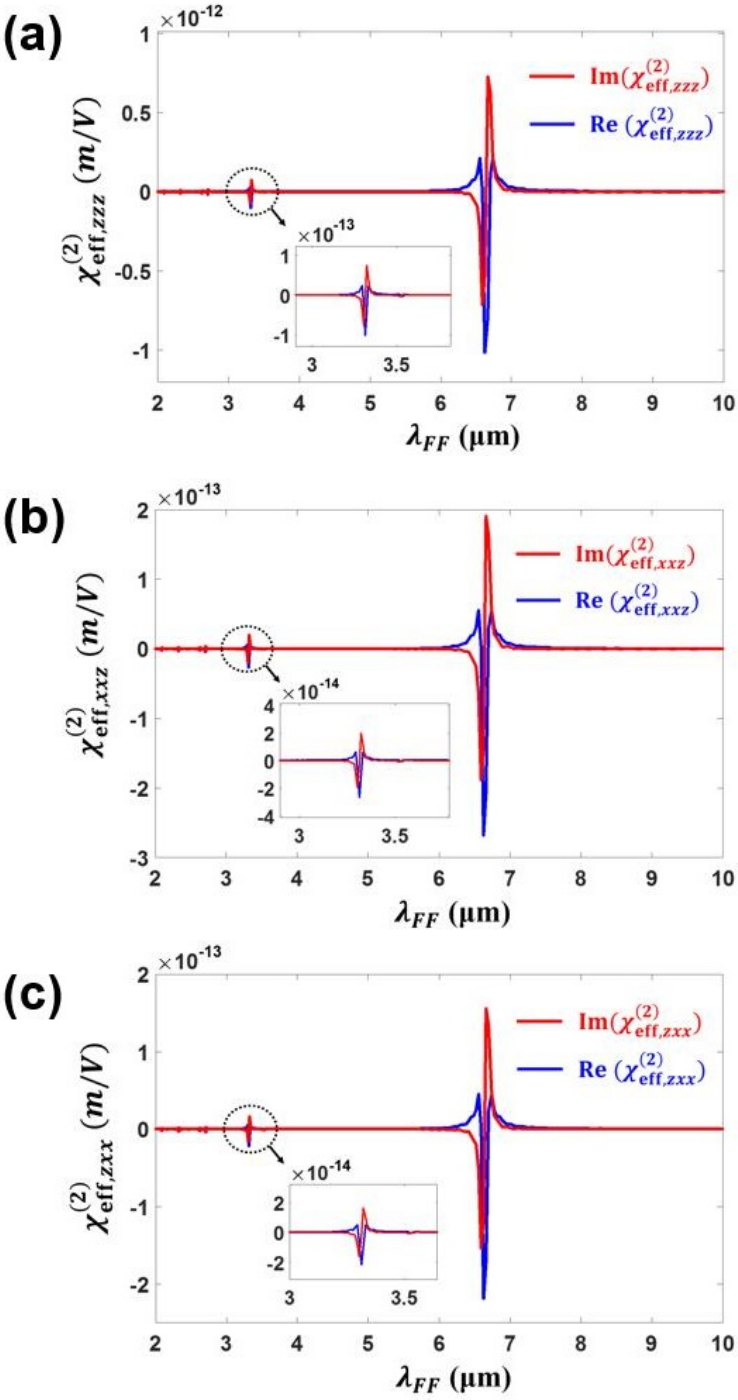

Figure 4.11: The same as in Fig. 4.10, but corresponding to the 2D graphene metasurface.

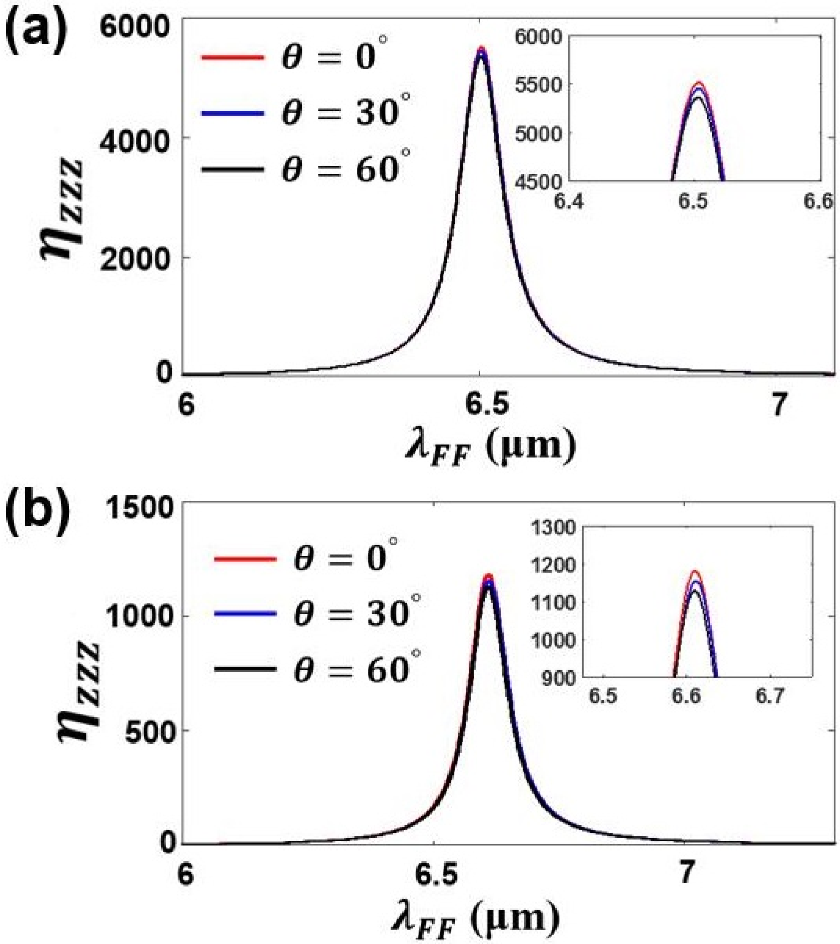

Figure 4.12: (a) Wavelength dependence of the enhancement factor of the dominant component of the effective second-order susceptibility, determined for the optimized 1D graphene metasurface for several values of the angle of incidence, θ. (b) The same as in (a), but determined for the 2D optimized graphene metasurface.

the size of these metaatoms is much smaller than the resonance wavelength at the SH, one can conclude that the nonlinear graphene gratings investigated in this study operate in the metasurface regime, too.

In order to further analyze the characteristics of the magnitude of the enhancement of the nonlinear optical response of the two graphene metasurfaces, we also calculated the enhancement factors $\eta_{zzz} = |\chi^{(2)}_{\text{eff},zzz}/\chi^{(2)}_{\text{gr},zzz}|$, $\eta_{xxz} = |\chi^{(2)}_{\text{eff},xxz}/\chi^{(2)}_{\text{gr},xxz}|$, and $\eta_{zxx} = |\chi^{(2)}_{\text{eff},zxx}/\chi^{(2)}_{\text{gr},zxx}|$ for several different values of the angle of incidence, θ. In these definitions, $\boldsymbol{\chi}^{(2)}_{\text{gr}}$ is the surface second-order susceptibility of a uniform graphene sheet placed on top of a silica substrate.

The results of this analysis are summarized in Fig. 4.12, where we show the data corresponding to the enhancement η_{zzz} of the dominant component of $\boldsymbol{\chi}_{\text{eff}}^{(2)}$ of the 1D and 2D metasurfaces. This figure demonstrates a remarkable enhancement of the second-order nonlinearity of the two metasurfaces, especially near the plasmon resonance. In particular, the dominant component $\chi_{\text{eff},zzz}^{(2)}$ of the homogenized graphene metasurfaces is larger by more than three orders of magnitude than the corresponding component $\chi_{\text{gr},zzz}^{(2)}$ of a graphene sheet placed on the same silica substrate. It can also be observed that η_{zzz} only slightly decreases as the angle of incidence increases, which further proves that the graphene elements of the metasurfaces behave as true metaatoms. We also stress that despite the fact that the nonlinear optical losses are enhanced as well around plasmon resonances, one expects that this is not a particularly detrimental effect as the graphene metasurfaces investigated in this work are not meant to be employed in applications where large propagation distances are required.

4.5 Conclusion

In summary, in this study we investigated the optical response of one- and two-dimensional graphene metasurfaces and their homogenized counterparts. In particular, using a recently developed homogenization technique, we retrieved the effective permittivity and effective second-order susceptibility of the homogenized metasurfaces and compared the values of several physical quantities characterizing the original and homogenized metasurfaces, such as the optical absorption, transmittance, and reflectance. Our analysis revealed that for metasurfaces whose graphene constituents have characteristic size of a few tens of nanometers there is an excellent agreement between the predictions of the homogenization method and the results obtained by rigorously solving the Maxwell equations. This was explained by the fact that the characteristic size of graphene resonators is much smaller than their resonance wavelength.

Our theoretical analysis of the two types of homogenized graphene metasurfaces showed that their nonlinear response can be greatly enhanced when surface plasmons are excited in their graphene constituents. Additional nonlinearity enhancement is achieved when plasmons exist at both the fundamental-frequency and second-harmonic, the overall effect of this double-resonance effect being an enhancement of the effective second-order susceptibility of the graphene metasurfaces by more than three orders of magnitude. Moreover, it should be noted that this double-resonance phenomenon could also be observed in other more complex configurations, *e.g.* when plasmons are excited in different plasmonic materials, such as metasurfaces containing coupled metallic-graphene nanostructures. Equally important, the proposed homogenization method can be readily extended to other cases, too, such as three-dimensional configurations or incident waves with arbitrary polarization and angle of incidence, which further underscores the importance of the results reported in this study.

Bibliography

[1] A. Alu, M. G. Silveirinha, A. Salandrino, and N. Engheta, Phys. Rev. B **75**, 155410 (2007).

[2] T. Cao, C. W. Wei, R. E. Simpson, L. Zhang, and M. J. Cryan, Sci. Rep. **4**, 3955 (2014).

[3] J. W. You and N. C. Panoiu, Opt. Express **26**, 1882 (2018).

[4] M. Veysi, C. Guclu, O. Boyraz, and F. Capolino, J. Opt. Soc. Am. B **32**, 318 (2015).

[5] G. Ren, Z. Lai, C. Wang, Q. Feng, L. Liu, K. Liu, and X. Luo, Opt. Express **18**, 18151 (2010).

[6] C. Ma and Z. Liu, Opt. Express **18**, 4838 (2010).

[7] I. Al-Naib, G. Sharma, M. M. Dignam, H. Hafez, A. Ibrahim, D. G. Cooke, T. Ozaki, and R. Morandotti, Phys. Rev. B **88**, 195203 (2013).

[8] P. Ding, E. Liang, G. Cai, W. Hu, C. Fan, and Q. Xue, J. Opt. **13**, 075005 (2011).

[9] J. Zhang, W. Liu, Z. Zhu, X. Yuan, and S. Qin, Opt. Express **22**, 30889 (2014).

[10] B. Kante, A. de Lustrac, and J. M. Lourtioz, Phys. Rev. B **80**, 035108 (2009).

[11] A. V. Kabashin, P. Evans, S. Pastkovsky, W. Hendren, G. A. Wurtz, R. Atkinson, and A. V. Zayats, Nat. Mater. **8**, 867 (2009).

[12] K. V. Sreekanth, Y. Alapan, M. ElKabbash, E. Ilker, M. Hinczewski, U. A. Gurkan, and G. Strangi, Nat. Mater. **15**, 621 (2016).

[13] C. Cao, J. Zhang, X. Wen, S. L. Dodson, N. T. Dao, L. M. Wong, and Q. Xiong, ACS Nano **7**, 7583 (2013).

[14] N. Vasilantonakis, G. A. Wurtz, V. A. Podolskiy, and A. V. Zayats, Opt. Express **23**, 14329 (2015).

[15] N. I. Landy, S. Sajuyigbe, J. J. Mock, D. R. Smith, and W. J. Padilla, Phys. Rev. Lett. **100**, 207402 (2008).

[16] R. Alaee, M. Farhat, C. Rockstuhl, and F. Lederer, Opt. Express **20**, 28017 (2012).

[17] S. Song, Q. Chen, L. Jin, and F. Sun, Nanoscale **5**, 9615 (2013).

[18] D. Schurig, J. J. Mock, B. J. Justice, S. A. Cummer, J. B. Pendry, A. F. Starr, and D. R. Smith, Science **314**, 977 (2006).

[19] D. Shin, Y. Urzhumov, Y. Jung, G. Kang, S. Baek, M. Choi, and D. R. Smith, Nat. Commun. **3**, 1213 (2012).

[20] Z. Liu, S. Durant, H. Lee, Y. Pikus, Y. Xiong, C. Sun, and X. Zhang, Opt. Express **15**, 6947 (2007).

[21] D. Korobkin, B. Neuner, C. Fietz, N. Jegenyes, G. Ferro, and G. Shvets, Opt. Express **18**, 22734 (2010).

[22] S. Maslovski and S. Tretyakov, New J. Phys. **14**, 035007 (2012).

[23] G. Rosenblatt and M. Orenstein, Phys. Rev. Lett. **115**, 195504 (2015).

[24] J. S. Gomez-Diaz, M. Tymchenko, J. Lee, M. A. Belkin, and A. Alu, Phys. Rev. B **92**, 125429 (2015).

[25] A. Rose and D. R. Smith, Opt. Mater. Express **1**, 1232 (2011).

[26] C. Argyropoulos, G. D'Aguanno, and A. Alu, Phys. Rev. B **89**, 235401 (2014).

[27] E. Almeida, G. Shalem, and Y. Prior, Nat. Commun. **7**, 10367 (2016).

[28] G. Li, S. Zhang, and T. Zentgraf, Nat. Rev. Mater. **2**, 17010 (2017).

[29] F. Qin, L. Ding, L. Zhang, F. Monticone, C. C. Chum, J. Deng, and S. Zhang, Sci. Adv. **2**, e1501168 (2016).

[30] Y. Zhao and A. Alu, Phys. Rev. B **84**, 205428 (2011).

[31] Y. Yang, I. I. Kravchenko, D. P. Briggs, and J. Valentine, Nat. Commun. **5**, 5753 (2014).

[32] J. Sautter, I. Staude, M. Decker, E. Rusak, D. N. Neshev, I. Brener, and Y. S. Kivshar, ACS Nano **9**, 4308 (2015).

[33] S. A. Maier, *Plasmonics: Fundamentals and Applications* (Springer: New York, 2007).

[34] A. V. Zayats, I. I. Smolyaninov, and A. A. Maradudin, Phys. Rep. **408**, 131 (2005).

[35] F. J. Garcia-Vidal, L. Martin-Moreno, T. Ebbesen, and L. Kuipers, Rev. Mod. Phys. **82**, 729 (2010).

[36] N. C. Panoiu, W. E. I. Sha, D. Y. Lei, and G. C. Li, J. Opt. **20**, 083001 (2018).

[37] J. B. Khurgin, Nat. Nanotechnol. **10**, 2 (2015).

[38] T. Christopoulos, O. Tsilipakos, N. Grivas, and E. E. Kriezis, Phys. Rev. E **94**, 062219 (2016).

[39] T. Christopoulos, O. Tsilipakos, G. Sinatkas, and E. E. Kriezis, Phys. Rev. B, **98**, 235421 (2018).

[40] V. G. Ataloglou, T. Christopoulos, and E. E. Kriezis, Phys. Rev. A, **97**, 063836 (2018).

[41] F. H. Koppens, D. E. Chang, and F. J. Garcia de Abajo, Nano Lett. **11**, 3370 (2011).

[42] S. H. Lee, M. Choi, T. T. Kim, S. Lee, M. Liu, X. Yin, and X. Zhang, Nat. Mater. **11**, 936 (2012).

[43] J. W. You, S. R. Bongu, Q. Bao, and N. C. Panoiu, Nanophotonics **8**, 63 (2019).

[44] J. W. You, J. You, M. Weismann, and N. C. Panoiu, Philos. Trans. R. Soc. London, Ser. A **375**, 20160313 (2017).

[45] Y. Q. An, J. E. Rowe, D. B. Dougherty, J. U. Lee, and A. C. Diebold, Phys. Rev. B **89**, 115310 (2014).

[46] G. D. Mahan, *Many-particle physics* Springer Science and Business Media (2013).

[47] J. J. Dean and H. M. van Driel, Phys. Rev. B **82** 125411 (2010).

[48] J. W. You and N. C. Panoiu, Opt. Lett. (submitted).

[49] C. L. Holloway, E. F. Kuester, and A. Dienstfrey, IEEE Antennas Wirel. Propag. Lett. **10**, 1507 (2011).

[50] O. Tsilipakos, T. Koschny, and C. M. Soukoulis, ACS Photon. **5**, 1101 (2018).

[51] M. Weismann and N. C. Panoiu, Phys. Rev. B **94**, 035435 (2016).

[52] J. W. You, E. Threlfall, D. F. Gallagher, and N. C. Panoiu, J. Opt. Soc. Am. B **35**, 2754 (2018).

Chapter 5

Comparison of homogenization approach of graphene and silicon-based metasurfaces

5.1 Introduction

Metamaterials, whose emergence has opened up exciting new opportunities to create novel media with pre-designed physical properties, have been proven to have a significant impact on the development of new approaches and devices for controlling light interaction with matter and achieving key functionalities, including light focusing [1, 2, 3], perfect lensing [4, 5], perfect absorption [6, 7, 8, 9, 10], electromagnetic cloaking [11, 12, 13], imaging with sub-diffraction resolution [14, 15, 16, 17, 18], and optical sensing [19, 20, 21, 22]. One of the most important functionalities provided by metamaterials is the enhancement of the local optical field [23, 24, 25, 26, 27, 28, 29, 30]. This feature is particularly relevant to nonlinear optics since nonlinear optical interactions grow nonlinearly with the applied field. Promising applications of metamaterials can be found in a broad area of science and engineering, including optical filters, sensing and infrastructure monitoring, medical devices, remote aerospace applications, and smart solar power management.

As research in metamaterials advanced, it became clear that the two-dimensional (2D) counterpart of metamaterials, the so-called metasurfaces, would offer the fastest route to functional devices and applications. This is so chiefly because most nanofabrication techniques can conveniently be applied to the planar configuration of metasurfaces. These ultrathin and lightweight optical devices are generally made of sub-wavelength dielectric or metallic elements arranged in one-dimensional (1D) or 2D periodic arrays. Equally important from a practical perspective, the single-layer characteristics of photonic devices based on metasurfaces make them particularly amenable to system integration. Because of their small thickness, light-matter interaction occurs in a reduced volume and as such optical losses in metasurfaces are relatively small. Importantly in nonlinear optics applications, this reduced light propagation distance in metasurfaces means that phase-matching requirements can be relaxed, which greatly reduces the design constraints of nonlinear optical devices based on metasurfaces [31, 32, 33, 34, 35, 36].

Metasurfaces can mainly be divided into two categories, namely metallic (plasmonic) [37, 38] and dielectric metasurfaces [39, 40]. Plasmonic metasurfaces, which exploit the resonant excitation of surface plasmons at specific frequencies [41, 42, 43], can greatly enhance the local optical field, but this phenomenon is usually accompanied at optical frequencies by large dissipative losses. Dielectric metasurfaces, on the other hand, experience much smaller optical losses but only provide limited optical field enhancement. Moreover, another difference between the two classes of metasurfaces, which is directly related to the magnitude of the optical losses, is that whereas the resonances in the plasmonic metasurfaces are relatively broad, the (Mie) resonances associated to dielectric metasurfaces are particularly narrow. As a result, dielectric metasurfaces are usually much more dispersive than the plasmonic ones. One effective approach to study metasurfaces is using homogenization methods, which reduce the metasurface to a homogeneous material with specific linear and nonlinear retrieved optical coefficients. These effective physical quantities are determined in such a way that the metasurface and homogenous layer of material have the same optical response, which is useful to deal complex structures with simple method considering only the homogeneous material.

In this chapter, we propose a homogenization method and investigate its accuracy when applied to plasmonic and dielectric metasurfaces. As plasmonic metasurface we consider a graphene metasurface [44, 45, 46] consisting of a square array of free-standing graphene cruciform patches, whereas the dielectric metasurface is made of a rectangular array of photonic crystal (PhC) cavities possessing high-Q optical modes, embedded in a silicon PhC slab waveguide. The rationale for our choice is that the two metasurfaces capture the general characteristics of the two main classes of metasurfaces, *i.e.* plasmonic and dielectric metasurfaces. In particular, the cruciform graphene patches possess strong plasmon resonances characterized by highly confined, enhanced optical near-field. As optical nonlinearity, we consider second-harmonic generation (SHG) by the nonlocal nonlinear polarization, as symmetry considerations imply that the SHG by the the local nonlinear polarization is zero [47, 48]. Moreover, the silicon PhC cavities were designed so as to possess two high-Q optical cavity modes separated by the Raman frequency of silicon, which ensures a strong effective Raman nonlinearity of the metasurface [49].

The remainder of the chapter is organized as follows: In the next section we present the geometrical configurations and material parameters characterizing the two metasurfaces considered in this work. Then, in Sec. 5.3, we introduce the linear and nonlinear homogenization method used to extract the constitutive parameters of the metasurfaces, whereas in Sec. 5.4 we apply our homogenization approach to the two metasurfaces and derive general principles regarding the conditions in which the predictions of the homogenization method are valid. In particular, we extract the linear and nonlinear constitutive parameters of the metasurfaces and then compare the optical response of the metasurfaces with that of their homogenized counterparts. Finally, we conclude this chapter by summarizing the main findings of our study and discussing some of their implications to future developments pertaining to metamaterials research.

5.2 Description of the graphene and silicon metasurfaces

In this section, we describe the geometrical configuration and material parameters of the two metasurfaces investigated in this work, namely the graphene cruciform metasurface illustrated in figure 5.1(a) and the silicon PhC nanocavity metasurface shown in figure 5.1(b). In addition, we explain the rationale for our choice of metasurfaces by presenting their main physical properties.

5.2.1 Geometrical configuration of the graphene and silicon metasurfaces

The graphene metasurface lies in the x-y plane and consists of a square array of cruciform graphene patches. The symmetry axes of the array coincide with the x- and y-axes and are oriented along the arms of the crosses, as per figure 5.1(a). The length and width of the arms of the crosses along the two axes are L_x (L_y) and w_x (w_y), respectively, whereas the corresponding periods of the metasurface are P_x and P_y. In this work, unless otherwise specified, $L_x = L_y = 60\,\text{nm}$, $w_x = w_y = 30\,\text{nm}$, and $P_x = P_y = 100\,\text{nm}$.

The relative electric permittivity of graphene is given by the relation:

$$\varepsilon_g = 1 + \frac{i\sigma_s}{\varepsilon_0 \omega h_g}, \tag{5.1}$$

where $h_g = 0.3\,\text{nm}$ is the thickness of graphene, ω is the frequency, and the graphene surface conductivity, σ_s, is described by the Kubo's formula [50]:

$$\begin{aligned}\sigma_s = \; & \frac{e^2 k_B T \tau}{\pi \hbar^2 (1 - i\omega\tau)} \left[\frac{\mu_c}{k_B T} + 2 \ln \left(e^{-\frac{\mu_c}{k_B T}} + 1 \right) \right] \\ & + \frac{i e^2}{4\pi\hbar} \ln \frac{2|\mu_c|\tau/\hbar - i(1 - i\omega\tau)}{2|\mu_c|\tau/\hbar + i(1 - i\omega\tau)}. \end{aligned} \tag{5.2}$$

Here, μ_c, T, and τ are the chemical potential, temperature, and relaxation time, respectively. In this study, we use $\mu_c = 0.6\,\text{eV}$, $\tau = 0.1\,\text{ps}$, and $T = 300\,\text{K}$.

The wavelength dependence of the real and imaginary parts of graphene permittivity, as described by Eq. (5.1) in conjunction with Eq. (5.2), are depicted in figure 5.2. It can be seen in this figure that $\mathfrak{Im}(\varepsilon_g) > 0$ and $\mathfrak{Re}(\varepsilon_g) < 0$, which are spectral characteristics shared by most noble metals.

The silicon metasurface, illustrated in figure 5.1(b), consists of a rectangular array of PhC cavities embedded in a PhC slab waveguide made of silicon ($n_{Si} = 3.4$) [49]. The PhC slab waveguide comprises a 2D hexagonal lattice of air holes in a

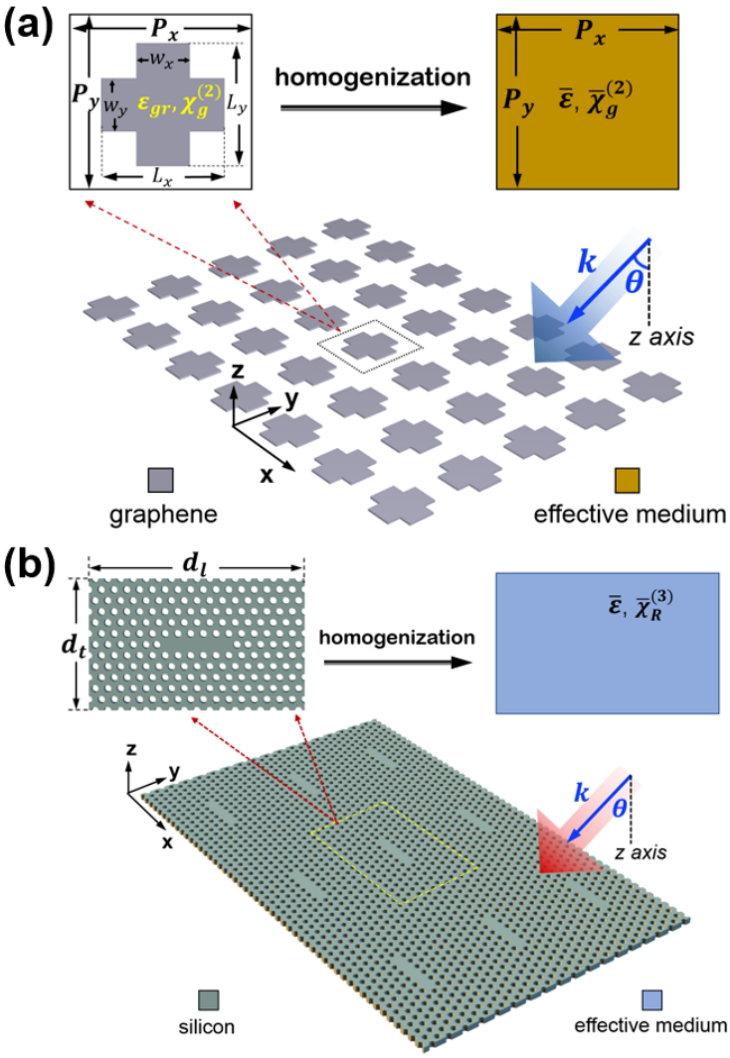

Figure 5.1: Schematic of homogenization of two metasurfaces. (a) Geometry of a graphene metasurface consisting of a 2D array of graphene crosses. The unit cell is homogenized into a uniform layer of material characterized by effective parameters. (b) Geometry of a silicon metasurface consisting of a rectangular array of silicon PhC nanocavities in a hexagonal PhC slab waveguide made of silicon. The unit cell is homogenized into a uniform layer of material with effective parameters.

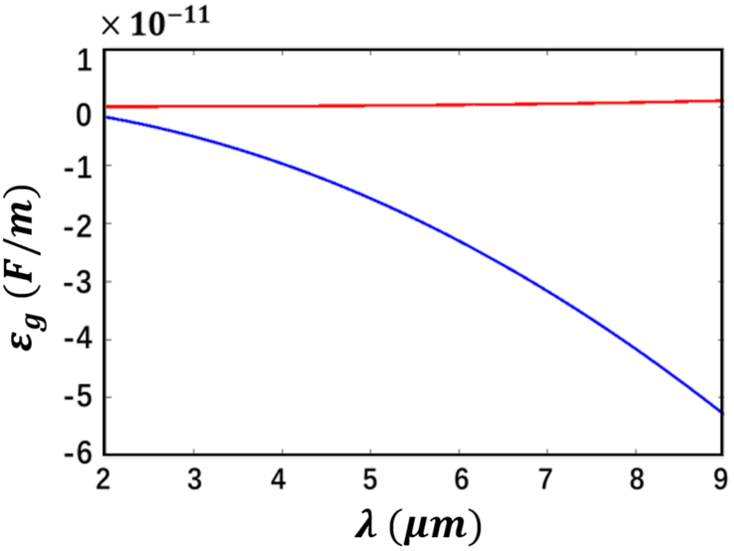

Figure 5.2: Wavelength dependence of the real (blue curve) and imaginary (red curve) parts of the graphene relative permittivity.

silicon slab with the hole radius $r = 0.29a$ and slab thickness $t = 0.6a$, where a is the lattice constant. Moreover, the optical nanocavities are the so-called $L5$ PhC cavities, namely they are created by filling in 5 consecutive holes oriented along the ΓK symmetry axis of the hexagonal lattice. The periods of the PhC metasurface, defined as the center-to-center distance along the x- and y-axes between adjacent PhC cavities, are $d_l = 17a$ and $d_t = 6\sqrt{3}a$, respectively. In order to increase the Q-factor of the optical modes of this PhC nanocavity, we shifted outwardly the end-holes of the cavity by $0.15a$ [51].

The PhC cavity is designed in such a way that it possesses two optical modes whose frequencies are separated by the Raman frequency of silicon, $\Omega = 2\pi \times 15.6\,\text{THz}$ [52]. This ensures a very strong nonlinear coupling between the two optical modes, both because of the large optical field enhancement inside the cavities and also due to favorable spatial overlap between the two optical modes. Consequently, one can achieve an efficient Raman interaction between the two optical modes. This means that the PhC nanocavities can be viewed as artificially engineered, strongly nonlinear “silicon meta-atoms”, which when arranged in some spatial pattern give rise to photonic metasurfaces with large Raman nonlinearity. In particular, if one chooses the lattice constant $a = 333\,\text{nm}$, the resonance frequency of the pump and Stokes modes are $\omega_p = 1572.5\,\text{THz}$ and $\omega_S = 1474.6\,\text{THz}$, respectively, and therefore the condition $\omega_p - \omega_S = \Omega$ is fulfilled. Expressed in terms of normalized frequency of $2\pi c/a$, the frequencies of the two optical modes are $\omega_p = 0.2778$ and $\omega_S = 0.2605$. Also, the Q-factors of the two modes are $Q_p = 1804$ and $Q_S = 1.12 \times 10^5$. Note that the photonic band structure of the PhC slab and the corresponding cavity modes were computed with RSoft's BandSOLVE [53], with the cavity modes lying in the transverse-magnetic bandgap of the PhC slab waveguide (see figure 5.3).

The linear optical response of graphene and silicon metasurfaces is presented in figures 5.4(a) and 5.4(b), respectively, and correspond to an x-polarized plane wave normally incident onto the metasurface. This figure clearly shows that, in the

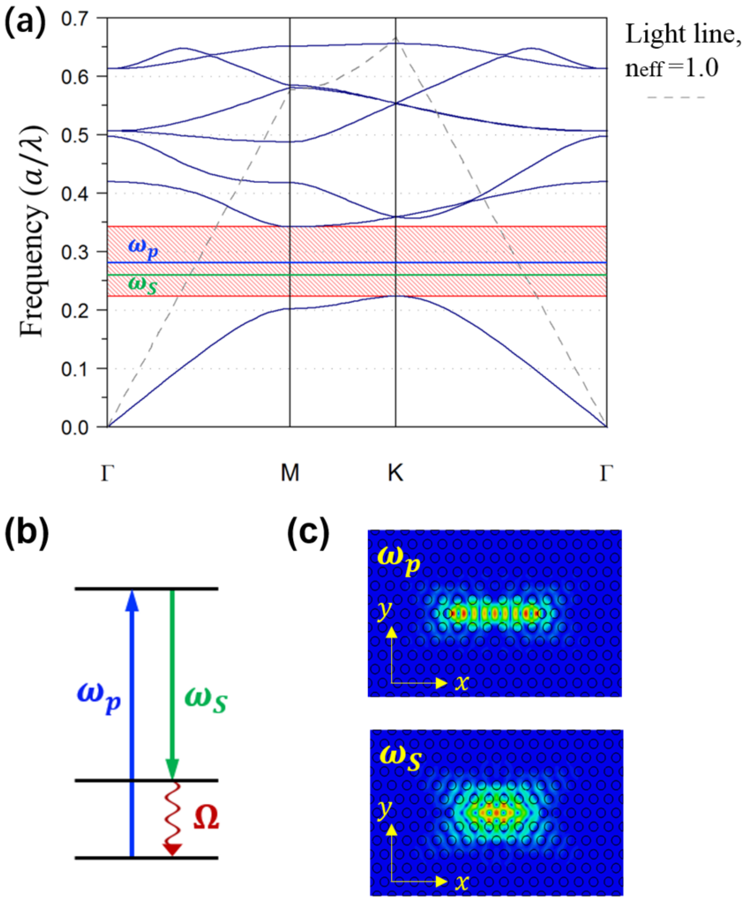

Figure 5.3: a) Transverse-magnetic band structure of the PhC and two optical modes of the PhC cavity withe frequencies of ω_p and ω_S. The dashed lines indicate light lines. b) Diagrammatic representation of the stimulated Raman scattering. c) The field profiles of the optical modes at the pump and Stokes frequencies.

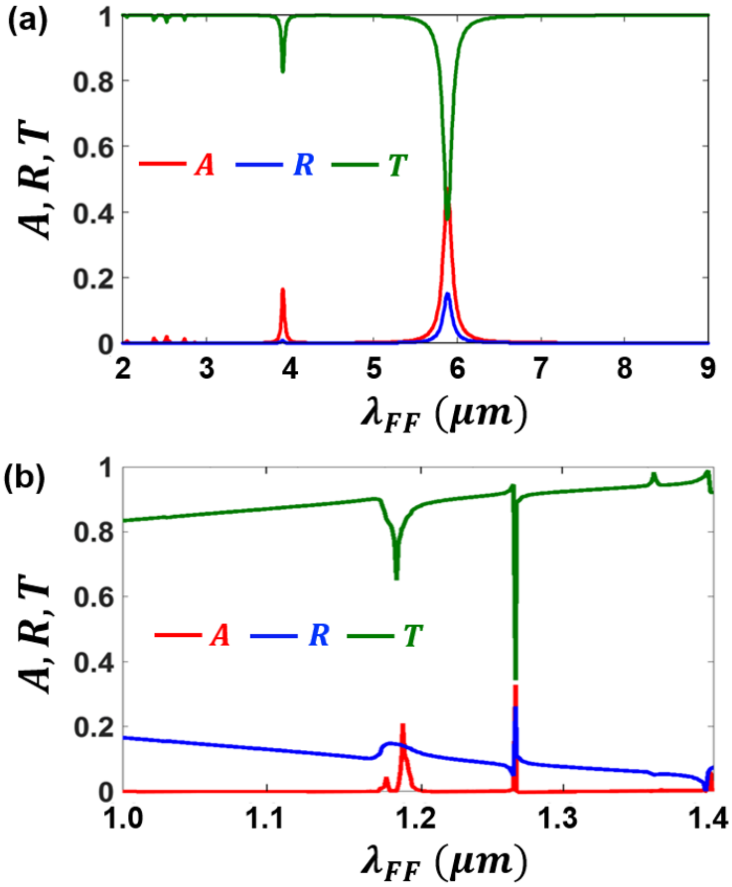

Figure 5.4: a) Wavelength dependence of absorption, reflectance, and transmittance of the graphene metasurface. b) The same as in a), but determined for the silicon metasurface.

case of the graphene metasurface, absorption, A, reflectance, R, and transmittance, T, have a series of spectral resonances occurring at common wavelengths. These resonances are due to the generation of localized surface plasmons in the graphene crosses, the resonance wavelength of the fundamental plasmon being $\lambda = 5.88\,\mu\text{m}$. Moreover, it can be seen that the excitation of surface plasmons is accompanied by a large increase of the optical absorption, which suggests that at the corresponding resonance wavelengths the optical near-field is significantly enhanced. Moreover, the spectra of the silicon metasurface show two resonances at the frequencies of the two cavity modes, the width of these resonances being much smaller than that of plasmon resonances.

5.3 Linear and nonlinear homogenization method

In this section, we present first the homogenization approach used to describe the effective optical response of the metasurfaces investigated in this paper and retrieve their effective permittivities and nonlinear susceptibilities and then compare the linear optical response of the original and homogenized metasurfaces so as to clarify the circumstances in which our homogenization approach is accurate.

5.3.1 Theory of the effective permittivity of metasurfaces

The general linear homogenization method presented here amounts to establishing a relationship between the averaged electric displacement field, **D**, and the electric field, **E**, and is known as the field averaging method. It will be expanded later on to the nonlinear case. As it is well known, the constitutive relation of a linear anisotropic material is expressed as $D_i = \sum_j \varepsilon_{ij} E_j$, where ε_{ij} is the permittivity tensor and the subscripts $i, j = x, y, z$. The field-average method relies on this relation, the effective permittivity of the medium being defined via a similar relation between the electric field and the electric displacement field:

$$\overline{\mathbf{E}}(\omega) = \frac{1}{V}\int_V \mathbf{E}(\mathbf{r},\omega)d\mathbf{r}, \tag{5.3}$$

$$\overline{\mathbf{D}}(\omega) = \frac{1}{V}\int_V \mathbf{D}(\mathbf{r},\omega)d\mathbf{r}. \tag{5.4}$$

This method is particularly suitable for describing metasurfaces, because in this case the averaging domain can be naturally defined as the unit cell of the metasurface. Therefore, in the equations above, V is the volume of the unit cell of the metasurface.

According to the field averaging method, for an isotropic medium whose permittivity tensor is diagonal, the effective permittivity is evaluated as $\overline{\varepsilon}_i = \overline{D}_i/\overline{E}_i$. This definition can be extended to anisotropic media as follows: First, one defines an auxiliary quantity, $d_{ij} = \varepsilon_{ij}E_j$, and express the displacement field as $D_i = \sum_j d_{ij}$, and then calculate the averaged value of each component of the auxiliary quantity:

$$\overline{d}_{ij}(\omega) = \frac{1}{V}\int_V d_{ij}(\mathbf{r},\omega)d\mathbf{r} = \frac{1}{V}\int_V \varepsilon_{ij}(\mathbf{r},\omega)E_j(\mathbf{r},\omega)d\mathbf{r}. \tag{5.5}$$

If we assume that the averaged fields are related by a constitutive relation similar to that corresponding to the local fields, namely $\overline{D}_i = \sum_j \overline{\varepsilon}_{ij}\overline{E}_j$, and by requiring that the average of the field $\mathbf{D}(\mathbf{r},\omega)$ of the metasurface and the field $\overline{\mathbf{D}}(\omega)$ in the homogenized layer of material are termwise equal, the effective permittivity is determined by the following equation:

$$\overline{\varepsilon}_{ij}(\omega) = \frac{\overline{d}_{ij}(\omega)}{\overline{E}_j(\omega)} = \frac{\int_V \varepsilon_{ij}(\mathbf{r},\omega)E_j(\mathbf{r},\omega)d\mathbf{r}}{\int_V E_j(\mathbf{r},\omega)d\mathbf{r}}. \tag{5.6}$$

This formula has been used to determine the effective permittivity of both metasurfaces. Before moving on to the calculation of the effective nonlinear susceptibilities of the metasurfaces, we note that in the case of the graphene metasurface the volume integrals can be reduced to surface integrals across the midsection of the graphene sheet because the fields across the ultrathin graphene layer vary only slightly.

5.3.2 Calculation of effective second-order susceptibility of graphene metasurfaces

As we assume that the graphene crosses are free standing, symmetry considerations imply that the dipole (local) nonlinear polarization at the second harmonic (SH) exactly cancels. Consequently, the lowest order SHG is due to the nonlocal nonlinear polarization whose sources are magnetic dipoles and electric quadrupoles oscillating at the SH frequency (The nonlocal SHG can be ignored in this case). It should be noted that if the graphene patches lie onto a substrate the inversion symmetry is broken and consequently the generated SH is due to the dipole nonlinear polarization. The homogenization of such graphene metasurfaces has been recently studied [54].

This nonlinear polarization and the associated nonlinear surface current in the case of graphene metasurfaces characterized by nonlocal nonlinear polarization can be expressed as [47]:

$$\mathbf{P}(\mathbf{r},\Omega) = \varepsilon_0 \boldsymbol{\chi}_g^{(2)}(\Omega;\omega,\omega) \vdots \mathbf{E}(\mathbf{r},\omega)\nabla\mathbf{E}(\mathbf{r},\omega), \tag{5.7}$$

$$\mathbf{J}_s(\mathbf{r},\Omega) = \boldsymbol{\sigma}_g^{(2)}(\Omega;\omega,\omega) \vdots \mathbf{E}(\mathbf{r},\omega)\nabla\mathbf{E}(\mathbf{r},\omega), \tag{5.8}$$

where $\boldsymbol{\chi}_g^{(2)}(\Omega;\omega,\omega)$ and $\boldsymbol{\sigma}_g^{(2)}(\Omega;\omega,\omega)$ are the *bulk* nonlinear second-order susceptibility and *surface* nonlinear second-order optical conductivity, respectively, and are related by the following formula:

$$\boldsymbol{\chi}_g^{(2)}(\Omega;\omega) = \frac{i}{\varepsilon_0 \Omega h_g} \boldsymbol{\sigma}_g^{(2)}(\Omega;\omega). \tag{5.9}$$

We stress that instead of a bulk nonlinear susceptibility one can use a surface one, defined as $\boldsymbol{\chi}_{s,g}^{(2)} = h_g \boldsymbol{\chi}_g^{(2)} = (i/\varepsilon_0\Omega)\boldsymbol{\sigma}_g^{(2)}$, but we decided to use bulk quantities so that it is more convenient to compare these nonlinear optical coefficients of graphene with those of other centrosymmetric materials.

The surface nonlinear second-order optical susceptibility of graphene has been recently derived in [55] and is given by the following equation:

$$\sigma_{g,ijkl}^{(2)}(\Omega;\omega) = \sigma_{g,\Omega}^{(2)}(\omega)\left(\delta_{ik}\delta_{jl} - \frac{5}{3}\delta_{ij}\delta_{kl} - \frac{1}{3}\delta_{il}\delta_{jk}\right), \tag{5.10}$$

where the scalar part of the surface second-order conductivity tensor is:

$$\sigma_{g,\Omega}^{(2)}(\omega) = \frac{3e^3 v_F^2 \tau^3}{8\pi\hbar^2(1-i\omega\tau)^3}. \tag{5.11}$$

where v_F is Fermi velocity and τ is the relaxation time. Componentwise, the nonlinear polarization can be evaluated as:

$$P_i(\mathbf{r},\Omega) = \varepsilon_0 \sum_{jkl} \chi^{(2)}_{g,ijkl} E_j(\mathbf{r},\omega) \nabla_k E_l(\mathbf{r},\omega) \equiv \sum_{jkl} q_{ijkl}, \tag{5.12}$$

where we introduced a new nonlinear auxiliary quantity defined as $q_{ijkl} = \varepsilon_0 \chi^{(2)}_{g,ijkl} E_j \nabla_k E_l$. Moreover, the spatial average of this quantity is:

$$\overline{q}_{ijkl}(\Omega) = \frac{1}{V} \int_V \varepsilon_0 \chi^{(2)}_{ijkl}(\mathbf{r}) E_j(\mathbf{r},\omega) \nabla_k E_l(\mathbf{r},\omega) d\mathbf{r}, \tag{5.13}$$

where $\chi^{(2)}_{ijkl}(\mathbf{r}) = \chi^{(2)}_{g,ijkl}$ if $\mathbf{r}$ corresponds to a point inside the graphene crosses and $\chi^{(2)}_{ijkl}(\mathbf{r}) = 0$ if $\mathbf{r}$ is in the air region.

If we express the nonlinear polarization in the homogenized metasurface as:

$$\overline{P}_i(\Omega) = \varepsilon_0 \sum_{jkl} \overline{\chi}^{(2)}_{ijkl} \overline{E}_j(\omega) \overline{\nabla_k E_l}(\omega), \tag{5.14}$$

where $\overline{\chi}^{(2)}_{ijkl}$ is the effective nonlinear second-order susceptibility of the homogenized metasurface, and impose the condition that the spatial average of the nonlinear polarization described by Eq. (5.12) is *termwise* equal to the polarization in Eq. (5.14), we obtain the following formula for the effective nonlinear susceptibility:

$$\overline{\chi}^{(2)}_{ijkl}(\Omega;\omega) = \frac{\overline{q}_{ijkl}}{\overline{E}_j \overline{\nabla_k E_l}}. \tag{5.15}$$

In this formula and in Eq. (5.14), the quantity $\overline{\nabla_i E_j}$ is defined as:

$$\overline{\nabla_i E_j} = \frac{1}{V} \int_V \nabla_i E_j(\mathbf{r},\omega) d\mathbf{r}. \tag{5.16}$$

5.3.3 Theory of effective Raman susceptibility of silicon metasurfaces

The calculation of the effective Ramman susceptibility of the silicon based PhC metasurface described in Sec. 5.2 is similar to that of the effective second-order susceptibility presented in the preceding subsection, so that here we present only the main steps. A more detailed derivation can be found in [49].

We start our analysis with the nonlinear Raman polarization at the Stokes frequency, $\mathbf{P}_R(\mathbf{r},\omega_S)$, which can be written as:

$$\mathbf{P}_R(\mathbf{r},\omega_S)=\frac{3}{2}\varepsilon_0\boldsymbol{\chi}_R^{(3)}(\mathbf{r})\vdots\mathbf{E}(\mathbf{r},\omega_p)\mathbf{E}^*(\mathbf{r},\omega_p)\mathbf{E}(\mathbf{r},\omega_S), \tag{5.17}$$

where $\boldsymbol{\chi}_R^{(3)}(\mathbf{r})$ is the Raman susceptibility and $\mathbf{E}(\mathbf{r},\omega_p)$ and $\mathbf{E}(\mathbf{r},\omega_S)$ are the optical fields at the pump and Stokes frequencies, respectively. For the sake of simplicity, we assume that the symmetry axes of the array of PhC cavities coincide both with the x- and y-axes and with the principal axes of silicon. Under these circumstances, the nonzero components of $\boldsymbol{\chi}_R^{(3)}$ are $\chi_{R,ijij}^{(3)}=\chi_{R,jiji}^{(3)}=\chi_{R,jiij}^{(3)}=\chi_{R,ijji}^{(3)}$, with $i,j=x,y,z$ and $i\neq j$. The value at resonance of the only independent component is $\chi_{R,1212}^{(3)}=-i11.2\times10^{-18}\,\mathrm{m}^2\,\mathrm{V}^{-2}$ [56].

We then define the spatially averaged effective Raman polarization:

$$\overline{\mathbf{P}}_R(\omega_S)=\frac{1}{V}\int_V\mathbf{P}_R(\mathbf{r},\omega_S)d\mathbf{r}, \tag{5.18}$$

where the volume integration is taken over the unit cell of the metasurface, together with the effective Raman polarization in a homogenized slab of nonlinear optical medium with the same thickness as that of the PhC slab:

$$\mathbf{P}_R^{\mathrm{eff}}(\omega_S)=\frac{3}{2}\varepsilon_0\overline{\boldsymbol{\chi}}_R^{(3)}\vdots\overline{\mathbf{E}}(\omega_p)\overline{\mathbf{E}}^*(\omega_p)\overline{\mathbf{E}}(\omega_S). \tag{5.19}$$

Here, $\overline{\boldsymbol{\chi}}_R^{(3)}$ is the effective Raman susceptibility of the homogenized metasurface.

As in the case of the graphene metasurface, we cannot simply impose the condition that the components of the nonlinear polarizations in Eq. (5.18) and Eq.

(5.19) are equal because in the general case the effective Raman susceptibility tensor, $\overline{\boldsymbol{\chi}}_R^{(3)}$, has 81 independent components, so that the corresponding system of equations is overdetermined, meaning that there are more unknown equations than the equations. Consequently, we impose the condition that the r.h.s. of equations Eq. (5.18) and Eq. (5.19) are *termwise identical*. Using this constraint, it can be seen that the components of $\overline{\boldsymbol{\chi}}_R^{(3)}$ are determined by the following relations:

$$\overline{\chi}_{R,ijkl}^{(3)} = \frac{\frac{1}{V}\int_V \chi_{R,ijkl}^{(3)}(\mathbf{r})E_j(\mathbf{r},\omega_p)E_k^*(\mathbf{r},\omega_p)E_l(\mathbf{r},\omega_S)d\mathbf{r}}{\overline{E}_j(\omega_p)\overline{E}_k^*(\omega_p)\overline{E}_l(\omega_S)}. \tag{5.20}$$

Note that the components of $\overline{\boldsymbol{\chi}}_R^{(3)}$ and $\boldsymbol{\chi}_R^{(3)}$ cancel for the same set of indices i, j, k, and l.

5.4 Results and Discussions

In this section, we study the circumstances in which our method produces accurate results and use it to understand the main differences between the physical properties of graphene and silicon PhC metasurfaces. Since the two metasurfaces have general structures, we expect the conclusions applied to other dielectric and graphene metasurfaces.

5.4.1 Effective permittivities of the graphene and silicon photonic crystal metasurfaces

Based on our theoretical analysis, the effective permittivity of the two metasurfaces investigated in this work can be calculated using Eq. (5.6). The results of our calculations, corresponding to the graphene and silicon PhC metasurfaces, are presented in Fig. 5.5(a) and Fig. 5.5(b), respectively. These figures show some similarities between the two spectra but also significant differences. Thus, the effective permittivity of graphene metasurface displays a series of spectral resonances of Lorentzian nature, which occur at the plasmon resonance wavelengths of the graphene crosses. This means that the graphene crosses behave as meta-atoms that possess a series of resonant states, the overall optical response of the metasurface being primarily determined by these resonances. The main reason for this behavior can be traced to the size of the graphene crosses relative to the resonance wavelengths of the plasmons of the graphene crosses. Specifically, since the size of the crosses is much smaller than the plasmon wavelengths, the overall optical response of the graphene metasurface can be viewed as a superposition of the response of weakly interacting Lorentz-type oscillators.

The spectrum of the effective permittivity of the silicon PhC metasurface, on the other hand, presents a series of complex features, which are the result of several phenomena. Thus, the two main resonances of the effective permittivity are due to the excitation of the two optical modes of the PhC cavity. The spectral separation between the frequencies of the two cavity modes is relatively small and this leads to

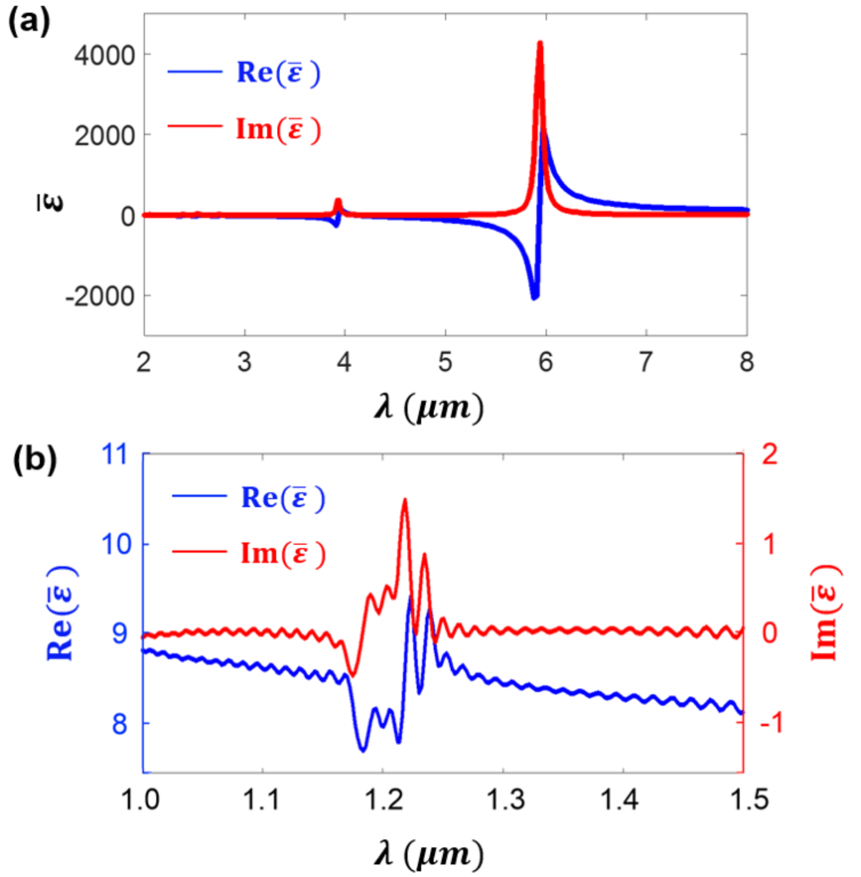

Figure 5.5: a) Spectra of the real and imaginary parts of the effective permittivity of the graphene metasurface. b) The same as in a), but calculated for the silicon metasurface.

interference features in the spectrum of the effective permittivity. The other, weaker spectral peaks are due to leaky modes of the PhC slab.

5.4.2 Validation of the homogenization approach

In order to validate the conclusions drawn in the preceding subsection and to investigate the situations in which our homogenization method is accurate, we calculated the absorption, A, reflectance, R, and transmittance, T of both metasurfaces and their homogenized counterparts. The main results of these calculations are summarized in Fig. 5.6 and they reveal several important ideas. Thus, it can be seen in this

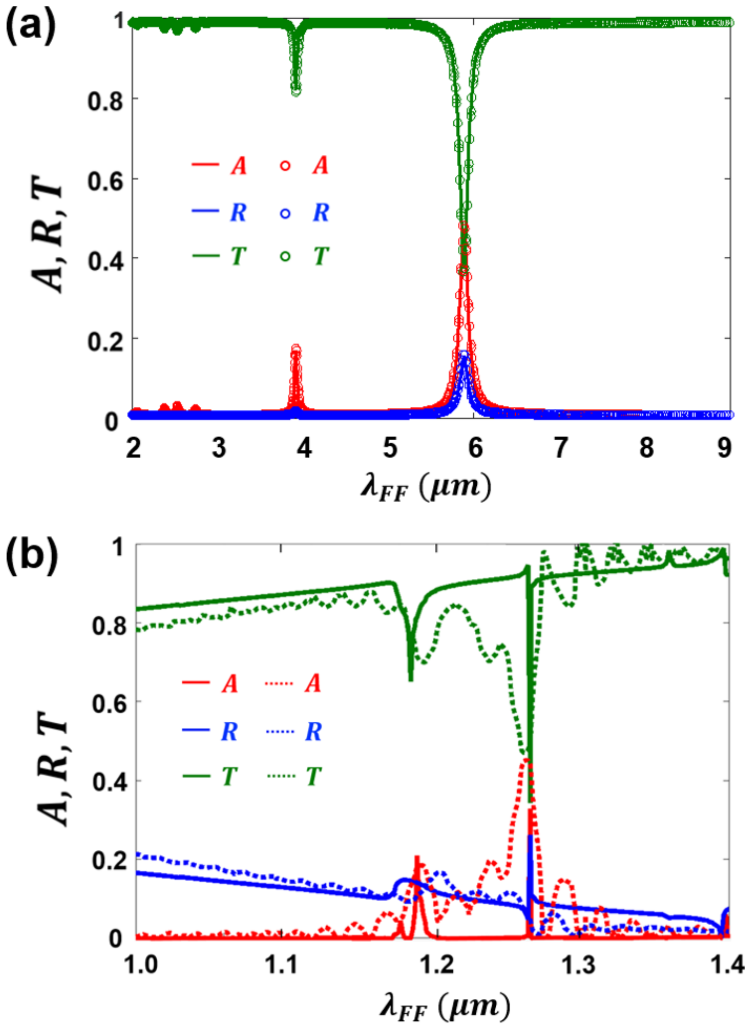

Figure 5.6: a) Wavelength dependence of absorption, reflectance, and transmittance of the graphene metasurface (solid lines) and its homogenized counterpart (marked with circles). b) The same as in a), but determined for the silicon metasurface. The spectra corresponding to the homogenized metasurface are depicted with dotted lines.

figure that in the case of the graphene metasurface the resonances of the transmittance occur at the same wavelengths as the resonances of the effective permittivity, whereas for the silicon PhC metasurface the two sets of resonances differ to some extent. In order to explain these results, one should note that generally the resonances of the transmittance of a planar optical system correspond to excitation of bound modes of the optical system. In the cases investigated here, the bound modes are localized surface plasmons of graphene crosses for the graphene metasurface and optical modes of the PhC cavities and leaky modes of the PhC slab. Moreover, the excitation of these resonances induces a resonant response of the medium, via the polarization of the medium, which in turn leads to resonances in the spectrum of the effective permittivity of the homogenized metasurfaces.

Fig. 5.6(b) also shows that whereas the linear optical responses of the graphene metasurface and its homogenized counterpart are almost identical, in the case of the silicon PhC metasurface they markedly differ from each other. The main reason for this dichotomy is that the graphene crosses are much smaller than the operating wavelength, which makes them respond to the incident optical field as if they were point-like resonators. By contrast, the size of the PhC cavities is comparable to the resonance wavelength of the cavity modes, which renders our homogenization method to be less accurate in this case. It should also be noted, however, that although the homogenization approach for silicon PhC metasurface cannot provide extremely accurate quantitative values for the effective permittivity, it can still provide us with valuable qualitative insights into the governing physics.

These ideas are further illustrated by the dependence of the linear optical response of the graphene metasurface on the angle of incidence, θ, of the incoming plane wave, which is presented in Fig. 5.7. Thus, it can be observed that the spectral resonances of the graphene metasurface, calculated for $\theta = 0^\circ$, 30° and 60°, only slightly varies with θ, whereas the values of A, R, and T at the resonance wavelengths depend more pronouncedly on θ. These findings are explained by the fact that the plasmon resonances depend chiefly on the shape of the graphene nanopatches, and thus are independent of θ, whereas the particular values of A, R, and

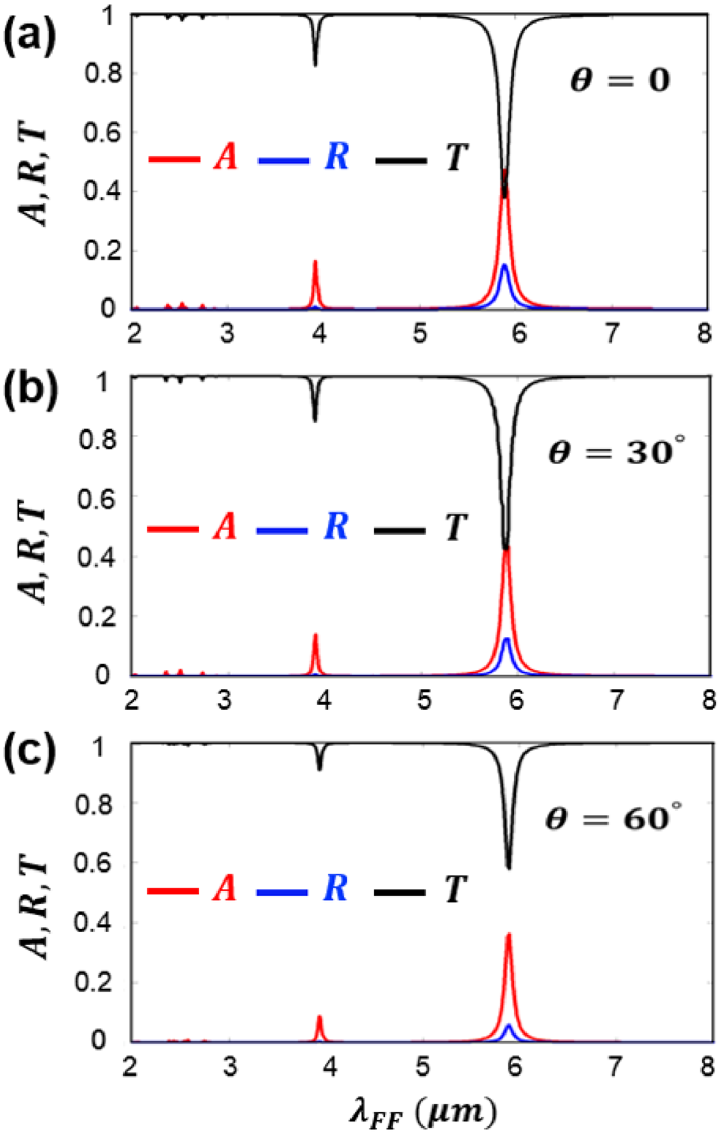

Figure 5.7: Spectra of absorption, reflectance, and transmittance, calculated for different values of the incident angle: a) $\theta = 0$, b) $\theta = 30^{\circ}$, and c) $\theta = 60^{\circ}$.

T depend on the coupling between the incident field and graphene crosses, more specifically on the spatial overlap between the incident wave and the optical field of the graphene plasmons, which is obviously θ-dependent.

5.4.3 Effective second-harmonic susceptibility of graphene metasurfaces

Let us now consider the nonlinear optical properties of the two optical structures and start with the graphene metasurface. The excitation of graphene localized plas-

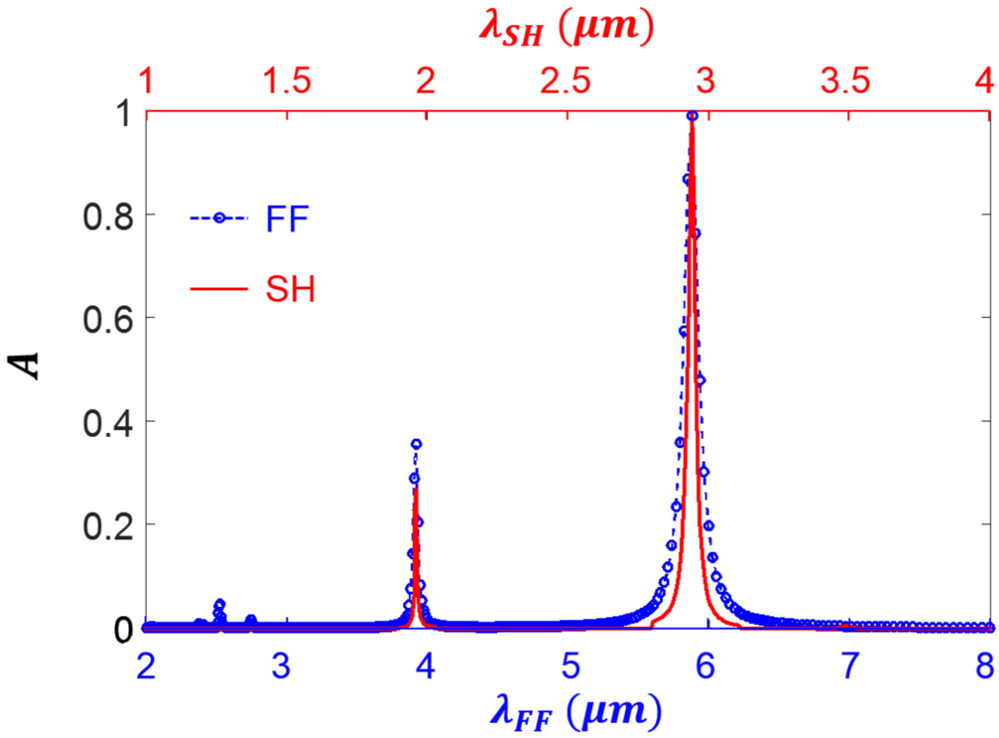

Figure 5.8: Spectrum of optical absorption at FF (blue curve) and SH (red curve).

mons at the fundamental frequency (FF) induces a strong optical near-field and consequently enhanced nonlinear polarization, which is the source of the generated SH. This phenomenon can be clearly seen in Fig. 5.8, where we present the absorption spectra at the FF and SH. In particular, it can be observed in this figure that the occurrence of a resonance at the FF is accompanied by a resonance at half of its wavelength in the SH spectrum. For example, the plasmon resonance at the FF of $\lambda_{FF} = 5.878\,\mu\text{m}$ has a corresponding response in the SH spectrum at $\lambda_{SH} = \lambda_{FF}/2 = 2.939\,\mu\text{m}$.

As can be easily inferred from Eq. 5.9 and Eq. 5.10, the dominant components (in absolute value) of the second-order susceptibility of graphene are $\chi^{(2)}_{g,xxyy} = \chi^{(2)}_{g,yyxx}$. The value of this component, determined for a FF wavelength $\lambda = 1\,\mu\text{m}$, is $\chi^{(2)}_{g,xxyy} = (-8.37 + 0.133i) \times 10^{-19}\,\text{m}^2\,\text{V}^{-1}$. Moreover, as a consequence of our approach to the calculation of the effective second-order susceptibility, it is equal to zero for the same set of indices for which the graphene second-order susceptibility is equal to zero. Therefore, in order to quantify the enhancement of the nonlinear optical response of the graphene metasurface, we computed the enhancement factor, $\eta_{SH} = |\overline{\chi}^{(2)}_{xxyy}/\chi^{(2)}_{g,xxyy}|$, for several values of the angle of incidence, $\theta = 0^\circ$, 30° and 60°. We summarize the results of these calculations in Fig. 5.9.

The most important conclusion of this analysis is that, at the wavelength of the fundamental plasmon, the effective second-order susceptibility of the homogenized graphene metasurface is enhanced by 175×, which means that the maximum value of the effective second-order susceptibility of the homogenized graphene metasurface is $|\overline{\chi}^{(2)}_{xxyy}| = 1.46 \times 10^{-16}\,\mathrm{m^2\,V^{-1}}$. For comparison, the bulk second-order susceptibility of two centrosymmetric materials widely used in nonlinear optics, gold and silicon, are $\gamma = 7.13 \times 10^{-21}\,\mathrm{m^2\,V^{-1}}$ (gold at $\lambda = 810\,\mathrm{nm}$) [57] and $\gamma = 1.3 \times 10^{-19}\,\mathrm{m^2\,V^{-1}}$ (silicon at $\lambda = 800\,\mathrm{nm}$) [58]. Moreover, it can be inferred from Fig. 5.9 that the enhancement factor is smaller for higher-order plasmons, as in this case the plasmon-induced field enhancement decreases. Another feature revealed by Fig. 5.9 is that the enhancement factor decreases as the angle of incidence increases, a finding explained by the fact that when θ increases the spatial overlap between the incident wave and the plasmon mode becomes less favorable and thus the enhancement of the local optical field decreases.

5.4.4 Effective Raman susceptibility of the silicon photonic crystal metasurface

Due to the symmetry properties of the silicon PhC metasurface and the orientation of the cavity array with respect to the principal axes of silicon, the only non-zero component of the effective Raman susceptibility of the metasurface is $\overline{\chi}^{(3)}_{R,1212} \equiv \overline{\chi}^{(3)}_{R}$. Therefore, similarly to the case of the graphene metasurface, we define the enhancement factor $\eta_R = |\overline{\chi}^{(3)}_{R}/\chi^{(3)}_{R}|$, where $\chi^{(3)}_{R} \equiv \chi^{(3)}_{R,1212}$ is the dominant component of the Raman susceptibility of silicon. The parameter η_R quantifies the enhancement of the Raman nonlinearity of the silicon PhC metasurface. Moreover, in order to investigate the dependence of the enhancement factor on the angle of incidence, these calculations were performed for $\theta = 0^\circ$, 30° and 60°.

Following the procedure we just described, we found out that for the values of the incidence angle of 0°, 30° and 60°, the enhancement factor was 2.29×10^4, 3.19×10^3 and 1.99×10^3, respectively. Thus, it can be seen that a giant enhance-

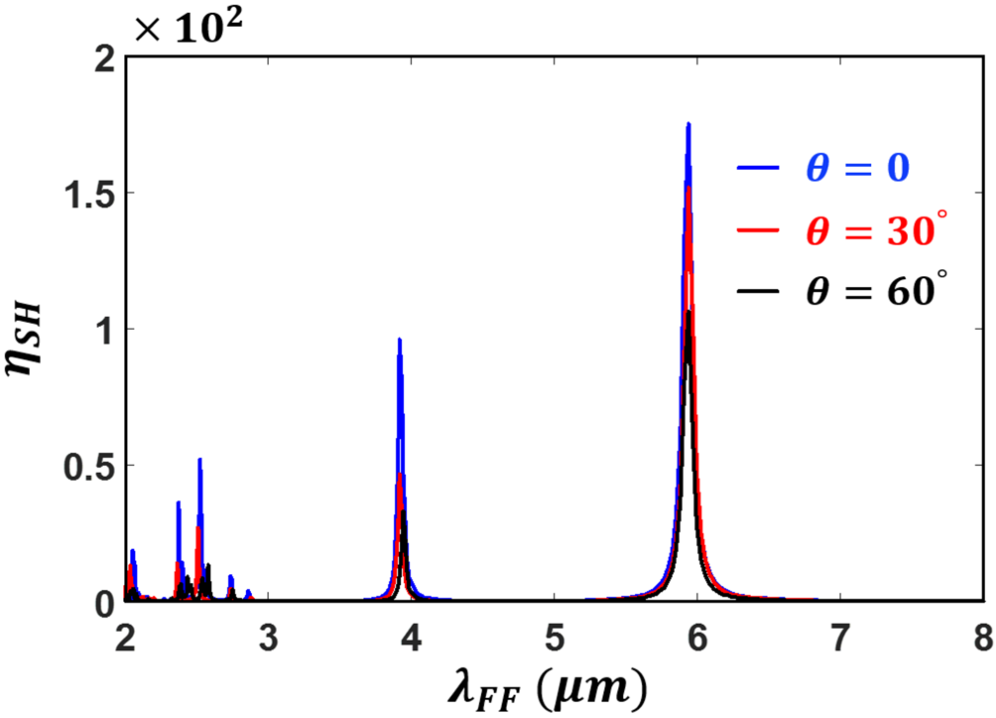

Figure 5.9: Enhancement of effective SH susceptibility of the graphene metasurface, determined for different values of the incident angle, θ. The blue, red, and black curves correspond to $\theta = 0^{\circ}$, 30° and 60°, respectively.

ment of the effective Raman susceptibility of the silicon PhC metasurface of more than 4 orders of magnitude can be achieved at normal incidence. In order to understand the main reason for this remarkable nonlinearity enhancement, one should note that due to the large Q-factor of the pump and Stokes cavity modes the field is significantly enhanced as compared to the amplitude of the incident wave, which in conjunction with the fact that the Raman intensity is proportional to the local field to the power of 6, leads to the extremely large resonant enhancement of the Raman response of the silicon PhC metasurface. Moreover, the cavity field enhancement decreases when the angle of incidence increases, due to a weaker coupling between the incoming wave and the cavity modes, which results in reduced nonlinearity enhancement at larger θ.

As a final remark, it should be noted that the specific design of our metasurface ensures a particularly efficient Raman amplification. To be more specific, let us compare the spectral width of Raman interaction in silicon, $\Delta\nu_R = 105\,\text{GHz}$ [59], with the spectral width of the cavity mode at the Stokes frequency, $\Delta\nu_S =$

$\omega_S/(2\pi Q_S) = 2.1\,\text{GHz}$. Thus, since $\Delta\nu_S \ll \Delta\nu_R$, an efficient Raman interaction can be achieved.

5.5 Conclusion

In summary, two generic metasurfaces, a graphene metasurface based on graphene cruciform patches and a silicon metasurface with photonic crystal cavities as building blocks, are studied using a versatile and powerful homogenization method. In particular, in order to quantify the linear and nonlinear optical response of the two metasurfaces, we computed their effective permittivities and nonlinear susceptibilities. Our calculations revealed that, in both cases, the nonlinear optical response of the metasurfaces was enhanced by several orders of magnitude at the resonances of the metasurface building blocks. Moreover, by comparing the optical response of the metasurfaces and their homogenized counterparts, we showed that the homogenization approach is more suitable for graphene-based metasurfaces, because in this case the size of the resonant graphene nanostructures is much smaller than the operating wavelength. Even though the homogenization approach for silicon-based metasurfaces appeared to be less accurate, it could still provide valuable qualitative insights into their nonlinear optical response.

It should be noted that our homogenization approach is rather general, in that it can be readily extended to metasurfaces of different configurations or made of optical media with various dispersive and nonlinear optical properties. Moreover, the ideas presented in this chapter have broad applicability, as they can be easily extended to other nonlinear optical interactions of practical interest, including third-harmonic generation, four-wave mixing, and sum- and difference frequency generation.

Bibliography

[1] Veysi M, Guclu C, Boyraz O and Capolino F 2015 Thin anisotropic metasurfaces for simultaneous light focusing and polarization manipulation *J. Opt. Soc. Am.* B **32** 318-323

[2] Ren G, Lai Z, Wang C, Feng Q, Liu L, Liu K and Luo X 2010 Subwavelength focusing of light in the planar anisotropic metamaterials with zone plates *Opt. Express* **18** 18151-18157

[3] Ma C and Liu Z 2010 Focusing light into deep subwavelength using metamaterial immersion lenses *Opt. Express* **18** 4838-4844

[4] Maslovski S and Tretyakov S 2012 Perfect lensing with phase-conjugating surfaces: toward practical realization *New J. Phys.* **14** 035007

[5] Rosenblatt G and Orenstein M 2015 Perfect lensing by a single interface: defying loss and bandwidth limitations of metamaterials *Phys. Rev. Lett.* **115** 195504

[6] Landy N I, Sajuyigbe S, Mock J J, Smith D R and Padilla W J 2008 Perfect metamaterial absorber *Phys. Rev. Lett.* **100** 207402

[7] Feng S and Halterman K 2012 Coherent perfect absorption in epsilon-near-zero metamaterials *Phys. Rev.* B **86** 165103

[8] Alaee R, Farhat M, Rockstuhl C and Lederer F 2012 A perfect absorber made of a graphene micro-ribbon metamaterial *Opt. Express* **20** 28017-28024

[9] Jin Y, Xiao S, Mortensen N A and He S 2011 Arbitrarily thin metamaterial structure for perfect absorption and giant magnification *Opt. Express* **19** 11114-11119

[10] Song S, Chen Q, Jin L and Sun F 2013 Great light absorption enhancement in a graphene photodetector integrated with a metamaterial perfect absorber *Nanosc*ale **5** 9615-9619

[11] Schurig D, Mock J J, Justice B J, Cummer S A, Pendry J B, Starr A F and Smith D R 2006 Metamaterial electromagnetic cloak at microwave frequencies *Science* **314** 977-980

[12] Alitalo P and Tretyakov S 2009 Electromagnetic cloaking with metamaterials *Mater. Today* **12** 22-29

[13] Shin D, Urzhumov Y, Jung Y, Kang G, Baek S., Choi M, Park H, Kim K and Smith D R *et al* 2012 Broadband electromagnetic cloaking with smart metamaterials *Nat. Commun.* **3** 1213

[14] Luo C, Johnson S G, Joannopoulos J D and Pendry J B 2003 Subwavelength imaging in photonic crystals *Phys. Rev. B* **68** 045115

[15] Foteinopoulou S and Soukoulis C M 2005 Electromagnetic wave propagation in two-dimensional photonic crystals: A study of anomalous refractive effects *Phys. Rev. B* **72** 165112

[16] Decoopman T, Tayeb G, Enoch S, Maystre D and Gralak B 2006 Photonic crystal lens: from negative refraction and negative index to negative permittivity and permeability *Phys. Rev. Lett.* **97** 073905

[17] Liu Z, Durant S, Lee H, Pikus Y, Xiong Y, Sun C and Zhang X 2007 Experimental studies of far-field superlens for sub-diffractional optical imaging *Opt. Express* **15** 6947-6954

[18] Chatterjee R, Panoiu N C, Liu K, Dios Z, Yu M B, Doan M T, Kaufman L J, Osgood R M and Wong C W 2008 Achieving Subdiffraction Imaging through

Bound Surface States in Negative Refraction Photonic Crystals in the Near-Infrared Range *Phys. Rev. Lett.* **100** 187401

[19] Osley E J, Biris C G, Thompson P G, Jahromi R R F, Warburton P A and Panoiu N C 2013 Fano Resonance Resulting from a Tunable Interaction between Molecular Vibrational Modes and a Double Continuum of a Plasmonic Metamolecule *Phys. Rev. Lett.* **110** 087402

[20] Kabashin A V, Evans P, Pastkovsky S, Hendren W, Wurtz G A, Atkinson R, Pollard R, Podolskiy V A and Zayats A V 2009 Plasmonic nanorod metamaterials for biosensing *Nat. Mater.* **8** 867

[21] Sreekanth K V, Alapan Y, ElKabbash M, Ilker E, Hinczewski M, Gurkan U A, De Luca A and Strang G 2016 Extreme sensitivity biosensing platform based on hyperbolic metamaterials *Nat. Mater.* **15** 621

[22] Cao C, Zhang J, Wen X, Dodson S L, Dao N T, Wong L M, Wang S, Li S, Phan A T and Xiong Q *et al* 2013 Metamaterials-based label-free nanosensor for conformation and affinity biosensing *ACS Nano* **7** 7583-7591

[23] Al-Naib I, Sharma G, Dignam M M, Hafez H, Ibrahim A, Cooke D G, Ozaki T and Morandotti R 2013 Effect of local field enhancement on the nonlinear terahertz response of a silicon-based metamaterial *Phys. Rev.* B **88** 195203

[24] Ding P, Liang E, Cai G, Hu W, Fan C and Xue Q 2011 Dual-band perfect absorption and field enhancement by interaction between localized and propagating surface plasmons in optical metamaterials *J. Opt.* **13** 075005

[25] Zhang J, Liu W, Zhu Z, Yuan X and Qin S 2014 Strong field enhancement and light-matter interactions with all-dielectric metamaterials based on split bar resonators *Opt. Express* **22** 30889-30898

[26] Liu Z, Boltasseva A, Pedersen R H, Bakker R, Kildishev A V, Drachev V P amd Shalaev V M 2008 Plasmonic nanoantenna arrays for the visible *Metamaterials* **2** 45-51

[27] Kante B, de Lustrac A and Lourtioz J M 2009 In-plane coupling and field enhancement in infrared metamaterial surfaces *Phys. Rev.* B **80** 035108

[28] Shcherbakov M R, Neshev D N, Hopkins B, Shorokhov A S, Staude I, Melik-Gaykazyan E V, Decker M, Ezhov A A, Miroshnichenko A E, Brener I, Fedyanin A A and Kivshar Y S 2014 Enhanced third-harmonic generation in silicon nanoparticles driven by magnetic response *Nano Lett.* **14** 6488-6492

[29] Fan W, Zhang S, Panoiu N C, Abdenour A, Krishna S, Osgood R M, Malloy K J and Brueck S R J 2006 Second Harmonic Generation from a Nanopatterned Isotropic Nonlinear Material *Nano Lett.* **6** 1027-1030

[30] Kruk S, Weismann M, Bykov A Y, Mamonov E A, Kolmychek I A, Murzina T, Panoiu N C, Neshev D N and Kivshar Y S 2015 Enhanced Magnetic Second-Harmonic Generation from Resonant Metasurfaces *ACS Photon.* **2** 1007-1012

[31] Panoiu N C and Osgood R M 2007 Enhanced optical absorption for photovoltaics via excitation of waveguide and plasmon-polariton modes *Opt. Lett.* **32** 2825-2827

[32] Gomez-Diaz J S, Tymchenko M, Lee J, Belkin M A and Alu A 2015 Nonlinear processes in multi-quantum-well plasmonic metasurfaces: electromagnetic response, saturation effects, limits, and potentials *Phys. Rev.* B **92** 125429

[33] Rose A and Smith D R 2011 Overcoming phase mismatch in nonlinear metamaterials *Opt. Mater. Express* **1** 1232-1243

[34] Argyropoulos C, Aguanno G D and Alu A 2014 Giant second-harmonic generation efficiency and ideal phase matching with a double e-near-zero cross-slit metamaterial *Phys. Rev.* B **89** 235401

[35] Almeida E, Shalem G and Prior Y 2016 Subwavelength nonlinear phase control and anomalous phase matching in plasmonic metasurfaces *Nat. Commun.* **7** 10367

[36] Li G, Zhang S and Zentgraf T 2017 Nonlinear photonic metasurfaces *Nat. Rev. Mater.* **2** 17010

[37] Qin F , Ding L, Zhang L, Monticone F, Chum C C, Deng J, Mei S, Li Y, Teng J, Hong M, Zhang S, Alu A and Qiu C W 2016 Hybrid bilayer plasmonic metasurface efficiently manipulates visible light *Sci. Adv.* **2** e1501168

[38] Zhao Y and Alu A 2011 Manipulating light polarization with ultrathin plasmonic metasurfaces *Phys. Rev.* B **84** 205428

[39] Yang Y, Kravchenko I I, Briggs D P and Valentine J 2014 All-dielectric metasurface analogue of electromagnetically induced transparency *Nat. Commun.* **5** 5753

[40] Sautter J, Staude I, Decker M, Rusak E, Neshev D N, Brener I and Kivshar Y S 2015 Active tuning of all-dielectric metasurfaces *ACS Nano* **9** 4308-4315

[41] Khurgin J B 2015 How to deal with the loss in plasmonics and metamaterials *Nat. Nanotechnol.* **10** 2

[42] Naik G V, Kim J and Boltasseva A 2011 Oxides and nitrides as alternative plasmonic materials in the optical range *Opt. Mater. Express* **1** 1090-1099

[43] Tanaka K, Plum E, Ou J Y, Uchino T and Zheludev N I 2010 Multifold enhancement of quantum dot luminescence in plasmonic metamaterials *Phys. Rev. Lett.* **105** 227403

[44] Koppens F H, Chang D E and Garcia de Abajo F J 2011 Graphene plasmonics: a platform for strong light–matter interactions *Nano Lett.* **11** 3370-3377

[45] Lee S H , Choi M, Kim T T, Lee S, Liu M, Yin X, Choi H K, Lee S S, Choi C G, Choi S Y, Zhang X and Min B 2012 Switching terahertz waves with gate-controlled active graphene metamaterials *Nat. Mater.* **11** 936

[46] Li Z, Yao K, Xia F, Shen S, Tian J and Liu Y 2015 Graphene plasmonic metasurfaces to steer infrared light *Sci. Rep.* **5** 12423

[47] Heinz T F 1991 Second-order nonlinear optical effects at surfaces and interfaces *Nonlinear Surface Electromagnetic Phenomena* ed H E Ponath and G I Stegeman (Amsterdam: Elsevier) p 353

[48] Panoiu N C, Sha W E I, Lei D Y and Li G C 2018 Nonlinear optics in plasmonic nanostructures *J. Opt.* **20** 083001

[49] Ren Q, You J W and Panoiu N C 2018 Giant enhancement of the effective Raman susceptibility in metasurfaces made of silicon photonic crystal nanocavities *Opt. Express* **26** 30383-30392

[50] Goncalves P A D and and Peres N M 2016 *An introduction to graphene plasmonics* (World Scientific, Singapore)

[51] Yang X and Wong C W 2005 Design of photonic band gap nanocavities for stimulated Raman amplification and lasing in monolithic silicon *Opt. Express* **13** 4723-4730

[52] Temple P A and Hathaway C E 1973 Multiphonon Raman spectrum of silicon *Phys. Rev.* B **7** 3685

[53] BandSOLVE$^{\mathrm{TM}}$, https://www.synopsys.com

[54] Ren Q, You J W and Panoiu N C 2019 Large enhancement of the effective second-order nonlinearity in graphene metasurfaces *Phys. Rev.* B **99** 205404

[55] Cox J D, Silveiro I and Garcia de Abajo F J 2016 Design of photonic band gap nanocavities for stimulated Raman amplification and lasing in monolithic silicon *ACS Nano* **10** 1995-2003

[56] Jalali B and Fathpour S 2006 Silicon photonics *J. Lightwave Technol.* **24** 4600-4615

[57] Krause D, Teplin C W and Rogers C T 2004 Optical surface second harmonic measurements of isotropic thin-film metals: Gold, silver, copper, aluminum, and tantalum *J. Appl. Phys.* **96** 3626-3634

[58] Falasconi M, Andreani L C, Malvezzi A M, Patrini M, Mulloni V and Pavesi L 2001 Bulk and surface contributions to second-order susceptibility in crystalline and porous silicon by second-harmonic generation *Surf. Sci.* **481** 105-112

[59] Osgood R M, Panoiu N C, Dadap J I, Liu X, Chen X, Hsieh I-W, Dulkeith E, Green W M J and Vlasov Y A 2009 Engineering nonlinearities in nanoscale optical systems: physics and applications in dispersion-engineered silicon nanophotonic wires *Adv. Opt. Photon.* **1** 162-235

Chapter 6

Light transport in two-mode Raman quantum waveguides made of coupled photonic crystal nanocavities

6.1 Introduction

Quantum optics [1] has completely changed our classical view of light and contributed to the development of powerful new technologies [2, 3, 4, 5, 6, 7]. In recent years, it has played an essential part in the emerging science of nanophotonics and quantum information. As photons are the carriers of information, quantum manipulation of photons is at the heart of quantum communication and quantum information processing [8, 9, 10, 11, 12, 13, 14]. In particular, new approaches for controlling the propagation of photons at a quantum level have been developed over the past decade [15, 16, 17, 18, 19, 20]. Among them, photonic nanocavities are the focus of much interest because of their ability to confine light at deep-subwavelength scale [21, 22, 23, 24].

Photonic crystal (PhC) nanocavities, which in our case are implemented in a PhC slab waveguide by introducing structural defects, have attracted much attention because they can facilitate strong light-matter interactions [25, 26, 27, 28]. In addition, they can have extremely high quality (Q) factor, ranging from tens of thousands to millions, together with ultrasmall volume. This is particularly favorable to optical devices, contributing to excellent sensitivity, low operating power, and enhancement of the strength of nonlinear process [29, 30]. Since such photonic nanocavities confine light in the spatial domain and filter it in the frequency space, they are instrumental in manipulating photons for different practical applications. Thus, it is well known that the photons propagating in free space do not mix, making them efficient carriers for quantum information communications over long distances. Photonic nanocavities are key photonic devices, which boost nonlinear optical processes and enable the interaction among photons [31, 32, 33, 34, 35, 36]. Many nonlinear optical processes are available for different information-processing purposes, including sum- and difference-frequency generation, second-harmonic generation, four-wave mixing, and Raman amplification [37, 38, 39, 40, 41, 42, 43, 44, 45].

In this chapter, we design a PhC nanocavity that facilitates enhanced stimulated Raman scattering (SRS), namely, in this process a photon with the frequency ω_p emits another photon with ω_S and a phonon inside the PhC nanocavity. Then we consider a chain of such coupled PhC nanocavities, namely a so-called quantum waveguide, and explore the photon propagation through the waveguide when the input nanocavity is optically pumped. The cavities have large Q-factors, especially at the Stokes frequency, which leads to particularly strong Raman interaction between the cavity modes. In addition, because of the strong optical coupling between the cavities, the group velocities of the propagating modes can be slowed down greatly, to less than 10^{-6} of the speed of light. The influence of the slow-light effects on the photon dynamics in the waveguide are also investigated.

The chapter is organized as follows. In the next section, we present the approach used to design the PhC nanocavities, the aim being to optimize the cavity configuration so as to maximize the SRS interaction between the cavity modes. Then, in Sec. 6.3, the coupling constants with different spacings between nanocavities are calculated. In Sec. 6.4, we construct the Hamiltonian describing the photon dynamics in a quantum waveguide consisting of optically coupled PhC nanocavities and derive the corresponding equations of motions for the photon numbers characterizing each cavity and solve the equations that describe their quantum dynamics.

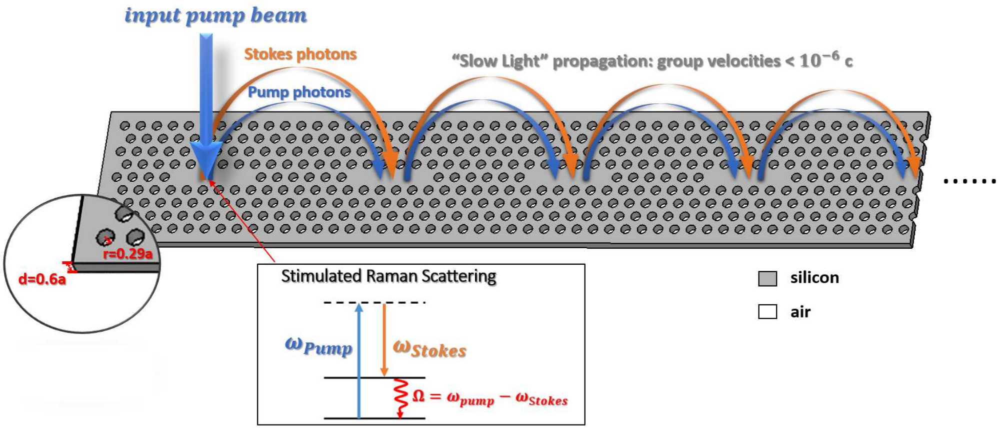

Figure 6.1: Schematic depiction of the photonic structure investigated in this work. It represents a quantum waveguide made of coupled PhC nanocavities. ω_p and ω_s indicate the pump and signal (Stokes) frequencies, respectively, Ω is the frequency of phonons, d the thickness of the slab waveguide, r the radius of air holes, and a the lattice constant. The schematics of the energy levels involved in the stimulated Raman scattering is also shown.

In Sec. 6.5 we present the main results regarding the physical properties of our quantum waveguides, and discuss the implications of these results to practical applications. The main conclusions of our study, together with some perspectives on future possible developments of our ideas, are presented in the last section.

6.2 Design of Photonic Crystal Nanocavities

In this section, we present the approach we used to design a PhC nanocavity with two defect modes at a pump and Raman frequency of silicon, and calculate the corresponding quality factors, resonance frequencies, lattice constant, and other system parameters.

The basic structure considered in this study is a PhC slab waveguide which contains a series of PhC optical nanocavities. The PhC slab waveguide consists of a two-dimensional (2D) hexagonal array of cylinders in a homogeneous dielectric background material. If the refractive index contrast between the cylinders and background is sufficiently large, a photonic bandgap will be formed. In our analysis we assume that the slab is made of silicon, as this photonic material has large Raman susceptibility together with other favorable linear and nonlinear optical properties.

A PhC optical nanocavity can be created in a PhC slab waveguide by perturbing the crystal around a lattice site. The resulting optical nanocavity confines light at certain resonance frequencies. As shown in the zoomed region in Fig. 6.1, our designed PhC cavity has air holes with the radius of $0.29a$ and the thickness of $0.6a$. The cavity is formed by filling five linearly aligned air holes, which is also termed as *L*5 cavity. The main guiding principle in designing the optical cavity is that it has two optical modes separated by the Raman frequency of silicon.

The photonic band structure of the PhC slab waveguide was calculated with BandSOLVE [46, 47, 48], a commercially available software, the results being shown in Fig. 6.2. The shadowed region represents the first bandgap of the PhC slab waveguide, and indicates the range of frequency where the light cannot propagate through the structure. Next, we set up the *L*5 optical cavity and compute its optical modes, indicated by flat lines (colored in blue and orange) located inside the band gap. The two plots on the right of Fig. 6.2 are the corresponding electric field profile of the pump and Stokes modes, respectively. Moreover, using MEEP [49], a computational tool based on the FDTD method, we calculate the corresponding Q-factors and resonance frequencies of the optical cavity modes. These calculations were performed for different values of the shift, S_l, of the end air holes of the cav-

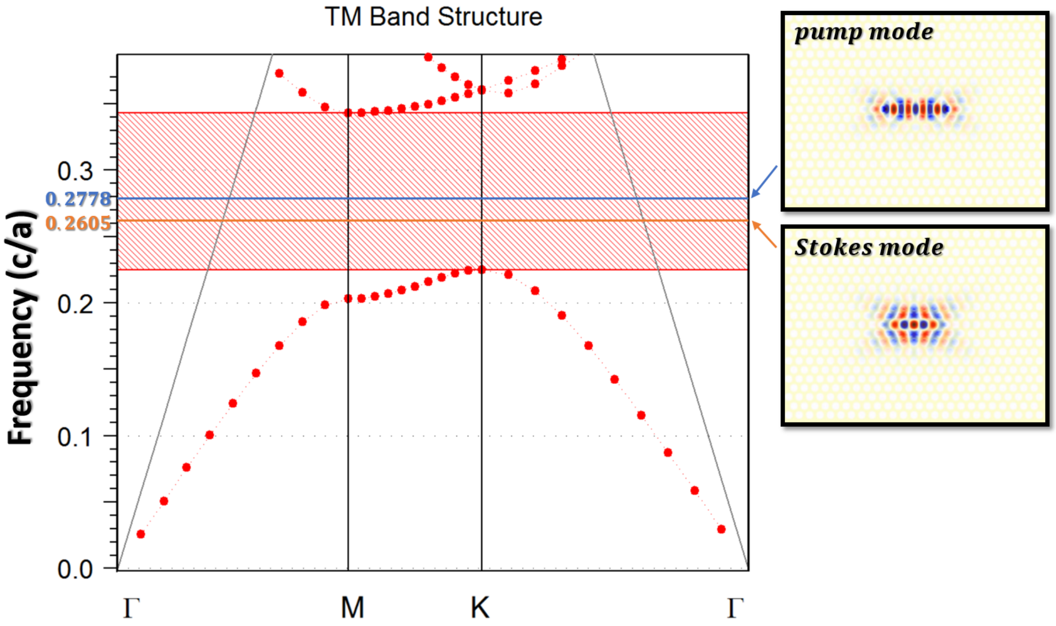

Figure 6.2: Band structure of the photonic crystal and the spatial profiles of the optical modes of the PhC nanocavity.

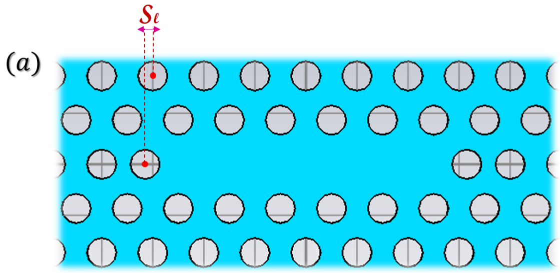

(b)

$S_l\ (x\ a)$	$a\ (nm)$	$f_{pump}(THz)$	$\lambda_{pump}(nm)$	Q_{pump}	$f_{Stokes}(THz)$	$\lambda_{Stokes}(nm)$	Q_{Stokes}
0	450	194.47	1542.68	591	178.87	1677.23	30115
0.05	410	211.83	1416.23	753	196.24	1528.71	38830
0.07	404	214.68	1397.44	790	199.08	1506.9	42899
0.10	373	231.15	1297.84	1043	215.55	1391.79	57296
0.15	333	250.27	1198.7	1804	234.68	1278.31	111693

Figure 6.3: Quality factor, Q, lattice constants a and resonance frequencies f (wavelength λ) with different shifts of air holes S_l.

ity, as shown in Fig. 6.3(a). Note that by varying S_l, the Q-factors can be increased significantly.

Following this procedure, we designed a PhC nanocavity that has pump and Stokes modes separated by the frequency of optical phonons in crystalline silicon, namely $f_p - f_s = \Omega = 15.6$ THz. The resonance frequencies (wavelengths) can be tuned by adjusting the value of S_l and other parameters of the PhC. Note that two conditions must be fulfilled in order to determine the resonance wavelengths, λ_p and λ_s, and lattice constant, a: *i*) the lattice constant depends on the resonance frequencies as $c(f_p - f_s)/a = \Omega$; *ii*) the resonance wavelength $\lambda_p = a/f_p$, $\lambda_s = a/f_s$. The above procedure can also be used to design nanocavities for anti-Stokes cavity-enhancement; however, the anti-Stokes process generally presents much weaker Raman scattering.

As can be seen in Fig. 6.3(b), in which we summarize the results of these calculations, when the shift S_l of the two air holes at cavity edge increases, the lattice constant and resonance wavelengths of the optical modes decreases. The Q-factors of the pump and signal modes, Q_p and Q_s, respectively, also increase because the field profile in the nanocavity overlaps less with the radiative modes of the PhC slab waveguide. In addition, Q_s is significantly larger than Q_p (there is much lower power leakage for the Stokes mode). Considering the current state-of-

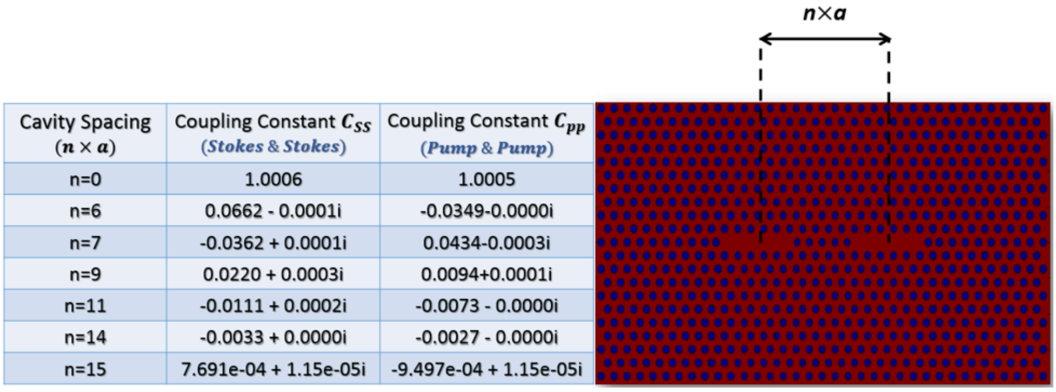

Cavity Spacing $(n \times a)$	Coupling Constant C_{ss} $(Stokes \,\&\, Stokes)$	Coupling Constant C_{pp} $(Pump \,\&\, Pump)$
n=0	1.0006	1.0005
n=6	0.0662 - 0.0001i	-0.0349-0.0000i
n=7	-0.0362 + 0.0001i	0.0434-0.0003i
n=9	0.0220 + 0.0003i	0.0094+0.0001i
n=11	-0.0111 + 0.0002i	-0.0073 - 0.0000i
n=14	-0.0033 + 0.0000i	-0.0027 - 0.0000i
n=15	7.691e-04 + 1.15e-05i	-9.497e-04 + 1.15e-05i

Figure 6.4: Coupling constant between two *L*5 PhC cavities, determined for different values of the cavity separation distance.

the-art in nanofabrication of photonic structures [50, 51, 52], the *Q*-factors used in our calculation can be readily realized experimentally.

6.3 Coupling between Nanocavities

In this section, we calculate the coupling constant between PhC optical cavities, which is a key parameter defining the system Hamiltonian. The coupling constant between two cavities is a physical quantity that measures the strength of the interaction between the optical fields in the cavities, and can be expressed in terms of the optical modes of cavities as follows:

$$C_{qp} = \frac{1}{4\sqrt{W_q W_p}} \int_V \left[\mu \mathbf{h}_q^* \cdot \mathbf{h}_p + \varepsilon_c^q \mathbf{e}_q^* \cdot \mathbf{e}_p\right] d\mathbf{r}, \tag{6.1}$$

where $\mathbf{h}_{p,q}$ and $\mathbf{e}_{p,q}$ are the magnetic and electric fields, respectively, of the p,qth cavity, μ and ε_c^q are the magnetic permeability and electric permittivity distributions of the photonic system containing a single PhC cavity located at the position of the qth cavity, respectively, and $W_{p,q}$ is the electromagnetic energy of the p,qth cavity. This energy of the optical mode is given by:

$$W_p = \frac{1}{4} \int_V \varepsilon(\mathbf{r},\omega) |\mathbf{e}_p(\mathbf{r},\omega)|^2 + \mu(\mathbf{r},\omega) |\mathbf{h}_p(\mathbf{r},\omega)|^2 d\mathbf{r}. \tag{6.2}$$

Note that in our case the PhC slab waveguide is made of non-magnetic material, so that $\mu(\mathbf{r},\omega) \equiv \mu_0$ is the vacuum permeability.

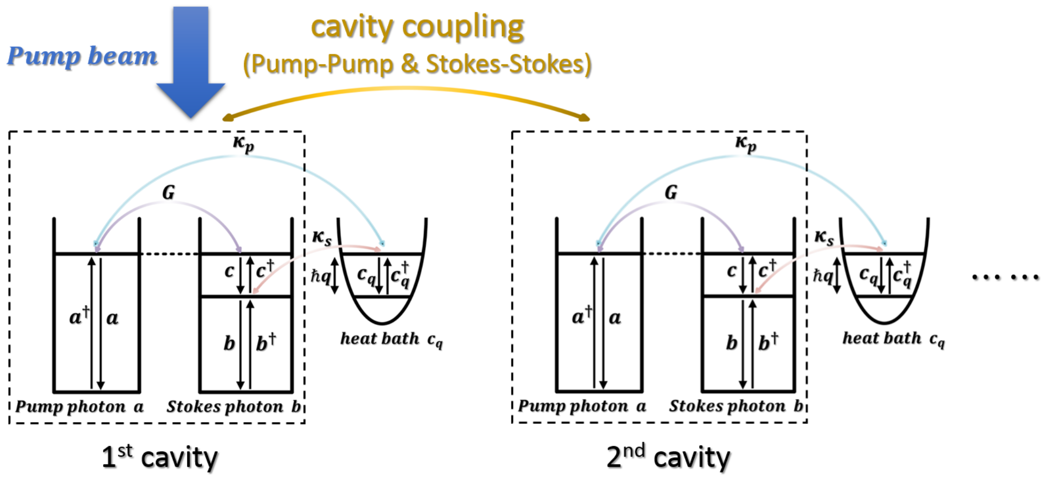

Figure 6.5: Quantum system with coupled cavities. a_i, b_i, and c_i are annihilation operators of pump photon, Stokes photons, and phonons in the ith cavity, respectively, with $a_i^\dagger$, $b_i^\dagger$, and $c_i^\dagger$ being the corresponding creation operators. The strength of the SRS is described by the constant G, ω_q is the frequency of the harmonic oscillators of the heat bath, $\kappa_p = \frac{\omega_p}{Q_p}$ $(\kappa_s = \frac{\omega_s}{Q_s})$ is the damping rate of the optical field with frequency ω_p (ω_s) inside the cavity with quality factor Q_p (Q_s).

In order to calculate the coupling constants and energy of the cavity modes given by (6.1) and (6.2), respectively, we computed first the magnetic and electric fields of the two optical modes of the cavity using MEEP. Subsequently, the overlap integrals in (6.1) and (6.2) were calculated in a computational domain large enough to achieve convergence. These calculations were performed for different values of the separation distance between the optical cavities.

The results of these calculations are summarized in Fig. 6.4. From this figure we can see that, expectedly, when the two cavities completely overlap, the coupling constants are close to unity within the numerical errors. With increasing cavity spacing, $d = na$ where n is an integer, the coupling constant rapidly decreases. This is due to the fact that the optical modes evanescently decay away from the cavity, and therefore the coupling constant decays exponentially with the separation distance. Note that the coupling constant could be positive or negative, but as we will see later on this does not change the photon dynamics in the quantum waveguide.

6.4 Hamiltonian of the Quantum Waveguide

The photon dynamics in the quantum waveguide is determined by the Hamiltonian of the system, so in this section we first construct the corresponding Hamiltonian and subsequently derive the equations of motion describing the photon numbers corresponding to each cavity.

Considering the interactions in the system, the Hamiltonian can be cast in the following form:

$$\begin{aligned} H_0 =& \sum_i \hbar\omega_p a_i^\dagger a_i + \sum_i \hbar\omega_s b_i^\dagger b_i + \sum_i \hbar\Omega \left(c_i^\dagger c_i + \frac{1}{2} \right) \\ &+ \sum_q \hbar\omega_q \left(c_q^\dagger c_q + \frac{1}{2} \right) + \sum_i \Big(\hbar C_{pp} a_i^\dagger a_{i+1} \\ &+ \hbar C_{pp}^* a_{i+1}^\dagger a_i + \hbar C_{ss} b_i^\dagger b_{i+1} + \hbar C_{ss}^* b_{i+1}^\dagger b_i \Big) \\ &+ G \sum_i \left(a_i^\dagger b_i c_i + a_i b_i^\dagger c_i^\dagger \right). \end{aligned} \tag{6.3}$$

The first four terms in the equation above describe the pump and signal photons, the phonons, and the heat bath composed of a continuum of harmonic oscillators, respectively, the fifth term describes the coupling of pump and signal photons located in adjacent optical cavities (due to the exponential decay with the separation distance between cavities of the coupling constant, only nearest-neighbor coupling is considered), and the sixth term describes two processes: a pump photon is destroyed simultaneously with the creation of a Stokes photon and a phonon, and the reverse process in which a Stokes photon and a photon combine to generate a pump photon.

Similar to how the Schrodinger equation describes how pure quantum states evolve in time, the von Neumann equation (also known as Liouville-von Neumann equation) describes how the density operator evolves in time. The von Neumann equation reads:

$$i\hbar \frac{\partial \rho}{\partial t} = [H, \rho] = H\rho - \rho H, \tag{6.4}$$

where the brackets denote a commutator.

Since our model is an open system, we introduce the collapse operator C, which describes the energy leakage from the cavities:

$$C = \sqrt{2\kappa_p}\sum_i^N a_i + \sqrt{2\kappa_s}\sum_i^N b_i. \tag{6.5}$$

Under these conditions, (6.4) can be rewritten in the standard Lindblad form:

$$\frac{\partial \rho}{\partial t} = -\frac{i}{\hbar}(H\rho - \rho H) + C\rho C^\dagger - \frac{1}{2}C^\dagger C\rho - \frac{1}{2}\rho C^\dagger C. \tag{6.6}$$

Given the density operator ρ, finding the expectation value of the number operator$N = a^\dagger a$ reduces to the calculation of the following trace:

$$\langle N\rangle = \mathbf{Tr}(\rho N). \tag{6.7}$$

Thus, for example, if we want to determine the expected pump photon number in the *i*th cavity, we will have (here we put a hat on the operators below to differentiate them from their expected values)

$$\begin{aligned}\frac{\partial \rho_{ii}^{aa}}{\partial t} =& \mathbf{Tr}\frac{\partial \widehat{\rho}^{aa}}{\partial t}\cdot \widehat{N}_{ii}^{aa}\\ =& \mathbf{Tr}\left(-\frac{i}{\hbar}(\widehat{H}\widehat{\rho}^{aa} - \widehat{\rho}^{aa}\widehat{H}) + \widehat{C}\widehat{\rho}^{aa}\widehat{C}^\dagger - \frac{1}{2}\widehat{C}^\dagger\widehat{C}\widehat{\rho}^{aa} - \frac{1}{2}\widehat{\rho}^{aa}\widehat{C}^\dagger\widehat{C}\right)\cdot \widehat{N}_{ii}^{aa}\\ =& -\frac{i}{\hbar}\left(\mathbf{Tr}\widehat{H}\widehat{\rho}^{aa}\widehat{N}_{ii}^{aa} - \mathbf{Tr}\widehat{\rho}^{aa}\widehat{H}\widehat{N}_{ii}^{aa}\right) + \mathbf{Tr}\widehat{C}\widehat{\rho}^{aa}\widehat{C}^\dagger\widehat{N}_{ii}^{aa} - \frac{1}{2}\mathbf{Tr}\widehat{C}^\dagger\widehat{C}\widehat{\rho}^{aa}\widehat{N}_{ii}^{aa}\\ &-\frac{1}{2}\mathbf{Tr}\widehat{\rho}^{aa}\widehat{C}^\dagger\widehat{C}\widehat{N}_{ii}^{aa}\end{aligned} \tag{6.8}$$

Applying the invariant cyclic permutations of the trace operation, we can cast the equation above in the following form:

$$\begin{aligned}\frac{\partial \rho_{ii}^{aa}}{\partial t} =& -\frac{i}{\hbar}\left(\mathbf{Tr}\widehat{\rho}^{aa}\widehat{N}_{ii}^{aa}\widehat{H} - \mathbf{Tr}\widehat{\rho}^{aa}\widehat{H}\widehat{N}_{ii}^{aa}\right) + \mathbf{Tr}\widehat{\rho}^{aa}\widehat{C}^\dagger\widehat{C}\widehat{N}_{ii}^{aa} - \frac{1}{2}\mathbf{Tr}\widehat{\rho}^{aa}\widehat{N}_{ii}^{aa}\widehat{C}^\dagger\widehat{C}\\ &-\frac{1}{2}\mathbf{Tr}\widehat{\rho}^{aa}\widehat{C}^\dagger\widehat{C}\widehat{N}_{ii}^{aa}\\ =& -\frac{i}{\hbar}\left(\langle\widehat{N}_{ii}^{aa}\widehat{H}\rangle - \langle\widehat{H}\widehat{N}_{ii}^{aa}\rangle\right) + \langle\widehat{C}^\dagger\widehat{C}\widehat{N}_{ii}^{aa}\rangle - \frac{1}{2}\langle\widehat{N}_{ii}^{aa}\widehat{C}^\dagger\widehat{C}\rangle - \frac{1}{2}\langle\widehat{C}^\dagger\widehat{C}\widehat{N}_{ii}^{aa}\rangle\end{aligned} \tag{6.9}$$

Applying a similar analysis for the density matrix ρ_{ij} for the pump and Stokes modes, we can obtain the equations describing their dynamics:

$$\dot{\rho}_{ij}^{aa} = -\frac{i}{\hbar}\left[\hbar C_{pp}(\rho^{aa}_{i,j+1} - \rho^{aa}_{i-1,j}) + \hbar C^*_{pp}(\rho^{aa}_{i,j-1} - \rho^{aa}_{i+1,j}) + G(a_i^\dagger b_j c - a_j b_i^\dagger c^\dagger)\right] - 2\kappa_p \rho^{aa}_{ij} \tag{6.10}$$

$$\dot{\rho}_{ij}^{bb} = -\frac{i}{\hbar}\left[\hbar C_{ss}(\rho^{bb}_{i,j+1} - \rho^{bb}_{i-1,j}) + \hbar C^*_{ss}(\rho^{bb}_{i,j-1} - \rho^{bb}_{i+1,j}) + G(-a_i^\dagger b_j c + a_j b_i^\dagger c^\dagger)\right] - 2\kappa_s \rho^{bb}_{ij} \tag{6.11}$$

Moreover, since the equation of motion for ρ_{ij} introduces new variables, namely $a_i^\dagger b_j c$, $a_i b_j^\dagger c^\dagger$, and $c^\dagger c$ other than density matrix for the pump and Stokes modes, the equations of motion for these variables must be derived as well. Simple operators manipulations lead to the following expressions:

if $i \neq j$,

$$\begin{aligned}
\frac{\partial\langle a_i^\dagger b_j c\rangle}{\partial t} = & -\frac{i}{\hbar}\{\hbar C_{pp}(-a^\dagger_{i-1} b_j c) + \hbar C^*_{pp}(-a^\dagger_{i+1} b_j c) + \hbar C_{ss}(a_i^\dagger b_{j+1} c) + \hbar C^*_{ss}(a_i^\dagger b_{j-1} c) \\
& + G[\rho^{aa}_{ij}(\rho^{bb}_{jj} + \rho_{cc} + 1) - \rho^{bb}_{ij}(\rho_{cc} - \rho^{aa}_{ii})]\} - (\kappa_p + \kappa_s) a_i^\dagger b_j c \quad (6.12) \\
\frac{\partial\langle a_i b_j^\dagger c^\dagger\rangle}{\partial t} = & -\frac{i}{\hbar}\{\hbar C_{pp}(a_{i+1} b_j^\dagger c^\dagger) + \hbar C^*_{pp}(a_{i-1} b_j^\dagger c^\dagger) + \hbar C_{ss}(-a_i b^\dagger_{j-1} c^\dagger) + \hbar C^*_{ss}(-a_i b^\dagger_{j+1} c^\dagger) \\
& + G[\rho^{bb}_{ji}(\rho_{cc} - \rho^{aa}_{ii}) - \rho^{aa}_{ji}(\rho^{bb}_{jj} + \rho_{cc} + 1)]\} - (\kappa_p + \kappa_s) a_i b_j^\dagger c^\dagger \quad (6.13)
\end{aligned}$$

if $i = j$,

$$\begin{aligned}
\frac{\partial\langle a_i^\dagger b_j c\rangle}{\partial t} = & -\frac{i}{\hbar}\{\hbar C_{pp}(-a^\dagger_{i-1} b_j c) + \hbar C^*_{pp}(-a^\dagger_{i+1} b_j c) + \hbar C_{ss}(a_i^\dagger b_{j+1} c) + \hbar C^*_{ss}(a_i^\dagger b_{j-1} c) \\
& + G[\rho^{aa}_{ij}(\rho^{bb}_{jj} + \rho_{cc} + 1) - \rho^{bb}_{ii}\rho_{cc}]\} - (\kappa_p + \kappa_s) a_i^\dagger b_j c \quad (6.14) \\
\frac{\partial\langle a_i b_j^\dagger c^\dagger\rangle}{\partial t} = & -\frac{i}{\hbar}\{\hbar C_{pp}(a_{i+1} b_j^\dagger c^\dagger) + \hbar C^*_{pp}(a_{i-1} b_j^\dagger c^\dagger) + \hbar C_{ss}(-a_i b^\dagger_{j-1} c^\dagger) + \hbar C^*_{ss}(-a_i b^\dagger_{j+1} c^\dagger) \\
& + G[\rho^{bb}_{ii}\rho_{cc} - \rho^{aa}_{ji}(\rho^{bb}_{jj} + \rho_{cc} + 1)]\} - (\kappa_p + \kappa_s) a_i b_j^\dagger c^\dagger \quad (6.15)
\end{aligned}$$

Finally, the equation of motion for phonons is:

$$\dot{\rho}^i_{cc} = G \sum_i^N \left(-a_i^\dagger b_i c_i + a_i b_i^\dagger c_i^\dagger\right). \tag{6.16}$$

6.5 Results and Discussion

Once we obtained the general expressions for the dynamics of density matrix of pump photons, Stokes photons and phonons, as well as the dynamics for the operators $a_i^\dagger b_j c$ and $a_i b_j^\dagger c^\dagger$, we can determine the time evolution for the photon numbers of the two cavity modes simply integrating the corresponding system of ordinary differential equations.

Let us first consider a waveguide formed of $N = 8$ cavities, and characterized by a transfer coefficient, $G = 0.05$ and incident pump rate $I = 0.05$. The initial condition is $\rho_{11}^{aa} = 1$ (one pump-mode photon in the first cavity), other ρ_{ii} for pump and Stokes modes being set to zero for all the other cavities. Also, we normalized the photon resonant frequency ω, coupling constant C, and the damping rate κ so that we could get generally applicable results and not conclusions valid exclusively for silicon. The physical quantity used in the normalization process is the pump frequency, ω_p.

The time evolution of the number of photons in the pump and Stokes modes, in cavities 1, 4, and 7, is presented in Fig. 6.6. As suggested by this figure, the photons propagate from the first to the last cavity in the waveguide due to the fact that the cavities are optically coupled. Moreover, due to the Raman scattering, photons can transfer from the pump to the Stokes mode while generating a phonon in the cavity. With increasing time, the photon numbers in each cavity asymptotically reach a steady state, when no longer depend on time. In this steady state, there is a balance between the energy transferred to the system by the pump beam and the energy lost via damping. The incident pump beam at the first cavity ensures there is an energy flow in the waveguide, as in the absence of this pump beam the photon numbers in each cavity would eventually decay to zero.

To enhance the amount of photons in each cavity of the quantum waveguide, we only need to increase the input pump rate at the first cavity. This process leads to an increase of the photon flux and in turn in each cavity increases the intensity of the pump and Stokes modes. These ideas are validated by our calculations of the photon numbers in the steady state, determined for different values of the input pump rate.

The results of these calculations are presented in Fig. 6.7, and correspond to the seventh cavity. From this figure it can be clearly observed that the steady state photon numbers in the seventh cavity increase practically linearly with the input power rate in the first cavity. It should be noted that this conclusion remains valid for each cavity in the waveguide. In addition, the difference in photon numbers between the pump and Stokes mode increases when the input pump rate increases,

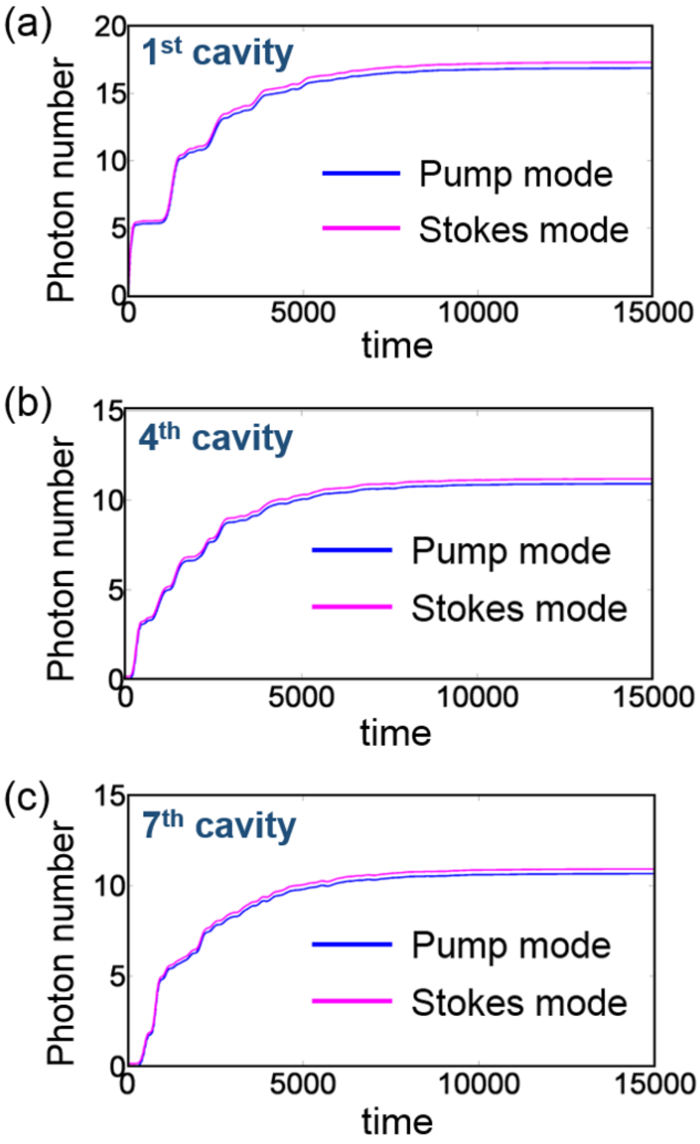

Figure 6.6: Time evolution of pump and Stokes photon numbers at cavity 1, 4, and 7 in a waveguide consisting $N = 8$ cavities. The mode interaction coefficient $G = 0.05$ and incident pump rate $I = 0.05$. Initially, there is one pump-mode photon in the first cavity. Quality factors are $Q_p = 1804$ and $Q_s = 111693$.

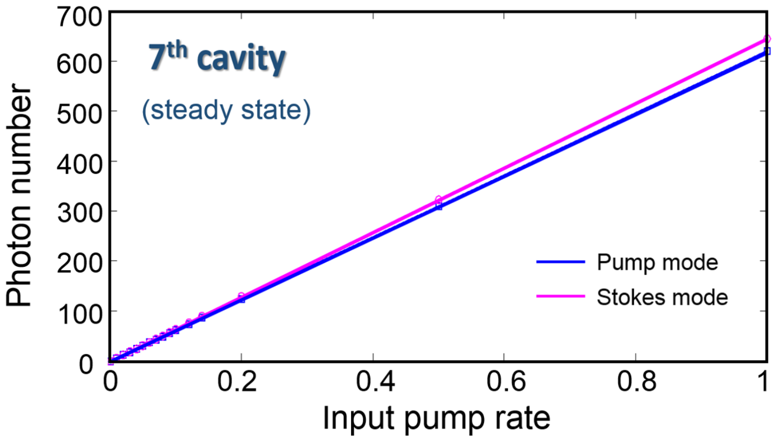

Figure 6.7: Dependence of steady state photon numbers in the seventh cavity on the input pump rate. The waveguide parameters are the same as those in Fig. 6.6.

that is, the number of Stokes photons is larger than the number of pump photons by a quantity that increases with the input pump rate.

In addition to the input pump rate, there are other relevant physical quantities that affect the steady state photon numbers in each cavity in the waveguide, e.g. quality factors, coupling constants, and mode transfer coefficient. In what follows, we will discuss the dependence of the steady state photon numbers on these physical quantities, in the case when the input pump rate at the first cavity is 0.1.

Our quantum waveguide is an open quantum system, which means that it transfers energy to the outside environment, leading to energy damping. The system energy could be prevented from decreasing too quickly by either inputting energy into the system, as described above, or by decreasing the damping rate of the system. This latter approach can be achieved by increasing the quality factors of the nanocavities in the quantum waveguide.

We investigate this effect by first fixing the quality factor of Stokes mode, and then increase the quality factor of the pump mode so as to analyse the dependence of steady state photon numbers on the quality factor of the pump mode. The results, presented in Fig. 6.8(a), demonstrate that when Q_p increases from 1,000 to 20,000, the steady state photon numbers increase linearly. As Q_p further increases from 20,000 to 40,000, the rates at which the photon numbers increase are becoming smaller. Additionally, the dependence of steady state photon numbers on Q_s is

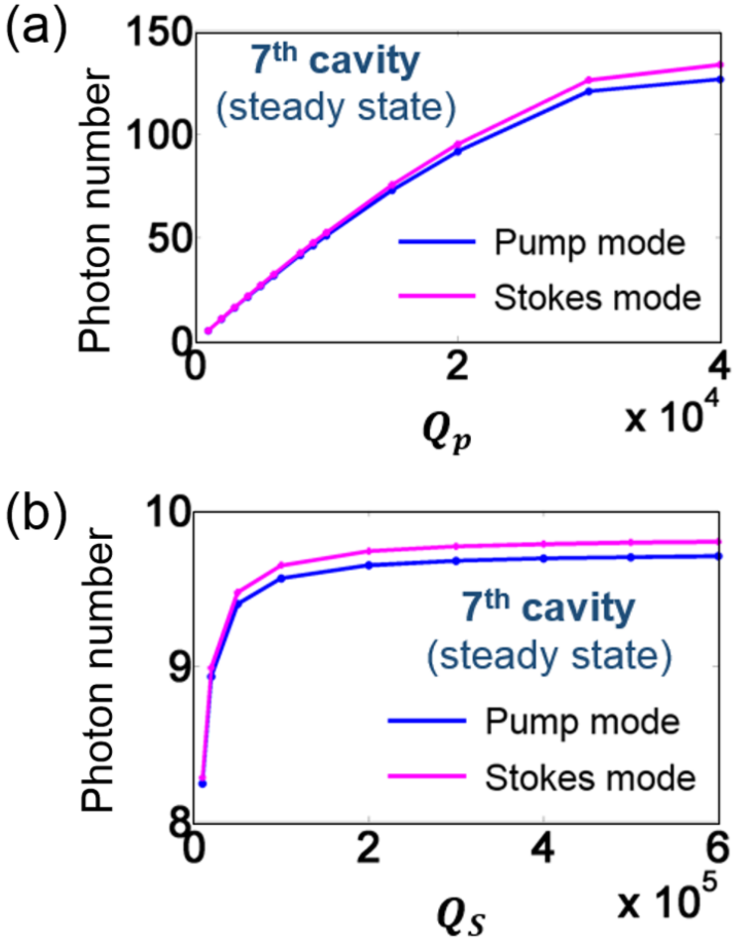

Figure 6.8: (a) Dependence of steady state photon numbers in the seventh cavity on the quality factor Q_p when $Q_s = 111,693$. (b) Dependence of steady state photon numbers in the seventh cavity on the quality factor Q_s when $Q_p = 1,804$.

presented in Fig. 6.8(b). The steady state photon numbers increase sharply when Q_s varies from 10,000 to 50,000, and after Q_s reaches 200,000, the photon numbers reach a plateau. From these results, it is concluded that there is a significant positive correlation between the steady state photon numbers and the quality factors when the Q-factors have relatively small values. After the Q-factors increases beyond certain values, the dependence of the steady state photon numbers on Q becomes rather weak.

A common approach of improving the quality factor is to increase the size of the nanocavity so that the electromagnetic field profile in the Fourier space is formed primarily of plane waves whose wave vector lies outside the light cone. This reason

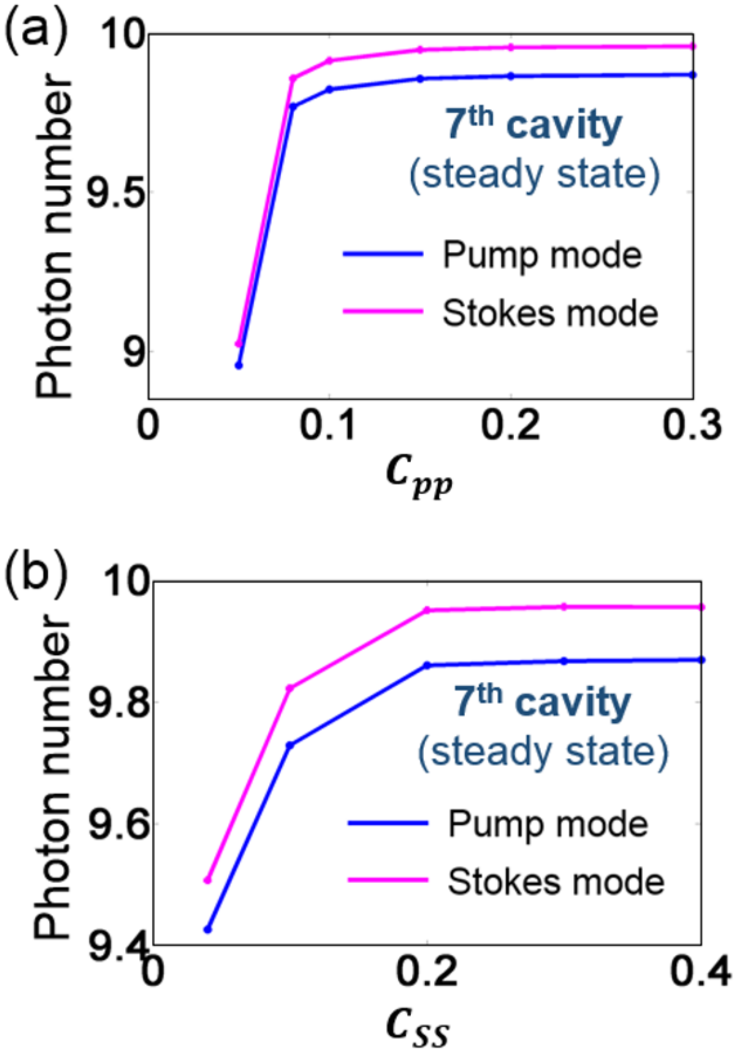

Figure 6.9: (a) Dependence of the steady state photon numbers in the seventh cavity on the coupling constant C_{pp} when $C_{ss} = 0.0662 - 0.0001i$. (b) Dependence of steady state photon numbers in the seventh cavity on the coupling constants C_{ss} when $C_{pp} = -0.0349$.

is behind the cavity tuning described in Sec. 6.2, where the shift of the air holes at the two ends of the cavity is fine-tuned so as to increase the size of the photonic crystal nanocavity, and also the Q-factor of the cavity.

As photons propagate through the waveguide due to the cavity optical coupling, a larger value of the coupling constant will lead to an increase in the photon flux in the waveguide. In order to validate this idea, we varied the coupling constants for the pump and Stokes modes separately so as to ascertain the corresponding de-

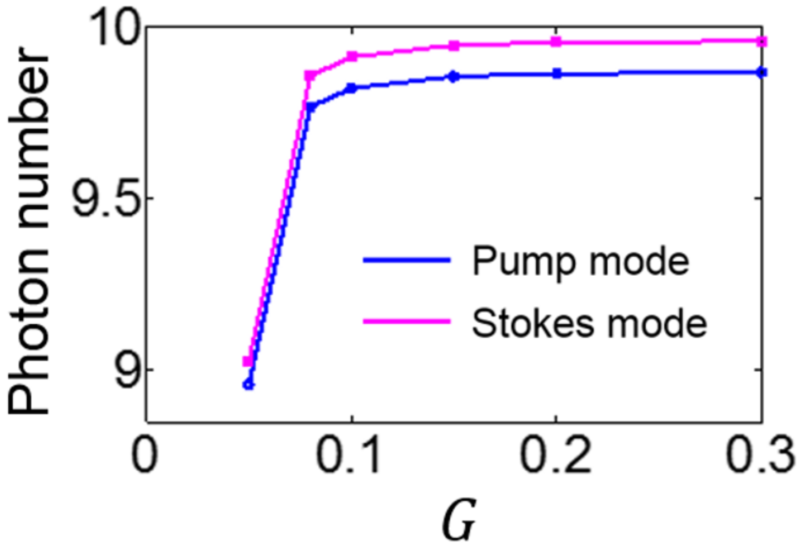

Figure 6.10: Dependence of steady state photon numbers in the seventh cavity on the mode transfer coefficient G.

pendence of the steady state photon numbers at the end of the waveguide on the coupling constants C_{pp} and C_{ss}. The results of these calculations are summarized in Fig. 6.9.

It can be clearly observed from Fig. 6.9(a) that the steady state photon numbers initially increase steeply when the coupling constant between the pump modes, C_{pp}, varies from 0.05 to 0.1, and then remains almost constant when C_{pp} further increases. Similarly, as shown in Fig. 6.9(b), the steady state photon numbers increase rapidly when C_{ss} rises up to 0.2. In practice, if one requires long propagation distance in the waveguide, the separation distance between the cavities should be as large as possible. On the other hand, the smaller the coupling constant, the smaller the photon number in the steady state, so that an optimum cavity separation distance between the cavities exists.

In addition to the Q-factor and coupling constant, which facilitate the photon propagation along the quantum waveguide, the mode transfer coefficient G also influences the photon transport along the quantum waveguide. Figure 6.10 illustrates the dependence of steady state photon numbers in the seventh cavity on the mode transfer coefficient. In the steady state, the pump mode photon number is larger than the Stokes mode photon for all values of G. This result indicates that the larger

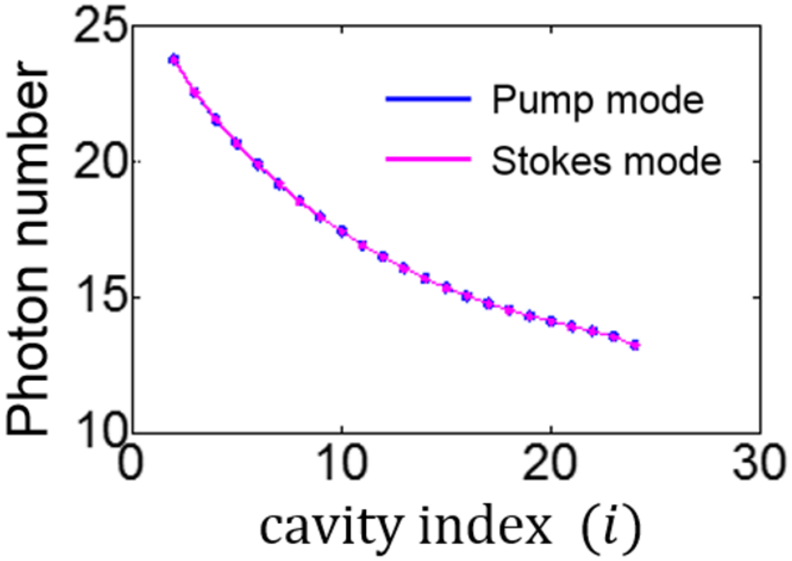

Figure 6.11: Dependence of steady state photon numbers on the cavity index i.

mode transfer coefficient boosts the transfer process from pump photons to Stokes photons, which improves the efficiency of the Raman amplification.

In the simulations discussed above, the number of cavities in the quantum waveguide was set to $N = 8$. In order to investigate the dependence of the physical properties of the quantum waveguide on its length we varied the number of optical cavities in the waveguide. To this end, we considered a quantum waveguide made of $N = 25$ optical cavities and simulate the light propagation through this waveguide. In this case, the input pump rate at the first cavity is 0.5, the quality factors of the pump and Stokes modes are $Q_p = 1,804$ and $Q_c = 111,693$, respectively, the coupling constant for pump mode and Stokes mode are 0.062 and 0.0349, respectively, and the mode transfer coefficient $G = 0.05$. The results of these calculations are presented in Fig. 6.11. It can be easily inferred from the data plotted in this figure the the steady state photon numbers decay exponentially with the cavity index, which suggests that, as expected, the waveguide losses are of a linear nature.

6.6 Conclusion

In conclusion, in this chapter we presented a quantum theoretical model describing photon propagation along a photonic nanocavity waveguide characterized by the quality factors of the cavity modes, coupling constants between the optical modes of the cavities, and the Raman scattering mode transfer coefficient. Our analysis started with the construction of the Hamiltonian describing the photon dynamics in the quantum waveguide. There are many factors that need to be considered: the photon energy of the two optical modes, inter-cavity coupling, phonon energy, mode transfer process, and the coupling between the quantum system and a heat bath. Another significant step in our research was to derive the density operator expression of photon numbers, so that we can calculate the time evolution of photon numbers as well as the steady state photon numbers as the two most relevant physical quantities.

This research work also provides a valuable reference for practical applications in quantum interconnects and quantum information processing, which aims at guiding light in nanostructures at a quantum level. Dependence results of steady state photon numbers on the input pump rate give the theoretical values of output in the open system with different input powers, which is beneficial for the understanding of the characteristics of light propagation and amplification in such quantum waveguides. Moreover, since our study is performed in a rather general case, where the parameters of silicon have been normalized, our findings can be applied to other waveguide structures, including waveguides made of other dielectric materials or waveguide made of coupled graphene nanoflakes.

Bibliography

[1] I. A. Walmsley, Science **348**, 525 (2015).

[2] W. W. Chow, S. W. Koch and M. I. Sargent, *Semiconductor-laser physics* (Springer Science and Business Media, 2012).

[3] P. R. Berman and V. S. Malinovsky, *Principles of laser spectroscopy and quantum optics* (Princeton University Press 2010).

[4] L. J. Radziemski and D. A. Cremers, *Laser-induced plasmas and applications* (1989).

[5] D. Meschede, *Optics, light and lasers: the practical approach to modern aspects of photonics and laser physics* (John Wiley and Sons, 2017).

[6] M. Bahl, N. C. Panoiu and R. M. Osgood, J. Opt. Soc. Am. B **26**, 1558 (2009).

[7] M. Bahl, N. C. Panoiu and R. M. Osgood, IEEE J. Quantum Electron. **41**, 1244 (2005).

[8] K. Stannigel, P.Komar, S. J. M. Habraken, S. D. Bennett, M. D. Lukin, P. Zoller and P. Rabl, Phys. Rev. Lett. **109**, 013603 (2012).

[9] A. Peruzzo, M. Lobino, J. C. Matthews, N. Matsuda, A. Politi, K. Poulios and Y. Bromberg, Science **329**, 1500 (2010).

[10] E. Knill, Nature **434**, 39 (2005).

[11] D. Z. Manrique, C. Huang, M. Baghernejad, X. Zhao, O. A. Al-Owaedi, H. Sadeghi and M. R. Bryce, Nat. Commun. **6** (2015).

[12] M. A. Nielsen and I. Chuang, Am. J. Phys. **70**, 558 (2002).

[13] H. K. Lo, T. Spiller and S. Popescu, *Introduction to quantum computation and information* (World Scientific, 1998).

[14] D. Bouwmeester, A. Ekert and A. Zeilinger, *The physics of quantum information* (Springer, Berlin, 2000).

[15] K. Ishizaki and S. Noda, Nature **460**, 367 (2009).

[16] H. Jin, F. M. Liu, P. Xu, J. L. Xia, M. L. Zhong and S. N. Zhu, Phys. Rev. Lett. **113**, 103601 (2014).

[17] J. C. Matthews, A. Politi, A. Stefanov and J. L. O'brien, Nat. Photonics **3**, 346 (2009).

[18] O. M. Maragò, P. H. Jones, P. G. Gucciardi, G. Volpe and A. C. Ferrari, Nat. Nanotechnol. **8**, 807 (2013).

[19] H. T. Chen, J. F. O'Hara, A. K. Azad and A. J. Taylor, Laser and Photonics Reviews **5**, 513 (2011).

[20] P. J. Shadbolt, M. R. Verde, A. Peruzzo, A. Politi, A. Laing, M. Lobino, and J. L. OBrien, Generating, manipulating and measuring entanglement and mixture with a reconfigurable photonic circuit, Nat. Photonics **6**, 45 (2012).

[21] Q. Quan and M. Loncar, Deterministic design of wavelength scale, ultra-high Q photonic crystal nanobeam cavities, Opt. Express **19**, 18529 (2011).

[22] H. Sekoguchi, Y. Takahashi, T. Asano, and S. Noda, Photonic crystal nanocavity with a Q-factor of 9 million, Opt. Express **22**, 916 (2014).

[23] D. A. Fuhrmann, S. M. Thon, H. Kim, D. Bouwmeester, P. M. Petroff, A. Wixforth, and H. J. Krenner, Dynamic modulation of photonic crystal nanocavities using gigahertz acoustic phonons, Nat. Photonics **5**, 605 (2011).

[24] F. Priolo, T. Gregorkiewicz, M. Galli, and T. F. Krauss, Silicon nanostructures for photonics and photovoltaics, Nat. Nanotechnol. **9**, 19 (2014).

[25] S. P. Yu, J. D. Hood, J. A. Muniz, M. J. Martin, R. Norte, C. L. Hung, and H. J. Kimble, Nanowire photonic crystal waveguides for single-atom trapping and strong light-matter interactions, Appl. Phys. Lett. **104**, 111103 (2014).

[26] F. H. Koppens, D. E. Chang, and F. J. Garcia de Abajo, Graphene plasmonics: a platform for strong lightmatter interactions, Nano Lett. **11**, 3370 (2011).

[27] M. Engel, M. Steiner, A. Lombardo, A. C. Ferrari, H. V. Lohneysen, P. Avouris, and R. Krupke, Lightmatter interaction in a microcavity-controlled graphene transistor, Nat. Commun. **3**, 906 (2012).

[28] Y. F. Xiao, Y. C. Liu, B. B. Li, Y. L. Chen, Y. Li, and Q. Gong, Strongly enhanced light-matter interaction in a hybrid photonic-plasmonic resonator, Phys. Rev. A **85**, 031805 (2012).

[29] E. E. Hoover and J. A. Squier, Advances in multiphoton microscopy technology, Nat. Photonics **7**, 93 (2013).

[30] A. Reiserer, S. Ritter, and G. Rempe, Nondestructive detection of an optical photon, Science **342**, 1349 (2013).

[31] C. G. Biris and N. C. Panoiu, Nonlinear pulsed excitation of high-Q optical modes of plasmonic nanocavities, Opt. Express **18**, 17165 (2010).

[32] C. G. Biris and N. C. Panoiu, Excitation of dark plasmonic cavity modes via nonlinearly induced dipoles: applications to near-infrared plasmonic sensing, Nanotechnology **22**, 235502 (2011).

[33] D. E. Chang, V. Vuletic, and M. D. Lukin, Quantum nonlinear opticsphoton by photon, Nat. Photonics **8**, 685 (2014).

[34] T. Peyronel, O. Firstenberg, Q. Y. Liang, S. Hofferberth, A. V. Gorshkov, T. Pohl, and V. Vuletic, Quantum nonlinear optics with single photons enabled by strongly interacting atoms, Nature **488**, 57 (2012).

[35] O. Firstenberg, T. Peyronel, Q. Y. Liang, A. V. Gorshkov, M. D. Lukin, and V. Vuletic, Attractive photons in a quantum nonlinear medium, Nature **502**, 71 (2013).

[36] Q. Guo, J. Bai, L. Y. Cheng, X. Q. Shao, H. F. Wang, and S. Zhang, Simplified optical quantum-information processing via weak cross-Kerr nonlinearities, Phys. Rev. A **83**, 054303 (2011).

[37] K. Nozaki, T. Tanabe, A. Shinya, S. Matsuo, T. Sato, H. Taniyama, and M. Notomi, Sub-femtojoule all-optical switching using a photonic-crystal nanocavity, Nat. Photonics **4**, 477 (2010).

[38] X. Chen, N. C. Panoiu, and R. M. Osgood, Theory of Raman-mediated pulsed amplification in silicon-wire waveguides, IEEE J. Quantum Electron. **42**, 160 (2006).

[39] R. M. Osgood, N. C. Panoiu, J. I. Dadap, X. Liu, X. Chen, I. W. Hsieh, and Y. A. Vlasov, Engineering nonlinearities in nanoscale optical systems: physics and applications in dispersion-engineered silicon nanophotonic wires, Adv. Opt. Photonics **1**, 162 (2009).

[40] S. Lavdas, S. Zhao, J. B. Driscoll, R. R. Grote, R. M. Osgood, and N. C. Panoiu, Wavelength conversion and parametric amplification of optical pulses via quasi-phase-matched four-wave mixing in long-period Bragg silicon waveguides, Opt. Lett. **39**, 4017 (2014).

[41] S. Lavdas and N. C. Panoiu, Theory of pulsed four-wave mixing in one-dimensional silicon photonic crystal slab waveguides, Phys. Rev. B **93**, 115435 (2016).

[42] W. Fan, S. Zhang, N. C. Panoiu, A. Abdenour, S. Krishna, R. M. Osgood, and S. R. J. Brueck, Second harmonic generation from a nanopatterned isotropic nonlinear material, Nano Lett. **6**, 1027 (2006).

[43] J. F. McMillan, X. Yang, N. C. Panoiu, R. M. Osgood, and C. W. Wong, Enhanced stimulated Raman scattering in slow-light photonic crystal waveguides, Opt. Lett. **31**, 1235 (2006).

[44] J. You, and N. C. Panoiu, Exploiting high-order phase-shift keying modulation and direct-detection in silicon photonic systems, Opt. Express **25**, 8611 (2017).

[45] J. W. You, J. You, M.Weismann, and N. C. Panoiu, Double-resonant enhancement of third-harmonic generation in graphene nanostructures, Phil. Trans. R. Soc. A **375**, 20160313 (2017).

[46] D. H. Thurnau, Algorithm 195: BANDSOLVE, Commun. ACM **6**, 441 (1963).

[47] URL: http://www. rsoftdesign. com

[48] URL: http://search.proquest.com/docview/447005181/

[49] A. F. Oskooi, D. Roundy, M. Ibanescu, P. Bermel, J. D. Joannopoulos, and S. G. Johnson, MEEP: A flexible free-software package for electromagnetic simulations by the FDTD method, Comput. Phys. Commun. **181**, 687 (2010).

[50] Y. Akahane, T. Asano, B. S. Song, and S. Noda, High-Q photonic nanocavity in a two-dimensional photonic crystal, Nature **425**, 944 (2003).

[51] P. E. Barclay, K. Srinivasan, and O. Painter, Nonlinear response of silicon photonic crystal microresonators excited via an integrated waveguide and fiber taper, Opt. Express **13**, 801 (2005).

[52] M. Notomi, A. Shinya, S. Mitsugi, G. Kira, E. Kuramochi, and T. Tanabe, Optical bistable switching action of Si high-Q photonic-crystal nanocavities, Opt. Express **13**, 2678 (2005).

Chapter 7

Quantum computational analysis of coupled graphene structures

Graphene is the thinnest known material, which is just a single layer of carbon atoms arranged in a hexagonal lattice. Its behavior follows the laws of quantum physics. Investigating bigger lattices of graphene via the approach described in this chapter may lead to observing where lays the boundary between quantum and classical regimes for these structures.

This chapter will first present a rigorous approach to calculate the energy levels of certain graphene flakes, which accounts for the interactions between all the atoms in the structure rather than the simple nearest-neighbor model. After simulating simple structures with this rigorous approach, more physical systems, such as two coupled disks (two graphene pieces with coupling interaction between them) with different spacings, will be studied in the later section, where we will discuss about the coupling between two graphene structures. Figuring out how the coupled system works is very important for us to further explore the photon propagation along coupled-disks waveguide made of graphene.

7.1 Generation of Graphene Lattice

In order to study the coupling between two graphene disks, we have to determine the Hamiltonian of the system and find their energy levels as well as the wave functions. Thus, in this section, a Matlab code was written so as to generate graphene lattice of the desired dimensions and pattern.

First of all, we develop an algorithm to create a honeycomb lattice of carbon atoms in a plane. Distance between neighboring atoms is always the same, which we set to be 1, therefore all of the coordinates generated will be in units of lattice constant of graphene ($\approx 1.42\AA$). Any point in the honeycomb lattice can be represented as a sum of multiples of two vectors:

$$\widehat{a}_n = [\sqrt{3}/2, 1/2], \quad \widehat{a}_m = [\sqrt{3}/2, -1/2] \tag{7.1}$$

Figure 7.1 below illustrates the method.

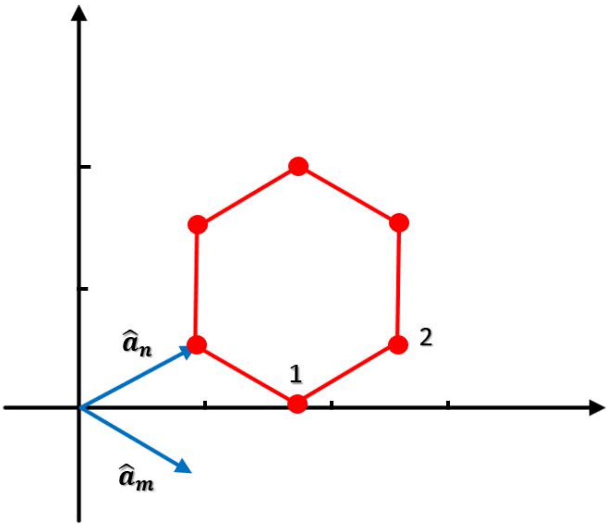

Figure 7.1: The coordinates of carbon atoms in graphene lattice.

In short, the coordinates of a point p can be expressed as $p = n_p\widehat{a}_n + m_p\widehat{a}_m$ where n_p and m_p are integers. For example, as shown in Fig. (7.1), point 1 has coordinates of $\widehat{a}_n + \widehat{a}_m$ i.e.$(\sqrt{3}, 0)$, point 2 is $2\widehat{a}_n + \widehat{a}_m$ i.e.$(\frac{3\sqrt{3}}{2}, 0.5)$ and so on. In this way, the algorithm creates a lattice of desired dimensions by adding rows of points. The default shape of generated structure is therefore a zig-zag ribbon. Armchair ribbon is created by truncating the “pointy ends” and a disk by including only points within a certain radius relevant to chosen size. Finally various shapes of graphene nano-disks can be created using the above method.

The simplest structure is a single hexagonal-shaped ring containing six atoms

- benzene. With larger numbers of atoms other shapes like triangles, ribbons or circular disks can be formed. Figure 7.2 below shows a few examples of such simple structures.

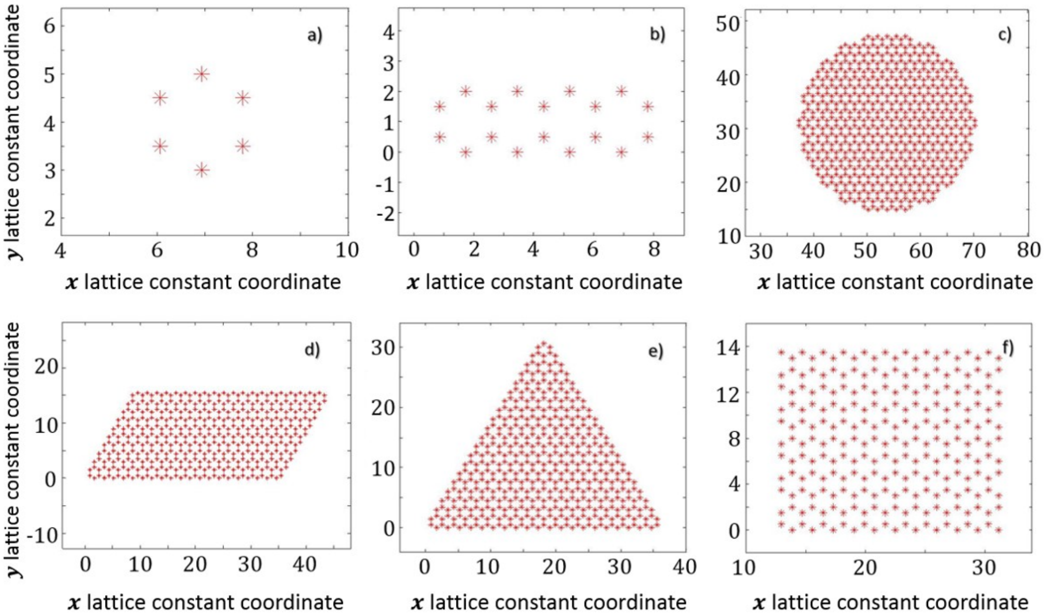

Figure 7.2: Various shapes of graphene lattice: a) single benzene ring, b) simple ribbon consisting of four rings, c) disk, d) zig-zag ribbon, e) triangle, f) armchair ribbon. The coordinates are in units of the lattice constant of graphene ($\approx 1.42\AA$).

7.2 Rigorous Approach to Quantum Mechanical Analysis of Graphene Nanostructures

After the graphene lattice generation was successfully implemented, we can further take the Hamiltonian matrix calculations, where full quantum approach was to be applied, including interactions between all the atoms in the structure. The wavefunction can be expressed as:

$$\Psi = \sum_{q=1}^{N} c_q \Psi_q \tag{7.2}$$

In Eq. (7.2)Ψ_q is the wavefunction at orbital q and c_q is the constant for Ψ_q. Or else, more specifically, Ψ can be represented with using radial and angular spherical wave functions, where the $2pz$ orbital are:

$$\Psi_{2p_z}(\overrightarrow{r}) = R_{2p}(r)Y_{2p_z}(\theta,\varphi) \tag{7.3a}$$

$$R_{2p}(r) = \frac{1}{\sqrt{6}}\frac{Zr}{na_0}\left(\frac{Z}{a_0}\right)^{\frac{3}{2}} e^{-\frac{Zr}{na_0}} \tag{7.3b}$$

$$Y_{2p_z}(\theta,\varphi) = \sqrt{\frac{3}{4\pi}}\cos\theta = \sqrt{\frac{3}{4\pi}}\frac{Z}{r} \tag{7.3c}$$

where Z is the atomic number ($Z = 6$ for carbon), n the orbital number ($n = 2$ in this case) and a_0 the Bohr radius. Eqs. (7.3a)∼(7.3c) above are performed in spherical coordinates. Afterwards, this calculation should convert to cylindrical system since it is better suited for the geometry of the problem. The Hamiltonian matrix elements will be calculated for each pair of atoms and will include interactions with all other atoms in the lattice as well.

$$H = \sum_{i=1}^{N} H_i \tag{7.4}$$

where the Hamiltonian for each atom $H(i)$ is expressed as

$$H(i) = -\frac{\hbar^2}{2m}\nabla^2_{\overrightarrow{r}_i} - \frac{Ze^2}{|\overrightarrow{r}_i - \overrightarrow{r}_{0\alpha}|} \tag{7.5a}$$

$$= -\frac{\hbar^2}{2m}\nabla^2_{\overrightarrow{r}_i} - \frac{Ze^2}{|\overrightarrow{r}_i - \overrightarrow{r}_{0i}|} - \sum_{\alpha\neq i}\frac{Ze^2}{|\overrightarrow{r}_i - \overrightarrow{r}_{0\alpha}|} \tag{7.5b}$$

$$= H_0(i) + V_0(i) \tag{7.5c}$$

where $H_0(i) = -\frac{\hbar^2}{2m}\nabla^2_{\overrightarrow{r}_i} - \frac{Ze^2}{|\overrightarrow{r}_i - \overrightarrow{r}_{0i}|}$ and $V_0(i) = -\sum_{\alpha\neq i}\frac{Ze^2}{|\overrightarrow{r}_i - \overrightarrow{r}_{0\alpha}|}$. The Hamiltonian operator in turn can be expressed as:

$$\widehat{H} = -\frac{\hbar^2}{2m^2}\nabla^2 + V_0 \tag{7.6}$$

The first part of Eq. (7.4) relates to kinetic energy and can be expressed in terms of orbital energy and overlap integral, which defines how much orbital of two atoms coincide. The V_0 term is the potential arising from Coulomb interactions between orbitals of an atom and all the other nuclei in the lattice. For single particle, the time-independent Schrodinger equation is

$$H\Psi(\overrightarrow{r}) = E\Psi(\overrightarrow{r}) \tag{7.7}$$

where E is the energy level of a single particle. Using Eq. (7.2),

$$\sum_{q=1}^{N} c_q H\Psi_q(\overrightarrow{r}) = E\sum_{q=1}^{N} c_q \Psi_q(\overrightarrow{r}) \tag{7.8}$$

multiplying $\int \Psi_s^*(\overrightarrow{r})d\overrightarrow{r}$ on both sides of the equation, and doing the integration for the wave functions,

$$\sum_{q=1}^{N} c_q \int \Psi_s^* H \Psi_q d\overrightarrow{r} = E\sum_{q=1}^{N} c_q \int \Psi_s^* \Psi_q d\overrightarrow{r} \tag{7.9}$$

using the representations $\widehat{c} = [c_1, c_2, \cdots, c_N]^T$, $\widehat{H} = \int \Psi_s^* H \Psi_q d\overrightarrow{r}$ and $\widehat{S}_{sq} = \int \Psi_s^* \Psi_q d\overrightarrow{r}$,

$$\widehat{H}\widehat{c} = E\widehat{S}\widehat{c} \Rightarrow (\widehat{H} - E\widehat{S})\widehat{c} = 0 \Rightarrow det(\widehat{H} - E\widehat{S}) = 0 \tag{7.10}$$

Thus for a single atom, the Hamiltonian operator can be expressed as

$$\widehat{H} = E\widehat{S}_{sq} \tag{7.11}$$

where $S_{sq} = \int \Psi_s^*(\mathbf{r})\Psi_q(\mathbf{r})d\mathbf{r}$. For the system with several atoms, combining above equations, the Hamiltonian operator can be rewritten as:

$$\widehat{H}_{sq} = E_0 S_{sq} - I_{sq}^a - I_{sq} \tag{7.12a}$$

$$E_0 = \frac{Z\varepsilon_0}{n^2}, \qquad \varepsilon_0 = -13.6eV \tag{7.12b}$$

where S_{sq} is the overlap integral, s and q are the orbitals of atoms s and q, α is any atom in the lattice, Ψ functions are defined with Eq. (7.2), $\mathbf{r}_s$, $\mathbf{r}_q$, $\mathbf{r}_a$, $\mathbf{r}$ are position vectors (of respective orbitals and atoms), θ is unit charge of an electron and Z the atomic number, and the Coulomb interactions can be expressed as

$$I^{a}_{sq} = \sum_{\alpha \neq s,q} Ze^2 \int \frac{\Psi^*_s(\mathbf{r})\Psi_q(\mathbf{r})}{|\mathbf{r}-\mathbf{r}_a|} d\mathbf{r} \tag{7.13a}$$

$$I_{sq} = \frac{Ze^2}{2} \int \left(\frac{1}{|\mathbf{r}-\mathbf{r}_s|} + \frac{1}{|\mathbf{r}-\mathbf{r}_q|} \right) \Psi^*_s(\mathbf{r})\Psi_q(\mathbf{r}) d\mathbf{r} \tag{7.13b}$$

7.3 Implementation of Quantum Model

To implement the rigorous approach of Hamiltonian calculation, each carbon should be coupled to all the atoms in the system, rather than just coupling with the closest neighbors. This section elaborately clarifies the algorithm of the rigorous model and presents the simulation results.

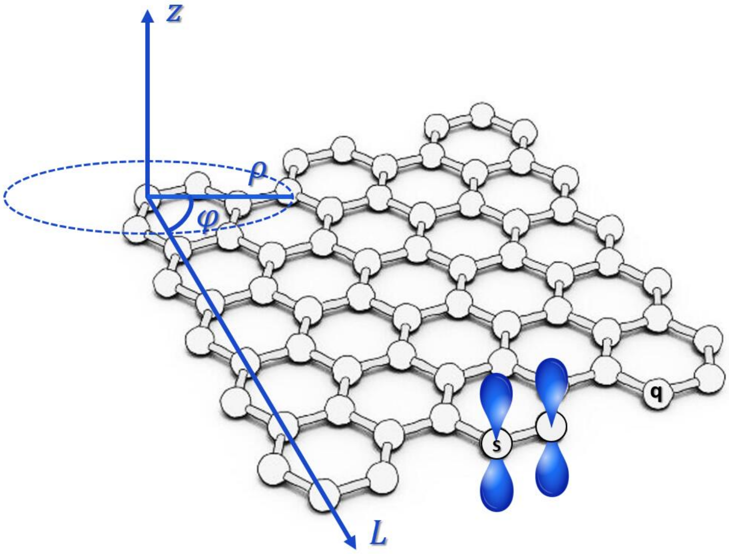

Figure 7.3: Graphene in cylindrical coordinate with the lattice in plane with $z = 0$.

For the purpose of calculating the integrals from Eqs. (7.13a)∼(7.13b), we use numerical methods because they cannot be calculated analytically. Firstly, we consider the geometry of the problem and the equations need to be expressed as functions of three variables: ρ, φ and Z, which are the coordinates in cylindrical system.

Figure 7.3 shows the graphene lattice in cylindrical coordinate system, while Fig. (7.4) a), b) and c) show the geometry of the problem and definitions of the vectors used in calculations.

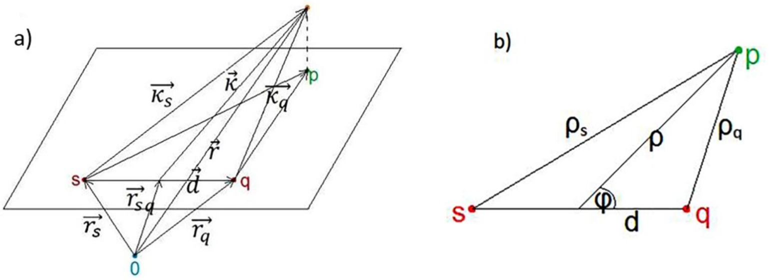

Figure 7.4: The geometry of the problem showing definitions of the vectors used in further calculations: a) definition of vectors to calculate the interaction between points s and q; b) definition of vectors at the plane $z = 0$.

Based on the geometry presented above in Fig. (7.4), lengths of vectors $\overrightarrow{K_s}$ and $\overrightarrow{K_q}$ can be expressed as:

$$|\overrightarrow{K_s}| = \sqrt{\rho^2 + d^2 + 2\rho d \cos(\varphi) + z^2} \tag{7.14a}$$

$$|\overrightarrow{K_q}| = \sqrt{\rho^2 + d^2 - 2\rho d \cos(\varphi) + z^2} \tag{7.14b}$$

where ρ, φ and Z are variables corresponding to the cylindrical coordinates system and d is length of vector **d**, which is half the distance between points s and q. The wavefunctions for orbitals s and q can be written as:

$$\Psi_s = \frac{1}{\sqrt{8\pi}} \frac{Z}{na_0} \left(\frac{Z}{a_0}\right)^{\frac{3}{2}} Ze^{-\frac{Z}{na_0}|\overrightarrow{K_s}|} \tag{7.15}$$

$$\Psi_q = \frac{1}{\sqrt{8\pi}} \frac{Z}{na_0} \left(\frac{Z}{a_0}\right)^{\frac{3}{2}} Ze^{-\frac{Z}{na_0}|\overrightarrow{K_q}|} \tag{7.16}$$

where $\frac{1}{\sqrt{8\pi}} \frac{Z}{na_0} (\frac{Z}{a_0})^{\frac{3}{2}}$ is the normalization constant A. Therefore S_{sq}, I^a_{sq} and I_{sq} can be expressed as follows:

$$S_{sq} = \int A^2 z^2 e^{-\frac{Z}{na_0}(|\overrightarrow{K_s}|+|\overrightarrow{K_q}|)} \rho d\rho d\varphi dz \tag{7.17a}$$

$$I^a_{sq} = \int \frac{A^2 z^2 e^{-\frac{Z}{na_0}(|\overrightarrow{K_s}|+|\overrightarrow{K_q}|)}}{\sqrt{\rho^2 + |R^a_{sq}|^2 - 2\rho |R^a_{sq}| \cos(\theta) + z^2}} \rho d\rho d\varphi dz \tag{7.17b}$$

$$I_{sq} = \int \left(\frac{1}{|\overrightarrow{K_s}|} + \frac{1}{|\overrightarrow{K_q}|} \right) A^2 z^2 e^{-\frac{Z}{na0}(|\overrightarrow{K_s}|+|\overrightarrow{K_q}|)} \rho d\rho d\varphi dz \tag{7.17c}$$

where $|R^a_{sq}|$ is the length of vector $\overrightarrow{R^a_{sq}} = \overrightarrow{r_{sq}} - \overrightarrow{r_a}$ and θ is the angle between vector $\overrightarrow{r}$ and the plane of the lattice.

Equations (7.17a)∼(7.17c) are subsequently plugged into Eq. (7.12a) and the elements of Hamiltonian matrix can be calculated. Each of the Eqs. (7.14a)∼(7.17c) are implemented as functions and then S_{sq}, I^a_{sq} and I_{sq} are integrated over ρ, φ and z in the main program with limits set to 0 to infinity for ρ, 0 to 2π for φ, and negative infinity to infinity for Z.

7.3.1 Simulations of Quantum Model

Using this algorithm, we have calculated the energy spectrum of graphene nanoflakes with different shapes. Figure 7.5 shows the energy spectrum for simple six-atom ring.

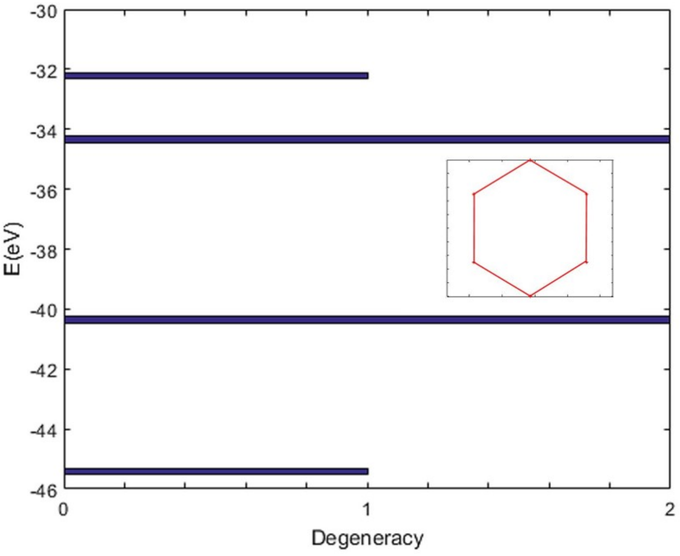

Figure 7.5: Energy level for simple six-atom ring.

Next, Hamiltonian matrices were calculated for several different shapes and sizes of graphene lattice and the results are presented below.

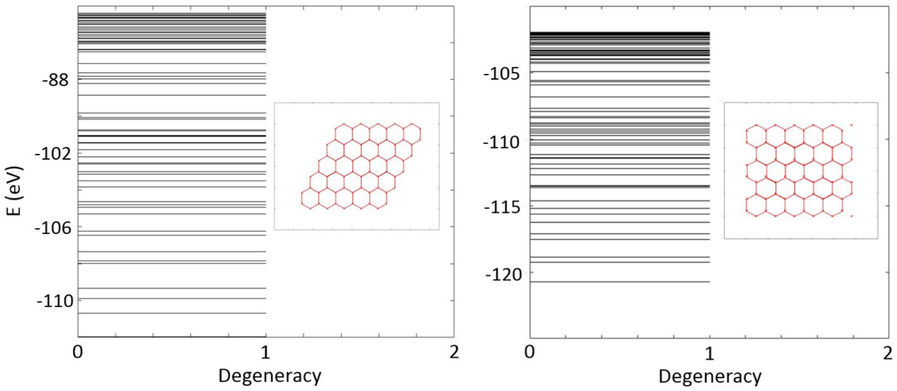

Figure 7.6: a) zig-zag and b)armchair ribbons energy levels calculated with the rigorous model. Inserts: lattice shapes.

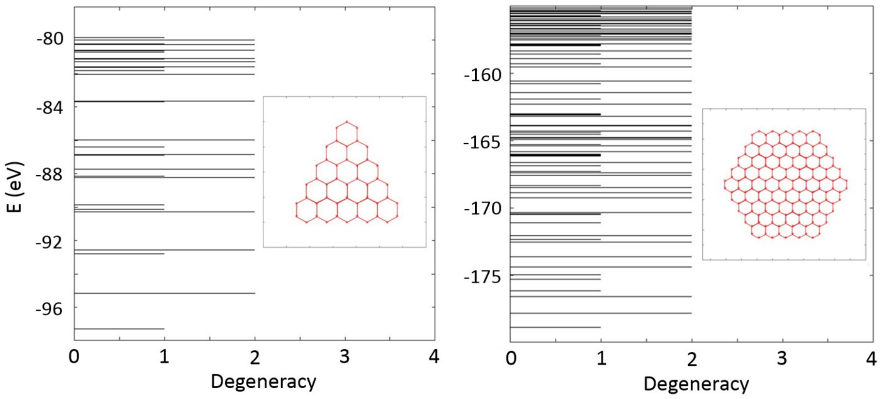

Figure 7.7: a) triangle and b)disk lattice shapes and energy levels calculated with the rigorous model.

After simulating simple structures with different atoms, we explored more complex structures in next section, e.g. two disks at different spacings to observe how coupling changes the band diagrams.

7.4 Coupling between Graphene Structures

After the rigorous models was successfully implemented, we simulate interactions between various structures in this section. As using the rigorous method for this would take a long time, only very small structures were simulated. The simplest case was considered first, just two benzene rings first right next to each other

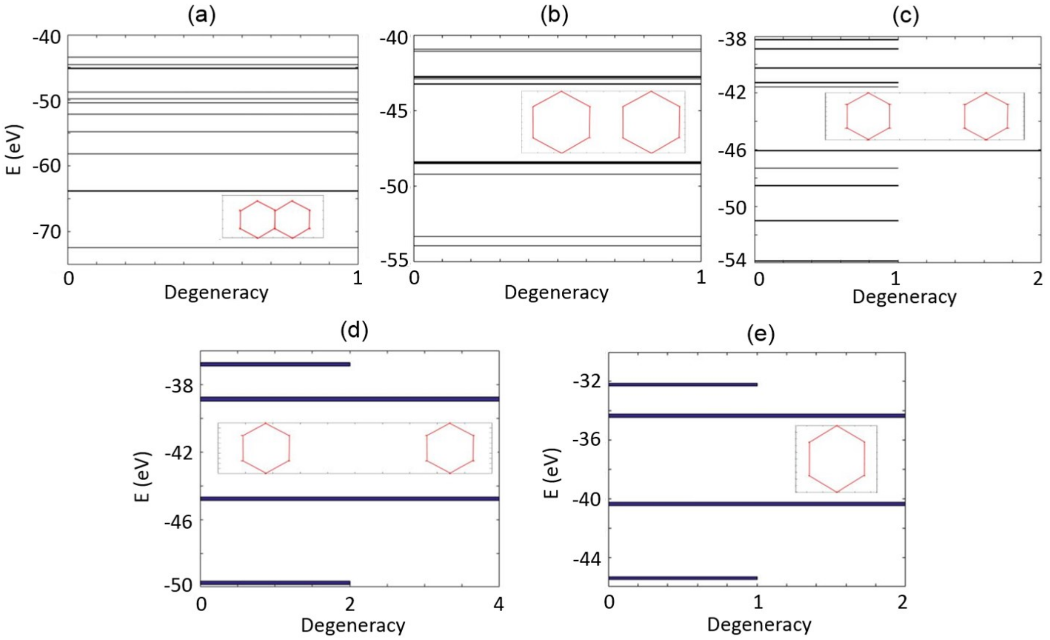

Figure 7.8: Band diagrams of a) two benzene rings merged, b) two benzene rings at 1 unit cell distance, c) at two unit cells distance, d) at three unit cells distance and d) a single benzene ring. Insets show lattice shapes.

(merged), then one lattice constant apart, and finally at large enough distance to be considered as separate structures, which in this case turned to be equal to only two lattice constants. The resultant band diagrams are shown in Fig. 7.8.

The band diagram for merged rings (a) shows the majority of energy levels are centered around middle value of around -20 eV, however there are also other levels much further away than observed for any other small shapes, i.e. at around 0 and -40 eV. In case of one lattice constant separation (b) we can see that the energy levels have moved away from the center and are at similar values as for the single or separated structures. The change in band diagrams for those cases confirms coupling. None of the levels in both of those cases are degenerate. Comparison of the bands of rings two lattice constants apart (c) and a single one (d) shows that the energies are of the same values, however the degeneracies have doubled, which is to be expected as there are twice as many atoms at each level now.

7.5 Conclusions

In conclusion, in this chapter we focused on investigating the properties of graphene from the quantum physics point of view. The lattice algorithm was created and the coordinates for various shapes successfully generated. The rigorous methods for calculating the Hamiltonian matrix and the energy levels of different structures were implemented. In addition, the energy bands formation for different graphene nanoflakes was demonstrated as well as the changes in those due to coupling between two structures.

I believe that the work presented in this chapter could be useful in the future work concerning graphene nanoflakes. It was demonstrated how the graphene geometrical and electrical properties are tuned with size. The effects of structure separation were also taken into account to better understand plasmonic properties of graphene and more realistically simulate its behaviour. More complicated geometries and arrays could be easily during this project. Plasmonic behavior could be investigated in devices where graphene arrays are used in combination with other materials such as gold sheets using models built in this project, as relatively small adjustments would have to be done to the design. Project continuation would also involve a closer investigation into the plasmon coupling in graphene arrays using the commercial simulation software like CST studio, which could further validate the numerical results. More advanced models could be built based on this project, which could include temperature dependence and graphene purity to better simulate real world situations.

Chapter 8

Light interaction with core-gap-shell nanoparticles

Electromagnetic wave scattering [1, 2, 3] from nanoparticles is an active, interdisciplinary research field with various practical applications ranging from medical imaging to atomic physics. Particularly, the topic of wave scattering by random scatterers and rough surfaces exhibits big theoretical challenges due to the large degree of freedom in these systems. Over the past few decades, crucial theoretical progress has been made in understanding and clarifying the scattering process pertaining to such problems [4, 5, 6, 7].

Numerical simulations allow us to solve the Maxwell equations without involving any approximations imposed in the analytical approaches. In this chapter, we will also discuss experimental results on scattering, near field intensity and two photon luminescence (TPL) of core-gap-shell nanoparticles (NPs), and then we present theoretical and numerical methods that are commonly used to study electromagnetic wave scattering problems. In the end, we compare the computational results with the corresponding experimentally measured values.

8.1 Experimental Characterization of Core-gap-shell Nanoparticles

Core-gap-shell nanoparticles are an assembly of nanoscale structures. This artificial structure is formed by using a particular nanomaterial to coat another kind of nanomaterial via chemical bonds or other interactions. This structure provides a few new properties and wider application prospects beyond those provided by single nanoparticle [8, 9, 10]. The design and controllable synthesis of composite nanomaterial with core-shell structures has been an increasingly significant frontier of material science in recent years. As functional materials, core-gap-shell NPs are favored by researchers because of their tunable optical properties of both core materials and shell materials.

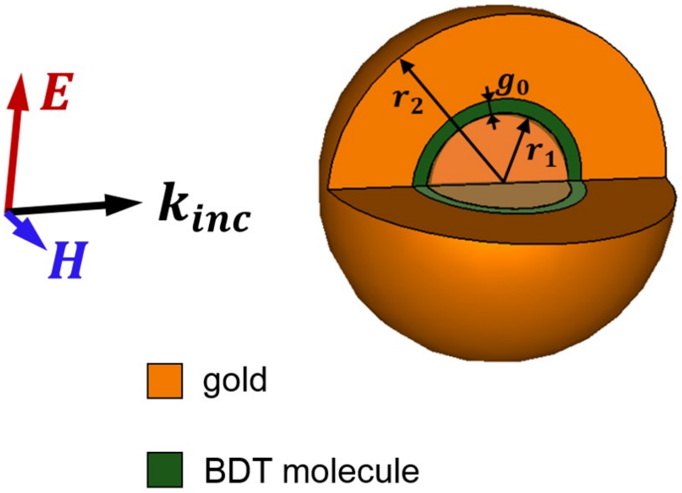

Figure 8.1: Geometrical configuration of core-gap-shell NPs with a BDT spacer layer, where the outer radius $r_1 = 30$nm and the inner radius $r_2 = 9$nm.

The experimental work on core-gap-shell NPs we present in this chapter was performed by Dr. Danjun Liu in Prof Dangyuan Lei's group at Hong Kong Polytechnic University. As shown in Fig. 8.1, the core-gap-shell NPs were composed of Au core and shell, as well as a benzodithiophene (BDT) molecule gap with the thickness g_0. The electric permittivity of BDT molecule ε_{BDT} is expressed by the equation below, where σ_{BDT} refers to the total conductivity of the BDT molecules.

$$\varepsilon_{BDT} = 1.59^2 + i\frac{\sigma_{BDT}}{\omega\varepsilon_0} \tag{8.1}$$

The experimental results are shown in Fig. 8.2. The dark-field optical image of BDT embedded core-gap-shell NPs with g_0=0.7 nm before and after nonlinear

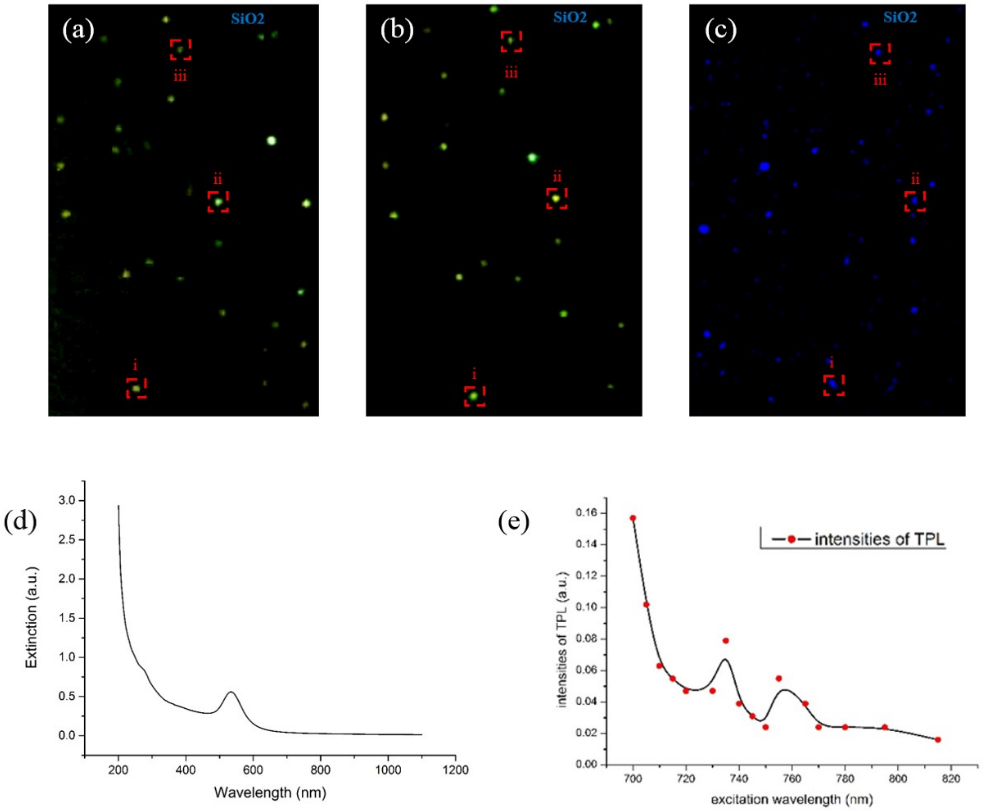

Figure 8.2: Dark-field optical image of BDT embedded core-gap-shell NPs (average 0.7 nm gap size) before (a) and after (b) nonlinear experiment. (c) TPL image with 700 nm excitation wavelength. (d) Extinction spectrum of BDT embedded core-gap-shell NPs (average 0.7 nm gap size). (e) TPL intensity of core-gap-shell NPs [11].

experiment are shown in Figs. 8.2(a) and (b), respectively. The nonlinear optical image with 700 nm excitation wavelength is presented in Fig. 8.2(c). The extinction spectrum (the part of incident light that is reduced after passing through the sample, including the absorption and scattering) and two-photon luminescence (TPL, two photons excite the sample, emiting a single photon, and generate the oscillation in the molecule) of BDT embedded core-gap-shell NPs are shown in Figs. 8.2(d) and (e), respectively. The TPL emission spectra of nanorods were interpreted by plasmon-enhanced interband transition, and exhibit two resonance peaks.

In the following sections of this chapter, we will demonstrate how to numerically compute the corresponding physical quantities and compare them with the experimental results.

8.2 Scattering of Electromagnetic Waves

The scattering of electromagnetic waves by systems whose size is smaller than the wavelength is a common and significant physical phenomenon. In particular it is convenient to regard the incident electromagnetic fields as inducing electric and magnetic multipoles that oscillate in definite phase relationship with the incident wave and radiate energy in directions other than that of incidence.

The exact form of the angular distribution of radiated energy is determined by the coherent superposition of multipoles induced by the incident fields and generally depends on the polarization state of incident wave. If the wavelength of the radiation is longer than the size of the scatter, only the lowest multipoles, generally electric and magnetic dipoles, are significant.

The basic scattering configuration amounts to a monochromatic plane wave incident on a scatterer. For simplicity, the surrounding medium is taken to have $\mu_r = \varepsilon_r = 1$. If the incident direction is defined by the unit vector $\boldsymbol{n}_0$, and the incident polarization vector is $\boldsymbol{\varepsilon}_0$, the incident fields are

$$\mathbf{E}_{inc} = \boldsymbol{\varepsilon}_0 E_0 e^{ik\mathbf{n}_0 \cdot \mathbf{x}} \tag{8.2a}$$

$$\mathbf{H}_{inc} = \mathbf{n}_0 \times \mathbf{E}_{inc}/Z_0 \tag{8.2b}$$

where $k = \omega/c$ is the wave number and a time-dependence $e^{-i\omega t}$ is understood [12]. These fields induce dipole moments $\mathbf{p}$ and $\mathbf{m}$ in the small scatterer and these dipoles radiate energy. Far from the scatterer, the scattered fields are

$$\mathbf{E}_{sc} = \frac{1}{4\pi\varepsilon_0} k^2 \frac{e^{ikr}}{r} [(\mathbf{n} \times \mathbf{p}) \times \mathbf{n} - \mathbf{n} \times \mathbf{m}/c] \tag{8.3}$$

$$\mathbf{H}_{sc} = \mathbf{n} \times \mathbf{E}_{sc}/Z_0 \tag{8.4}$$

where $\mathbf{n}$ is a unit vector in the direction of observation and r is the distance away from scatterer. The power radiated in the direction $\mathbf{n}$ with polarization $\boldsymbol{\varepsilon}$, per unit solid angle, per unit incident flux (power per unit area) in the direction $\mathbf{n}_0$ with polarization $\boldsymbol{\varepsilon}_0$, is a quantity with dimensions of area per unit solid angle. It is called the *differential scattering cross section*:

$$\frac{d\sigma}{d\Omega}(\mathbf{n},\boldsymbol{\varepsilon};\mathbf{n}_0,\boldsymbol{\varepsilon}_0) = \frac{k^4}{(4\pi\varepsilon_0 E_0)^2}|\boldsymbol{\varepsilon}^* \cdot \mathbf{p} + (\mathbf{n}\times\boldsymbol{\varepsilon}^*)\cdot\mathbf{m}/c|^2 \tag{8.5}$$

The dependence of the cross section on $\mathbf{n}_0$ and $\boldsymbol{\varepsilon}_0$ is implicitly contained in the dipole moments **p** and **m**. The variation of the differential (and total) scattering cross section with wave number k^4 (or in wavelength as λ^{-4}) is an almost universal characteristic of the scattering of long-wavelength radiation by any finite system. The dependence on frequency is known as *Rayleigh's law*.

Only if both static dipole moments vanish will the scattering fail to obey Rayleigh's law. The scattering is then via quadrupole or higher multipoles (or frequency-dependent dipole moments) and varies as ω^6 or higher. Sometimes the dipole scattering is known as Rayleigh scattering, but this term is usually reserved for the incoherent scattering by a collection of dipole scatterers.

8.2.1 Spherical Wave Expansion of a Vector Plane Wave

In discussing the scattering or absorption of electromagnetic radiation by spherical objects, of localized systems in general, it is useful to have an expansion of an electromagnetic wave in spherical coordinates.

For a scalar field $\psi(\mathbf{x})$ satisfying the wave equation, the necessary expansion can be obtained by using the orthogonality properties of the basic spherical solutions $j_l(kr)Y_{lm}(\theta,\phi)$. An alternative derivation makes use of the spherical wave expansion ($\frac{e^{ik|\mathbf{x}-\mathbf{x}'|}}{4\pi|\mathbf{x}-\mathbf{x}'|} = ik\sum_{l=0}^{\infty} j_l(kr_<)h_l^{(1)}(kr_>)\sum_{m=-l}^{l} Y_{lm}^*(\theta',\phi')Y_{km}(\theta,\phi)$) of the Green function ($e^{ikR}/4\pi R$). We let $|\mathbf{x}'| \longrightarrow \infty$ on both sides of the spherical wave expansion. Then we can put $|\mathbf{x}-\mathbf{x}'| \simeq r' - \mathbf{n}\cdot\mathbf{x}$ on the left hand side, where **n** is a unit vector in the direction of $\mathbf{x}'$. On the right side $r_> = r'$ and $r_< = r$. Furthermore we can use the asymptotic formfor $h_l^{(1)}(kr')$. Then we find

$$\frac{e^{ikr'}}{4\pi r'}e^{-ik\mathbf{n}\cdot\mathbf{x}} = ik\frac{e^{ikr'}}{kr'}\sum_{l,m}(-i)^{l+1}j_r(kr)Y_{lm}^*(\theta',\phi')Y_{lm}(\theta,\phi) \tag{8.6}$$

Cancelling the factor $e^{ikr'}/r'$ on either side and taking the complex conjugate, we arrive to the expansion of a plane wave

$$e^{i\mathbf{k}\cdot\mathbf{x}} = 4\pi \sum_{l=0}^{\infty} i^l j_l(kr) \sum_{m=-l}^{l} Y_{lm}^*(\theta,\phi) Y_{lm}(\theta',\phi') \tag{8.7}$$

where $\mathbf{k}$ is the wave vector with spherical coordinates k, θ', ϕ'. Put this in a more compact form

$$e^{i\mathbf{k}\cdot\mathbf{x}} = \sum_{l=0}^{\infty} i_l (2l+1) j_l(kr) P_l(\cos\gamma) \tag{8.8}$$

where γ is the angle between $\mathbf{k}$ and $\mathbf{x}$, P_l is the polarization at degree l and this can also be written as

$$e^{i\mathbf{k}\cdot\mathbf{x}} = \sum_{l=0}^{\infty} i_l \sqrt{4\pi(2l+1)}\, j_l(kr) Y_{l,0}(\gamma) \tag{8.9}$$

We now wish to make an equivalent expansion for a circularly polarized plane wave with helicity ±1 incident along the z axis,

$$\mathbf{E}(\mathbf{x}) = (\boldsymbol{\varepsilon}_1 + i\boldsymbol{\varepsilon}_2) e^{ikz} \tag{8.10a}$$

$$c\mathbf{B}(\mathbf{x}) = \boldsymbol{\varepsilon}_3 \times \mathbf{E} = \mp i\mathbf{E} \tag{8.10b}$$

Since the plane wave is finite everywhere, we can write its multipole expansion including only the regular radial functions $j_l(kr)$:

$$\mathbf{E}(\mathbf{x}) = \sum_{l,m} \left[a_+(l,m) j_l(kr) \mathbf{X}_{lm} + \frac{i}{k} b_\pm(l,m) \nabla \times j_l(kr) \mathbf{X}_{lm} \right] \tag{8.11}$$

$$c\mathbf{B}(\mathbf{x}) = \sum_{l,m} \left[\frac{-i}{k} a_\pm(l,m) \nabla \times j_l(kr) \mathbf{X}_{lm} + b_\pm(l,m) j_l(kr) \mathbf{X}_{lm} \right] \tag{8.12}$$

To determine the coefficients $a_\pm(l,m)$ and $b_\pm(l,m)$ we utilize the orthogonality properties of the vector spherical harmonics $\mathbf{X}_{lm}$. For reference purposes we summarize the basic relation, as well as some other useful relations:

$$\int [f_l(r)\mathbf{X}_{l'm'}]^* \cdot [g_l(r)\mathbf{X}_{lm}]d\Omega = f_l^* g_l \delta_{ll'}\delta_{mm'} \tag{8.13a}$$

$$\int [f_l(r)\mathbf{X}_{l'm'}]^* \cdot [\nabla \times g_l(r)\mathbf{X}_{lm}]d\Omega = 0 \tag{8.13b}$$

$$\frac{1}{k^2}\int [\nabla \times f_l(r)\mathbf{X}_{l'}m']^* \cdot [\nabla \times g_l(r)\mathbf{X}_{lm}]d\Omega = \delta_{ll'}\delta_{mm'}\left\{f_l^* g_l + \frac{1}{k^2r^2}\frac{\partial}{\partial r}\left[rf_l^*\frac{\partial}{\partial r}(rg_l)\right]\right\} \tag{8.13c}$$

In these relations $f_l(r)$ and $g_l(r)$ are linear combinations of spherical Bessel functions. The second and third relations can be proved using the operator identity, the representation

$$\nabla = \frac{\mathbf{r}}{r}\frac{\partial}{\partial r} - \frac{i}{r^2}\mathbf{r}\times\mathbf{L} \tag{8.14}$$

for the gradient operator, and the radial differential equation.

To determine the coefficients $a_{\pm}(l,m)$ and $b_{\pm}(l,m)$ we take the scalar product of both sides of Eq. 8.11 with $\mathbf{X}_{lm}^*$ and integrate over angles. Then with the first and second orthogonality relations in Eq. 8.13 we obtain

$$a_{\pm}(l,m)j_l(kr) = \int \mathbf{X}_{lm}^* \cdot \mathbf{E_x} d\Omega \tag{8.15}$$

and

$$b_{\pm}(l,m)j_l(kr) = c\int \mathbf{X}_{lm}^* \cdot \mathbf{B_x} d\Omega \tag{8.16}$$

With Eq. 8.10 for the electric field, the above equation becomes

$$a_{\pm}(l,m)j_l(kr) = \int \frac{(L_{\mp}Y_{lm})}{\sqrt{l(l+1)}}e^{ikz}d\Omega \tag{8.17}$$

where the components of **L** can be written conveniently in the combinations,

$$L_+ = L_x + iL_y = e^{i\phi}\left(\frac{\partial}{\partial\theta} + i\cot\theta\frac{\partial}{\partial\phi}\right) \tag{8.18a}$$

$$L_- = L_x - iL_y = e^{-i\phi}\left(-\frac{\partial}{\partial\theta} + i\cot\theta\frac{\partial}{\partial\phi}\right) \tag{8.18b}$$

$$L_z = -i\frac{\partial}{\partial\phi} \tag{8.18c}$$

And the results of their operating by

$$L_+Y_{lm} = \sqrt{(l-m)(l+m+1)}Y_{l,m+1} \tag{8.19a}$$

$$L_-Y_{lm} = \sqrt{(l+m)(l-m+1)}Y_{l,m-1} \tag{8.19b}$$

$$L_zY_{lm} = mY_{lm} \tag{8.19c}$$

Thus we obtain

$$a_\pm(l,m)j_l(kr) = \frac{\sqrt{(l\pm m)(l\mp m+1)}}{\sqrt{l(l+1)}}\int Y^*_{l,m\mp 1}e^{ikz}d\Omega \tag{8.20}$$

If expansion Eq. 8.9 for e^{ikz} is inserted, the orthogonality of the Y_{lm}'s evidently leads to the results,

$$a_\pm(l,m) = i^l\sqrt{4\pi(2l+1)}\delta_{m,\pm} \tag{8.21}$$

From Eq. 8.9 and Eq. 8.16, it is clear that

$$b_\pm(l,m) = \mp i a_\pm(l,m) \tag{8.22}$$

Then the multipole expansion of the plane wave is

$$\mathbf{E}(\mathbf{x}) = \sum_l^\infty i^l\sqrt{4\pi(2l+1)}\left[j_l(kr)\mathbf{X}_{l,\pm 1} \pm \frac{1}{k}\nabla\times j_l(kr)\mathbf{X}_{l,\pm 1}\right] \tag{8.23a}$$

$$c\mathbf{B}(\mathbf{x}) = \sum_l^\infty i^l\sqrt{4\pi(2l+1)}\left[-\frac{i}{k}\nabla\times j_l(kr)\mathbf{X}_{l,\pm 1} \mp i j_l(kr)\mathbf{X}_{l,\pm 1}\right] \tag{8.23b}$$

8.2.2 Scattering of Electromagnetic Waves by a Sphere

If an electromagnetic plane wave of radiation is incident on a spherical obstacle, as indicated schematically in Fig. 8.3, it is scattered, so that far away from the scatterer the fields are represented by a plane wave plus outgoing spherical waves. There may be absorption by the obstacle as well as scattering. Then the total energy flow away from the obstacle will be less than the total energy flow towards it, the difference being absorbed. We will ultimately consider the simple example of scattering by a sphere of radius a and infinite conductivity, but will for a time keep the problem more general.

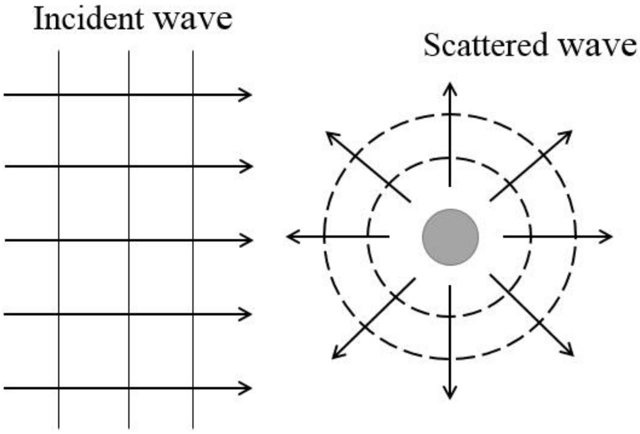

Figure 8.3: Scattering of radiation by a localized object.

The fields outside the sphere can be written as a sum of incident and scattered waves:

$$\mathbf{E}(\mathbf{x}) = \mathbf{E}_{inc} + \mathbf{E}_{sc} \tag{8.24a}$$

$$\mathbf{B}(\mathbf{x}) = \mathbf{B}_{inc} + \mathbf{B}_{sc} \tag{8.24b}$$

where $\mathbf{E}_{inc}$ and $\mathbf{B}_{inc}$ are given by Eq. 8.23a and 8.23b. Since the scattered fields are outgoing waves at infinity, their expansions must be of the form,

$$\mathbf{E}_{sc} = \frac{1}{2}\sum_{l=1}^{\infty} i^l \sqrt{4\pi(2l+1)} \left[\alpha_\pm(l) h_l^{(1)}(kr)\mathbf{X}_{l,\pm 1} \pm \frac{\beta_\pm(l)}{k}\nabla \times h_l^{(1)}(kr)\mathbf{X}_{l,\pm 1} \right] \tag{8.25a}$$

$$c\mathbf{B}_{sc} = \frac{1}{2}\sum_{l=1}^{\infty} i^l \sqrt{4\pi(2l+1)} \left[\frac{-i\alpha_\pm(l)}{k}\nabla \times h_l^{(1)}(kr)\mathbf{X}_{l,\pm 1} \mp i\beta_\pm(l) h_l^{(1)}(kr)\mathbf{X}_{l,\pm 1} \right] \tag{8.25b}$$

The coefficients $\alpha_\pm(l)$ and $\beta_\pm(l)$ will be determined by the boundary conditions on the surface of the scatterer. A priori, it is necessary to keep a full sum over m as well as l in Eq. 8.25, but for the restricted class of spherically symmetric problems considered here, only $m = \pm 1$ occurs.

Formal expressions for the total scattered and absorbed power in terms of the coefficients of $\alpha(l)$ and $\beta(l)$ can be derived from the scattered and total fields on the surface of a sphere of radius a surrounding the scatterer, with the scattered power being the *outward* component of the Poynting vector formed from the *scattered* fields, integrated over the spherical surface, and absorbed power being the corresponding *inward* component formed from the *total* fields. With slight rearrangement of the triple scalar products, these can be written

$$P_{sc} = -\frac{a^2}{2\nu_0} Re \int \mathbf{E}_{sc} \cdot (\mathbf{n} \times \mathbf{B}_{sc}^*) d\Omega \tag{8.26a}$$

$$P_{abs} = \frac{a^2}{2\nu_0} Re \int \mathbf{E} \cdot (\mathbf{n} \times \mathbf{B}^*) d\Omega \tag{8.26b}$$

Here $\mathbf{n}$ is a radially directed outward normal, $\mathbf{E}_{sc}$ and $\mathbf{B}_{sc}$ are given by Eq. 8.25, while $\mathbf{E}$ and $\mathbf{B}$ are the sum of the plane wave fields (8.23) and the scattered fields (8.23). Only the transverse. The other type of term in (8.23) and (8.25) is

$$\nabla \times f_l(r)\mathbf{X}_{lm} = \frac{i\mathbf{n}\sqrt{l(l+1)}}{r} f_l(r) Y_{lm} + \frac{1}{r}\frac{\partial}{\partial r}[r f_l(r)]\mathbf{n} \times \mathbf{X}_{lm} \tag{8.27}$$

where f_l is any spherical Bessel function of order l. When the multipole expansions of the fields are inserted in (eq:P), these result in a double sum over l and l' of various scalar products of the form $\mathbf{X}^*_{lm} \cdot \mathbf{X}_{l'm'}$, $\mathbf{X}^*_{lm} \cdot (\mathbf{n} \times X_{l'm'})$ and $(\mathbf{n} \times \mathbf{X}^*_{lm}) \cdot (\mathbf{n} \times \mathbf{X}_{l'm'})$. On integration over angles, the orthogonality relations reduce the double sum to a single sum. Each term in the sum involves products of spherical Bessel functions and derivatives of spherical Bessel functions. Use of the Wronskians ($W(j_l, n_l) = \frac{1}{i} W(j_l, h_l^{(1)}) = -W(n_l, h_l^{(1)}) = \frac{1}{x^2}$) permits the elimination of all the Bessel functions and yields the following expressions for the total scattering and absorption cross sections (the power scattered or absorbed divided by the incident flux, $1/\nu_0 c$):

$$\sigma_{sc} = \frac{\pi}{2k^2} \sum_l (2l+1)[|\alpha(l)|^2 + |\beta(l)|^2] \tag{8.28a}$$

$$\sigma_{abs} = \frac{\pi}{2k^2} \sum_l (2l+1)[2 - |\alpha(l)+1|^2 - |\beta(l)+1|^2] \tag{8.28b}$$

The total or extinction cross section is the sum of σ_{sc} and σ_{abs}:

$$\sigma_t = -\frac{\pi}{k^2} \sum_l (2l+1) Re[\alpha(l) + \beta(l)] \tag{8.29}$$

8.2.3 Transmission and Reflection through Spherically Layered Media

In this section, we use a scalar system to describe the electromagnetic wave so as to present the computation in simpler way. The derivation for an N-layer medium can be arrived at by first considering the case of a three-layer medium as shown in Fig. 8.4. As a result, Debye potentials are used to characterize the scalar waves.

In region 1, if there is an outgoing wave, the reflected wave will give rise to a standing wave. Hence, the Debye potential is in the form of

$$\pi_1 = c_1 \left[h_n^{(1)}(k_1 r) + \widetilde{R}_{12} j_n(k_1 r) \right] \tag{8.30}$$

where c_1 is the amplitude of the standing wave, while $\widetilde{R}_{12}$ is the generalized reflection matrix that relates an outgoing wave to a standing wave. The field in region 2 and 3 are

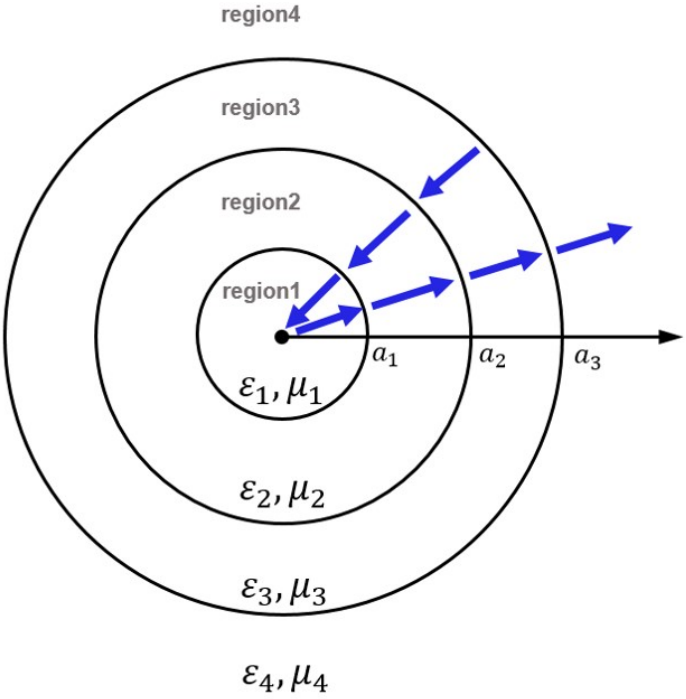

Figure 8.4: Theoretical calculation of extinction spectrum of BDT embedded core-gap-shell NPs with different BDT molecule gaps g_0.

$$\pi_2 = c_2 \left[h_n^{(1)}(k_2 r) + +\widetilde{R}_{23} j_n(k_2 r) \right] \tag{8.31}$$

$$\pi_3 = c_3 \left[h_n^{(1)}(k_3 r) + R_{34} j_n(k_3 r) \right] \tag{8.32}$$

Finally in region 4, there is only outgoing wave; therefore,

$$\pi_4 = c_4 h_n^{(1)}(k_4 r) \tag{8.33}$$

Since an outgoing wave in region 2 is a consequence of the transmission of an outgoing wave in region 1 plus the reflection of a standing wave in region 2, we have

$$c_2 = T_{12} \cdot c_1 + R_{21} \cdot R_{23} \cdot c_2 \tag{8.34}$$

Furthermore, the standing wave in region 1 is a result of the reflection of an outgoing wave in region 1 plus the transmission of a standing wave in region 2. Therefore, we have

$$\widetilde{R}_{12} \cdot c_1 = R_{12} \cdot c_1 + T_{21} \cdot R_{23} \cdot c_2 \tag{8.35}$$

The above two equations yields

$$c_2 = T_{12} \cdot c_1 + R_{21} \cdot R_{23} \cdot c_2 \tag{8.36}$$

and

$$\widetilde{R}_{12} = R_{12} + \frac{T_{21} R_{23} T_{12}}{1 - R_{21} R_{23}} \tag{8.37}$$

For an N=layer medium, the above can be used recursively to find the field in all regions.

$$\widetilde{R}_{i,i+1} = R_{i,i+1} + \frac{T_{i+1,i} \widetilde{R}_{i+1,i+2} T_{i,i+1}}{1 - R_{i+1,i} \widetilde{R}_{i+1,i+2}} \tag{8.38}$$

$$c_{i+1} = \frac{T_{i,i+1}}{1 - R_{i+1,i} \widetilde{R}_{i+1,i+2}} c_i = S_{i,i+1} c_i \tag{8.39}$$

In addition, a generalized transmission coefficient can be defined such that

$$\widetilde{T}_{1N} = S_{12} S_{23} \cdots T_{N-1,N} \tag{8.40}$$

which relates the outgoing wave amplitude in region N to that in region 1.

8.3 Numerical Modelling of Experimental Results

In this section, we present our numerical simulation work on fitting the experimental results of nonlinear optical properties of core-gap-shell NPs. Exciting the system with electromagnetic waves with wavelengths ranging from 200 nm to 1000 nm, we calculated the extinction scattering cross section of the BDT embedded core-gap-shell NPs with different BDT molecule gaps based on Eq. (8.29). The results are presented in Fig. 8.5. The corresponding extinction spectrum measured in the experiment is exhibited in Fig. 8.2(d), and there is good agreement between these two cases. Increasing the gap between the gold shell and core, the extinction spectrum of the core-gap-shell NPs decreases but does not change much.

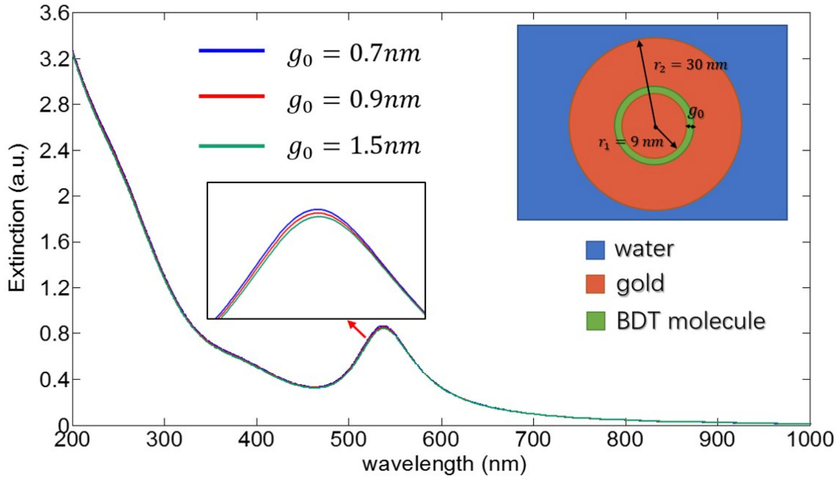

Figure 8.5: Theoretical calculation of extinction spectrum of BDT embedded core-gap-shell NPs with different BDT molecule gaps g_0.

To further explore the nonlinear optical properties of core-gap-shell NPs, the near field of the structure was also studied. As shown in Fig. 8.6(a), there are two resonance modes within the wavelength range, one corresponding to the extinction and one to the absorption. As the BDT molecule gap increases, the field intensity at the longer wavelength increases.

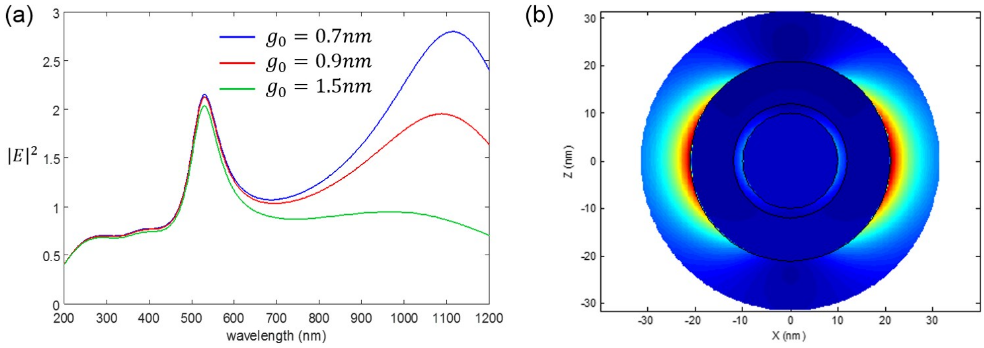

Figure 8.6: (a) Near field of core-gap-shell NPs with different molecule gaps g_0. (b) Two-dimensional near field distribution of core-gap-shell NPs.

The two-photon luminescence intensity of core-gap-shell NPs can be expressed using the near field and scattering cross section,

$$I_{TPL} = \left| \frac{E(r_1;\omega_a)}{E_0} \right|^2 \sigma_S(\omega_e) \tag{8.41}$$

The two-photon luminescence differs from fluorescence, in which the excitation wavelength is shorter than the emission wavelength, as the wavelengths of the two exciting photons are longer than the wavelength of the resulting emitted light. Two-photon luminescence involves two-photon absorption [13], and the most commonly used fluorophores have excitation spectra in the 400-500 nm range, whereas the laser used to excite TPL lies in the 700-1000 nm (infrared) range. According to the above analysis, the theoretical calculation of TPL intensity and corresponding experimental result are shown in Fig. 8.7(b) and (a), correspondingly.

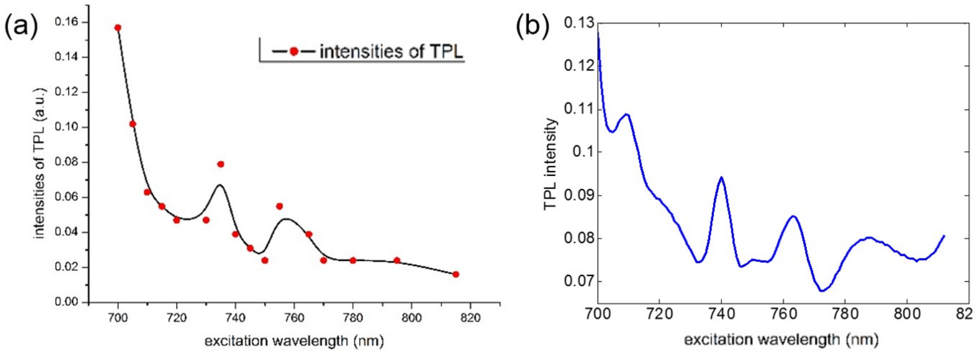

Figure 8.7: Experimental result (a) [11] and Theoretical calculation (b) of TPL intensity of core-gap-shell NPs.

The difference between the experimental and theoretical results on TPL spectrum are explained by the fact that only a few experimental data is recorded. In future work, many more experimental data will be recorded so that we can better fit the calculated TPL intensity.

8.4 Conclusions

In this chapter, we present the theoretical analysis of the scattering cross section of electromagnetic waves by spherical structures – core-gap-shell NPs. NPs with core/shell structure possess the properties of both core materials and shell materials, providing wider application prospects beyond those provided by single nanoparticle. These NPs made of Au and BDT molecules are often used in scattering based imaging and offer high sensitivity, high resolution, and multiplexing capability.

In the first part of this Chapter, we present experimental results pertaining to optical properties of core-gap-shell NPs, such as extinction and TPL spectrum. The experimental work on core-gap-shell NPs that we numerically investigated was performed by Dr. Danjun Liu in Prof Dangyuan Lei's group at Hong Kong Polytechnic University. The core-gap-shell NPs we studied were composed of Au and a BDT molecule gap. In the second part of the Chapter, we performed a numerical analysis and simulation work on fitting the experimental results of nonlinear optical properties of core-gap-shell NPs. The difference between the experimental and theoretical results is accounted by the small amount of recorded experimental data. As for the future, we would refine the experiment data so as to obtain more accurate TPL results.

Bibliography

[1] G. W. Kattawar, and G. N. Plass, Electromagnetic scattering from absorbing spheres, Appl. Opt. **6**, 1377-1382 (1967).

[2] P. C. Waterman, Symmetry, unitarity, and geometry in electromagnetic scattering, Phys. Rev. D **3**, 825 (1971).

[3] M. Kerker, D. S. Wang, and C. L. Giles, Electromagnetic scattering by magnetic spheres, J. Opt. Soc. Am. **73**, 765-767 (1983).

[4] K. A. Michalski, and D. Zheng, Electromagnetic scattering and radiation by surfaces of arbitrary shape in layered media. I. Theory, IEEE Trans. Antennas Propag. **38**, 335-344 (1990).

[5] O. J. Martin, C. Girard, and A. Dereux, Generalized field propagator for electromagnetic scattering and light confinement, Phys. Rev. Lett. **74**, 526 (1995).

[6] F. Onofri, G. Grehan, and G. Gouesbet, Electromagnetic scattering from a multilayered sphere located in an arbitrary beam, Appl. Opt. **34**, 7113-7124 (1995).

[7] L. P. Bayvel, *Electromagnetic scattering and its applications* (2012).

[8] M. Kerker, *The scattering of light and other electromagnetic radiation: physical chemistry: a series of monographs* (2013).

[9] C. F. Bohren, and D. R. Huffman, *Absorption and scattering of light by small particles* (2008).

[10] L. Novotny, and B. Hecht, *Principles of nano-optics* (2012).

[11] Research work by Dr Danjun Liu, MetaPhotonics and Metastructures Lab, Department of Applied Physics, Hong Kong Polytechnic University.

[12] J. D. Jackson, *Classical electrodynamics* (1999).

[13] M. Goppert-Mayer, Uber elementarakte mit zwei quantensprungen, Ann. Phys. **9**, 273-295 (1931).

Chapter 9

Conclusions and future work

The scientific and technical advances of photonics and optics have had a major impact on daily life. Study on photonics and optics captures dual nature of light: (1) as a propagating electromagnetic wave (2) as a collection of travelling particles which are so called photons. Applications of photonics are ubiquitous, ranging from spectroscopy, information processing to telecommunications and quantum computing. Particularly, nonlinear optics is one branch of optics that describes the light-matter interactions where the optical fields are strong enough to change material properties, such as Raman amplification, second-harmonic generation, third-harmonic generation and four-wave mixing. It has fundamental importance to physics, chemistry, and material science as a non-destructive probe of material properties and has important technological applications such as entangled photon generation and frequency conversion. Another significant research field is quantum optics, which utilizes semi-classical and quantum-mechanical physics to investigate phenomena involving light and its interactions with matter at submicroscopic levels.

This dissertation mainly explores the optical nonlinearities of different metamaterials and further utilizes the nonlinear optics to design quantum devices with specific functions. Two materials utilized in this thesis are silicon and graphene, respectively. Silicon offers a variety of nonlinear effects including Raman amplification that can be used to process optical signals as well as detect signals at unprecedented sensitivities for novel sensing applications and broadband electro-optic modulation. The electric field of the optical signal resonates with the electrons in the outer shells of the silicon atoms and thus causes nonlinear polarization. Graphene has high mobility and optical transparency, in addition to flexibility, robustness and environmental stability. The unique electronic properties of graphene originate from Dirac cones, features in electronic band structures that host charge carriers of zero effective mass, so-called massless Dirac fermions that occur in 2-D materials. Utilizing periodic structures with the above two materials, we could enhance the effective nonlinear optical susceptibilities of corresponding metamaterials.

The research work in chapter 3 and 4 introduce a powerful homogenization approach calculating optical properties for complicated metamaterial structures which is difficult to solve by Maxwell equations. Chapter 5 compares the homogenization approach for graphene-based and silicon-based metasurfaces, and illustrates that the homogenization approach is more suitable for graphene-based metasurfaces, because that the size of graphene unit cell is much smaller than the resonance wavelength. Chapter 6 provides a quantum dynamics algorithm which calculates the photon numbers with different optical parameters of the system.

The following sections will demonstrate my original contributions to the fields of nonlinear optics and quantum optics, as well as the future aspects to further extend my research work.

9.1 Contributions

The main contributions of this thesis can be separated into two aspects: firstly our research work provides a powerful homogenization technique to compute the effective nonlinear optical susceptibilities of different metamaterials made of silicon and graphene, correspondingly; the second one is related to the analysis of light propagation on a two-mode quantum system made of silicon photonic crystal nanocavities with the nonlinear Raman effect.

Specifically, in regard to the first part of this thesis, by designing a nonlinear optical metasurface made of two dimensional periodic array of silicon photonic crystal cavities, we utilized the novel homogenization approach to compute the effective nonlinear Raman susceptibility of the metasurface, and verified that it can be enhanced by more than 4 orders of magnitude as compared to that of silicon. Similarly, the graphene metasurfacs are also studied with the same numerical method. By investigating the optical response of one- and two dimensional graphene metasurfaces and their homogenized counterparts, we retrieved the effective permittivity and effective second-order susceptibility of one- and two dimensional graphene metasurfaces, respectively, and demonstrated that the effective second-order susceptibility can be enhanced by 3 orders of magnitude.

By comparing the optical response of these two metasurfaces and their effective counterparts, we illustrated that the homogenization approach is more suitable for graphene-based metasurfaces, because the characteristic size of the graphene constituents is much smaller than the wavelength, while the size of silicon cavity is comparable or larger than the wavelength of the interacting beams. Even though this developed homogenization approach on silicon-based metasurfaces is not as accurate as that on graphene, it can still give a qualitative analysis on the effective Raman susceptibility of silicon-cavity metasurfaces. Our developed homogenization approach is not only specific to these two types of metasurfaces, but can also be extended to other complex configurations, which will be discussed in detail in the next section. In addition, the ideas we presented have wide applicability, as they can be easily extended to other optical nonlinearities of practical interest, including third-harmonic generation, four-wave mixing, and sum- and difference frequency generation.

Concerning the second main contribution, particularly, a two-mode quantum waveguide made of coupled photonic crystal nanocavities was designed with specific quality factor, coupling constant, mode transfer coefficient, etc. We developed a quantum computational method to calculate the photon numbers at different nanocavities for each mode (pump mode and Stokes mode correspondingly). This work couples any number of nanocavities so as to realize the quantum manipulation of light in quantum systems, and thus providing a valuable reference for practical applications in quantum information processing and quantum interconnects. Dependence results of steady state photon numbers on different physical quantities could give the theoretical values of output with specific settings, which is beneficial to industrial fabrication of quantum devices.

Hamiltonian is the crux to investigate nano-structure from the quantum point of view. Starting from exploring how the quantum system operates, we could construct the Hamiltonian of this system which helps to study the photon dynamics. Another significant step is to find the general recursive expression of the density operator of photons, so as to simulate the time evolution of photon numbers as well as the steady state photon numbers. Additionally, since our study is performed in general cases, where the parameters of silicon have been normalized to fit any dielectric materials, our findings can be applied to explain many practical nanostructures by modifying certain coefficients, i.e. quantum waveguide made of coupled graphene disks.

In addition, the above two research works both utilize the optical nonlinearity, which has many applications:

- **THz generation** Broadband terahertz radiation can be generated by means of optical rectification from femtosecond pulses that rapidly change in time. Today, few THz systems have reached the stage of being practical, but this would provide great development space and vast prospective for the technology on THz generation.

- **Stimulated Raman lasers** Stimulated Raman scattering offers gain at frequencies separated from the laser pump by a molecular vibration. The variety of laser pump wavelengths and SRS materials provides exceptional diversity for lasers. Raman lasers have the greatest value when they generate wavelengths not available by other means.

- **Pulsing lasers** Nonlinear optics can create short laser pulses either by Q-switching or mode-locking. Some examples are traditional lasers with nonlinear photonic-crystal nanocavity and diode-pumped microchip lasers with a nonlinear Q-switch element.

- **Advanced spectroscopy** Nonlinear Spectroscopy uses an incident laser light field to perturb the optical properties of a molecule. Subsequent light probes see changes in molecular states. Experiments typically involve SHG or FWM.

- **Telecommunications** The dominant information technology impacted by nonlinear optics is fiber optic telecommunications. One of the most promising and cost effective ways to increase optical link throughput is a technique known as Wavelength Division Multiplexing, which is actually being used in commercial fibre telecommunication systems.

All in all, nonlinear optics provides major benefits to some very important applications in commercial lasers, telecommunications, sensors, environmental monitoring, medicine, manufacturing and materials processing, the military, and in scientific instrumentation. Taken together, these applications have considerable impact on daily life and advancing science.

9.2 Future Prospects

Research in this thesis mainly involves the enhanced optical nonlinearity of silicon and graphene metasurfaces as well as utilizing the nonlinear optics to design a two-mode quantum waveguide. Nonlinear optics on 2D materials is an important and promising research area and provides wide applicability and can be easily extended to many other nonlinear optical interactions of practical interest. Additionally, many other 2D materials besides graphene also exhibits extraordinary optical properties including extremely strong optical nonlinearities and the existence of tightly confined plasmon modes. Thus a full understanding of different nonlinear interactions of 2D materials is necessary for future needs of optical applications. Future prospects of my research work can be mainly divided into three parts, which will be discussed in detail in the following paragraphs.

Firstly, nonlinear optics, which explains nonlinear optical properties like frequency, polarization, phase and path of incident light, gives rise to numerous optical phenomena besides the second harmonic generation and Raman scattering we studied in this thesis. For example, some frequency-mixing processes such as four-wave mixing, and sum- and difference-frequency generation also deserve scientific research in like manner. An interesting idea is to design a graphene-based metasurface with FWM and to enhance the third-order susceptibility responsible for FWM using the homogenization approach. FWM can be used for a host of practical applications in optical telecommunications, such as wavelength conversion and optical switching.

In the second place, research on 2D materials is promising and fascinating in nonlinear optics nowadays due to their ultra-thin layer, strong light-matter interaction, ultra-broad band, large mechanical strength, high thermal conductivity and tunable absorption. Beyond graphene, other 2D materials like transition metal chalcogenides (MoS2, MoSe2, MoTe2, WS2, WSe2), perovskites, gallium selenide (GaSe), hexagonal boron nitride (BN) and black phosphorus can be studied in the similar method as we used for graphene in this thesis. These 2D materials have been successfully utilized in all-optical modulators, saturable absorbers used in passive mode locking and Q-switching, wavelength converters, and optical limiters.

As the final point, quantum waveguides have been studied by physicists, chemists and mathematicians for many years and the rate at which new contributions appear is still high. In this thesis, we design a one-dimensional quantum waveguide with two modes (pump mode and Stokes mode). As for the future work, 2D quantum system can also be studied using the similar algorithm we have developed in chapter 6. The complex pattern of the waveguide requires the higher-dimensional coordinates, which is possible to be used as a design principle for complicated photonic devices. Moreover, since photons have been used to test many of the counter-intuitive predictions of quantum mechanics such as entanglement and teleportation, related research involving such concepts provides plenty of interesting issues to solve in the future.